The BeppoSAX Gamma–Ray Burst Monitor response matrix and its application to the study of cosmic Gamma–Ray Bursts

Lorenzo Amati

Università di Roma "La Sapienza"

Dottorato di Ricerca in Astronomia
X Ciclo

Relatore: Dr. E. Costa

Referente: Prof. G.C. Perola

Coordinatore: Prof. P. Giannone

Introduzione

Questa Tesi descrive l' attivitá di ricerca finalizzata ad ottenere una descrizione delle funzioni di risposta spettrali e angolari dei rivelatori dell' esperimento Gamma–Ray Burst Monitor (GRBM) a bordo di BeppoSAX, il satellite Italo–Olandese dedicato all' astronomia X, e alla loro applicazione principalmente alla analisi spettrale a larga banda (1.5–700 keV) dei Gamma–Ray Bursts (GRB). L'attivitá di ricerca é stata svolta presso il gruppo di astrofisica delle alte energie dell' Istituto di Astrofisica Spaziale del CNR, Roma, e in collaborazione con l' Istituto TESRE del CNR, Bologna e con l'Universitá di Ferrara, nell' ambito del gruppo BeppoSAX/GRBM. Il testo é scritto in lingua inglese onde facilitarne la eventuale lettura da parte di colleghi stranieri e l' utilizzo di sue parti per la preparazione di pubblicazioni su riviste scientifiche internazionali.
In questa introduzione vengono riassunti il contesto astrofisico, le motivazioni e le fasi del lavoro.

Gamma–Ray Bursts: la sfida per l'astrofisica delle alte energie

I Gamma–Ray Bursts cosmici (GRB) sono le sorgenti piú misteriose nel campo dell'astrofisica delle alte energie. Si tratta di brevi ed intensi lampi di radiazione gamma provenienti da ogni direzione nel cielo e a tempi non prevedibili. Dalla scoperta, avvenuta nel 1967 e resa pubblica nel 1973, da parte di satelliti militari USA, molti esperimenti dedicati al loro studio hanno volato a bordo di missioni spaziali, aumentando il numero delle rivelazioni (piú di 2500) ma anche la complessitá del caso scientifico.
I GRB sono tipicamente rivelati nei raggi X–duri / gamma–molli (cioé tra circa 20 e 1000

keV), ma sono stati osservati anche fino a pochi keV e a decine di GeV. La loro tipica durata é di qualche decina di secondi, ma possono anche essere bevissimi (pochi millisecondi) o lunghi centinaia di secondi. I GRB sono eventi molto forti, con intensitá di picco che puó superare di un ordine di grandezza quella del fondo particellare ed elettromagnetico, esso stesso molto elevato. La morfologia dei gamma–burst é molto complessa e ne rende difficile la classificazione sulla base della forma della loro curva di luce, che puó essere caratterizzata da un singolo impulso o impulsi multipli, passando per un'ampia varietá di forme e tempi scala. Anche le loro proprietá spettrali variano molto da evento ad evento, ma con la generale tendenza dello spettro a diventare piú duro durante le salite degli impulsi e ad ammorbidirsi durante il loro decadimento.

A causa della complessitá della fenomenologia e delle scarse capacitá di localizzazione degli esperimenti nei raggi X–duri e nel gamma, la natura e l'origine dei GRB é rimasta completamente oscura fino all'inizio degli anni '90, senza nessuna possibilitá di potere discriminare tra modelli galattici e modelli cosmologici, con preferenza per i primi a causa della difficoltá nello spiegare l'enorme luminositá ($\sim 10^{51}$ erg/s per una distanza corrispondente a redshift ~ 1) richiesta per produrre i flussi osservati. Nemmeno modelli locali nei quali i GRB sono prodotti nella nube di Oort intorno al sistema solare potevano essere esclusi.

Un primo sostanziale passo avanti verso la comprensione dell'origine dei GRB é stato fatto negli anni '90 grazie all'esperimento BATSE (Burst and Transient Source Experiment) a bordo del Compton Gamma–Ray Observatory (CGRO) della NASA. Questo esperimento ha rivelato piú di 2000 eventi nella banda di energia 25–1000 keV e stimato per ciascuno di essi la durata, il flusso di picco, la fluenza ed in particolare la direzione di provenienza, con una precisione da circa 1 a 10 gradi. Le capacitá di localizzazione di BATSE sono alquanto scarse se confrontate con quelle dei telescopi utilizzabili a energie piú basse, ma hanno permesso di dimostrare due fondamentali proprietá della distribuzione dei GRB nel cielo: la isotropia delle direzioni di arrivo e il basso numero di eventi deboli rispetto a quello aspettato per una distribuzione spaziale omogenea. Questi risultati mettono in seria difficoltá i modelli galattici, mentre sono spiegati in modo naturale da quelli cosmologici. Tuttavia non escludono che i GRB possano essere originati in un alone esteso attorno alla galassia, con un raggio minimo dal centro galattico di 125 kPc.

Una svolta senza precedenti nella scienza dei GRB é stata prodotta nel 1997 dai risultati del satellite Italiano, con partecipazione Olandese, per l'astronomia X BeppoSAX. Questa missione non é progettato specificamente per osservazioni di GRB, ma trasporta la strumentazione adeguata per un nuovo approccio alle osservazioni di GRB. É stato in grado di rivelare simultaneamente con un rivelatore gamma (Gamma–Ray Burst Monitor, 40–700 keV) ed uno X (Wide Field Cameras, 1.5–26 keV), di localizzare con una precisione (pochi minuti d'arco) senza precedenti (utilizzando le capacitá di localizzazione del rivelatore X) e di eseguire il rapido (6–8 ore dopo la rivelazione) puntamento con telescopi X ad alta sensibilitá (0.2–10 keV, precisione di 1 arcmin) di 15 GRB, il primo dei quali il 28 Febbraio 1997 (GRB970228) e l'ultimo il 26 Dicembre 1998 (GRB981226). La precisione e la rapiditá della rivelazione e l'ampia diffusione dell'informazione hanno permesso ad altri osservatori di puntare questi eventi, portando alla scoperta per alcuni di essi di controparti ottiche e radio, ed alla misura della distanza tramite la stima del resdshift ottico.

Al momento della scrittura, BeppoSAX ha localizzato 17 eventi. Per tutti questi ha prodotto curve di luce e spettri in X e gamma, estendendo cosí fino a 1.5 keV la banda di energia sulla quale possono essere verificati i modelli di emissione. Per 15 eventi é stato rivelato un afterglow X, cioé una emissione tra 2 e 10 keV seguente l'evento e con decadimento secondo legge di potenza, rivelazione seguita in 8 casi dalla scoperta di sorgenti ottiche in decadimento in posizioni consistenti con quelle della sorgente X. In 6 casi é stata osservata emissione nel radio. La conseguenza piú importante di questi risultati é che i redshift stimati vanno da circa 0.8 (GRB970508) a 3.4 (GRB971214). Questo sembra confermare l'ipotesi cosmologica per l'origine dei GRB, coerentemente con i risultati di BATSE sulla distribuzione in cielo. Inoltre, é stata incrementata notevolmente la fenomenologia dei GRB; le curve di luce e gli spettri X del burst, l'emissione X, ottica e radio di afterglow hanno arricchito in modo straordinario il quadro osservativo, causando la messa in discussione di molti modelli esistenti e la elaborazione di nuovi.

Studio di GRB con il Gamma–Ray Burst Monitor di BeppoSAX

Il Gamma–Ray Burst Monitor (GRBM) a bordo di BeppoSAX é costituito dai 4 cristalli scintillatori di ioduro di cesio (attivato con sodio), aventi ciascuno 1 cm di spessore e area geometrica di 1136 cm^2, utilizzati primariamente come schermi di anticoincidenza laterale del Phoswich Detection System (PDS), ed equipaggiati con elettroniche e canali di acquisizione e trasmisisone dati per la rivelazione ('trigger') e la produzione di serie temporali ad alta risoluzione (fino a $\sim$0.5ms) di GRB nella banda 40–700 keV. Inoltre, vengono continuamente accumulati e trasmessi a terra tra i dati di housekeeping del PDS i conteggi al secondo misurati nelle bande 40–700 e $>$100 keV e spettri in energia tra 40 e 700 keV accumulati su 128 s.

La configurazione del payload di BeppoSAX é tale che due rivelatori del GRBM risultano co–allineati con le due Wide Field Cameras (WFC, rivelatori a immagine basati su contatori proporzionali sensibili alla posizione abbinati a maschere codificate, con banda tra 1.5 e 26 keV) a bordo dello stesso satellite. Questa particolare configurazione permette la simultanea rivelazione di GRB da parte del GRBM e delle WFC, fornendo alla missione BeppoSAX le capacitá senza precedenti per lo studio di questi oggetti descritte precedentemente.

In particolare, le capacitá di eseguire analisi spettrali a larga banda di GRB é in grado di fornire informazioni preziose e praticamente nuove sui meccanismi fisici alla base della emissione dei GRB, sull'ambiente in cui avviene il GRB e sulla connessione tra il burst e l'afterglow. Infatti, nonostante il grande passo in avanti fatto con la scoperta degli afterglows, l'origine e la fisica di questi misteriosi eventi cosmici rimane poco chiara e molto dibattuta, e l'estensione a bassa energia degli studi spettrali puó porre forti vincoli ai modelli teorici. Quasi tutti i rivelatori di GRB a bordo delle passate e delle attuali missioni spaziali operano ad energie superiori a ∼20 keV, come BATSE. Al di sotto di questa soglia di energia, poche misure erano disponibili prima di BeppoSAX, la maggior parte delle quali (una ventina) ottenute dal rivelatore di GRB a bordo del satellite giapponese Ginga, i cui dati a bassa energia soffrono peró di problemi legati alla non conoscenza della direzione di arrivo dell'evento.

Per potere sfruttare le potenzialitá della analisi spettrale simultanea dei dati del GRBM e delle WFC é necessaria una conoscenza soddisfacente delle funzioni di risposta dei rivelatori del GRBM nel campo di vista delle WFC. La collocazione del PDS al centro del payload di BeppoSAX fa sí che gli altri strumenti scientifici, le elettroniche associate, i servo–sistemi, le strutture del satellite, etc., oscurino in parte il campo di vista di ciascun rivelatore. Quindi, la ricostruzione della risposta dei rivelatori del GRBM in funzione della energia e della direzione di arrivo dei fotoni é complessa, e molti sforzi sono stati fatti in questo senso in termini di numerose e complete calibrazioni a terra e dello sviluppo di un modello Monte Carlo dell'intero satellite.
Lo scopo di questo lavoro di tesi é la ricostruzione delle funzioni di risposta dei rivelatori del GRBM a partire dall'analisi dei dati ottenuti dalle calibrazioni di terra, col fine principale di potere stimare il flusso e le proprietá spettrali delle sorgenti. Questo lavoro e' anche fondamentale per potere sfruttare le capacitá di localizzazione e per la verifica del modello Monte Carlo.
La prima rivelazione simultanea di un GRB (GRB960720, circa 3 mesi dopo il lancio del satellite) ha accelerato la necessitá della conoscenza della matrice di risposta del GRBM nel campo di vista delle WFC. Quindi é stata data la prioritá a questa attivitá. Anche il lavoro sulla localizzazione é in via di sviluppo, basandosi parialmente sul lavoro qui descritto.

Le calibrazioni mostrano che, a differenza delle alte due unitá, i due rivelatori co–

allineati con le WFC hanno un campo di vista sufficientemente pulito e uniforme e che la ricostruzione delle loro funzioni di risposta puó essere ottenuta analiticamente, utilizzando risultati preliminari delle simulazioni Monte Carlo per discriminare i contributi passivi e ambientali e per estrapolare l'efficienza dei rivelatori a energie non coperte dalle calibrazioni.

Struttura della Tesi

Questa Tesi riporta tutti i processi che a partire dalla analisi delle calibrazioni di terra hanno portato alla ricostruzione delle funzioni di risposta in particolare dei rivelatori GRBM co–allineati con le WFC, lo sviluppo di software e tecniche di analisi specifiche per la estrapolazione del flusso e della evoluzione spettrale di sorgenti dai ratemeters a 1 s e delle proprietá spettrali medie dagli spettri in energia accumulati ogni 128 s, le prestazioni e la calibrazione in volo tramite misure della Crab e confronto con i risultati di BATSE, e la applicazione delle matrici di risposta, del software e delle tecniche di analisi allo studio di flusso e propietá spettrali di GRB e Soft Gamma Repeaters (SGR).

Nel primo capitolo viene fornita una descrizione generale della stumentazione scientifica di BeppoSAX funzionale alla comprensione della distribuzione di massa attorno al GRBM, e dei software di riduzione e analisi dati il cui uso costituisce. Successivamente viene data una descrizione dettagliata dell'esperimento PDS/GRBM, con particolare enfasi sui dati cientifici prodotti dal GRBM.

I due capitoli successivi descrivono le fasi della costruzione delle matrici di risposta (capitolo 3), partendo da una dettagliata descrizione delle calibrazioni di terra e dei loro risultati (capitolo 2), passando attraverso la stima dell'area efficacie in asse in funzione dell'energia, descrivendo quindi l'interpolazione con funzioni analitiche della dipendenza dalla direzione di incidenza dei fotoni dell'efficienza dei due rivelatori co–allineati con le WFC, e giungendo infine alla descrizione della modellizzazione degli spettri delle sorgenti monocromatiche di calibrazione e alla stima dei contributi ambientali, al fine di ricostruire la risposta spettrale. Nel capitolo 3 viene fornita anche una breve descrizione del modello Monte Carlo, assieme al confronto dei risultati preliminari delle simulazioni con le calibrazioni. In questo capitolo viene anche descritto il software utilizzato per la riduzione e l'analisi dei dati di calibrazione, che é in parte stato prodotto dal BeppoSAX/GRBM team (spacchettamento, riduzione e quick–look dei dati), ed in parte é stato sviluppato per questo lavoro (software di analisi dei dati di calibrazione, di modellazione analitica e fitting della risposta dei rivelatori, di generazione delle matrici di risposta in formati standard).

Il capitolo 4 descrive i dati di volo, con particolare enfasi al fondo in orbita, alla riduzione dei dati, alla sottrazione del background e alle tecniche di analisi spettrale dai ratemeters a 1 s e dagli spettri a 128 s. Inoltre, vengono riportati i metodi sviluppati per la misura di flusso e spettro della Crab nebula al fine di verificare le funzioni di risposta del GRBM. Sono inoltre descritti e discussi confronti con i risultati di BATSE.

Il quinto capitolo contiene la descrizione ed i risultati della applicazione della funzione di risposta del GRBM alla analisi spettrale di GRB simultaneament rivelati da una delle due WFC, 15 al momento di scrivere questa tesi (GRB981226 l'ultimo). Per molti di loro, in funzione anche della qualitá statistica dei dati, sono stati ottenuti e analizzati lo spettro medio e la evoluzione spettrale GRBM e WFC+GRBM. Come discusso in precedenza, questi risultati sono di grande intersse per lo studio dei GRB e sono stati pubblicati in specifici articoli su riviste scientifiche (alcuni dei quali riportati in appendice).
Viene inoltre descritto un lavoro sulla osservazione GRBM del soft gamma repeater SGR1900+14, un interessante caso scientifico ed un esempio di applicazione delle matrici di risposta del GRBM al di fuori del campo di vista delle WFC.

Infine, nel capitolo 6 vengono brevemente riassunti i risultati del lavoro svolto e descritte le attivitá in corso e le prospettive future.

Contents

List of Figures

List of Tables

Introduction

This thesis describes the research work aimed to obtain a description of the spectral/angular response functions of the detectors of the Gamma–Ray Burst Monitor (GRBM) experiment on–board BeppoSAX, the Italian–Dutch X–ray astronomy satellite, and their application mainly to broad band (1.5–700 keV) spectral analysis of cosmic Gamma Ray Bursts (GRBs).

In this introduction we synthesize the astrophysical context, motivation and the steps of the work.

Gamma–Ray Bursts: the challenge of high energy astrophysics

The cosmic gamma-ray bursts (GRB) are the most mysterious objects in high energy astrophysics. They are intense and short flashes of gamma radiation arriving from any direction in the sky at unpredictable times. Since their discovery in 1967 (announced in 1973) by USA military satellites, many dedicated experiments have flown on scientific space missions, increasing the number of detections (more than 2500 nowadays) but also the complexity of the scientific case.

GRBs are typically detected in the hard X / soft gamma band (i.e. from 20 to 1000 keV), but they have been observed also down to few keV and up to tenths of GeV. Their typical duration is of few tenths of seconds, but event as short as one tenth of second and as long as hundreds of seconds have been measured. GRBs are very strong events, with peak intensity that can exceed of one order of magnitude that of the (huge) particle and electromagnetic background. The bursts morphology is very complex and makes it difficult to classify them on the shape of their light curve, which varies from single pulse events to multiple pulses, through a wide variety of shapes and time scales. Also their spectral properties vary a lot from event to event, but with the general trend of spectrum hardening during each pulse rise and softening during the pulse decay.

Due to the complexity of their phenomenology and to the very poor localizing capabilities of hard X–ray and gamma–ray experiments, the nature and origin of GRBs has remained very obscure till about 1990, with no possibility to choose between galactic and cosmological models, with the former preferred because of the difficulty in explaining the huge luminosity ($\sim 10^{51}$ erg/s for a distance corresponding to redshift 1) required to produce the observed fluxes. Even local models, in which GRBs are produced in the Oort cloud around the solar system, could not be excluded.

A first significative step forward GRBs origin has been made in the nineties with the BATSE experiment on–board the NASA Compton Gamma–Ray Observatory. This experiment has detected more than 2000 events in the 25–1000 keV energy range, estimating for each one duration, peak flux, fluence and, most important, a position in the sky with an accuracy going from about one to about 10 degrees. The BATSE localizing capabilities are still very poor in comparison with the capabilities of telescopes at lower wavelengths, but have permitted to demonstrate two fundamental properties of the GRBs distribution in the sky: the isotropy of the arrival directions and the paucity of weak events with respect to an homogeneous spatial distribution. These results put in serious difficulty classic galactic models and are naturally explained by cosmological models; nevertheless, they don't exclude that GRBs may origin from an extended galactic halo with a minimum radius of 125 kPc.

An unprecedented break–through in GRBs science has been produced in 1997 by the Italian/Dutch satellite for X–ray astronomy BeppoSAX results. The BeppoSAX satellite is not specifically designed for GRBs observations, but carries the right instrumentation for a new approach to GRBs observations. It has been able to detect simultaneously with a gamma (40–700 keV) and X (1.5–26 keV) detectors, localize with an unprecedented (few arcmin) accuracy (by exploiting the localizing capabilities of the X–ray detector) and perform fast (6–8 hours after the detection) follow-up with high sensitivity X–ray telescopes (0.2–10 keV, 1 arcmin accuracy) of 15 GRBs up to now, allowing for the discovery of X-ray afterglows of GRB, the first of which in February, 28 1997 and the last in December, 26 1998. The precision and rapidity of the detection, and the wide dissemination of information has permitted other observatories to point the events, leading to the discovery for some of them of optical and radio counterparts, and the measurement of their distance through the optical redshift estimation. At the time of writing, BeppoSAX has localized 17 events, GRB960720 the first and GRB981226 the last. For all of these it has provided X and gamma–ray light curves and spectra, extending down to 1.5 keV the energy band on which the emission models can be tested. For 15 of them an X–ray afterglow, i.e. a power–law decay emission in the 0.2–10 keV energy band following the burst, has been detected, followed in 8 cases by the discovery of optical fading sources in position consistent with the X–ray source error box. In 6 cases also radio emission was observed. The most important consequence of these results is that the redshifts estimated from some of the optical counterparts range between 0.8 (GRB970508) and 3.4 (GRB971214). Thus, the cosmological origin of GRBs seems to be confirmed, consistently also with BATSE results on bursts distribution in the sky. In addition, the new phenomenology discovered, i.e. X–ray light curve and spectra of the burst, X, optical and radio afterglows, have enriched in an unprecedented way the observational picture, allowing the challenging of existing theoretical models and the growth of new ones.

GRB science with the BeppoSAX Gamma–Ray Burst Monitor

The BeppoSAX Gamma–Ray Burst Monitor (GRBM) consists of the four cesium iodide (sodium activated) crystal scintillators, 1 cm thick, 1136 cm^2 geometric area each, acting primarily as lateral anticoincidence shields of the Phoswich Detection System (PDS), equipped with dedicated electronics and data storage/transmission for detection (trigger) and high resolution (down to ∼0.5 ms) timing of GRBs in the 40–700 keV energy range. In addition, the measured counts/s in the 40–700 and >100 keV bands and energy spectra in the 40–700 keV band accumulated over 128 s time intervals are continuously stored and transmitted to ground among the PDS housekeeping.

The BeppoSAX payload design is such that two GRBM detectors are co–aligned with the two Wide Field Cameras (WFC, two coded mask proportional counters, 1.5–26 keV energy band) on–board the same satellite. This particular configuration allows for detecting GRBs in the WFC and the GRBM simultaneously, giving the BeppoSAX mission unprecedented capabilities in the study of these objects. In particular, the BeppoSAX broad band GRB spectral study capabilities, can give us a lot of almost new information on the physical mechanisms underlying GRB emission, on the environment in which the event takes place and on the connection between the GRB proper and its afterglow. Indeed, despite the improvements due to the afterglows discovery, the origin and physics of these mysterious cosmic events is still unclear and debated, and the extension of spectral study to low energies (i.e. few keV) can put several constraints on theoretical models. Almost all GRB detectors on–board past and still active missions operate above about 20 keV, as BATSE. Very few spectral data down to 2 keV of GRB were available before BeppoSAX detections and most of them are from the GRB detector on–board the Japanese mission Ginga, whose low–energy data suffered the lack of the knowledge of the event direction.

To exploit the GRBM + WFC spectral capabilities, a satisfactory knowledge of the response functions of the GRBM detectors in the field of view of the WFC is required. The location of the PDS at the center of the BeppoSAX payload is such that other scientific instruments, associated electronics, satellite structures, etc., partially obscure the fields of view of each shield. Thus, the reconstruction of the GRBM detectors response as a function of incident photon energy and direction is complex, and many efforts have been made do address it by means of extensive on–ground calibrations and the development of a Monte Carlo model of the whole satellite. The analysis of calibration data is a the core of this thesis work, and, in addition to the reconstruction of GRBM capabilities of estimating source flux and spectral properties, it is the basis for event positioning and Monte Carlo model verification. The first simultaneous detection by GRBM and WFC of a GRB (GRB960720, about three months after the satellite launch) soon evidenziated the urgent need for an accurate knowledge of the GRBM response function, especially in the part of the field of view overlapped with the WFC. This work was then given the highest priority. The work on GRB localization is also improving, based partially on the work described here.

As expected from the payload configuration, calibrations show that the the fields of view the two detectors co–aligned with the WFC are rather clean and uniform, and their response functions can be reconstructed analytically using on ground calibrations, with use of preliminary Monte Carlo simulations results as a tool to discriminate environmental and other passive contributions and to extrapolate detectors efficiency at energies not covered by calibrations.

Thesis structure

This thesis reports all the processes that starting from on–ground calibrations data analysis have led to the reconstruction of the response functions of the GRBM detectors co–aligned with the WFC, the development of specific software and data analysis technique needed to extrapolate source flux and spectral evolution from the 1 s ratemeters and average spectra from the 128 s energy spectra, in–flight calibration against Crab measurements and BATSE results, and the application of response matrices, data reduction and analysis techniques and software to the study of spectral properties of GRBs and soft gamma repeaters (SGR).

In chapter 1 we give an overall description of the BeppoSAX scientific payload which is functional to understanding the mass distribution around each GRBM detector. A detailed description of the PDS/GRBM experiment is then given, with particular stress on those scientific data available from it from which we can obtain spectral information.

The next two chapters describe the steps followed in the construction of the response functions (chapter 3), starting from a detailed description of on–ground calibrations and their results (chapter 2), going through the estimation of on–axis effective area as a function of energy, the interpolation with analytical functions of the effective area dependency on source direction for the two detectors co–aligned with the WFC, and finally the modeling of calibration line spectra, together with estimation of spurious contributions estimation, to reconstruct the spectral response functions. A brief description of the Monte Carlo model is also given in chapter 3, together with comparison between calibration and simulation results. In this chapter we give also a detailed description of calibrations data formats and of the software that was utilized for data reduction and analysis, which is partly work of the PDS/GRBM hardware group (data reduction and quick analysis) and partly original work for this thesis (specific on–ground calibration data analysis software, modeling and fitting of detectors response, response matrices writing in standard formats).

Chapter 4 describes the GRBM in–flight performances and data analysis techniques and software, with particular emphasis on in–orbit background, data reduction, background subtraction and spectral analysis techniques for 1 s ratemeters in the GRBM and AC bands and 240 channel / 128 s spectra. In addition, here are reported the methods developed to obtain measurements of Crab Nebula flux and spectrum in order to verify GRBM response functions. Cross–checks with BATSE results are also described and discussed.

The fifth chapter contains the description and results of the application of GRBM response function to the spectral analysis of GRBs simultaneously detected by one of the WFC. At the time of this thesis writing, 15 such events have been detected (GRB981226 is the last). For most of them, depending also on the statistical quality of the data) GRBM average spectrum and spectral evolution analysis have been performed, and for many of them also WFC+GRBM data analysis has been done. As discussed above, the results presented here are of high interest in GRB science and have been published in scientific papers (reported in the appendix).

Work and results on the GRBM detection of the soft gamma repeater SGR1900+14 is also reported, being a very interesting scientific case and an example of application of the GRBM response matrix outside the WFC FOV.

Finally, chapter 6 resumes the work done and describes the work in progress and the future perspectives.

Chapter 1

The BeppoSAX Gamma Ray Burst Monitor experiment

1.1 The BeppoSAX satellite

1.1.1 Mission overview

BeppoSAX (Boella et al. 1997a, Piro et al. 1995, Scarsi 1993) is a space mission dedicated to X–ray astronomy of the Italian Space Agency (ASI, Agenzia Spaziale Italiana) with participation of the Netherlands Agency for Aerospace Programs (NIVR). The project started about 15 years before the launch and involves several Italian institutions (IAS–CNR and IOA–'La Sapienza' University in Rome, IFCAI–CNR and GIFCO in Palermo, IFCTR–CNR and GIFCO in Milan, ITESRE–CNR in Bologna, Department of Physics–University of Ferrara), one Dutch institution (SRON in Utrecht) and the SSD–ESA in Noordwijk (NL). ASI prime contractors are Alenia Aerospazio, Torino (Italy), for the spacecraft and Telespazio, Roma (Italy), for the ground segment. The original mission name was SAX (Satellite per l 'Astronomia X); it was renamed BeppoSAX after launch in honor of the Italian physicist Giuseppe "Beppo" Occhialini. The spacecraft carries a set of instruments allowing simultaneous high sensitivity ($\sim$10 mCrab) observations of sources in the unprecedented wide energy band 0.1– 300 keV, the monitoring (at $\sim$ 10 mCrab sensitivity) of large regions of the sky in 1.5–26 keV with 3 arcmin angular resolution, and the detection and spectral study in 40–700 keV of high energy transients

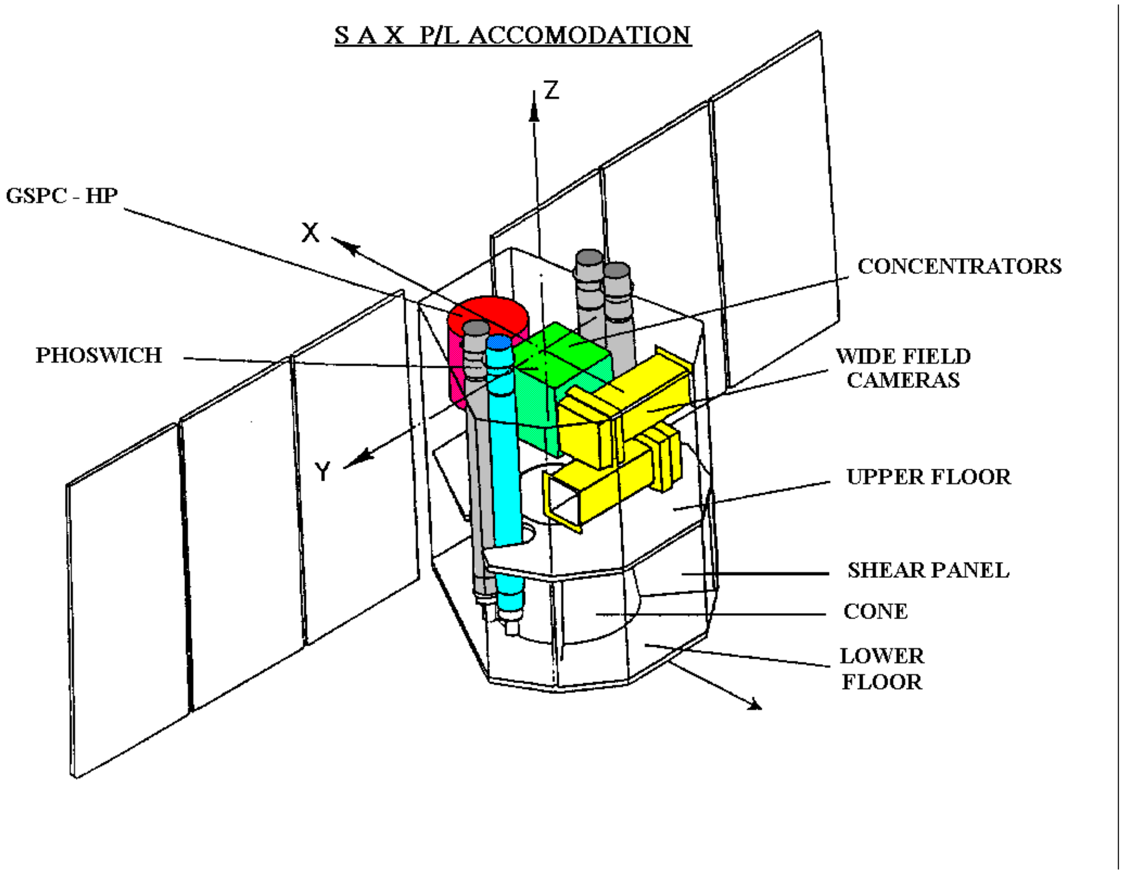

Figure 1.1: Schematic representation of the BeppoSAX satellite *(from the BeppoSAX Observers' Handbook)*

(GRB, SGR). The satellite (sketched in Fig. 1.1) is composed of two basic structures: the service module, in the lower part, housing subsystems and electronics of the scientific instruments, and the payload module, with scientific instruments and star trackers. A thermal shade structure surrounds the payload module. The total mass is 1400 kg (480 kg the payload alone), for an height of 3.6 m and a diameter of 2.7 m (with solar panels closed).

BeppoSAX was successfully launched from Cape Canaveral on April 30, 1996 into a 600 Km nearly equatorial (3.9° inclination) orbit by an Atlas G–Centaur rocket. This orbit was chosen in order to minimize background intensity (by taking advantage of the reduction of the flux of cosmic –rays contribution due to the screening effect of Earth's magnetic field) and because of the marginal passage through the South Atlantic Geomagnetic Anomaly (SAGA) and of the very low modulation of the Earth magnetic field rigidity cut-off and consequently of the particle induced background. The time needed to cover a complete orbit is 97 minutes. The Earth' s angular diameter at this distance is about 130°. The pointing is three axis stabilized with an accuracy of the order of 1 arcmin, which is therefore the limiting angular resolution for BeppoSAX observations. During each orbit up to 450 Mbits of data are stored to the on-board mass memory and transmitted to ground during the radio contact with the Malindi (Kenya) ground station. The time window for data retrieval and commands transmitting is $\sim$10 minutes per orbit. The Operational Control Center (OCC), the Scientific Operation Center (SOC) and the Scientific Data Center (SDC) are all located in Telespazio, Rome, where the data are finally received and commands transmitted to Malindi through a dedicated intelsat bi–directional link (Bruca et al. 1998). The OCC performs orbital management and telecommands uplinking. The SOC is responsible for scientific instruments monitoring, planning of the on–board scientific activities, archiving of the orbit–by–orbit raw telemetry data for quick look analysis. The SDC manages the observation proposals and sends them to the Time Allocation Committee (TAC), collects and checks approved observations, performs long period observation planning. It is responsible for raw data final archiving and the release of the Final Observation Tapes (FOT) to the final users after quality check and standard analysis. The overall Ground Segment (GS) operations are resumed in Fig. 1.2.

The observational strategy is to dedicate most of the time to Narrow Field Instruments (see next subsection) pointings, with the Wide Field Cameras (see next subsection) monitoring the galactic plane in secondary mode. The flexibility of the planning allows for several Target of Opportunity (TOO) observations. The observing program is divided in a Core Program (CP, assuming an optimal use of the satellite), open for proposals from Italian and Dutch institutions, ESA/SSD and MPE/Garching, and the Guest Observer Program (GOP) open to the worldwide scientific community. Data of every observation

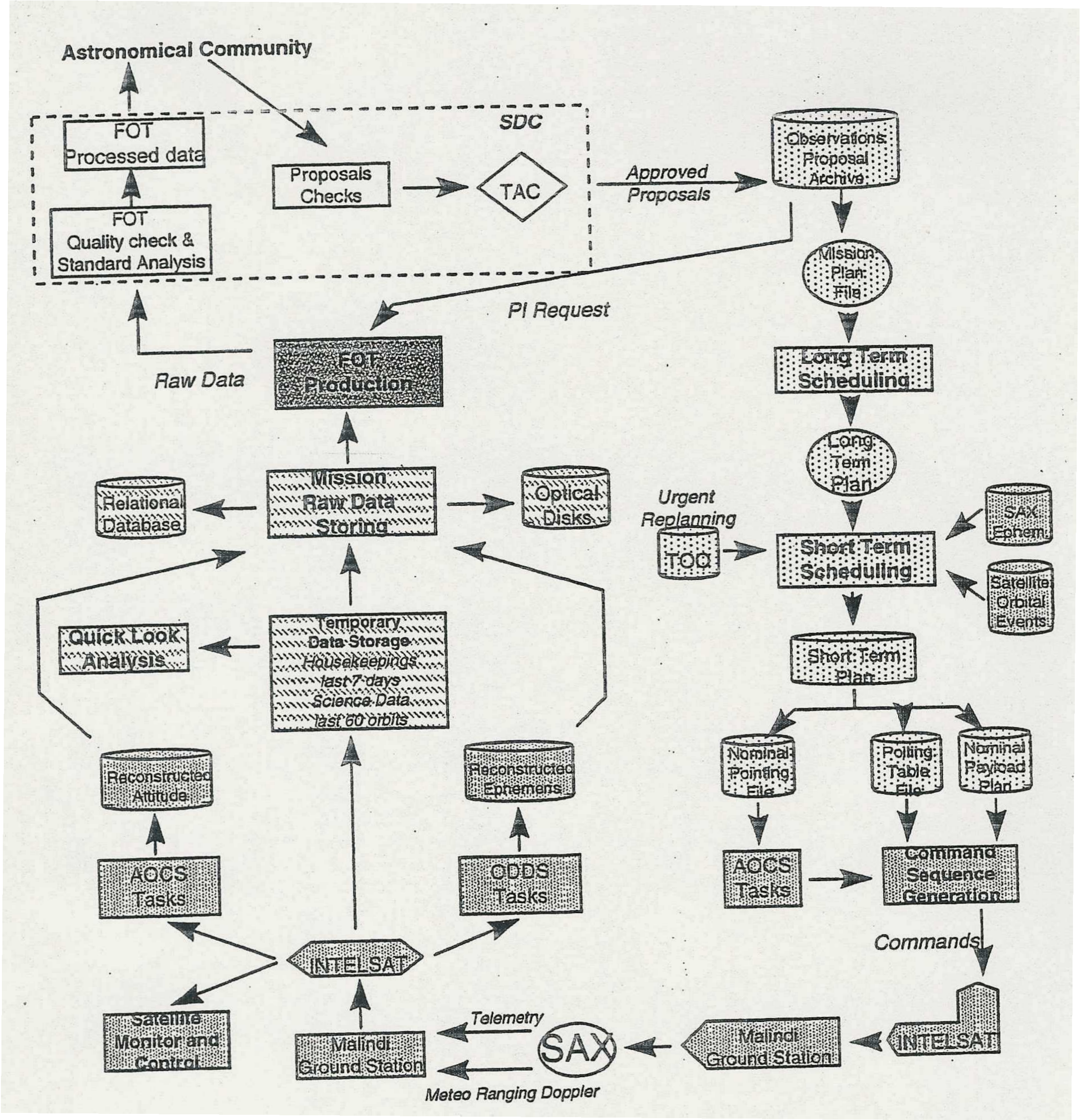

Figure 1.2: BeppoSAX ground segment operations (from Bruca et al. 1998)

are made public after 1 year. Every year an Announcement of Opportunity is issued; at the time of writing (December 1998), BeppoSAX is successfully completing AO2 observations, and the AO3 has already been issued.

The first 2 year and a half of operation (the nominal duration of the mission was 2 year, expected 4 years) have demonstrated the high quality of BeppoSAX scientific instrumentation and servo-systems, with standard of performances above the average of other missions. The only real problems have been the loss of one of the three medium energy concentrators (see next subsection) and the shorter than expected duration of four (out of six) gyroscopes, supplied by the development of software able to manage satellite operations in 1–gyro and 'gyro–less' mode. From the scientific point of view, in addition to the well–known discoveries on GRBs, BeppoSAX is providing a large number of outstanding scientific results on the several classes of X–ray sources.

1.1.2 The scientific payload

The scientific instruments of BeppoSAX (Boella et al. 1997a, Piro et al. 1995, Scarsi 1993) can be classified in Narrow Field Instruments (NFI) and Wide Field Instruments (WFI). The NFI consists of a Low Energy Concentrator Spectrometer (LECS, 0.1–10 keV), three Medium Energy Concentrator Spectrometers (MECS, 2–10 keV), a High Gas Pressure Scintillator Proportional Counter (HPGSPC, 20–120 keV), a Phoswich Detection System (PDS, 15–300 keV), all pointing along the satellite +Z axis. The WFI consists of two Wide Field Cameras (WFC, 1.5–26 keV), pointing along the +Y (WFC2) and -Y (WFC1) axis, and the GRBM, whose detectors axis are co–aligned with the ±X and ±Y satellite axis. The geometry of the BeppoSAX payload is shown in Fig. 1.3

The LECS (Parmar et al. 1997) and MECS (Boella et al. 1997b) units all consists of grazing incidence X–ray concentrators, composed of 30 nested Nickel Au coated coaxial and co-focal mirrors with a double cone approximation to Wolter I geometry, and of a gas scintillation proportional counter using Xenon at about 1.0 atm. The MECS make use of a 50 μm beryllium window , while the LECS window, in order to extend the energy

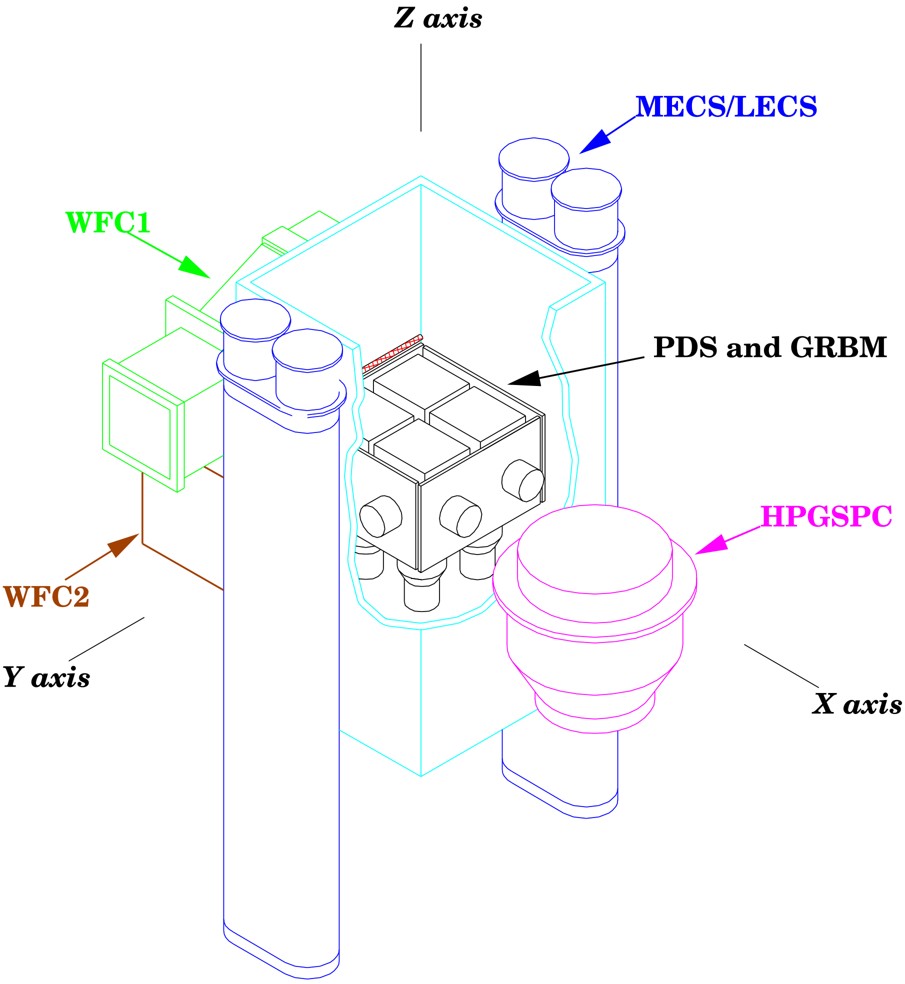

Figure 1.3: BeppoSAX scientific payload

Table 1.1: BeppoSAX instruments main characteristics

Instrument	Detecting units$^{(a)}$	Band (keV)	FOV (° FWHM)	Ang. res. (arcmin)	Eff. Area (cm^2)	Energy Re. (% FWHM)
LECS	1(+Z)	0.1–10	0.5	3.5@0.25 keV	22@0.25 keV	8x$(E/6)^{-0.5}$
MECS	3(+Z)	1.3–10	0.5	1.2@6 keV	150@6 keV	8x$(E/6)^{-0.5}$
HPGSPC	1(+Z)	4–120	1.1	collimated	240@30 keV	4x$(E/60)^{-0.5}$
PDS	1(+Z)	15–300	1.3	collimated	600@80 keV	15x$(E/60)^{-0.5}$
WFC	2(-Y,+Y)	1.5–26	20x20	3	140@10 keV	18x$(E/6)^{-0.5}$
GRBM$^{(b)}$	4(±X,±Y)	40–700	open	–	500@300 keV	30x$(E/100)^{-0.4}$

(a) The directions of the detectors axis are reported between parenthesis

(b) For the GRBM we report effective area and energy resolution for unit 1; the determination of this values is discussed in chapter 3.

band down to 0.1 keV, is made of 1.25 μm of Polymide, 0.035 μm of aluminum nitride and 0.044 μm of Al. The support structure of the concentrators is made of carbon fiber tubes an each pair of tubes is contained in a 2cm thick Al box.

The HPGSPC (Manzo et al. 1997) is an high pressure scintillator proportional counter filled with a 5 atm gas mixture (90% Xe and 10% He). The gas cell is cylindrical and made of a Titanium body 3 mm thick and with a diameter of 360 mm and a depth of 184.5 mm. The entrance window is made of two Beryllium foils 0.5 and 0.8 mm thick and has a diameter of 30 cm.

The WFC (Jager et al. 1997) consist of two coded aperture cameras, with detector and mask of the same size, about 25.6 x 25.6 cm^2. The mask is made of Iron and is located 0.7 m away from the detector, which is a multi wire proportional counter filled with a gas mixture (94% Xe, 5% CO_2, 1% He) and with an entrance window made of Beryllium 150 μm thick. The gas cell is made of Titanium coated with 1 mm of Al, and the mask and the detector are supported by a stainless steel structure. The FOV of the WFC is 20° X 20° FWHM (40° x 40° at zero response).

Finally, The PDS is described in section 1.2, where we outline in detail the GRBM experiment.

The main detecting characteristics of the instruments are reported in Tab. 1.1.

1.1.3 Data formats and data reduction software

The raw telemetry data, consisting of housekeeping and scientific data, are stored, processed and checked by the SOC, made available to Quick Look Analysis (QLA) and temporarily archived per orbit (last 10 orbits on–line). After that, SOC organizes telemetry data in Observing Periods (OP), covering several orbits, and archives them as FOT, together with auxiliary data such as On–Board Time(OBT)/Universal Time(UT) conversion, reconstructed attitude, satellite ephemeris, experiment configuration. Raw–data decompression and reduction to formats suitable for data analysis is possible by means of specific softwares (in the case of PDS/GRBM the raw data pre–processing software was developed ad hoc by the hardware team, as described in section 4.10).

The software for BeppoSAX data reduction has been developed in two different environments:

- XAS (X-ray Astronomy Analysis System, (Chiappetti and Dal Fiume 1997), specifically for the PDS, HPGSPC and MECS instruments. XAS software was developed mainly in FORTRAN language, with some modules in C, and is maintained at IFCTR/CNR (Milan), ITESRE/CNR (Bologna), and SDC. In this environment all files are in ASCII or specific XAS format. Programs are available to convert these files to FITS/OGIP format, for data analysis with standard packages like XSPEC, XRONOS, XIMAGE, etc. The dialog with the programs is through run-string and/or environmental variables. The software can operate both on the pre–processed raw data and the FOT data. XAS software is available for DEC Ultrix 4.3, DEC Unix 3.2, HP-UX 9.01/9.05 and SUN Os 4.1.x operating systems. As a XAS contributed software, a sophisticated IDL (Interactive Digital Language) program has been developed at ITESRE/CNR for XAS data analysis and plotting (see section 4.10).

- FTOOLS, initially for the LECS, MECS and WFC instruments but now also for PDS and HPGSPC. The NFI softwares are part of the same package, SAXDAS, and share a number of programs. This software was adapted from existing programs developed for other missions and is maintained by SSD/ESA, SAX/SDC and IAS/CNR. SAXDAS software is available for Alpha OSF-1, SUN OS 4.1.x, HP-UX operating systems. The WFC software constitutes a different package and was developed at SRU/SRON. In this environment all files that are newly created by any of the software moduli (Jager et al. 1997, in 't Zand 1992) are exclusively in FITS format (OGIP compatible). The dialog with the programs is through run-string and parameter files.

We will go in some more detail with the PDS/GRBM specific data reduction and analysis tools in chapter 4, where we outline GRBM data analysis techniques.

1.2 The Gamma–Ray Burst Monitor experiment

The BeppoSAX GRBM is part of the PDS experiment and is based on inorganic scintillator counters. Thus, before going in detail with the experiment description, we remind the basic concepts on these class of gamma radiation detectors, for a better understanding of the descriptions and discussions that will follow.

1.2.1 Inorganic scintillator detectors

Inorganic scintillation counters are conventional detectors for gamma–ray radiation (above ∼10 keV) measurements. Detailed description of these instruments can be found e.g. in Knoll (1989), more exhaustively in Birks (1964), and e.g. in Giacconi & Gursky (1974) for their application in X–ray astronomy. The basic mechanism consists in measuring the scintillation light produced by a ionizing high energy photon (or alpha or beta particle) interacting with the scintillating material. The most commonly used inorganic scintillators are the activated alkali–alidi crystals NaI(Tl) and CsI(Na or Tl). Conventionally, the element the element used to activate the crystal is indicated between parenthesis. A gamma–ray photon arriving on the detector deposits all or part of its energy in the material (see section 2.1) in the form of kinetic energy of one or more electrons, depending on the type and number of interactions. These electrons are able to excite to the conduction band other electrons which can be captured by a trace impurity (the activator) and cause transitions leading to the emission of visible light. The role of the activator is to generate meta–states between the pure crystal valence and conduction bands, so that an electron excited to the conduction band can drop in one of this meta–states and de–excite from it to the valence band. This has the advantages of being a more efficient mechanism with respect to the normal de–excitation from crystal conduction band and to lead to the emission of visible light photons, because of the lower energy of meta–states with respect to the conduction band. The scintillation light pulse is then collected through a light pipe (typically a quartz pipe) to a Photomultiplier Tube (PMT), which finally converts it to an electric signal to be amplified and measured. Since in principle a linear relation exists between the energy released by the photon in the crystal and the intensity of the light produced, to get spectral information on detected photons the associated electronics is designed to perform Pulse Height Analysis (PHA): the amplified signal is fed to a multi–channel analyzer which associates it to the relevant channel, according to the signal amplitude.

The relevant factors that contribute to the detector performances are:

- crystal transparency to its own emitted radiation (typically in the UV range)
- the number of photons emitted (*light yield*, usually measured in photons/keV) for each detected event and its proportionality to the incident photon energy (*linearity*). The maximum efficiency in converting initial electron energy into photons is $\sim$13% for NaI(Tl). The NaI and CsI light yields are not exactly linear with energy, decreasing with increasing incident photon energy and are affected by temperature changes;
- decay time of the induced scintillation, determined by the decay time of the meta–state involved in the scintillation, limiting the detector temporal resolution;
- scintillation light collection efficiency, which depends on the geometry of the detector, on crystal coating and on the position in the detector in which the interaction with the incident photon takes place;
- crystal/PMT coupling; in particular the crystal refraction index should be as close as possible to that (1.5) of the glass for efficient coupling with the PMT;
- PMT quantum efficiency (typically 10–15%);
- PMT gain (typically from 10^5 to 10^8) and its stability. The potential needed to bias the PMT photocathode and the succeeding multiplier stage is provided by an High Voltage supply (HV) and is of the order of 1000 Volts. HV stability affects PMT gain stability.

Table 1.2: NaI(Tl) and CsI(Na) characteristics

	NaI(Tl)	CsI(Na)	CsI(Tl)
Light output (% relative to NaI(Tl)	100	85	45
Wavelength of maximum emission (nm)	410	420	565
Decay constant (μs)	0.23	0.63	1.0
Density (g/cm^3)	3.67	4.51	4.51
Refraction index	1.85	1.84	1.80

The physical and mechanical properties of the material are also important. It should be manufacturable in sizes large enough to be of interest for practical detectors.

Although they have poorer energy resolution (see chapter 3) than gas proportional counters, the use of scintillators is preferable (unavoidable above 100 keV) because of their much higher detection efficiency (100% up to ∼100 keV for NaI and CsI), due to the high Z of their atoms and their density three orders of magnitudes greater than those of the gas in a typical proportional counter.

In Tab.1.2 the main characteristics of the NaI(Tl), CsI(Na) and CsI(Tl) scintillators, the most widely used in X and gamma–ray astronomy are reported.

1.2.2 The Phoswich Detection System

The PDS (Frontera et al. 1997a) is the high energy experiment of BeppoSAX, extending to 300 keV the NFI energy range and including as a subsystem the GRBM, which extends to 700 keV the WFI energy band. The main features of the experiment are reported in Tab.1.3 and a sketch of the detector and electronic units are shown in Fig. 1.4. The experiment was conceived and designed at ITESRE/CNR, Bologna (PI Prof. F. Frontera, deputy PIs D. Dal Fiume and E. Costa), was assembled at Laben and tested and calibrated at Laben, ESA/ESTEC, ITESRE/CNR,Universitá di Ferrara and IAS/CNR (Rome). The crystals constituting the active part of the PDS main detectors and of the PDS/GRBM have been manufactured and tested by Bicron Corporation, USA. The PDS/GRBM hardware team is composed by scientists at Istituto TESRE/CNR, Bologna, Universitá di Ferrara and Ferrara, IAS/CNR, Roma.

The detection system of the PDS is based on the PHOSWICH (acronym of PHOSphor sandWICH technique (e.g. Knoll 1989), in which the detector units are made of two layers of different crystals optically coupled. The PHOSWICH techniques exploits the different decay constants of the crystals to perform background rejection by means of Pulse Shape Analysis (PSA). In the case of PDS the detection plane (Fig. 1.5) is constituted by a square array of four phoswich units made of NaI(Tl) and CsI(Na), whose thickness are reported in Tab.1.3. Each detector unit is viewed by a PMT through a quartz light pipe. The entrance window is made of 1500 μm of Be, 800 μm of Silicon rubber, 76.1 μm of AL–coated Kapton and 100 μm of Teflon. The detectors FOV is limited by two rocking collimators made of Tantalum tubes with 1.3° hexagonal aperture, internally partially covered by a Sn/Cu gradual radiation shield. During operation, a collimators rocking strategy allows a simultaneous monitoring of source and background (Frontera et al. 1997a).

Besides the PSA, the background radiation rejection is obtained through a system of active anti–coincidence. From the side it is provided by four optically independent rectangular slabs of CsI(Na) scintillators 10 mm thick, 275 mm high and 402 mm wide. If a signal in one of the slab exceeds a programmable Anti Coincidence (AC) threshold then a veto signal (AC flag) is generated by the PDS analog processor. As anticipated, these detectors constitute also the Gamma–Ray Burst Monitor, which will be described in full detail in next section.

The active shielding in the +Z direction is provided by a top shield constituted by a 1mm thick plastic scintillator covered with Al–coated Kapton and located above the collimator assembly. It works for charged particles, in particular high energy electrons produced by interaction of cosmic rays with the satellite structure.

Other relevant features that make the PDS a high quality experiment are: an Automatic Gain Control (AGC) system, a Movable Calibration System (MCS, made of a 32 cm long wire of radioactive ^{57}Co contained in a cylinder of lead with a small aperture towards the detectors located above the top shield and which can scan by command the whole FOV to check in–flight calibration), a Light Emitting Device (LED) encapsulated in each phoswich to simulate an energy loss in the crystal and monitor gain stability and a Particle Monitor (PM) located near the instrument which monitors the level of environmental particle fluxes and turns off the High Voltage (HV) if the flux exceeds a programmable threshold in order to prevent damage to the experiment.

The electronic unit and its main functions are sketched in Fig. 1.4. In addition to the power supply module, it includes an analog processor, devoted to analog data processing and digital conversion, and a digital processor, for data management and instrument control. The ADC uses the slading scale technique (Gatti et al. 1970, Frontera et al. 1992) and has a conversion time of 5μs.

Finally, the on–board data are formatted in different transmission modes, which can be direct or indirect. Direct modes are used to transmit to telemetry events from the phoswiches and include information for each individual event on energy, pulse shape, time , detecting unit and the AC flag. With indirect modes, data are accumulated in histograms before being transmitted (they are used for observation of strong sources, for not saturating the experiment telemetry). Housekeeping (HK) information is provided in indirect mode and consists of spectra accumulated over 128 s time intervals (e.g. phoswiches pulse shape spectra), 1 s ratemeters (e.g. dead time counters, AC ratemeters, GRBM ratemeters, etc.) and engeenering data (e.g. HV, temperatures, status of collimators) which can be accumulated over time intervals ranging from 16 to 64 s.

1.2.3 The Gamma–Ray Burst Monitor

The BeppoSAX Gamma–Ray Burst Monitor (Costa et al. 1998, Frontera et al. 1997a, Pamini et al. 1990) is an experiment derived from a secondary function of the four CsI(Na) scintillators assembly described in previous sub–section acting as active lateral coincidence of the PDS experiment and forming a square box around the main PDS detectors (Fig.

Table 1.3: PDS main characteristics

Energy range	15–300 keV
Window	1.5 mm Be
NaI(Tl) phoswich thickness	3 mm
CsI(Na) phoswich thickness	50 mm
Geometrical area	795 cm^2
Total area through collimator	640 cm^2
Effective area	600 cm^2@20 keV 500 cm^2@60 keV 500 cm^2@100 keV 140 cm^2@200 keV
Field of view (FWHM)	$1.3^{\sim}$ hexagonal
Energy resolution at 60 keV	$\leq$15% (on the average)
Maximum time resolution	16 μs
Gain control accuracy	0.25%
In-flight calibration accuracy	0.1%
Energy spectra	512 channels
Rise time distribution	512 channels
Minimum channel width of energy spectra	0.3 keV
Maximum throughput	4000 events s^{-1}

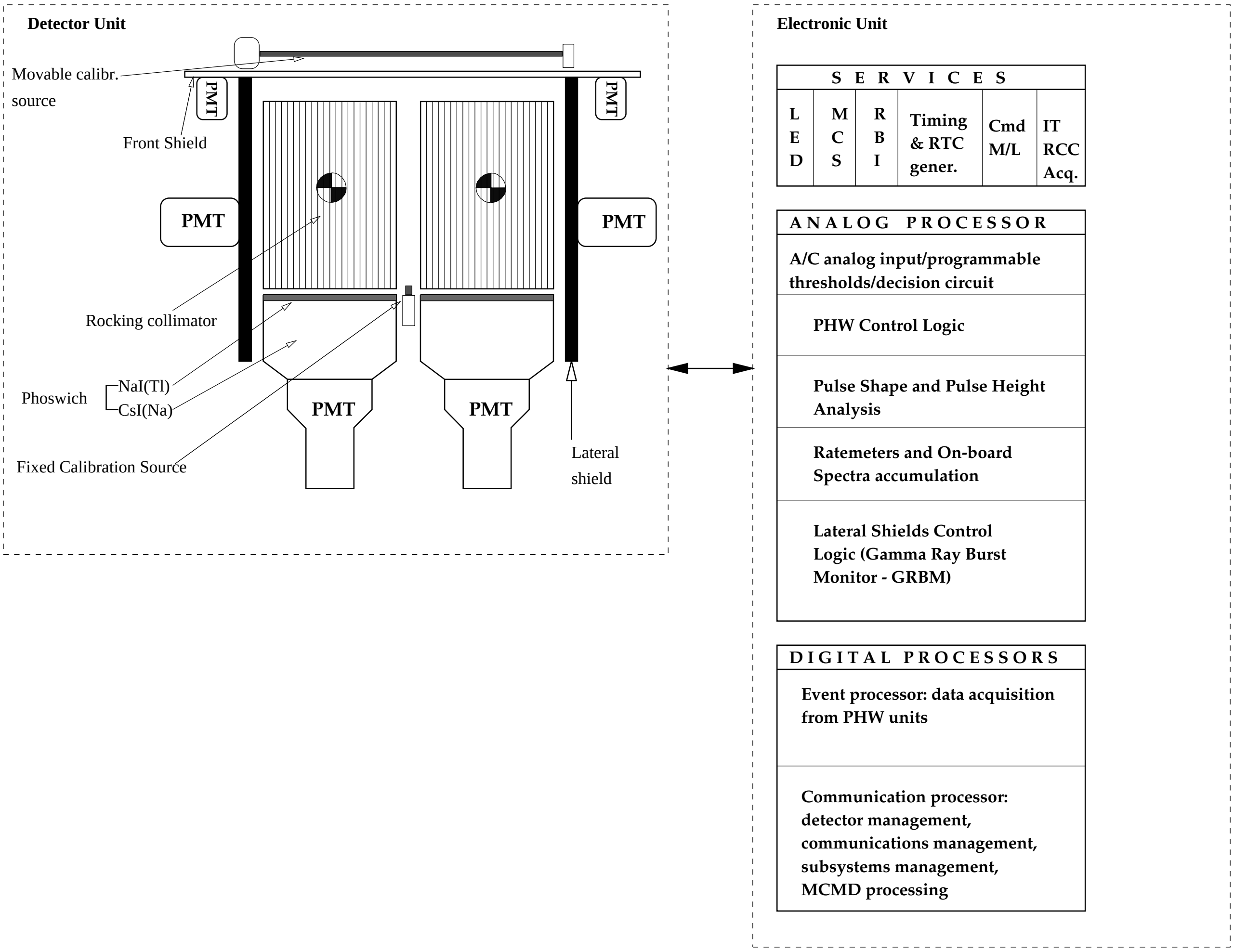

Figure 1.4: Scheme of the PDS detecting and electronic units

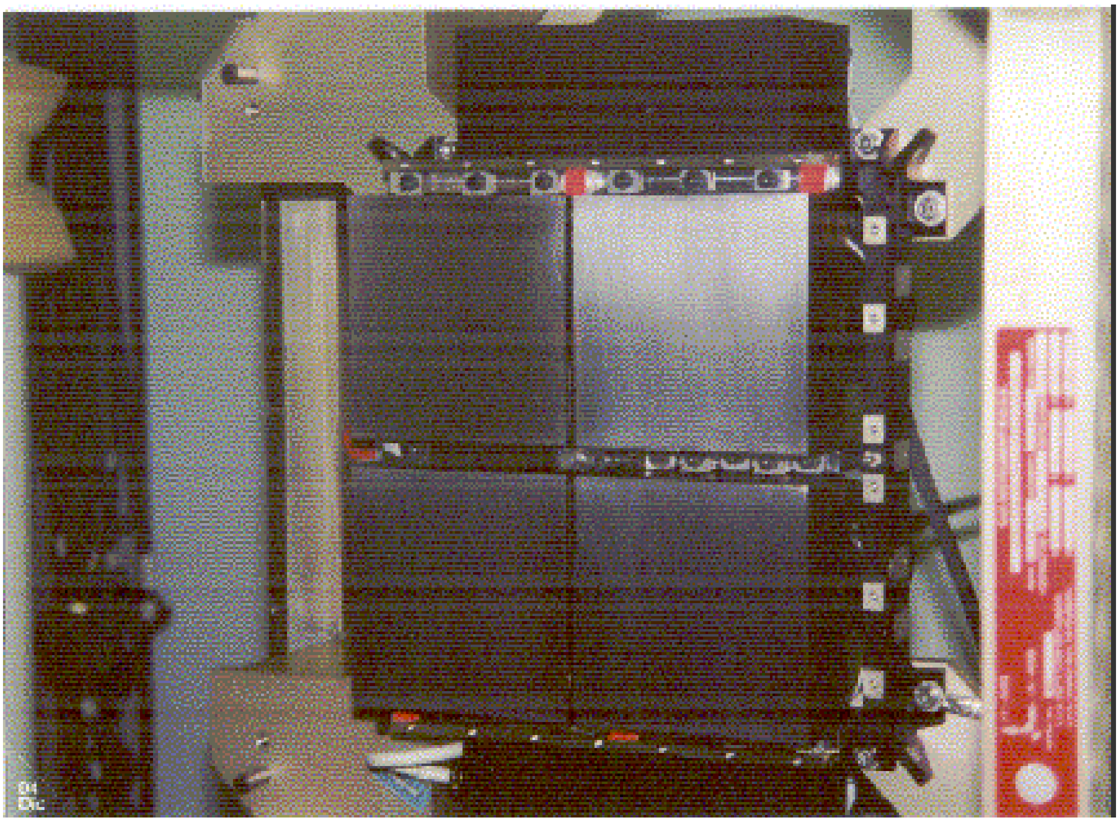

Figure 1.5: PDS detector plane view

1.6). Each detector is 1 cm thick and has a geometric area of about 1136 cm^2 and an open field of view. The choice of CsI(Na) as the constituting and detecting material of the shields depended on standard considerations on its physical properties, mainly the high efficiency in stopping high energy photons, its resistance to thermal and mechanical shocks and its plasticity, that makes it easy to fabricate it into the desired detector geometry. The four detecting units are optically independent. Each one is composed by two optically coupled halves, whose light is seen by two independent photomultipliers (Fig. 1.7) Hamamatsu R2238 through Quartz light pipes. A light source obtained with an Am^{241} source embedded in a NaI crystal is attached to each of the four detectors. Its light is then seen as a permanent source in the detector through a grey filter and its function is to help in monitoring detectors PMT gain variations.

The GRBM units are named LS1, LS2, LS3 and LS4, where LS stands for Lateral Shield. Due to the geometry of the PDS experiment and the BeppoSAX scientific payload (see Fig. 1.3), the axis of the slabs are orthogonal to the NFI axis (+Z). In particular, LS1 is co–aligned with the -Y axis, LS2 with the +X axis, LS3 with the +Y axis and LS4 with the -X axis. Therefore, LS1 and LS3 are co–aligned with WFC1(-Y) and WFC2(+Y) respectively.

The signals coming from each of the lateral shield are multiplexed and fed to a dedicated ADC converter , after a set of analog thresholds has been satisfied. In particular, for each of the four lateral shields a Low Level Threshold (LLT) can be adjusted by telecommand among 16 steps, nominally ranging from 20 to 90 keV, and an Upper Level Threshold (ULT) can be adjusted in 8 steps, from nominal 200 to 700 keV. In addition, the GRBM has been equipped with specific electronics for GRB detection. Due to the unpredictability of GRBs, an on-board specific trigger criterion is needed. The GRBM trigger operates on the signals detected between the LLT and ULT. With a time resolution on 7.8125 ms a moving average is continuously computed on a Long Integration Time (LIT) that is adjustable between 8 and 128 s. The counts in a Short Integration

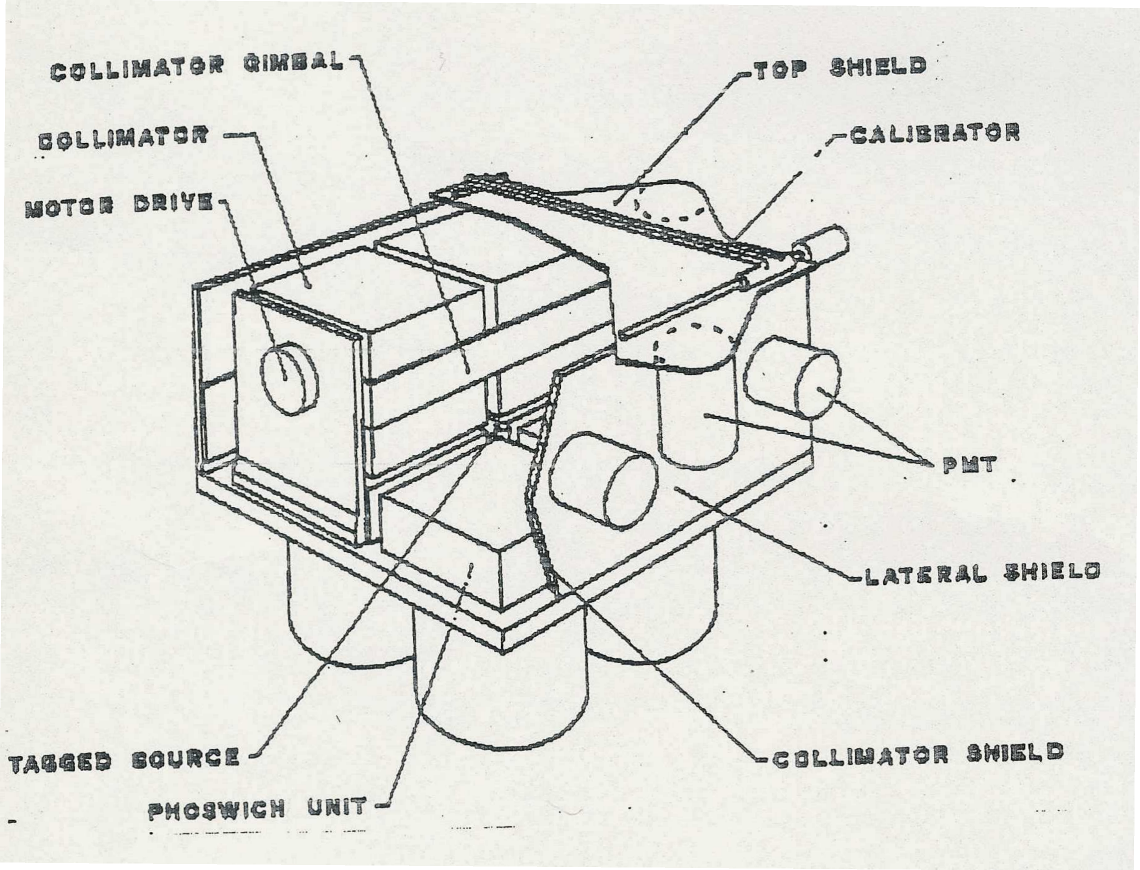

Figure 1.6: PDS/GRBM design

Time (SIT, adjustable between 7.8125 ms and 4 s) are compared to the moving average, and if they exceed of nσ (where σ is the Poissonian standard deviation and n can be 2, 4, 8 or 16) this average then the trigger condition is satisfied for that shield. If the same condition is simultaneously active, within the SIT, for at least two shields, then the GRBM trigger condition is satisfied, and the relevant scientific data are produced.

The main characteristics of the GRBM are summarized in Tab.1.4, where we anticipate properties (e.g. effective area, energy resolution) that will be the subject of chapter 3.

1.2.4 GRBM scientific data

We can classify the GRBM scientific data products in 3 types:

•*1 s ratemeters*: the signals detected in each shield between the LLT and the ULT are continuously counted, with a time resolution of 1 s, and recorded by a proper PDS housekeeping, the GRBM ratemeter; another housekeeping counter, the AC ratemeter, records, for each shield, the count rate detected above the PDS Anti Coincidence Threshold (ACT), that is used as a lower level discriminator for any AC signal, adjustable on 8 steps between nominal 100 and 300 keV. This data are transmitted to ground in indirect temporal mode; the dead time is 4 μs and the number of bits of the counter is 16 (maximum number of counts is 65536);

•*GRBM PHA spectra*: the counts accumulated every 128 s in the GRBM band (LLT–ULT) are continuously histogrammed on–board in 240 channels spectra by means of PHA analysis (as described above in the PDS section) and transmitted to ground in Spectral Indirect Mode; the real number of PHA channels is 256, but channels from 241 to 256 don't contain scientific data, due to the use of the sliding scale technique. The dead time introduced by the ADC is 14 μs; the number of bits for each channel is 16;

•*High Resolution Time Profiles (HRTP)*: when the on–board trigger is satisfied, time count profiles are stored independently for each of the four detectors and for any trigger occurring during an orbit and transmitted with the following modality:
a) 8 s before the trigger time, with a time resolution of 7.8125 ms
b) 10 s from the trigger time, with a time resolution of 0.488 ms
c) 88 s starting from 10 s after the trigger time, with a time resolution of 7.8125 ms
The dead time needed to accumulate and store the data packets for each trigger is about 400 s.. This means that it is not possible to trigger an event occurring before 400 s after the former trigger. The telemetry allocated to the GRBM allows to detect up to 12 events each orbit. These data are transmitted to ground in a specific GRBM Direct Mode.

The first two data sets are used to extrapolate sources flux and spectral properties (see following chapters); both raw and FOT data are reduced using the PDS specific tools

Table 1.4: GRBM main characteristics

Energy range	40–700 keV
CsI(Na) thickness	10 mm
Geometrical area per detecting unit	1136 cm^2
LS1/LS3 On–axis effective area	$\sim$85 cm^2@40 keV $\sim$200 cm^2@60 keV $\sim$500 cm^2@120 keV $\sim$590 cm^2@300 keV $\sim$280 cm^2@600 keV
Field of view (FWHM)	open (2π)
Energy resolution	from 43% @40 keV to 15% @600 keV
Maximum time resolution	0.5 ms for HRTP 1 s for GRBM and AC ratemeters 128 s for PHA spectra
Energy spectra	256 channels
Minimum channel width of energy spectra	2.7 keV
ADC dead time	4 μs for the ratemeters 14 μs for PHA spectra
Memory allocation	16 bit for each ratemeter bin 16 bit for each PHA spectra channel

contained in the XAS package. The HRTP can be used to perform temporal analysis of GRBs. The relative packets, containing also the trigger time in OBT are present in the orbit per orbit PDS raw data set and are provided to the GRBM hardware team in a specific FOT version. HRTP reduction and trigger time conversion to UT is performed by specific programs developed by the GRBM group. The output of these dedicated programs is a set of ASCII light curves for each of the four LS and for each trigger.

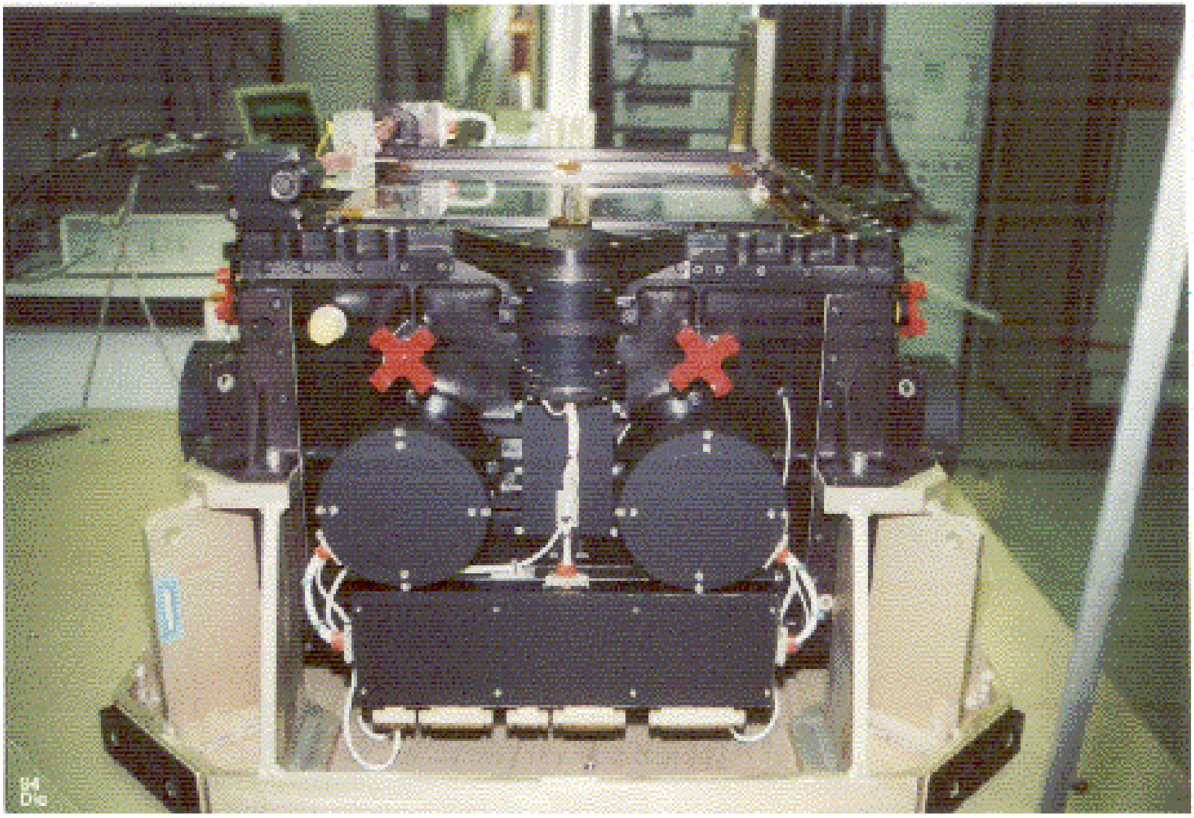

Figure 1.7: PDS lateral shield view

Chapter 2

GRBM on–ground calibrations

In this chapter we describe the GRBM on–ground calibrations, with major emphasis on those performed with the full (except for solar panels) integrated satellite. The calibrations results are the basis of the derivation of the efficiency as a function of energy and photon direction in order to allow for counts to flux deconvolution with the GRBM and AC ratemeters, and of the building of the 240 channels response matrices for LS1 and LS3 for time averaged spectral analysis. In the last section of the chapter we discuss the preliminary analysis of calibrations data.

2.1 On–ground performance tests of GRBM detectors

In this section we briefly describe the calibrations performed on GRBM crystal detectors before and after their integration in the PDS assembly. Although the reconstruction of the actually used response matrices of LS1 and LS3 is mainly based on the calibrations with the integrated satellite described in next section, some of the information on detectors performances obtained with these calibrations has been already accounted for and will be very extensively used in upgrading response reconstruction with Monte Carlo simulations results.

2.1.1 Functional tests on plain crystals

The CsI slabs constituting the GRBM detectors have been manufactured and preliminary tested by Bicron Corporation, New Bury, OH, USA. The most relevant tests performed in Bicron, with detectors illuminated from the inside are:

- measurements of *gain and energy resolution* of each slab by using radioactive monochromatic sources of gamma–rays with energies between 22 and 662 keV; the crystals showed a very good linearity and energy resolution values and dependency on energy very close to that reported in table 1.4 and estimated from the calibrations reported in next section;

- estimate of the *gamma–equivalent energy of the light pulsers* inserted in each slab as gain calibrator, which resulted to range from 350 to 450 keV;

- testing of gain and energy resolution variations with *HV changes*; no significant energy resolution changes occur within HV variations of ±200 Volts;

- *uniformity tests*: signal amplitude as a function of the site of photon interaction in the crystal was tested using a collimated ^{57}Co (122 keV) radioactive source. The irradiation spots on the crystal had a 10 mm diameter. As expected and as shown in Fig. 2.1 for LS1, the signal amplitude is much higher for photons incident directly underneath PMTs and minimum at the edges. This results in different PHA channel assignments for signals generated by the detection of photons of the same energy. This disuniformity, expressed as $\frac{maximum\ channel-minimum\ channel}{average\ channel}$ ranges from 68% to 77% depending on the slab.

2.1.2 Detectors calibrations with PDS experiment integrated

The PDS was assembled and intensively tested at LABEN SpA, Vimodrone, Milano, Italy. After successful thermal–vacuum tests and vibration tests, the following main response calibrations were performed on GRBM detectors in late 1994/early 1995:

- *window transparency*: each GRBM detector was illuminated in 30 different points on its surface with 2 collimated radioactive sources of 122 keV (^{57}Co) and 662 keV (^{137}Cs)

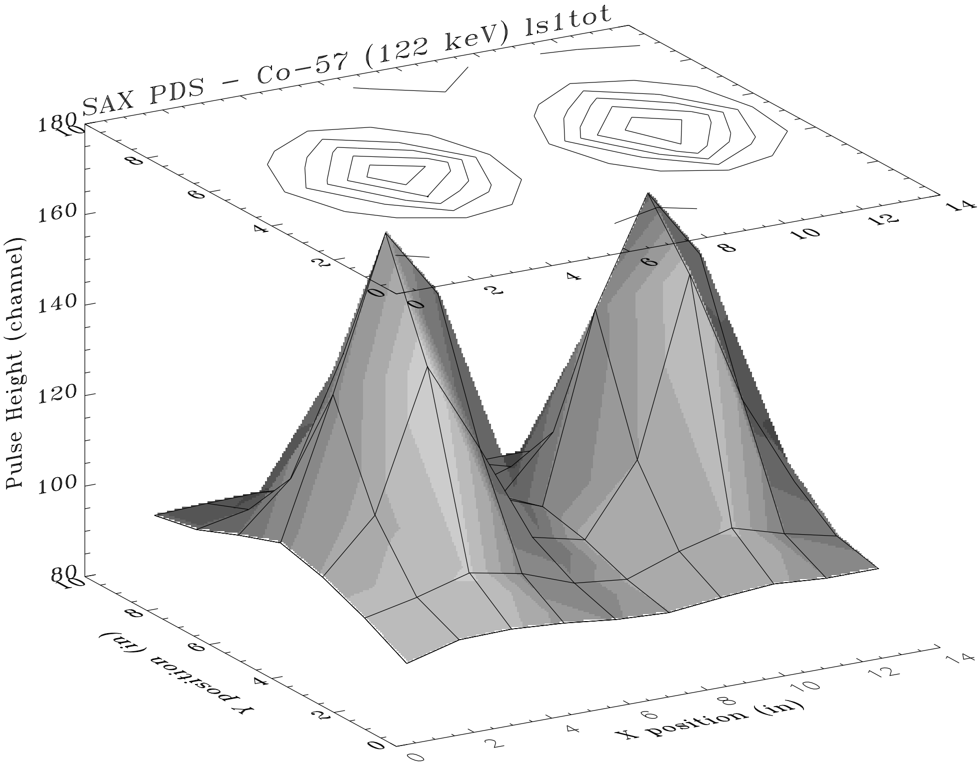

Figure 2.1: Mapping of the gain of LS1 at 122 keV

photons at a distance of 20 cm and giving a spot size on the slab of 20 mm. These measurements, compared with those similar undertaken in Bicron, show the effect of the surrounding materials like PMT and their electronics on GRBM detectors response and are important to verify the correct modeling of the PDS structures for the Monte Carlo simulations;

- *PHA channel vs. energy relation*: each slab has been irradiated with collimated monochromatic sources of photons with energies ranging from 60 to 662 keV located at a distance of 4 m in order to illuminate the entire shield. The PHA channel centroids of the photopeaks of the measured spectra at the various energies were determined by fitting the peaks with a Gaussian. In this way a preliminary energy to channel conversion was obtained for each GRBM detector. In addition, from these measurements it was possible to evaluate the detectors response at the various energies;

- *calibration of GRBM and AC band thresholds and related effects*: the energy values and spectral shapes corresponding to the different steps of the thresholds delimiting the GRBM (LLT–ULT) and AC (>ACT) bands have been determined using some of the radioactive sources used in the previous set of measurements, located at the same distance from the detector. For the GRBM LLT and ULT calibration, 60 and 662 keV source was used respectively. What is observed in the 240 channels spectra collected with the thresholds at different steps is not a straight cut at a given channel value but an ∼exponential decrease of the counts below LLT or above ULT. This effect is due to the fact that the electronic thresholds assume a fixed pulse shape, which is not exactly true, especially at low energies, where the signal is weaker and more affected by statistical and non–linearity effects, and must be taken in serious account in modeling detectors response. The ACT threshold steps values have been measured using a 122 keV source. The count rate in the AC ratemeter with the threshold at its minimum value was measured. The spectrum of the 122 keV source consists mainly of a photo-peak, with a little Compton scattering contribution. Thus, the ratios between the AC counts measured with each step value and those measured with the minimum step depend on the area of the Gaussian photo-peak which is lost because of the cut, i.e. to the threshold energy. Another relevant threshold effect is that of the GRBM ULT on the gain calibrator light pulser line. Photons produced by the light pulser are generated in a NaI scintillator which has a different decay constant with respect to CsI. As a consequence, the electronics discriminator circuits have a different effect on the calibrator signals with respect to the CsI signal. The result is a distortion of the calibrator photo-peak, with its higher energy photons decreased by the ULT. This effect as a function of ULT must be considered in evaluating calibrator line value to check detector gain.

2.2 On–ground GRBM calibrations performed after spacecraft integration

This section is mainly devoted to the description of the tests of the GRBM carried out by the BeppoSAX/GRBM hardware team on August 1995 at the ESA Technology Center (ESTEC) in Noordwijk, with the satellite almost fully (except solar panels) integrated. The goal of these calibrations was to define the shielding effect of the satellite materials in front of the lateral shields field of view (Fig. 1.3).

2.2.1 Radioactive sources

The calibration sources used for the calibration tests are reported in Table 2.1. The sources supplied by Product Laboratory (IPL) had an active diameter of 5.0 mm, while those produced by Amersham had a diameter of 1.0 mm. Each of the radioactive sources was arranged in a low back-scattering polystyrene foam case ($60 \times 60 \times 120$ mm) on a side of which a round window was carved, in order to make the source directly visible from the satellite. The source case was held by a 200 mm long (5 mm diameter) Aluminum rod, connected with a proper interface to the horizontally extended arm (Al tube, 20 mm external diameter) of a vertical 600 cm long tooling bar (Fig. 2.2). The horizontally

Table 2.1: Calibration sources used during the ESTEC campaign

Source	Activity μCi	Supplier	Main line keV	Branch	Other lines keV	Half life
Am241	100	Amersham	60	0.353	12-22-26	432 y
Co57	101	IPL	122	0.963	6-14-136	271.79 d
Ce139	104	IPL	166	0.799	33-39	137.64 d
Hg203	39.6	IPL	279	0.815	71-85	46.60 d
Sn113	96.7	IPL	392	0.649	24-28	115.09 d
Sr85	99.9	IPL	514	0.984	13-15	64.84 d
Cs137	95.4	IPL	662	0.851	32	30.1 y

extended arm of the tooling bar was about 700 mm long and allowed the source to be located at any positions at different distances from the tooling bar.

2.2.2 Measurement set-up and strategy

SAX was set onto a rotary table, in the Z axis vertical direction, and the tooling bar was located at about 570 cm from the PDS center (Fig. 2.3). By means of a coordinated shift of the movable horizontal arm of the tooling bar and a movement of the source support onto the extended arm it was possible to reach positions lying onto a virtual spherical surface centered on PDS and having 500 cm radius. During the calibrations, the energy thresholds were fixed at the following levels: LLT at minimum value (nominal 20 keV), ULT at maximum value (nominal 700 keV) and ACT at minimum value (nominal 100 keV). A first set of measurements was carried out with the SAX satellite that rotated around Z axis on the rotary table at a fixed angular speed of $\sim$9 arcmin/s. With this angular speed, a complete rotation of SAX lasted 2304 s, which means 18 time periods of 128 s (accumulation time of GRBM spectra). The sources were positioned at various elevation angles, ranging from $-45°$ to $+60°$ with respect to the horizontal (X,Y) plane. The angular response of each GRBM shield was thus measured from GRBM and AC ratemeters.

Also, average energy response over 128 s, corresponding to a rotation of 20 degrees,

Table 2.2: ESTEC satellite rotating calibrations log. First column contains the calibration sources and the other columns contain a flag (Y=Yes, space=No) indicating whether measurements have been made at the relative θ angle value

Energy	-45	-30	-15	0	$+15$	$+30$	$+45$	$+60$
^{241}Am	Y	Y	Y	Y	Y	Y	Y	Y
^{57}Co				Y		Y		Y
^{139}Ce		Y	Y	Y	Y	Y		
^{203}Hg,				Y				
^{113}Sn		Y	Y	Y	Y	Y		
^{85}Sr				Y				
^{137}Cs				Y				

was determined.

Hereafter we will express source direction with respect to each LS in the altazimuthal coordinates θ*, i.e. the angle between source direction and the satellite XY plane, and* ϕ*, i.e. the angle between the projection of source direction onto the XY plane and the detector axis.*

In Tab. 2.2 we report the energy and θ values 'covered' by these kind of measurements. The number of runs was limited by time constraints. Several background measurements ware made, with no source in the tooling bar arm end without altering the calibration set–up.

A second set of measurements was carried out with the SAX satellite fixed in some particular positions, in order to better understand some shielding effects. This was done, in particular, for LS2 and LS4, whose angular responses were expected to be more complex because of the presence in front of them of the HPGSPC and WFCs respectively.

During these calibrations, the PDS was operated in standard mode and all the other scientific instruments were off.

2.2.3 Monitoring of spurious contributions

In order to evaluate the possible modifications induced in the source energy spectrum by the calibration environment (e.g. walls, measurement set-up, source supporting struc-

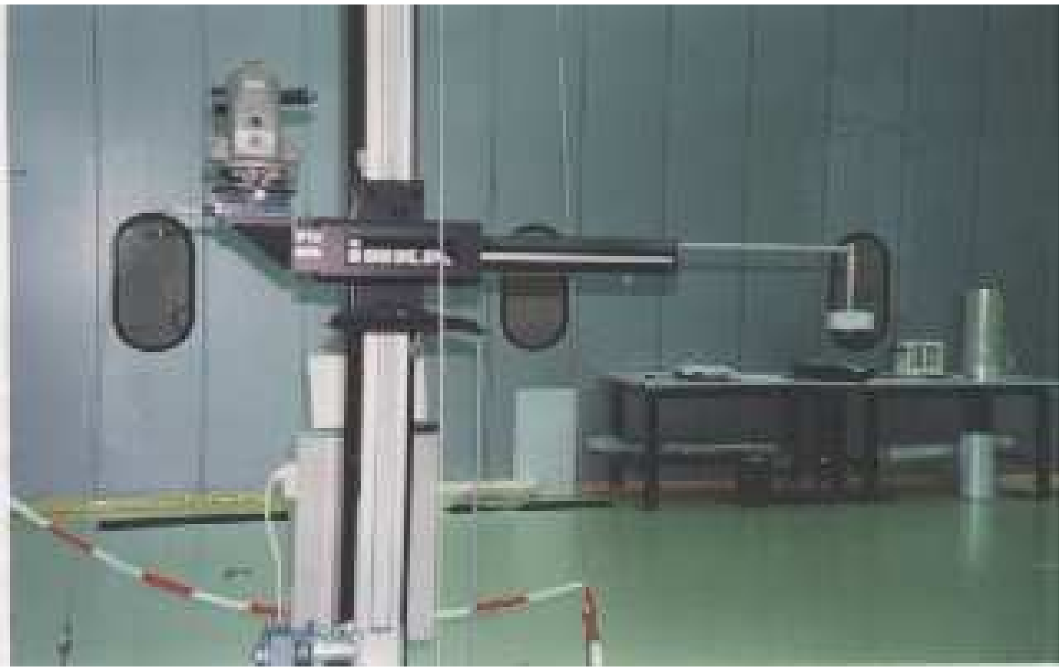

Figure 2.2: ESTEC calibrations: radioactive sources set–up

tures), as discussed in section 3.1.2, a calibration of the radioactive sources was performed using a 1.4 cm thick NaI scintillator located at the satellite position in a configuration similar to the GRBM calibration configuration.

Other measurements of calibration sources spectra were carried out before and after the ESTEC campaign with a Germanium (Beryllium window) detector at the ENEA and IAS/CNR laboratories (Frascati, ITALY) to study possible effects of the source support on the shape of the source spectra.

2.3 Calibrations database and preliminary analysis

All the GRBM data collected in the ESTEC calibration campaign were stored on–board and acquired with standard telemetry. Thus, the data products are in the standard telemetry formats and can be reduced with the softwares described in section 1.1.3. The preliminary analysis reported in this section was performed with specific programs developed with IDL package ver. 5.0.

The ESTEC calibrations database consists of the following sets of data:

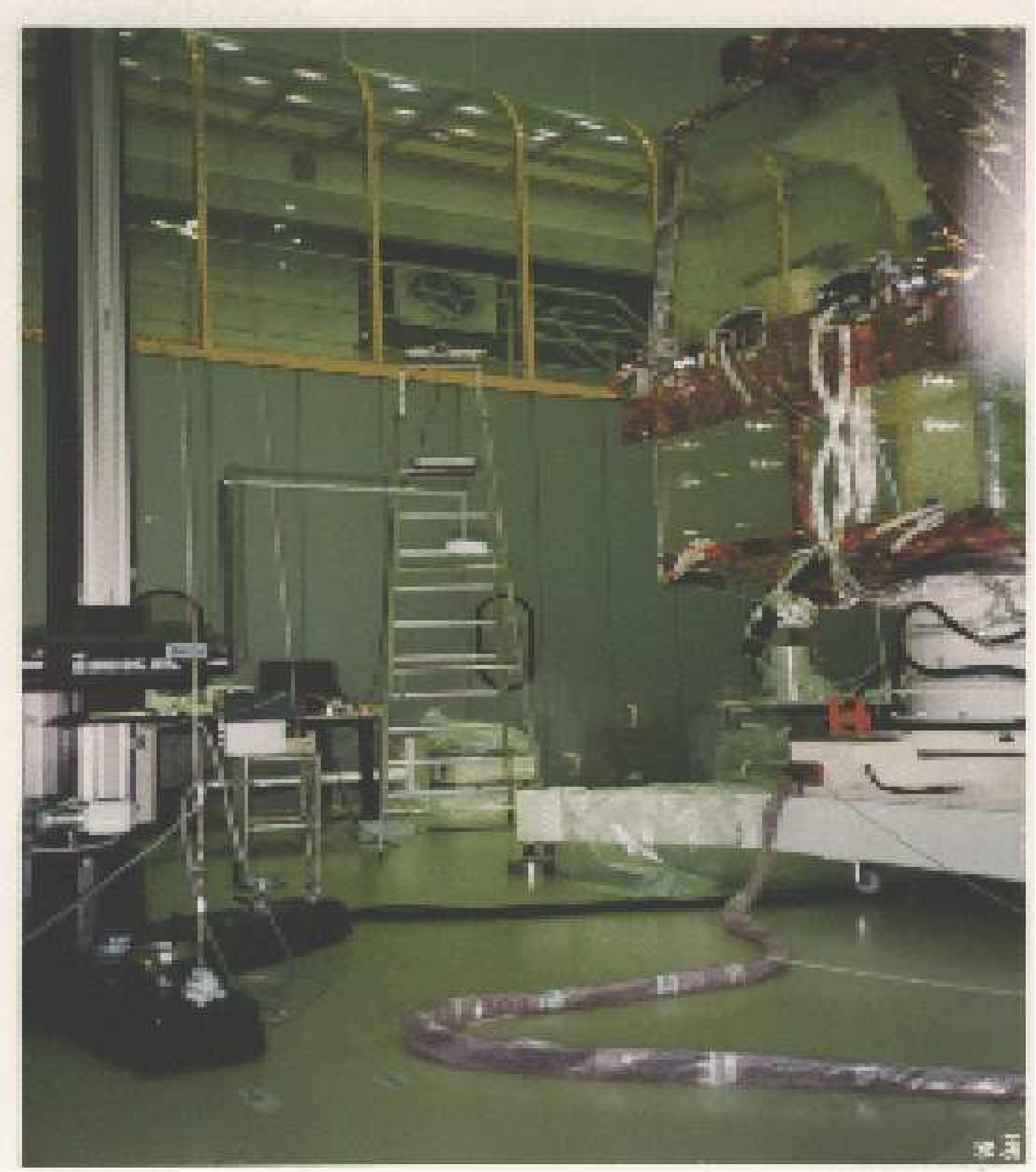

Figure 2.3: ESTEC calibrations: global set–up

- ϕ angular light curves with ∼9 arcmin resolution (from the combination of the ratemeters 1 s time resolution and the satellite angular speed) in the GRBM and AC bands and 240 channels energy spectra averaged on ϕ angles of ∼20° (from the combination of the PHA spectra 128 s time resolution and the satellite angular speed) for each of the energy and elevation angles reported in Tab. 2.2, and for the background measurements ;

- counts/s and energy spectra for relevant fixed values of energy, θ and ϕ;

- calibration sources spectra in the ESTEC calibration environment taken with a NaI detector in place of the satellite;

- calibration sources spectra taken at ENEA laboratories in Frascati with a Germanium detector.

The first set of data is the main base for detectors responses first order reconstruction, and the other sets, together with Monte Carlo simulations outputs, are used for spurious effects estimation and subtraction.

2.3.1 Ratemeters data

From 1 s count rates measured when the satellite was uniformly rotating around Z axis, it was straightforward, after taking into account small variations in the speed of the rotary table and offsets in the origin of the azimuthal angle (which was fixed to correspond to LS4 axis) and after background subtraction, to reconstruct the angle dependency of the shield efficiencies in the GRBM and AC bands at the various calibration energies. In figures from 2.4 to 2.10 we show the GRBM band counts dependency on ϕ for each LS at each calibration energy and with sources positioned at θ=0°. The change of the GRBM band ϕ angular curves with θ is shown in figures from 2.11 to 2.14 for each detector at the calibration energy of 166 keV. It is evident the increasing of LS2 efficiency at ϕ between -90° and +90° as the elevation angle increases and the HPGSPC exits from its field of view. Also we notice that LS1 and LS3 efficiency dependency on ϕ remains uniform and close to the co-sinusoidal shape also at non zero elevation angles, except for LS1 light curve at θ=-30, in which there is evidence of an important shielding effect at $\phi < 0$. . Finally, in figures from 2.15 to 2.21 we plot GRBM and AC light curves (upper panels) and their ratio (lower panels) for LS3 at θ=0 and at the various calibration energies. This last set of figures gives an idea of the effect of the ACT threshold on the detectors efficiency, effect which in turns depends on the detectors spectral response, as discussed in section 3.1.2. For the 662 keV measurements we also have an effect due to the ULT threshold, which cuts part of the photo-peak counts. In each of these figures two vertical dotted lines indicate the ϕ region in which the ratio between GRBM and AC counts can be well determined without strong statistical uncertainties (as is outside the region). At 60 keV we obviously have no counts in the AC band. It is noticeable that as the energy increases the ϕ range in which the GRBM/AC ratio can be well determined and is nearly constant enlarges, till reaching nearly the whole field of view at 662 keV. The same behavior is observed for LS1 and in the elevation range ±30°. This means that once we have reconstructed the angular/energy responses of LS1 and LS3 in the GRBM band, we can derive the efficiency in the AC band at least in the azimuthal range between ±60° by dividing for a factor which depends solely on photon energy.

In every figure we plotted the geometrical co-sinus function normalized to the LS1 counts at θ and $\phi = 0$, to put in evidence the deviation of detectors responses from the pure geometrical law and make a comparison between the efficiencies of the different shields. For figures 2.11,2.12,2.13,2.14, the theoretical geometrical shape has been corrected to account for the elevation angle by multiplying it by a factor cosθ. All this data refer to counts accumulated over a time period corresponding to a 2.5° azimuth angle width. Typical 1–sigma error are plotted in each figure at three ϕ values.

From all these figures it is apparent how the angular responses of LS2 and LS4 are remarkably distorted by the payload instruments and support structures in front of them, while those of LS1 and LS3 are roughly approximated by a simple cosine-like law times

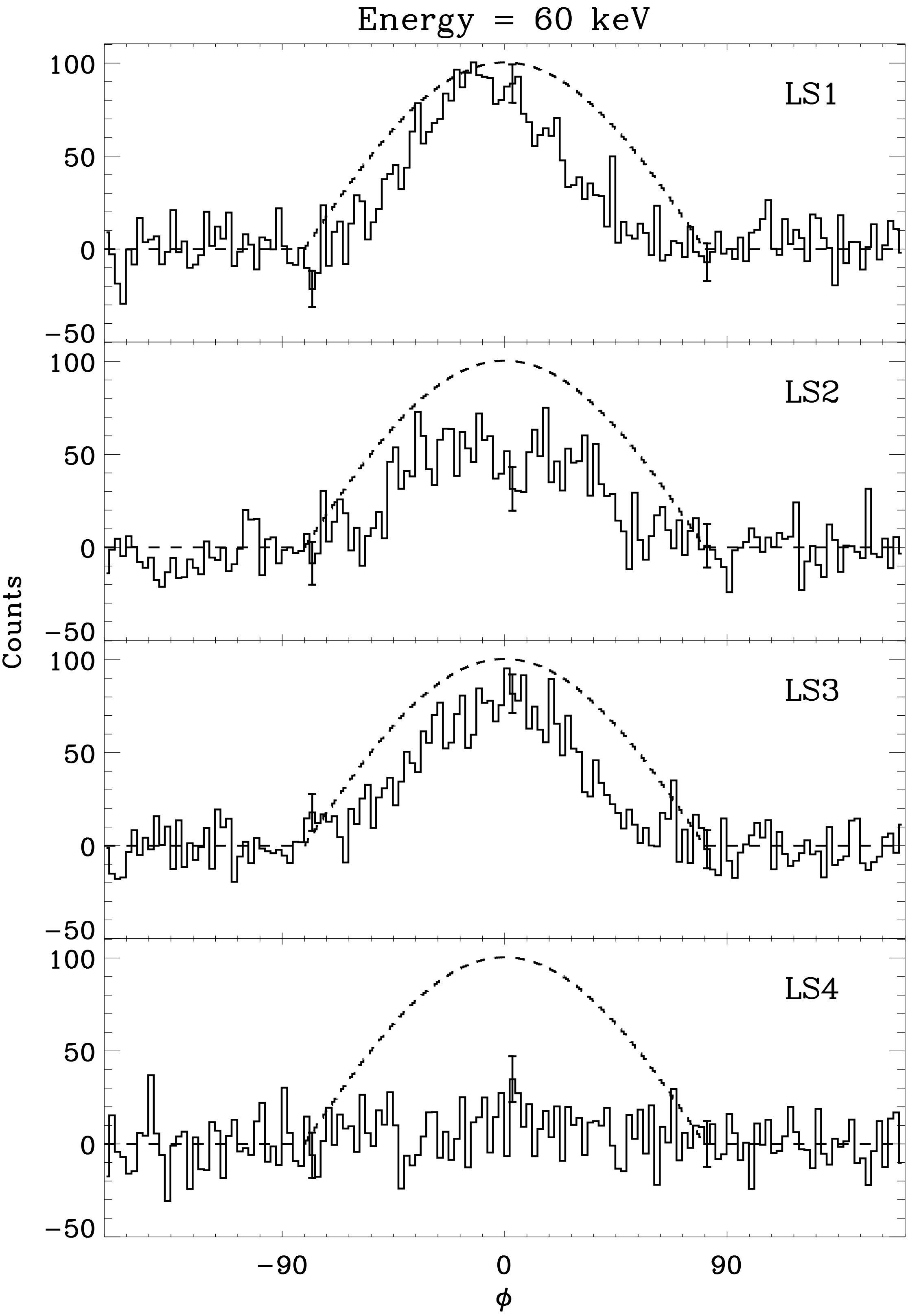

Figure 2.4: 60 keV angular light curves for the four LS.

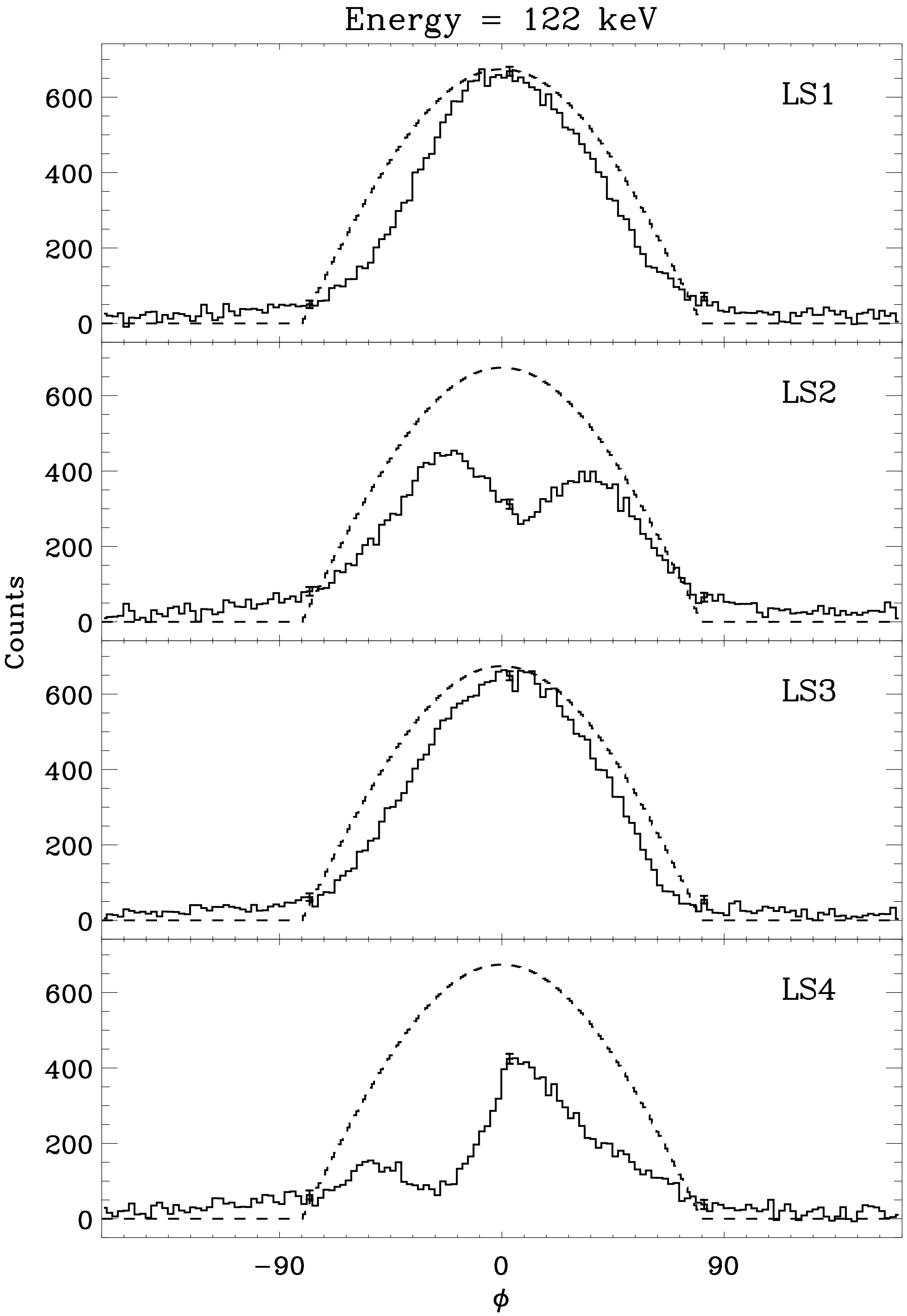

Figure 2.5: 122 keV angular light curves for the four LS.

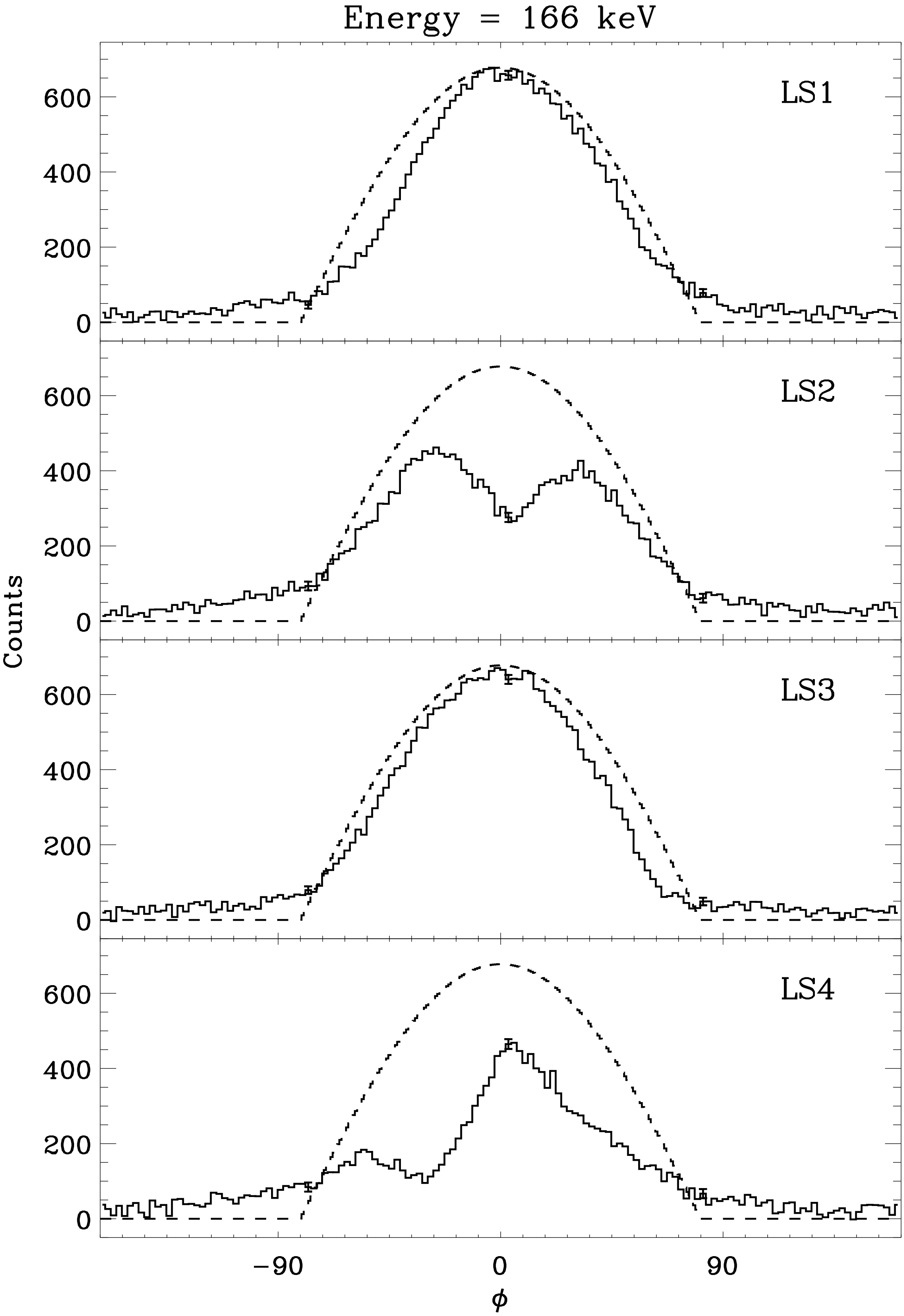

Figure 2.6: 166 keV angular light curves for the four LS.

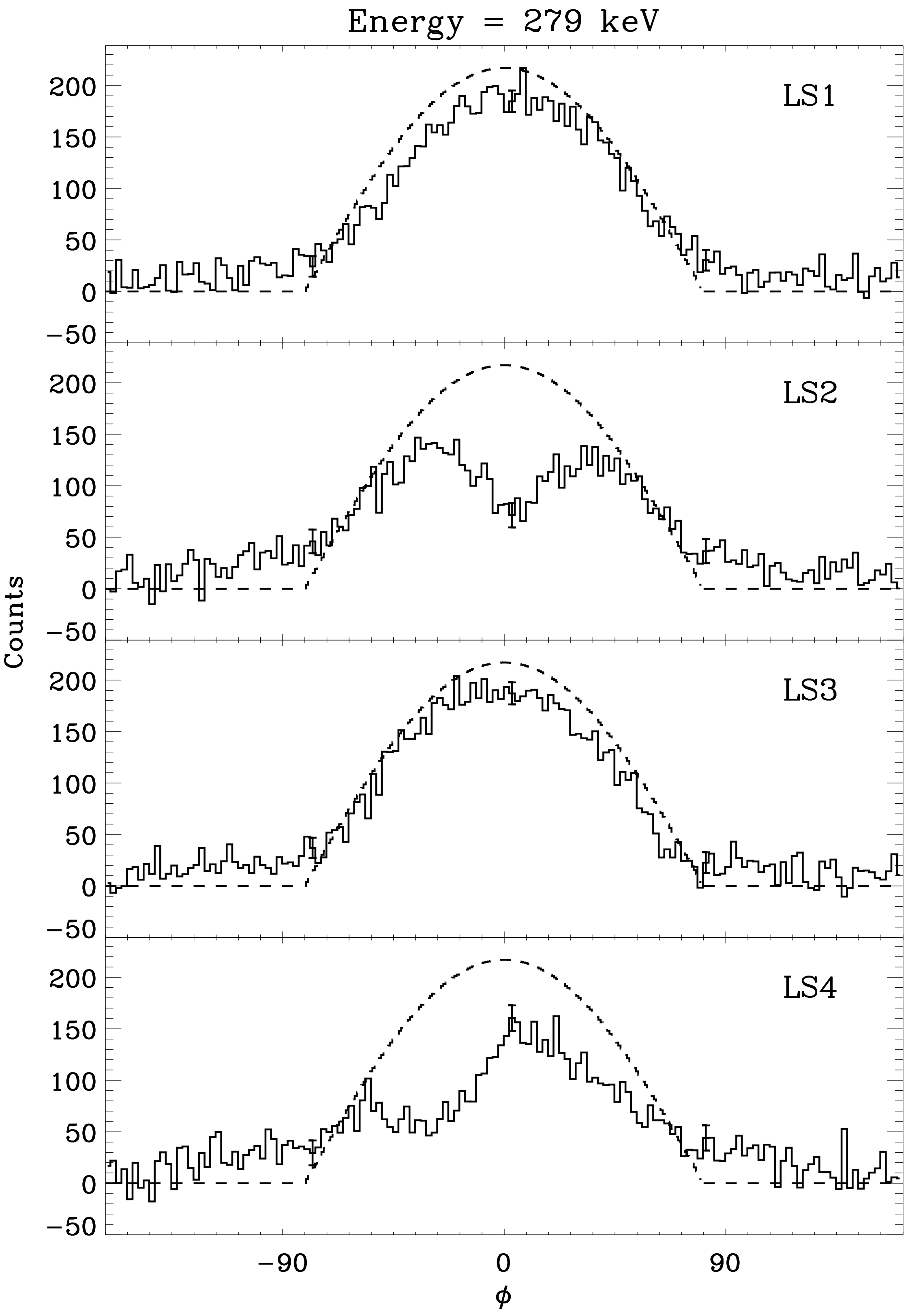

Figure 2.7: 279 keV angular light curves for the four LS.

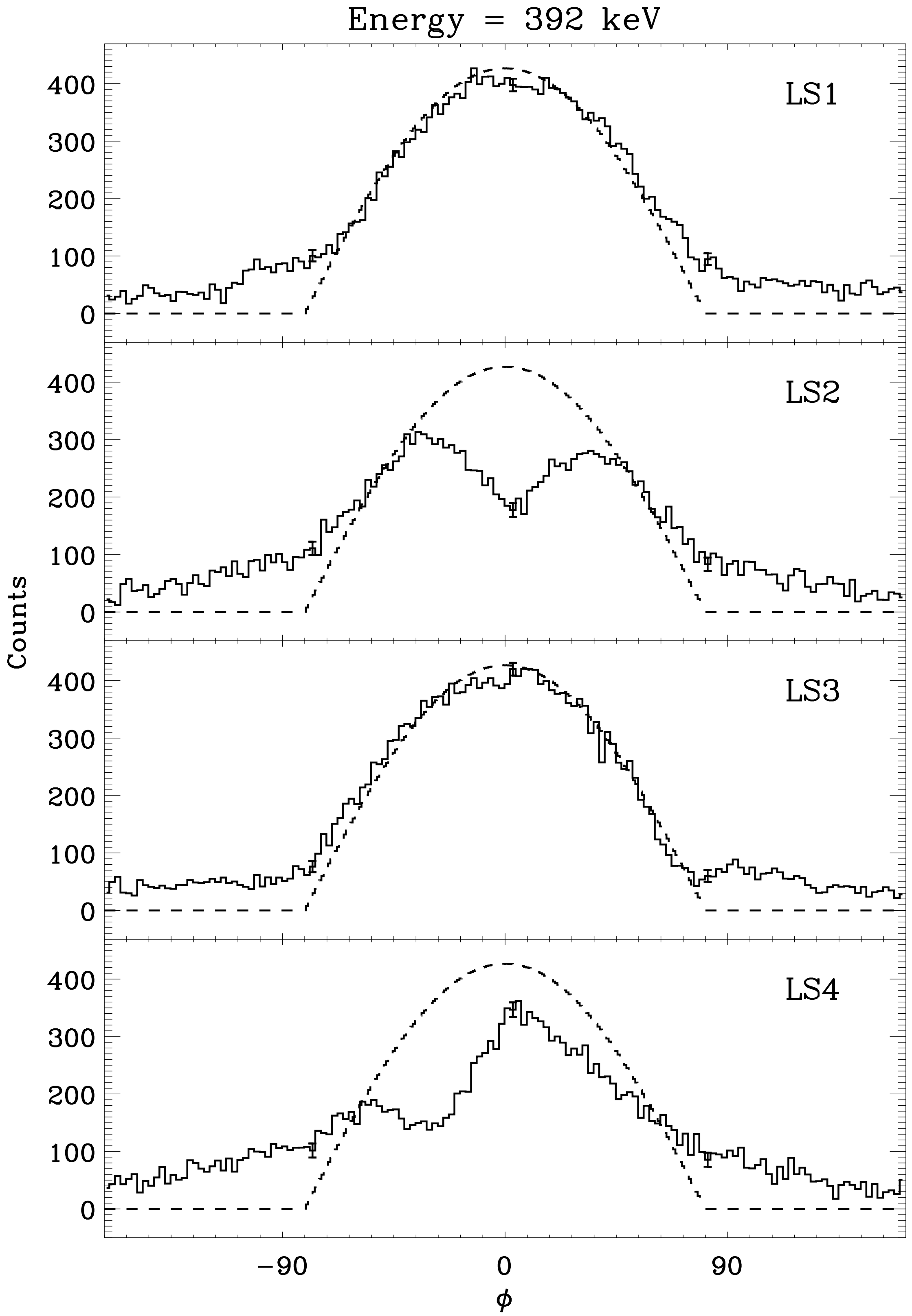

Figure 2.8: 392 keV angular light curves for the four LS.

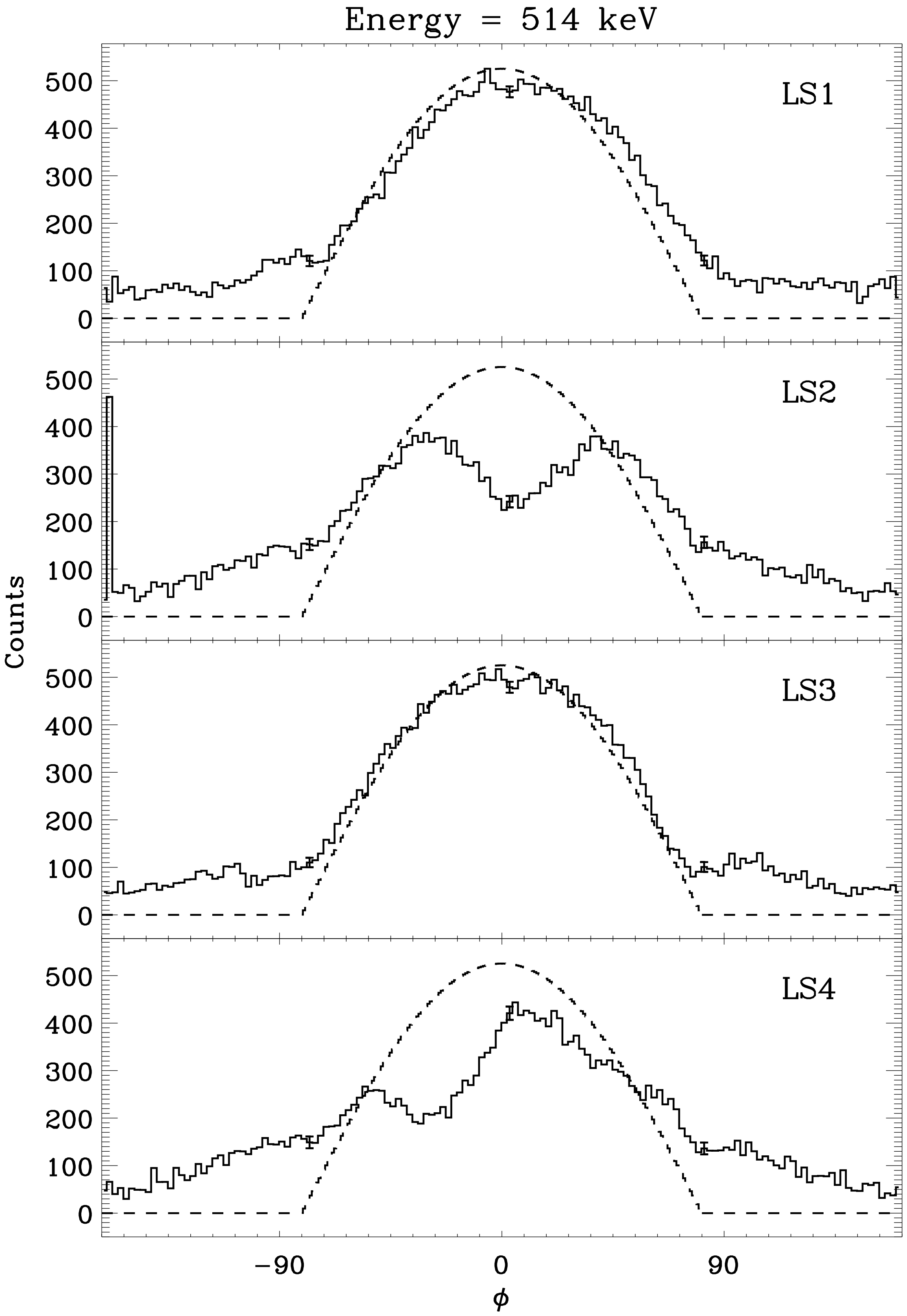

Figure 2.9: 514 keV angular light curves for the four LS.

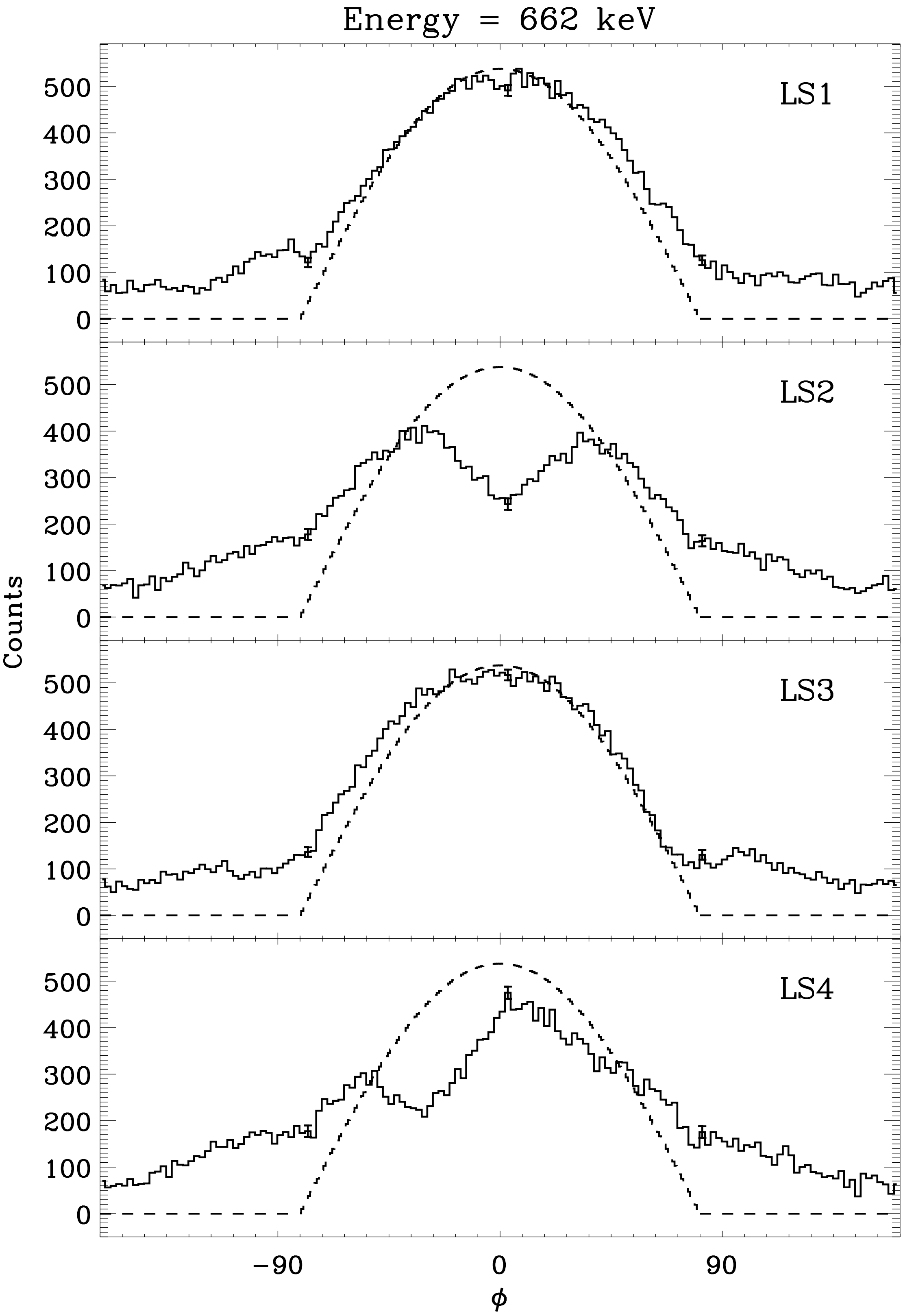

Figure 2.10: 662 keV angular light curves for the four LS.

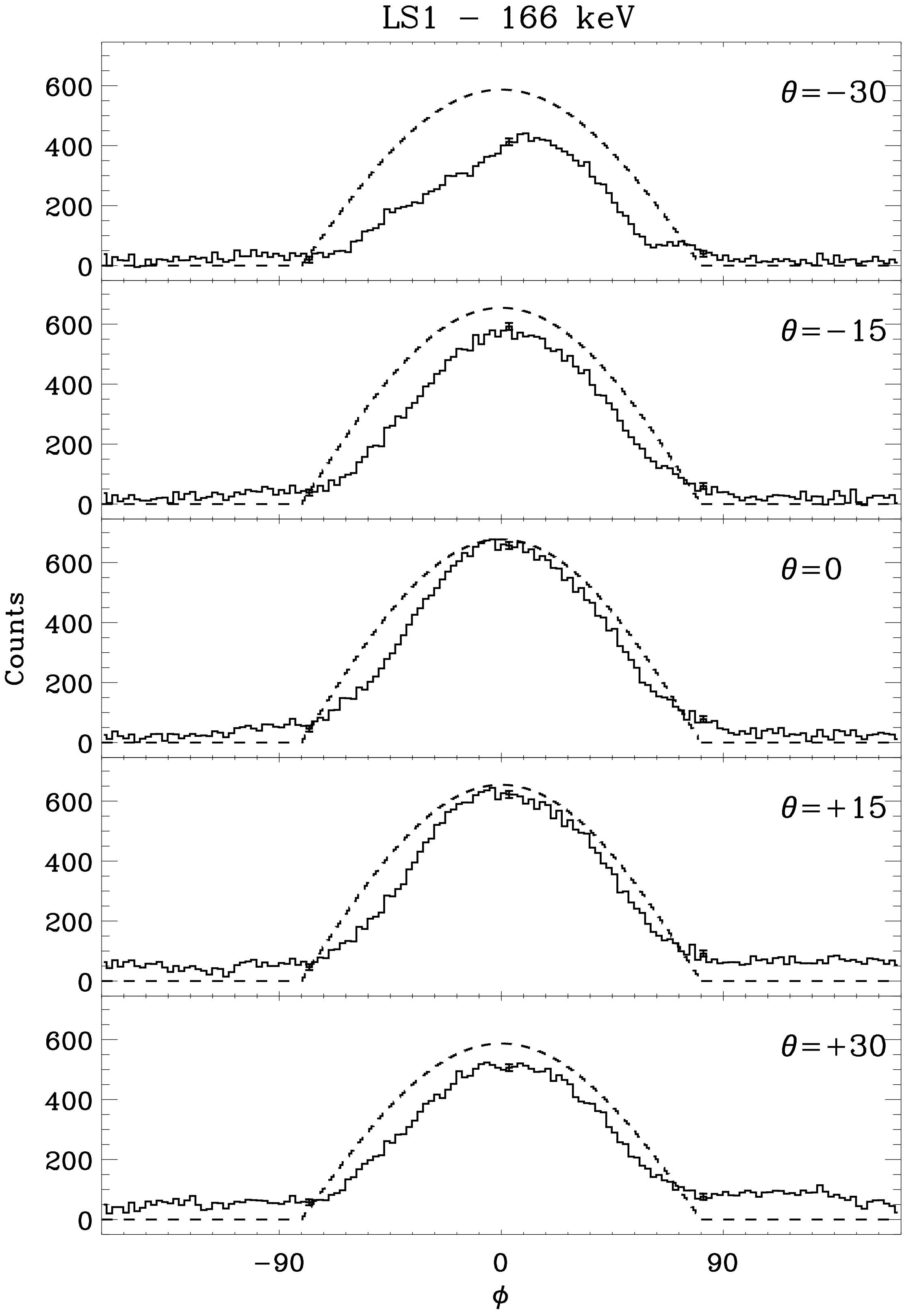

Figure 2.11: 166 keV LS1 angular light curves at different elevation angles

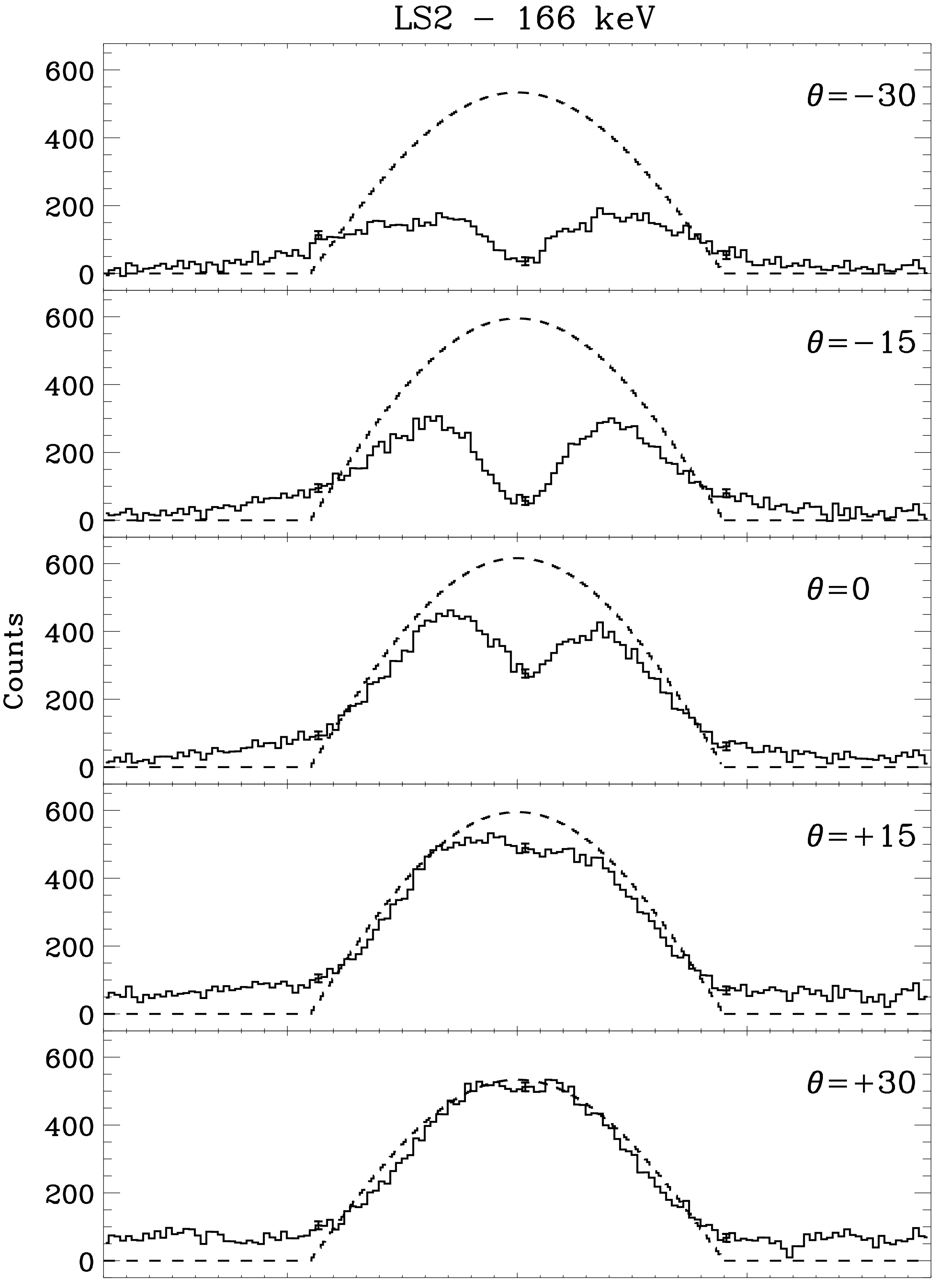

Figure 2.12: 166 keV LS2 angular light curves at different elevation angles

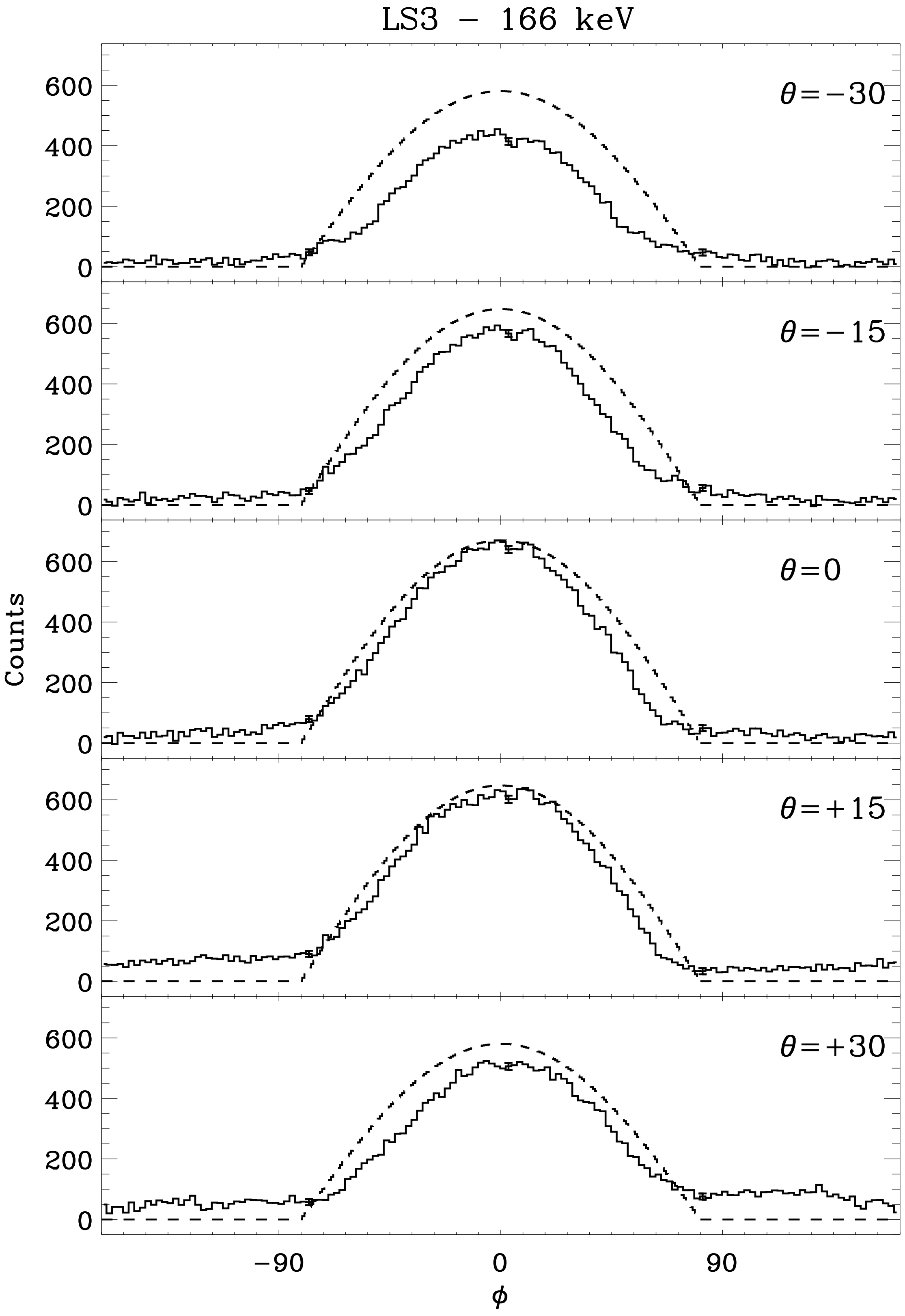

Figure 2.13: 166 keV keV angular light curves at different elevation angles

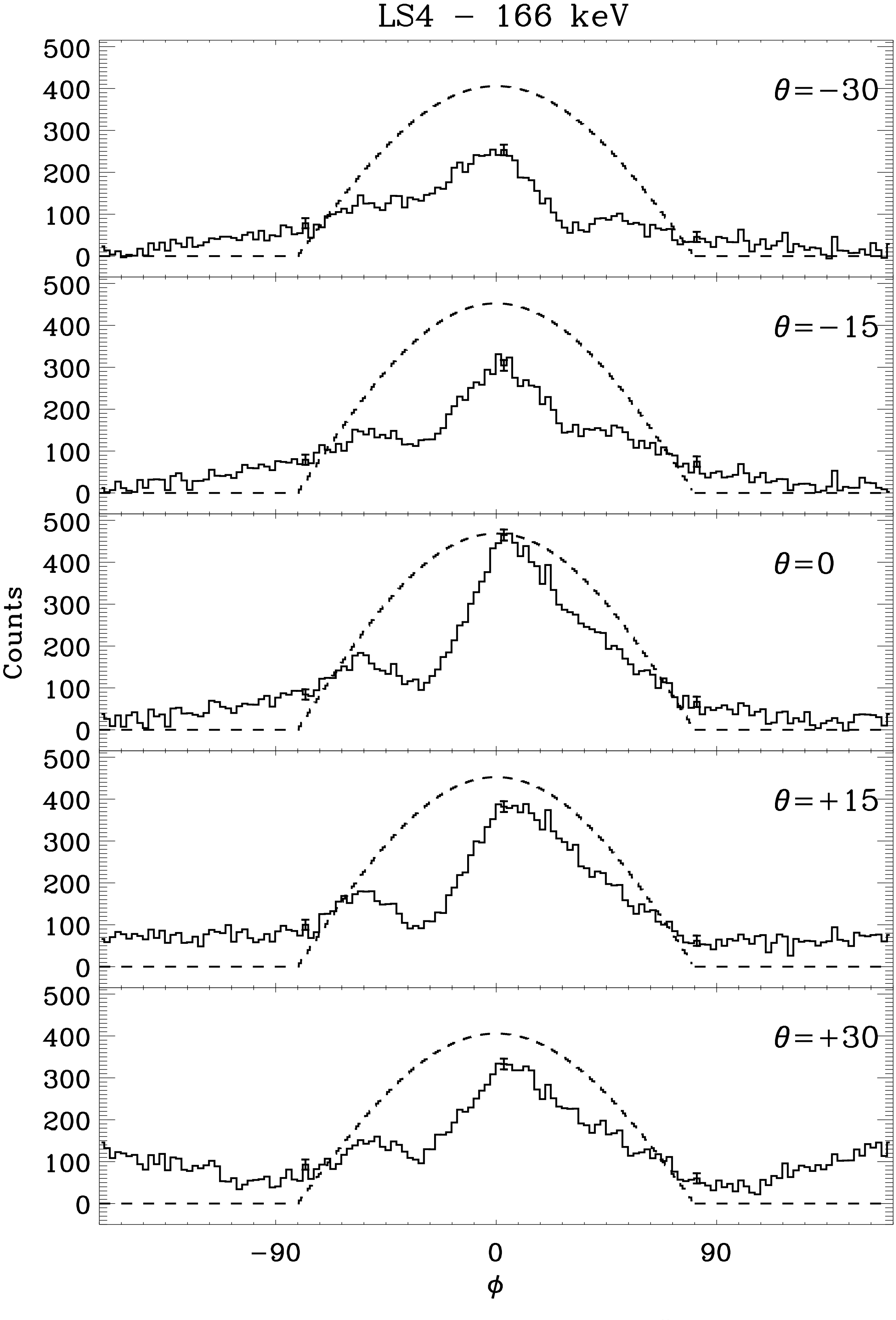

Figure 2.14: 166 keV keV angular light curves at different elevation angles

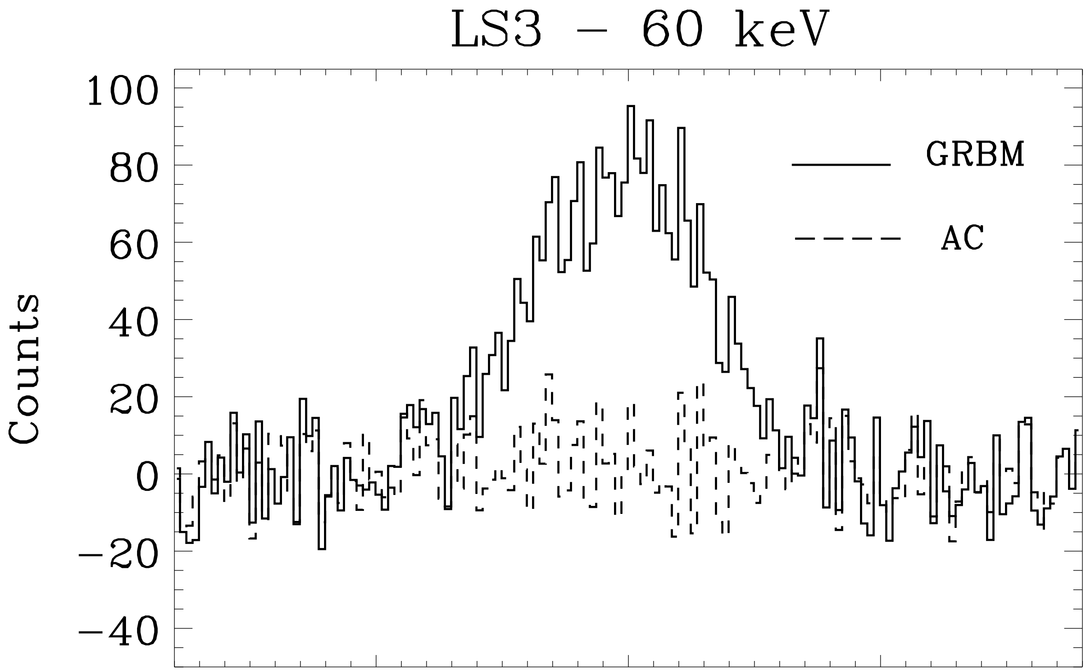

Figure 2.15: LS3 angular light curves in the GRBM and AC bands at 60 keV

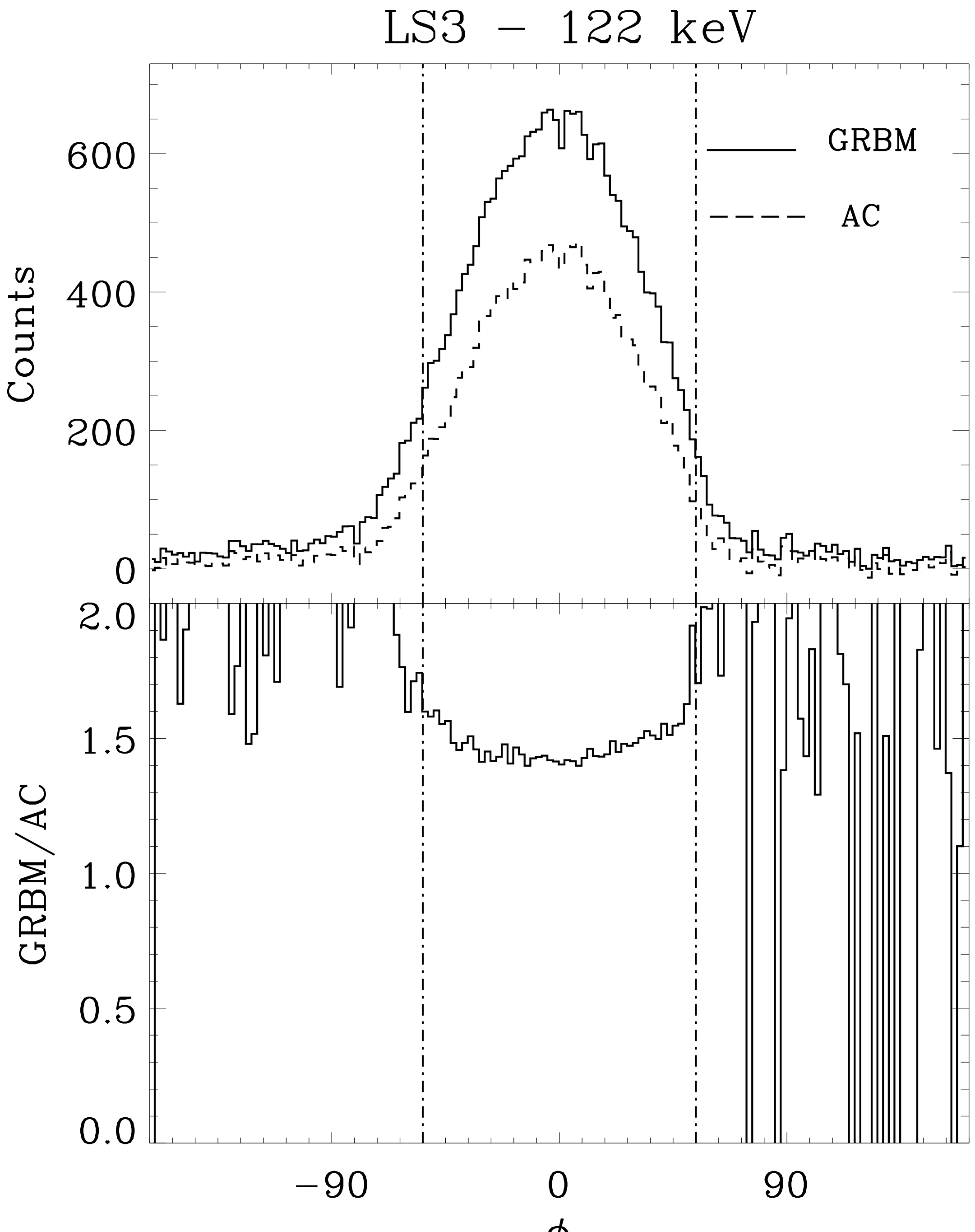

Figure 2.16: LS3 angular light curves in the GRBM and AC bands at 122 keV

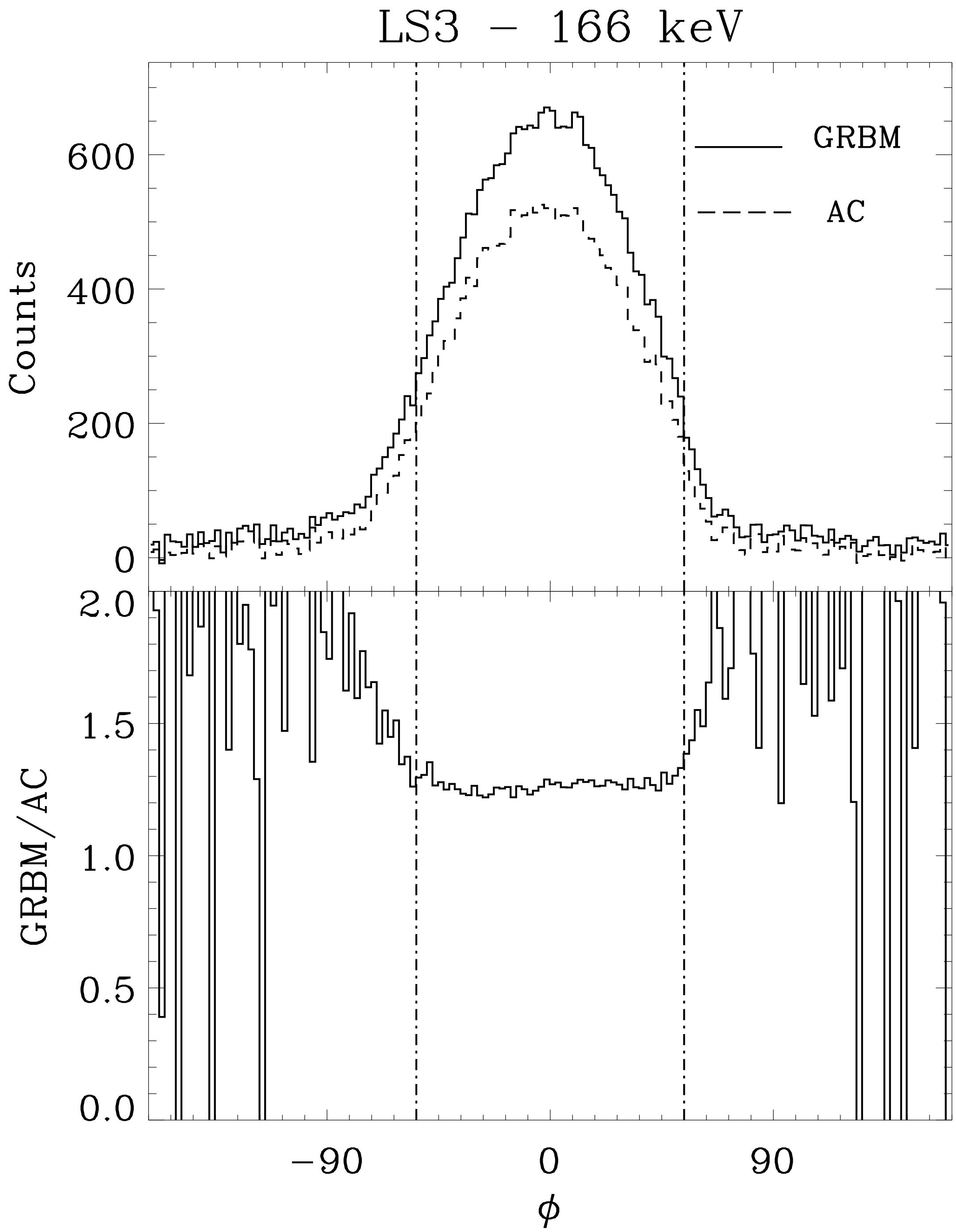

Figure 2.17: LS3 angular light curves in the GRBM and AC bands at 166 keV

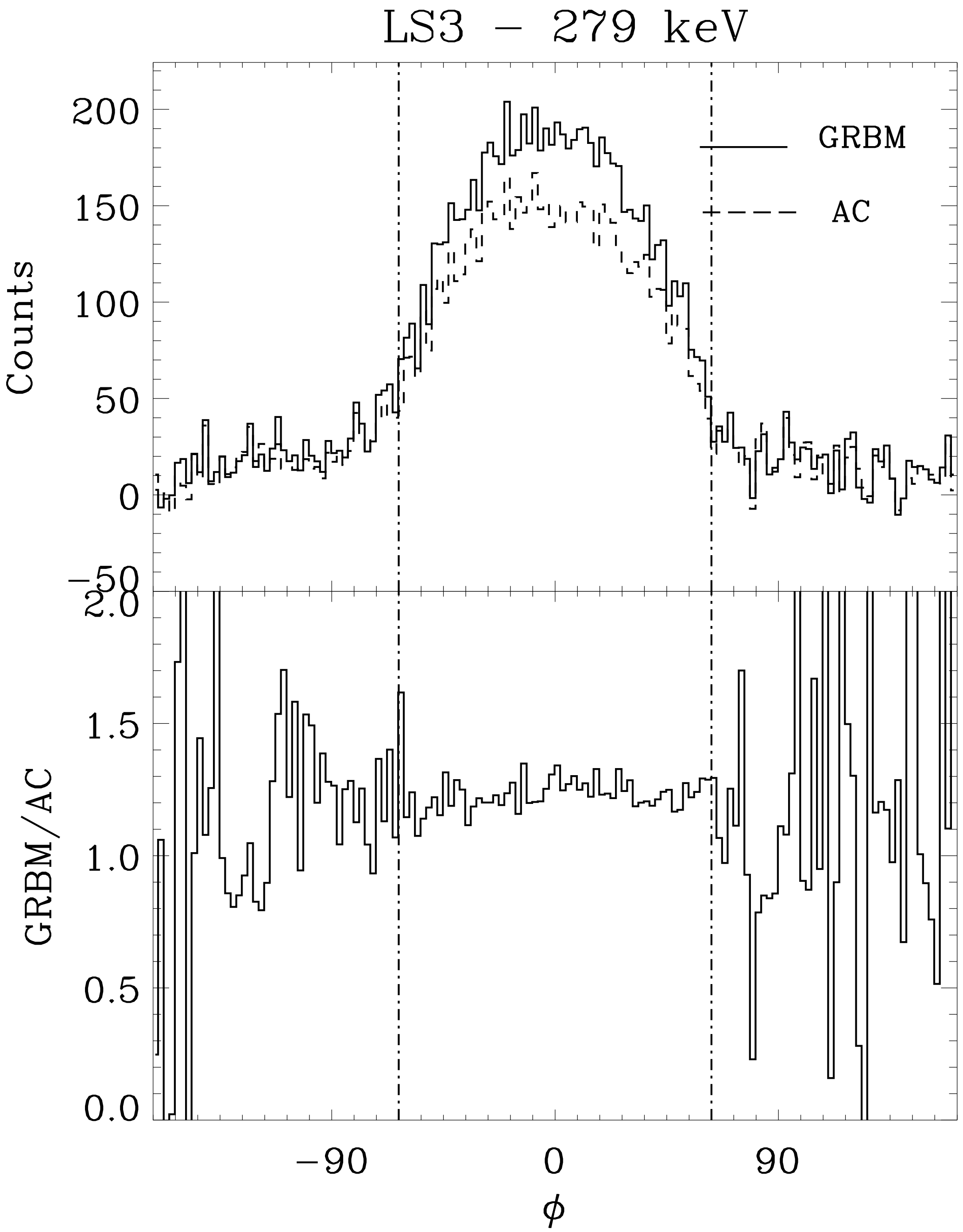

Figure 2.18: LS3 angular light curves in the GRBM and AC bands at 279 keV

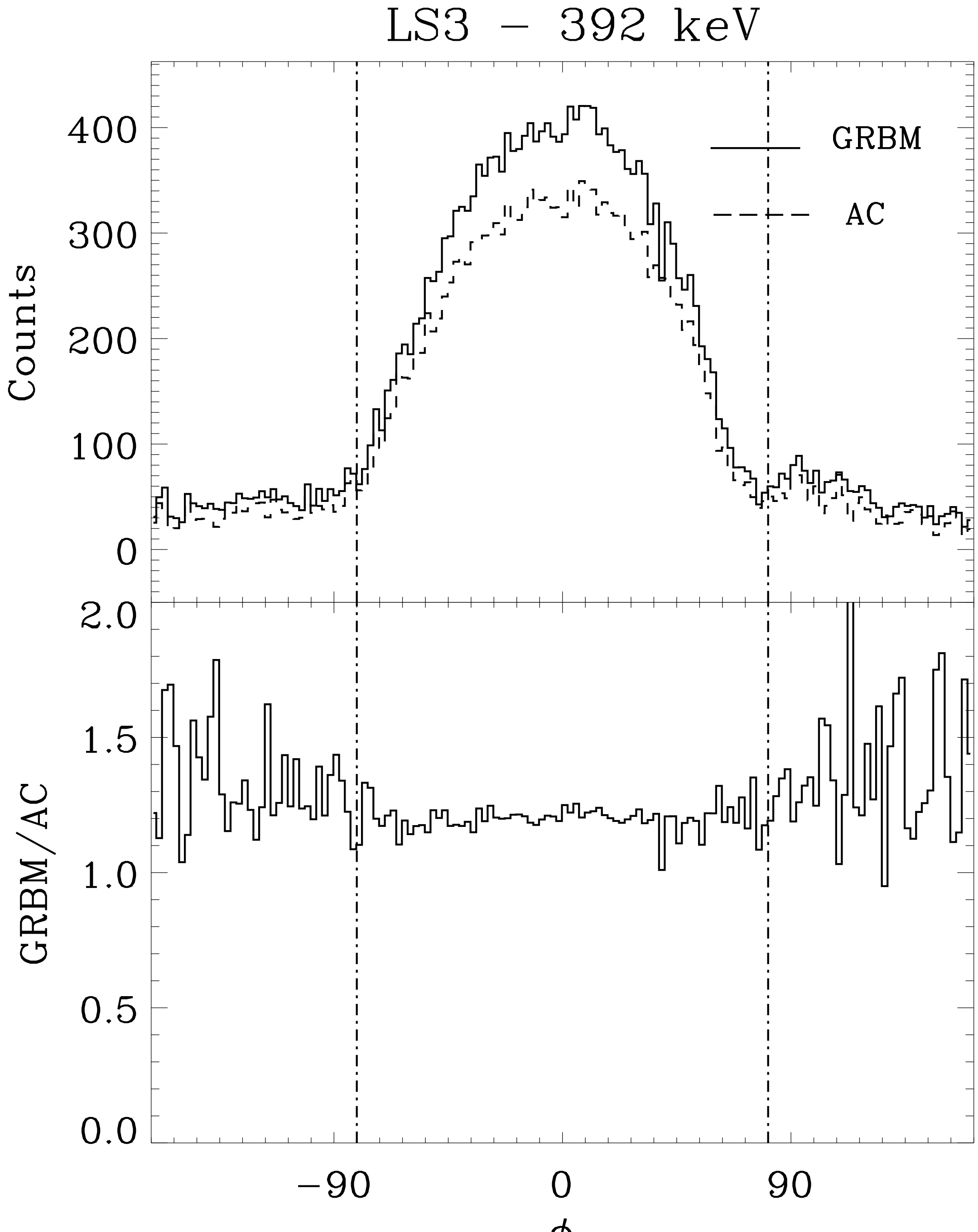

Figure 2.19: LS3 angular light curves in the GRBM and AC bands at 392 keV

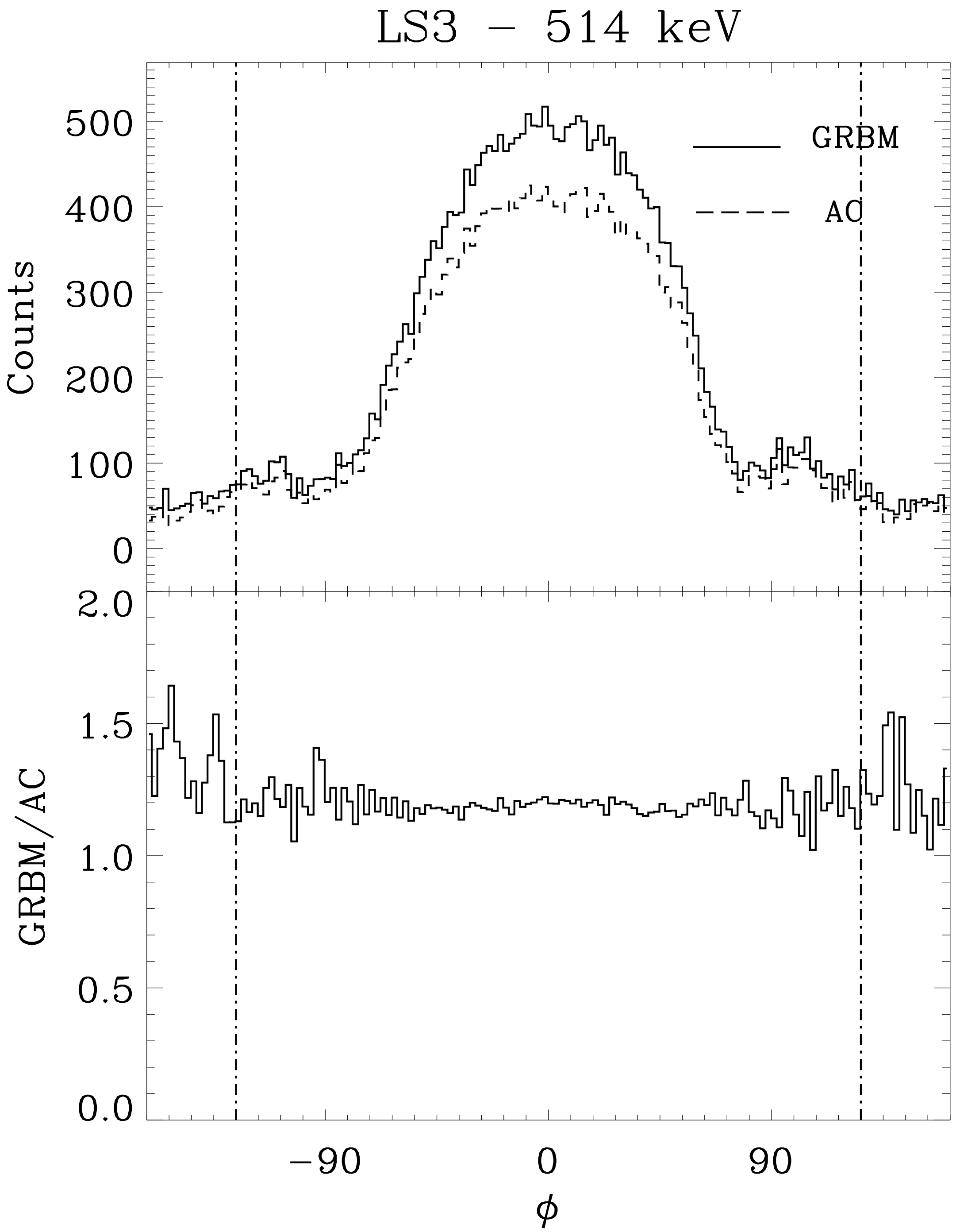

Figure 2.20: LS3 angular light curves in the GRBM and AC bands at 514 keV

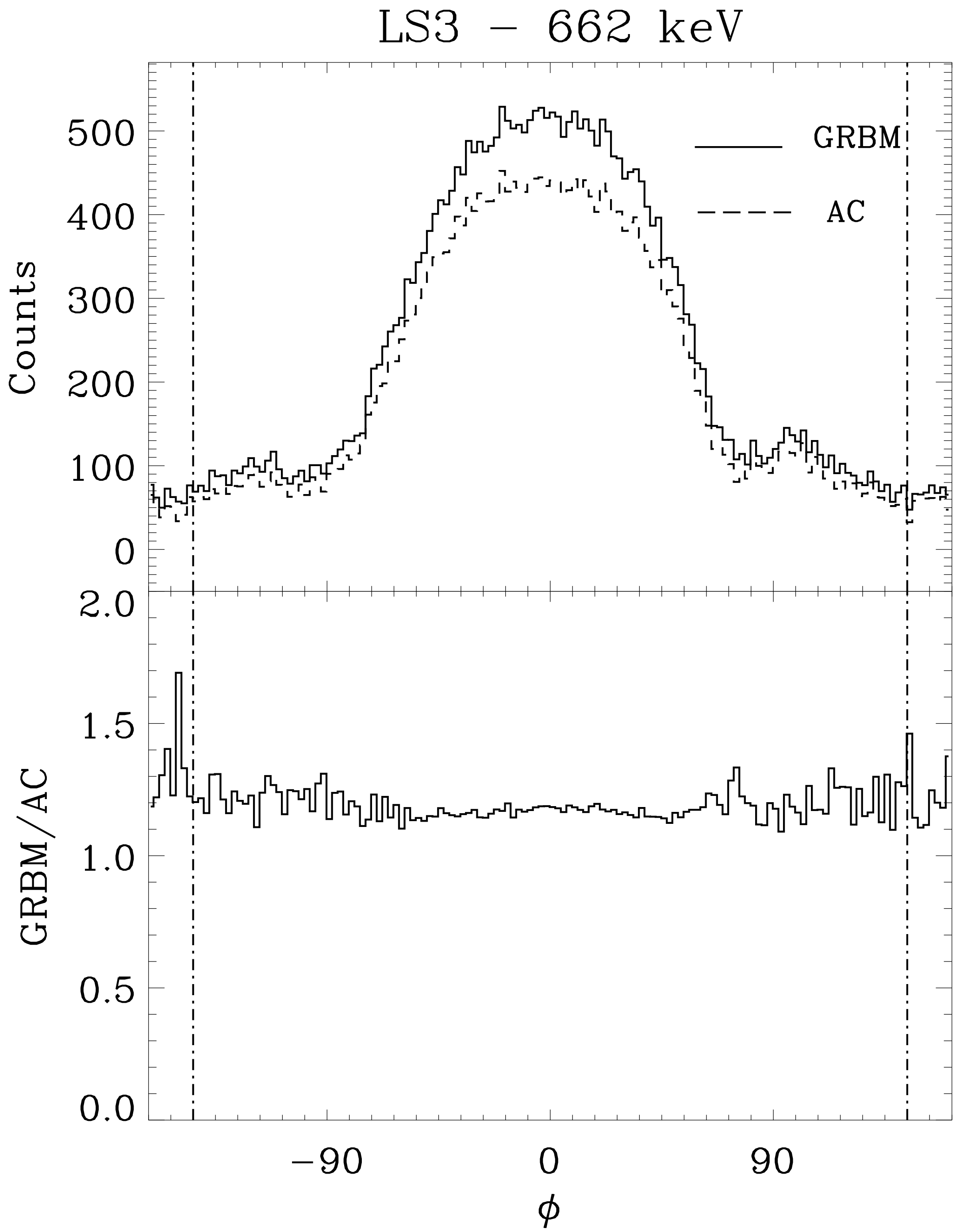

Figure 2.21: LS3 angular light curves in the GRBM and AC bands at 662 keV

an exponential function (see section 3.3.2). Indeed, the latter shields are in front of the support structures of the X–ray optics (LS1 in front of 2 MECS, LS3 in front of one MECS and 1 LECS). These optics are made of nested coaxial mirrors of nickel gold-coated, while their support structures is made of carbon fiber tubes about 2 m long. Each pair of tubes is contained in a 2 cm thick Al box whose width is of the order of that of the shields. This geometry allows a relatively uniform absorption of the radiation entering the field of view of LS1 and LS3. The azimuthal response of LS2 shows clearly the shielding effect of the HPGSPC instrument.

Finally, the angular response of LS4 is strongly distorted by the presence of WFC1 in front of it (the presence of WFC2 is apparent at negative elevation angles). The heavy shielding and asymmetry observed in the LS4 angular response can be directly associated to the camera design. Its stainless steel external structure causes a strong absorption; for elevation angles $< 0°$ the shadowing effect is due to the gas proportional counter and its associated electronics, while for angles $> 0°$ it is mainly due to the mask, its support structures and to the square stainless steel camera support.

By considering LS1 and LS3 light curves, we can see that at low energies (60, 122 and 166 keV) the absorption of the materials in front of the shields discussed above causes the counts to be below the geometrical co-sinus curve. At intermediate energies (279, 392 keV) the detector response is very close to the co-sinusoidal function, with some excess of counts with respect to the theoretical zero–level at $\phi < -90$ and $\phi > 90$. At high energies there is an evident excess with respect to the geometrical form and the counts (and thus detectors efficiency) are always above the zero–level in the whole ϕ range.
This means that, as confirmed by the energy spectra (see next section), there is a strong contribution to the calibration sources flux from the calibration environment and possibly by other PDS components and satellite instruments and structures. In addition, a fraction of the high energy excess at large ϕ angles may be due to photons crossing one shields and PDS collimators without being absorbed and finally depositing their energy into

an adiacent or even the opposite shield. As discussed in chapter 4, this last effect is also observed in in–flight data, in which a GRB whose position is very close (within 20 degrees) to one detector axis is also seen, if sufficiently intense and hard, in the two closer shields and in some cases even in the opposite shield (also if some contribution may well come from source gamma–rays reflection by the outer layers of Earth-s atmosphere).

In conclusion, these results show that, after estimating and subtracting spurious contributions, an analytical modeling of LS1 and LS3 responses basing on calibration data is possible, while for LS2 and LS4 a satisfactory response description can be obtained only by simulations with the Monte Carlo model.

2.3.2 Energy spectra

In figures 2.22 and 2.23 we show the LS1 and LS3 calibration sources spectra at θ=0 and averaged on the azimuthal interval $\phi \sim \pm 10$. The spectra are background subtracted. The channels 241–256 have been excluded because they do not contain scientific data (see section 1.2.3). Typical 1–sigma error are plotted in three points.

The spectra show the expected features discussed in section 3.1.2. At 60 keV the spectrum is composed by the photo-peak and the characteristic X–ray escape peak. At 122 keV we observe no more escape peak, which theoretically should still be present but here is 'merged' with the photo-peak due to the detectors low energy resolution, and it begins to apparent a contribution from Compton scattered photons at the left of the photo-peak. As the energy increases the Compton continuum and a back–scattering component superimposed to it becomes more and more evident. The Compton edge is very smoothed as the energy increases, and the gap between it and the photo-peak is filled by multiple–scattered photons and the low–energy wing of the photo-peak itself. No signature of pair production absorption is observed, as expected, because the maximum source calibration energy, 662 keV, is lower than the 1022 keV required for this process to occur. Also, in the low–energy part of the 166, 392 and 662 keV spectra, peaks due to the secondary lines at 33–39, 24–28 and 32 keV (Tab. 2.1) are apparent. Again, the low detector resolution do not allow to see these blends as separate peaks.

In figures 2.24 and 2.25, spectra at 60 keV for LS1 and at 662 keV for LS3 taken on ϕ ranges between -50° and +50° at θ=0. are shown. The indications that come out from these data is that, at least not too far from detectors axis, the overall shape of the spectral response does not depend significatively on source direction. It is also well seen the dependency of the overall efficiency on ϕ, accordingly with what is seen in ratemeters data. In particular, in the 662 keV spectra there is indication that the backscattering peak area decreases proportionally to the photo-peak area. Thus, the backscattering contributed counts can assumed to be a constant fraction of the source photons over this angular range. We finally note that in the 60 keV spectra, a little feature is present at channel corresponding to the gain calibrator energy, indicating a slight change in PMT gain between the different measurements.

The preliminary analysis of these calibration spectra shows that, in order to reconstruct LS1 and LS3 spectral response functions, in addition to the modeling of the main spectral components (photo-peak, characteristic X–ray escape peak, Compton continuum, multiple scattering events), a satisfactory estimation and subtraction of the backscattering contribution due to interaction of source photons with the calibration room walls and floor is required. The better way to to this is to introduce calibration room walls and floor in the Monte Carlo model and then compare the simulations results with these calibrations. Because the MC was not still developed to a satisfactory stage, we addressed this problem by a straight comparison between LS line spectra and the ESTEC and ENEA sources calibration spectra described in previous section.

2.3.3 Background

On–ground calibrations background is mostly originated by gamma–rays emitted by means of natural radioactivity by the materials composing the room walls and floor. Occasionally, some specific element lines may be observed. Also, calibration sources of other satellite instruments may generate background lines. The dependency of the back-

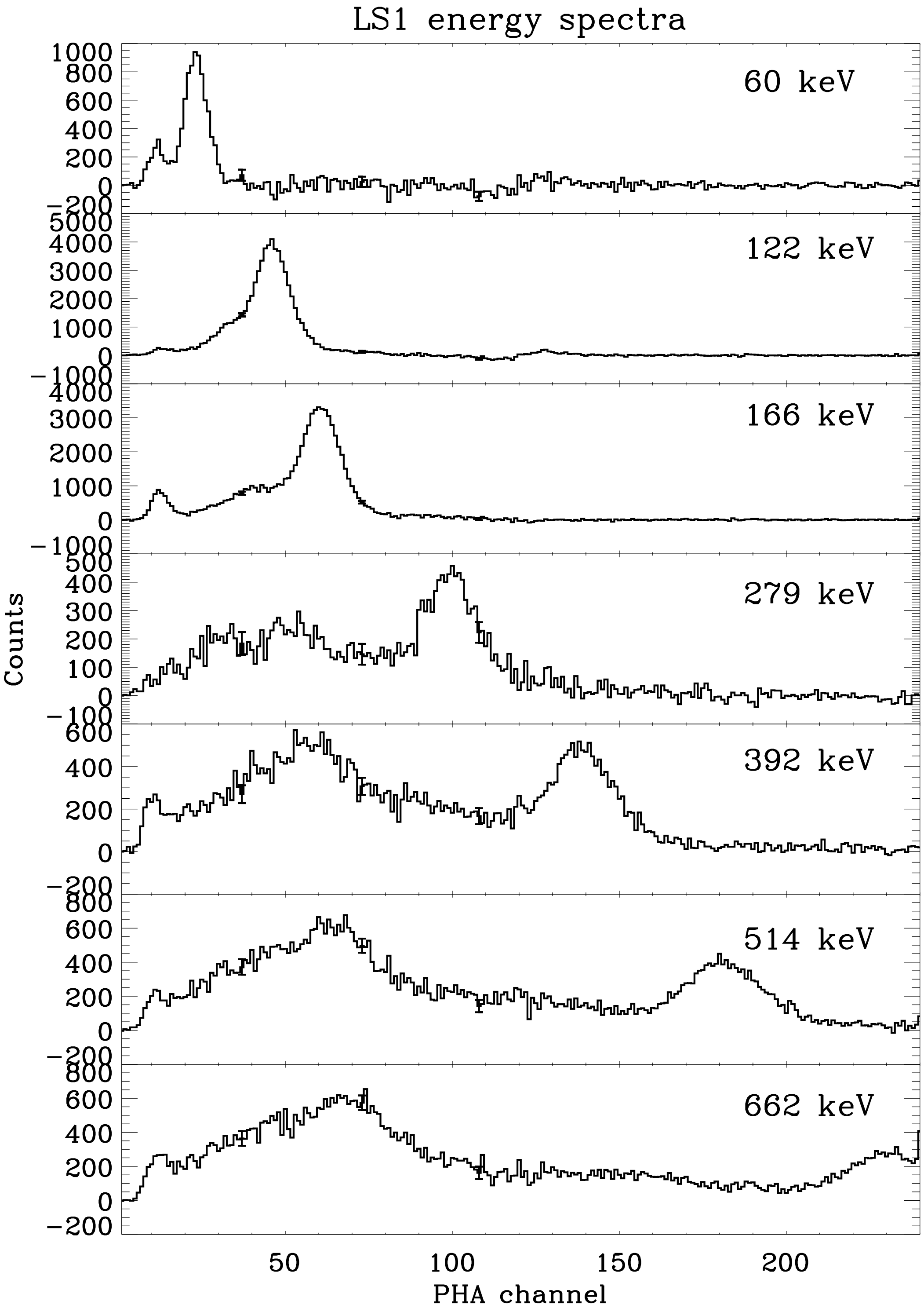

Figure 2.22: LS1 line spectra at the various calibration energies.

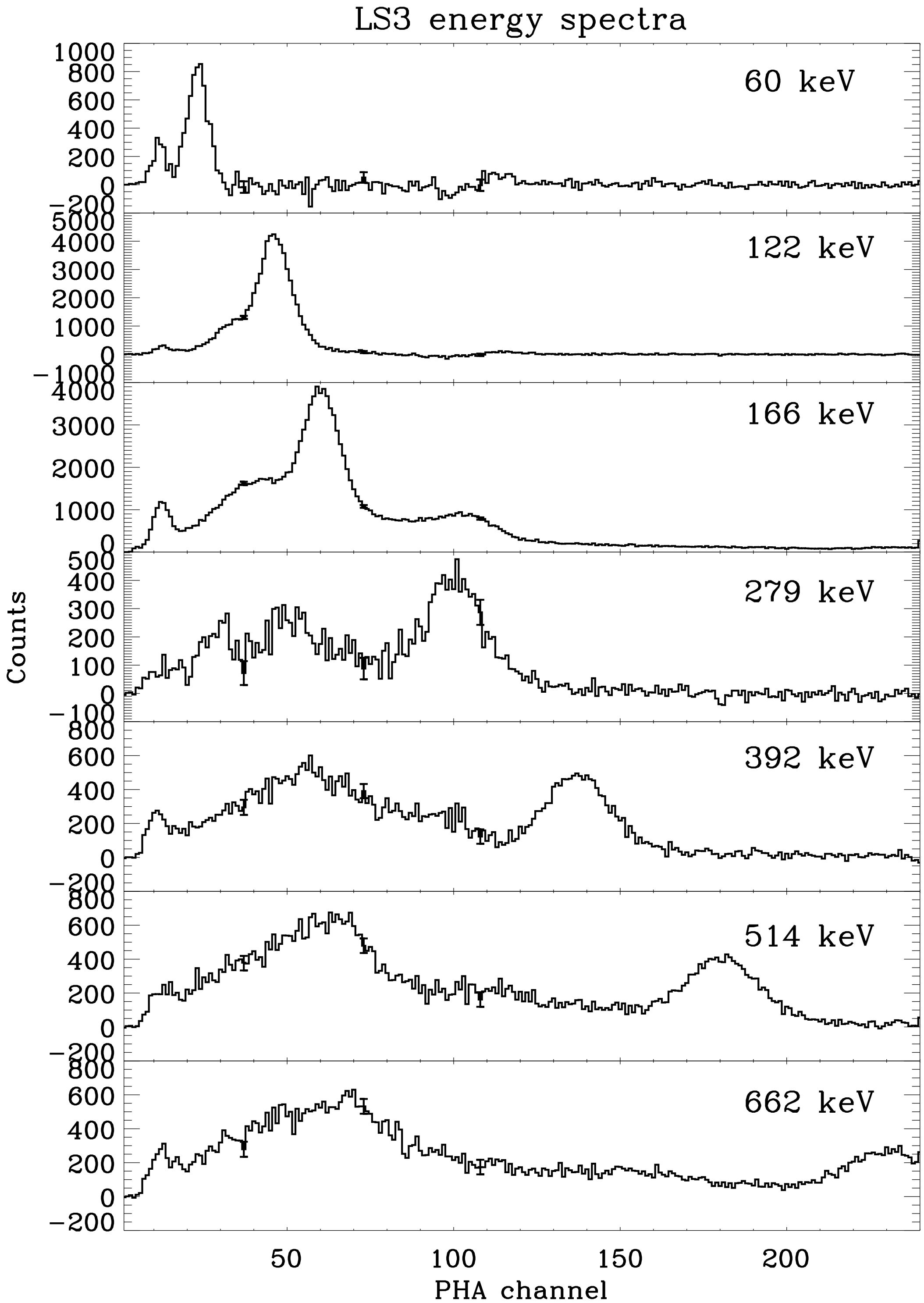

Figure 2.23: LS3 line spectra at the various calibration energies.

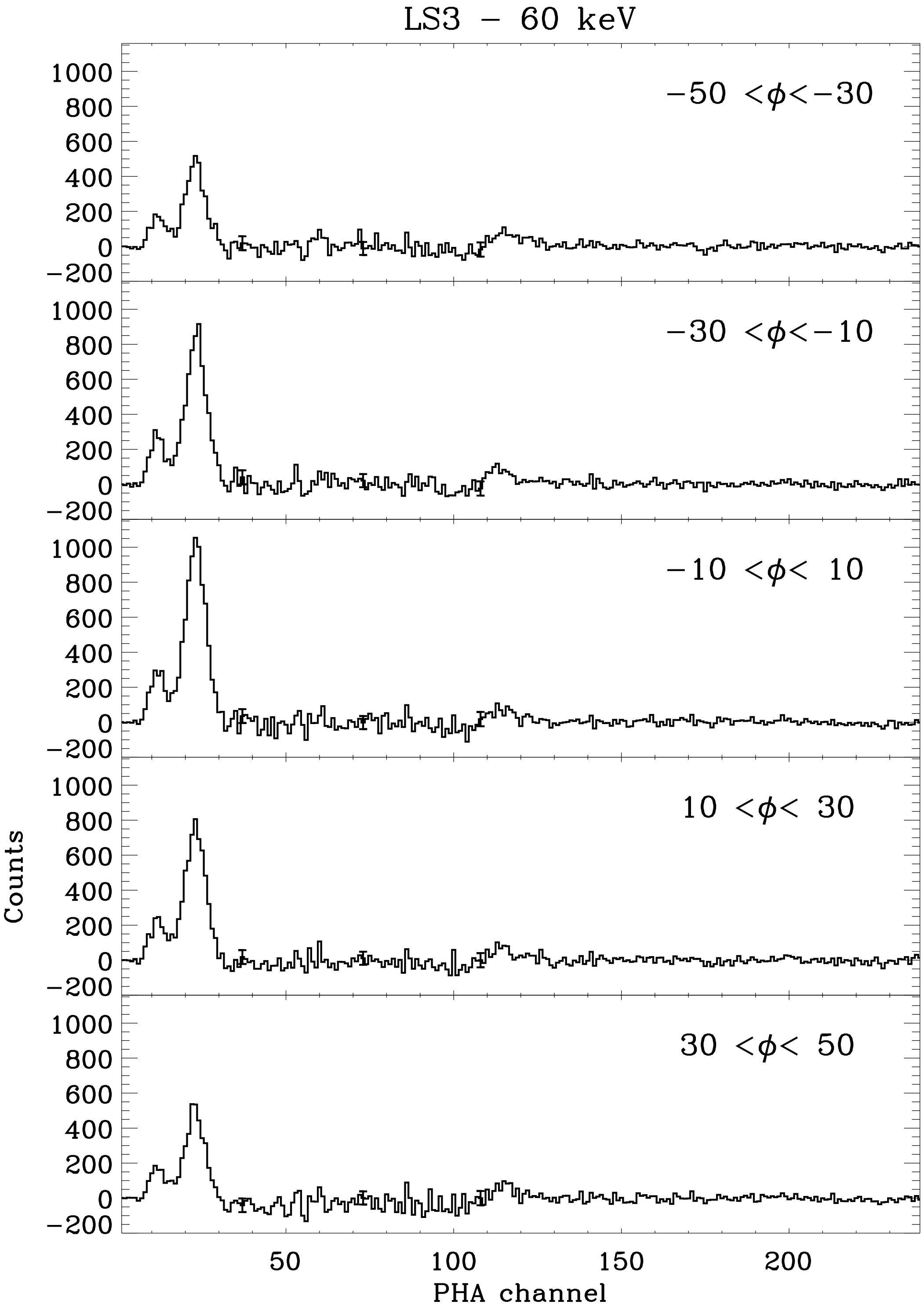

Figure 2.24: LS3 spectra of the 60 keV source at different azimuthal angles.

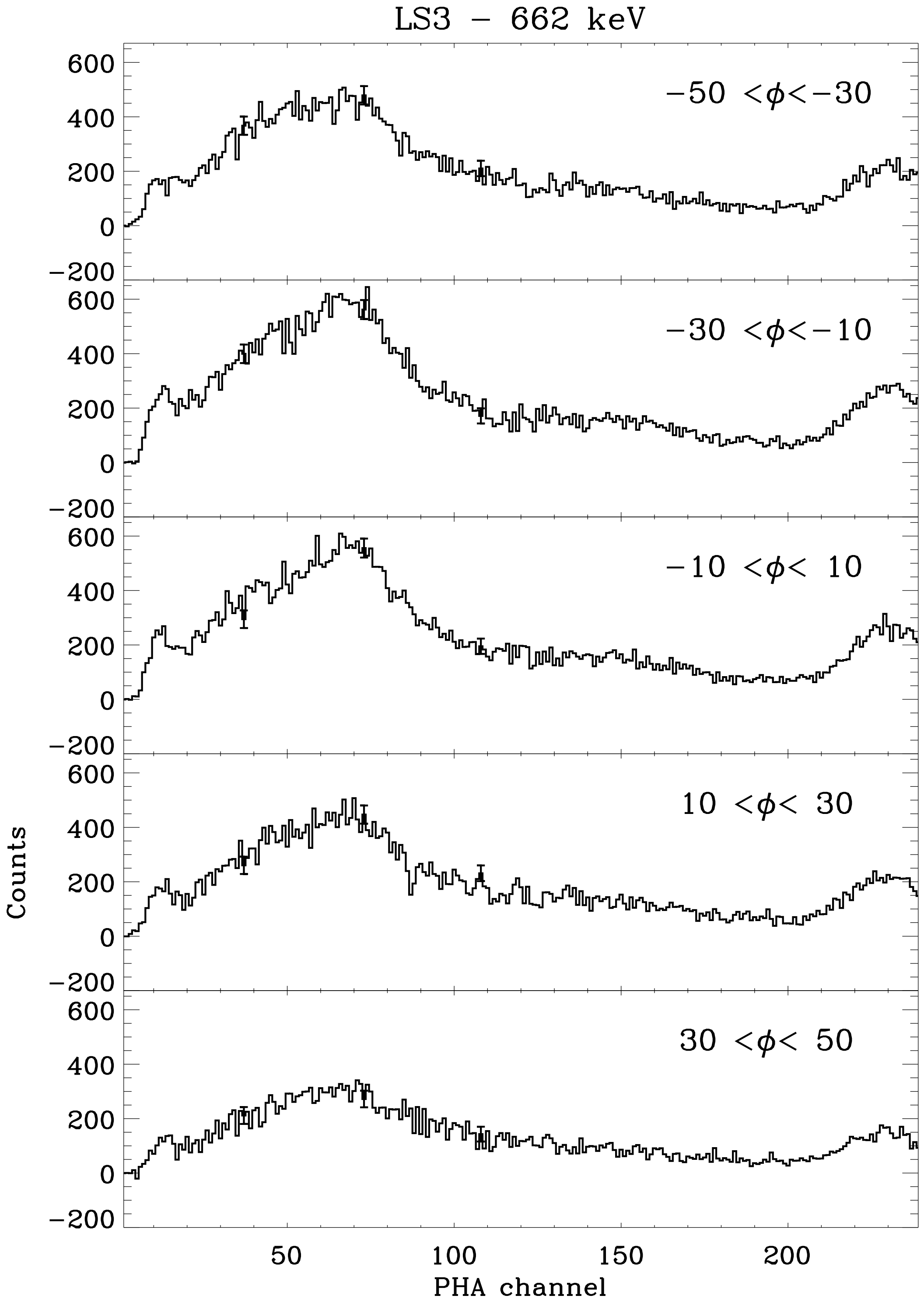

Figure 2.25: LS3 spectra of the 662 keV source at different azimuthal angles.

ground in the GRBM band on ϕ at θ=0° is shown for the four LS in Fig. 2.26. As can be seen, there was a variation of the background level, with the maximum reached when the detectors were facing the same wall of the calibration room. This wall was made of different and probably more radioactive material with respect to the others. It can also be seen that the LS4 background level is higher; this is due to contamination from the 692 keV secondary line emitted by the ^{57}Co MCS (section 1.2.2), whose parking position is above this shield and whose shielding is not very efficient for these high energy photons.

The spectra of the background in the four detectors are shown in Fig. 2.27. These data have been collected during an entire satellite rotation. In all detectors we observe a continuum which is due to the environmental background photon spectrum. Superimposed to this component, we observe other important features which are due to PDS experiment materials and are thus also observed in in–flight spectra (see section 4.1). At energies of $\sim$ 350 keV there is the photo-peak of the gain calibrator line. We see that the line is not exactly at the same energy for all the detectors, depending mainly on different PMT gains. In the LS2 spectrum the most prominent feature is the photo-peak due to the 88 keV photons emitted by the ^{109}Cd radioactive sources that are part of the HPGSPC which stands in front of this shield. The 692 keV low energy part of the photo-peak component due to the MCS emitted line is well visible in the LS4 spectrum and marginally in LS2 and LS4.

2.3.4 Sources calibration and spurious contributions

Some results of the radioactive sources calibrations described in section 2.4.3 and performed in order to estimate spurious contributions to GRBM detectors measured spectra by the calibration environment and/or sources set–up are shown in figures 2.28 and 2.29. In Fig. 2.28 we show the spectra of all the calibration sources taken at ESTEC with the NaI detector in place of the satellite. Two remarkable results are clearly visible in comparing these spectra to the GRBM spectra (Fig. 2.22, Fig. 2.23). The first is that the low–energy blends photo-peaks are clearly seen in the NaI spectra, showing the absorbing

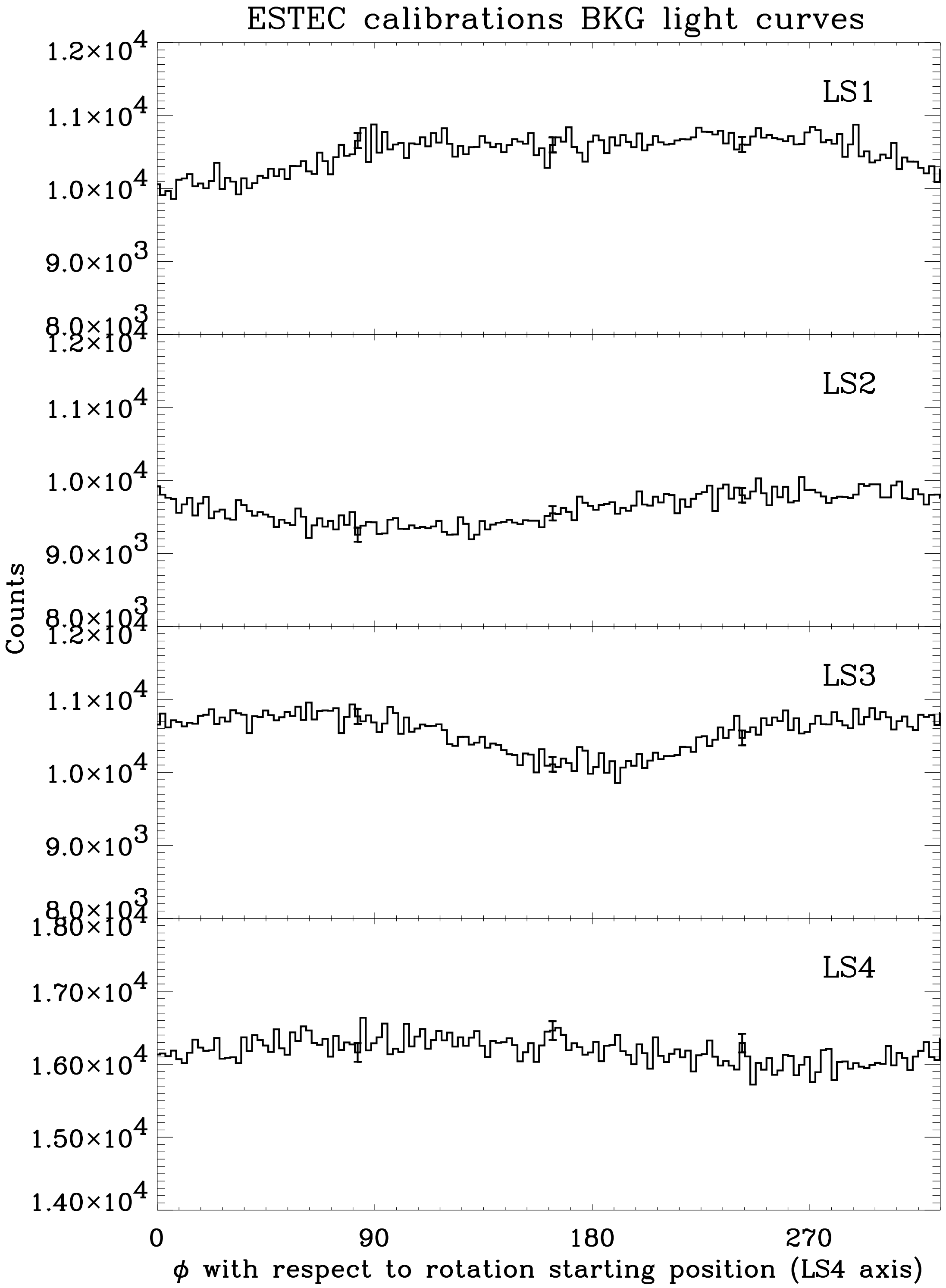

Figure 2.26: ESTEC calibrations background variation with ϕ

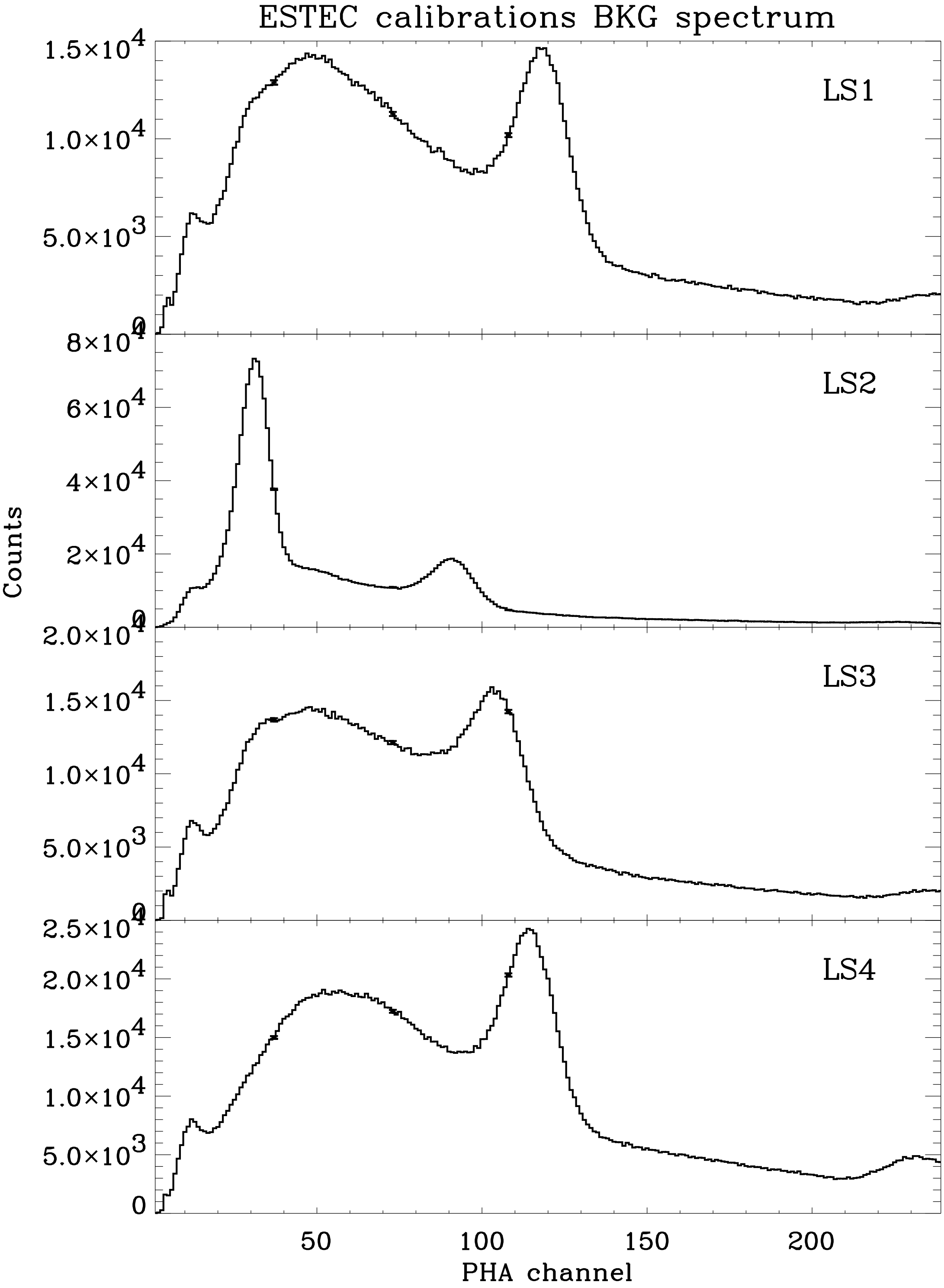

Figure 2.27: ESTEC calibrations background spectra

effect of the materials in front of LS1 and LS3. The second is that the backscattering component superimposed to the Compton continuum at medium to high energies is of the same amplitude in the two sets of spectra, indicating that most of the backscattered photons come from the walls and floor of the room and not from satellite structures.

In addition, the spectra of the high energy sources taken at ENEA laboratories with a Germanium detector (in Fig. 2.29 we show the 662 keV source spectrum) with much higher energy resolution (the photo-peak is very close to a delta function), show a very little backscattering component. Measurements performed with and without the sources polystyrene container, indicate that this low contribution is not due to the sources set–up, and thus it probably comes from backscattered photons from the ENEA calibration room.

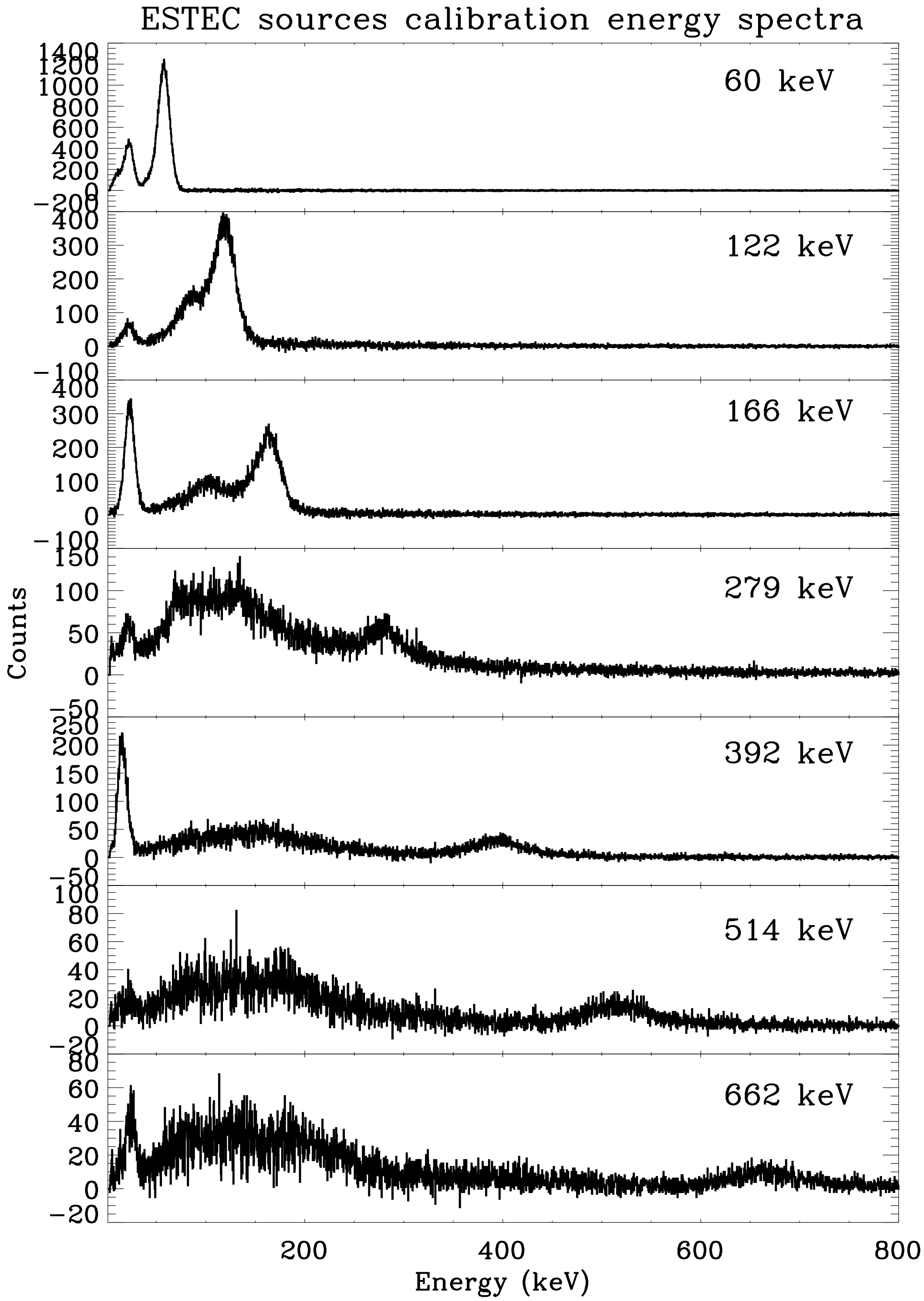

Figure 2.28: ESTEC NaI detector sources calibration spectra

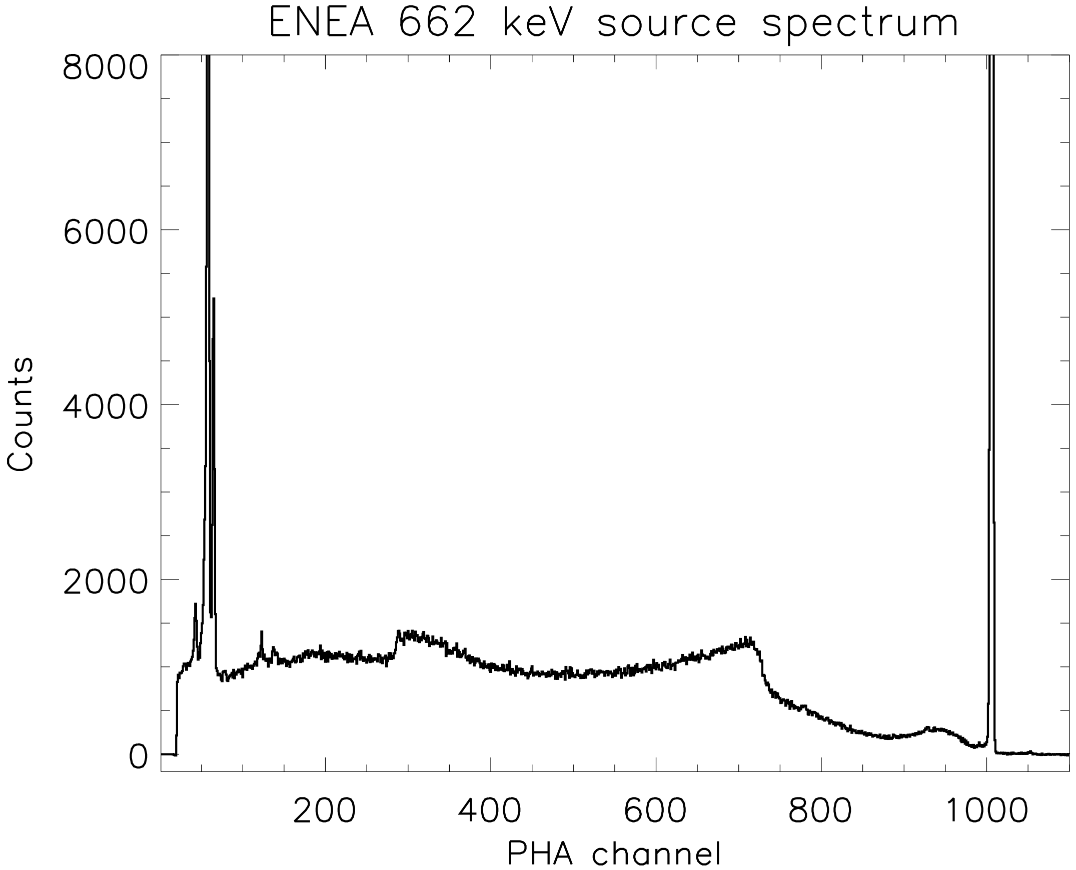

Figure 2.29: Germanium detector spectrum of the 662 keV source

Chapter 3

GRBM detectors response functions

This chapter describes calibrations data analysis methods and results and their application to the construction of GRBM LS1 and LS3 detectors In the first section we give basic notions on gamma–ray spectroscopy, in particular with inorganic scintillators, in order to introduce concepts and definitions that will be widely used in the following sections. In the second we outline generalities on X and gamma–ray spectral data managing with non dispersive detectors, introducing the basilar concept of response function.

Finally, at the end of the chapter we give a brief description of the Monte Carlo model of the experiment and of the satellite, still under refinement. The results from simulations were compared to the calibrations results.

3.1 Gamma–ray spectroscopy with inorganic scintillators

As discussed in section 1.2.1, the principle of scintillator detectors consists in converting photon energy into electrons kinetic energy, which in turn will be converted into light piped out of the scintillator and measured by a PMT. The first step is called the deposition of energy in the detector, and, for an ideal detector, it should be equal to the photon energy. This is not the case in real gamma detectors, especially at energies above $\sim$100 keV, depending on the type of interaction that each photon undergoes into the detector, detector geometry and the surrounding environment. A good knowledge of these factors is crucial to an understanding of the response of a scintillator detector.

3.1.1 Interaction of gamma radiation with matter

The relevant interaction mechanisms of gamma–rays with matter (e.g. Knoll 1989, Siegbahn 1966) are photo-electric absorption, Compton scattering and pair production. The relative probability of one of these interactions to occur is a function of the incident photon energy and the atomic number (Z) of the absorbing elements, and is shown in Fig. 3.1.

In *photo-electric absorption*, all the energy of the incident photon is absorbed by a bound electron of an atom, most likely, for typical gamma–ray energy, a K–shell electron. As a result, a photoelectron is produced, with kinetic energy equal to the initial photon energy minus the shell binding energy. With the loss of an internal electron the atom is left in an excited state from which it relaxes by emitting a characteristic X–ray photon (*fluorescence photon*) or Auger electrons. The relative probability of fluorescence versus Auger de–excitation is a function of Z and of the interested shell and it is called *fluorescence yield* (Dyson 1990, Heitler 1984). For the K–shell of Cs its value is about 90%. The energy of the Auger electrons ranges from few keV for low–Z materials to tens of keV for atoms with higher atomic number. The atom de–excites with the emission of a characteristic X–ray photon or Auger electrons. If nothing escapes from the detector (the Auger electron has a very short range, due to its low–energy, and the characteristic X–ray photon in CsI has an absorption length of about 1mm), then the whole incident photon energy is deposited in the detector. Thus, the ideal detector (i.e. no photon or electron escape and perfect spectral resolution) spectrum of a monochromatic beam of photons all undergoing photo-electric absorption is a single delta peak at the incident photon energy (Fig. 3.2). The photo-electric cross section goes approximately with the -3 power of photon energy and with the 4th power of atomic number Z.

In the *Compton scattering process*, incident photons are scattered by the electrons with a partial energy loss, which depends on the angle θ between the directions of the photon before and after the interaction. The energy of the scattered photon,E_{γ}, and electron, E_e are given by:

$$E_{\gamma'} = \frac{E_{\gamma}}{1 + E_{\gamma}/m_0c^2(1 - cos\theta)} \tag{3.1}$$

$$E_e = E_{\gamma} - E_{\gamma'} \tag{3.2}$$

Thus, the maximum energy E_c deposition occurs when θ=180°, while for θ close to 0° nearly all the incident photon energy goes to the scattered photon and only a small part is converted into electron energy. The resulting 'ideal' spectrum of a monochromatic beam whose photons undergo only Compton scattering is then given by a continuum distribution, which can be calculated from the Klein–Nishina cross section, going from 0 to E_c (called the 'Compton edge'), which is always lower than the incident photons energy. The gap between the incident photon energy and the Compton edge energy can be calculated with the above formulas with θ=180°:

$$E_{\gamma} - E_c = \frac{E_{\gamma}}{1 + 2E_{\gamma}/m_0c^2} \tag{3.3}$$

The probability of Compton scattering is approximately proportional to E and to Z^{-1}.

Finally, *pair production* can occur if the incident photon has an energy greater than 1.022 MeV (i.e. twice the electron rest energy), consisting in the annihilation of the photon and the creation of an electron–positron pair in the field of a nucleus of the absorbing material. The photon energy in excess to 1.022 MeV is transformed in kinetic energy of the electron and positron. Thus, in ideal conditions, i.e. no electron or positron escape, no positron decay and perfect detector resolution, the spectrum of the monochromatic beam is given by a single delta peak with energy equal to the photon energy minus 1.022 MeV.

The transmitted intensity of a monochromatic gamma–ray beam of photon energy E and intensity I_0 crossing an absorbing layer is a function of the photons energy E, the layer thickness d and the total linear attenuation coefficient as a function of energy, $\mu_{Tot}(E)$, of the material constituting the layer, and is given by:

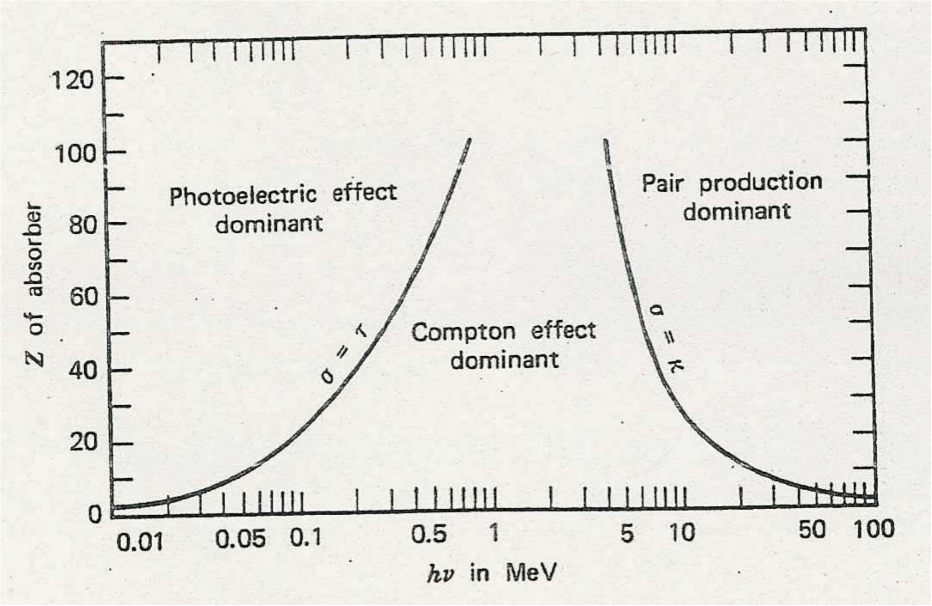

Figure 3.1: Relative importance of the three major types of gamma–ray interaction with matter

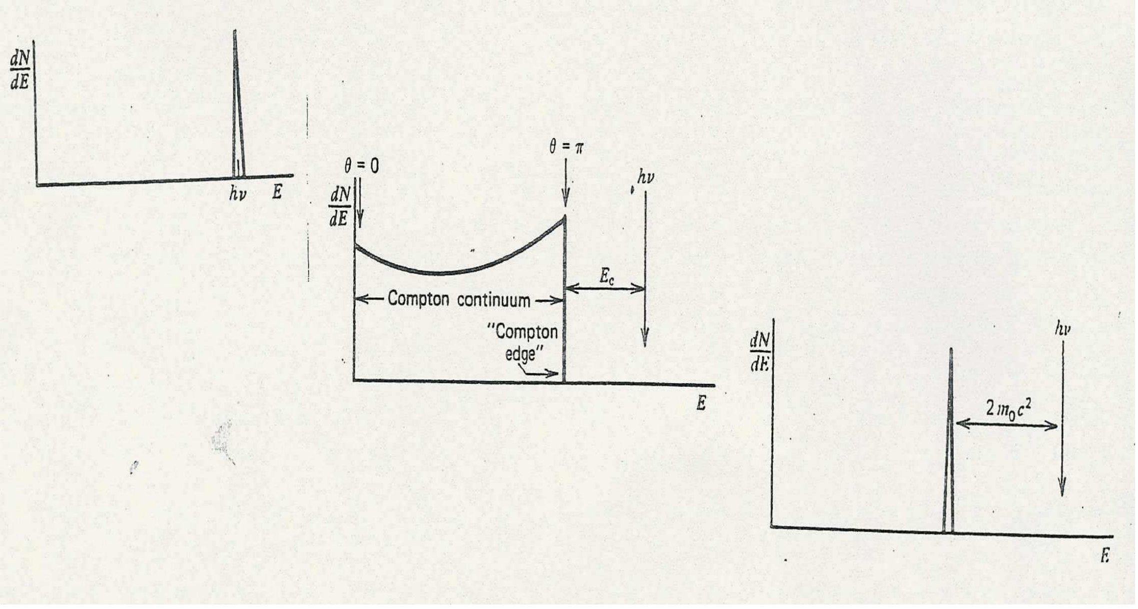

Figure 3.2: Ideal detector spectra of a monochromatic gamma source in the case of photoelectric absorption(upper panel), Compton scattering (middle panel) and pair production(lower panel)

$$I(E) = I_0(E) \exp\left(-\mu_{Tot}(E) d\right) \tag{3.4}$$

and the absorbed intensity is given by

$$I_0(E) - I(E) = I_0(E)(1 - \exp\left(-\mu_{Tot}(E) d\right)) \tag{3.5}$$

The linear attenuation coefficient is expressed in cm^{-1} and is obtained by multiplying the cross section (in cm^2/gr) with the absorbing medium density. The total linear attenuation coefficient accounts for absorption due to all the relevant interaction mechanisms:

$$\mu_{Tot}(E) = \mu_{Phot}(E) + \mu_{Comp}(E) + \mu_{Pair}(E) \tag{3.6}$$

The total linear coefficient of NaI and CsI as a function of energy and sum of the components due to the three different mechanisms described above are shown in Fig. 3.3.

3.1.2 Spectral response of real scintillators

In the ideal detector assumption made above, the resulting measured spectrum of a gamma–ray source with photons energy ranging e.g. from 20 to 2000 keV, would be the sum of the individual components relative to the different absorption mechanisms illustrated in Fig. 3.2. In real inorganic scintillator detectors the response function is complicated and distorted by different factors, that have to be taken in consideration; we describe below the most common and of interest for GRBM response reconstruction.

Effects due to geometry and size of the detector

For photons absorbed via photo-electric effect near the crystal surface, it may happen that the fluorescence photon escapes the detector without being re–absorbed. In this case the energy deposited in the detector is less than the incident photon energy, and this class of events forms a new peak called *escape peak* at an energy equal to the the photon energy minus the characteristic X–ray photons. This feature is important and evident in gamma–ray spectra of photons with energy less than about 100 keV and materials with

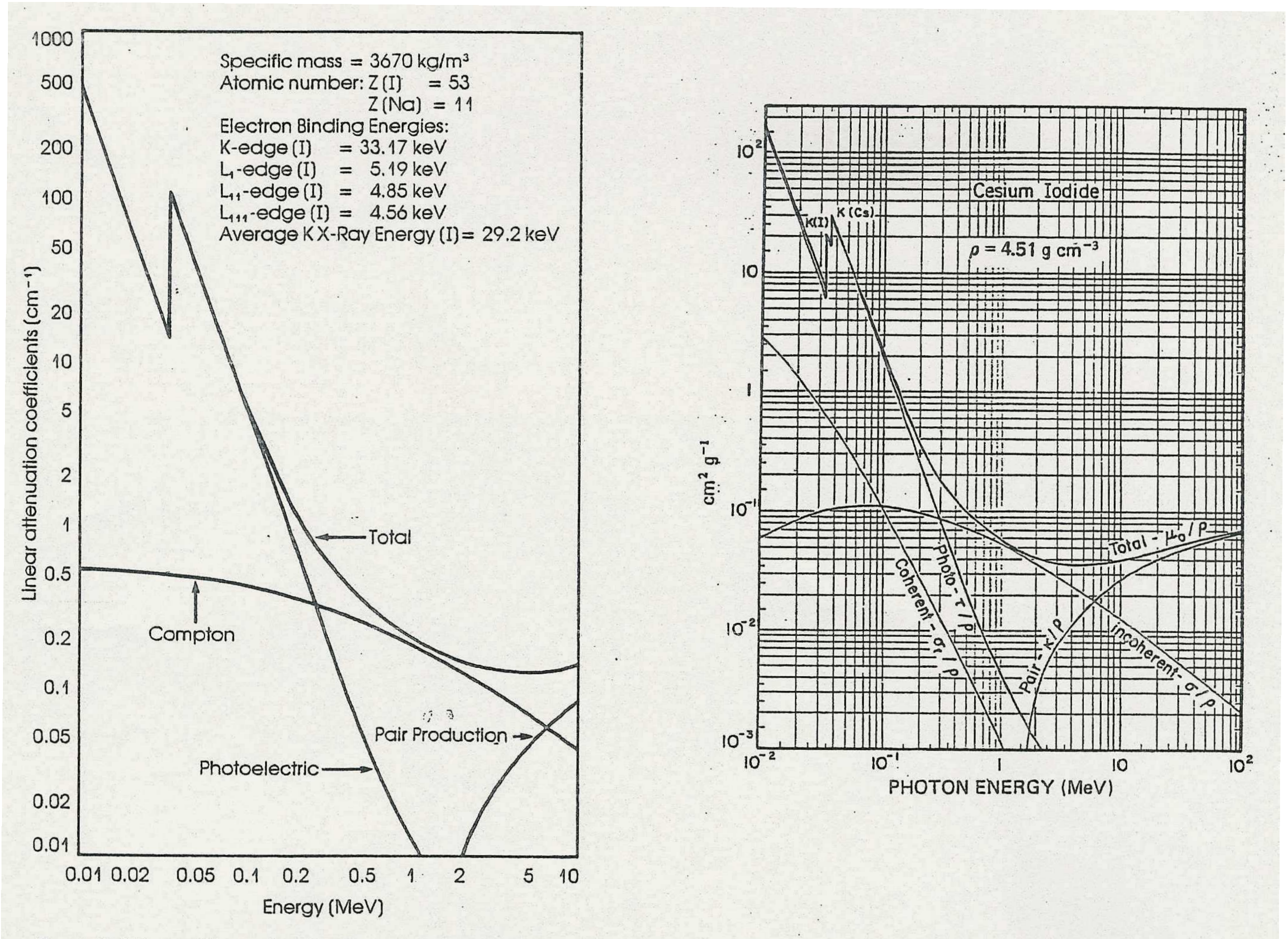

Figure C-1 Linear Attenuation Coefficient of NaI(Tl) Detector

Figure 3.3: Total linear absorption coefficient as a function of energy of NaI (left) and CsI (right)

high Z (the probability of emission of an X–ray characteristic photon with respect to that of an Auger electron increases with Z and decreases with photon energy) in detectors with high values of the surface to volume ratio (like the GRBM). Moreover, if the detector is sufficiently large and thick, photons interacting with the crystal via Compton scattering may undergo more than one single scatter, thus depositing an energy greater than that predicted by eq. 2.2., and possibly greater than the maximum energy represented by the Compton edge. The result in the observed spectrum is a distortion of the Compton continuum shape filling of the gap between the Compton edge and the photo-peak. These events are called *multiple scattering events*. Finally, in the case of pair production, one or both the generated electron and positron may escape the detector, resulting in a rather complex spectrum (Knoll 1989, Siegbahn 1966). Other effects which become important for photon energies above few MeV (thus of less interest for the GRBM response) include *secondary electron escape* and *bremsstrahlung escape*.

Surrounding material and environmental effects

In real detecting system, an important contribution to the measured spectrum of the source may be due to photons generated by the interaction of source photons with the surrounding materials and creating photons of lower energy that inpingue on the detector. The main environmental contribution is due to source photons that undergo Compton scattering with the surrounding materials and are deflected with angles greater than about 120° (backscattering). At these angles, the scattered photons have nearly the energy E_c reported in eq. 2.3. The effect on the measured spectrum is that a *backscattering peak* with its maximum at E_c superimposes to the lower–energy side of the Compton continuum. As we will discuss in next sections, this is a important factor to take into account in determining gamma–detectors spectral response by means of calibration spectra. Other minor environmental contribution may come from characteristic X–rays generated by photo-electric absorption of source photons in materials very close to the detectors.

Source set–up effects

In laboratory measurements, source photon interaction (e.g. backscattering) with the encapsulating material of the radioactive sources used to generate monochromatic beams of gamma–rays may cause the production of secondary radiation. If these secondary 'source photons' reach the detector, they can introduce additional distortion of the shape of the recorded spectrum.

Detector energy resolution

The basic components of a scintillator spectrometer include the detector crystal, the light piping system, a PMT, a pre–amplifier, a main amplifier and a single or multichannel analyzer. If all this components had ideal response, i.e. the crystal light yield exactly proportional to the energy deposited by the photon, the PMT response proportional to the crystal light output, the assignment of the signal to a PHA channel performed by the electronics proportional to the PMT pulse amplitude, then the full–energy peak (the photo-peak) of the resulting PHA spectrum of a monochromatic beam would be exactly a delta function. In practice, different factors contribute in worsening the correlation between the energy deposited in the detector and final energy channel assigned to the related signal. The result is the widening of the full–energy peak, escape peak, backscattering peak and all other peaks, the smoothing the Compton edge, etc. This effects are expressed introducing the concept of the detector energy resolution defined as:

$$R = \frac{FWHM}{H_0} \tag{3.7}$$

where FWHM is the Full Width Half Maximum of the full–energy peak and H_0 the mean pulse height corresponding to the same peak. An important contribution to energy resolution is due to Poissonian statistical fluctuations of the number of photoelectrons produced in the PMT photocathode for a given crystal light output. In this would be the only energy resolution factor, than the the full–energy peak would be a Gaussian with FWHM=$\sqrt{E}/\mathrm{E}_0$, where E_0 is the average energy to produce a photoelectron, and thus R would be proportional to $\mathrm{E}^{-0.5}$. In practice, there are many other contribution to the finiteness of detector's energy resolution, the main of which are: statistical fluctuations in light production in the crystal, crystal variations in light reflection, crystal internal light absorption, variation of the light collection efficiency as a function of the position in the crystal, non linearity of the crystal light output as a function of electron energy (because of this, the total light output for a given photon energy is different depending on if the energy is converted in kinetic energy of one or more electrons), non uniformity of the photocathode emission, statistical fluctuations in the electron multiplication within the PMT, el;ectronic noise within the pre–amplifier. All these contributions broaden the full–energy peak and cause the R dependency on energy to deviate from the simple proportionality to $E^{-0.5}$. Thus, the function R(E) in real detectors is better described as:

$$R(E) = KE^{(-0.5+q)} \tag{3.8}$$

, where R is usually expressed in terms of a percentage, as in Tabs. 1.3 and 1.4. Typical values for inorganic scintillators with an optimal optical coupling, e.g. for NaI, are about 18% at 60 keV and 8–10% at 662 keV; CsI energy resolution is generally a bit worse than that of NaI.

In Fig. 3.4, the main processes contributing to the final measured spectrum of a monochromatic gamma beam are illustrated.

3.2 Response matrix and spectral data fitting

3.2.1 Building the response matrix

As discussed above, the final step in the measurement of the incident photon energy by a scintillator counter (but this is true for all X–and gamma–ray astronomical detectors) is the Pulse Height Analysis performed by the electronics, which assigns the processed signal to a PHA value. Thus, the final measured spectrum of a source in a given exposure time is in the form of an histogram containing the number of counts for each PHA channel. To extract information on the spectrum of the source, one must know and describe in

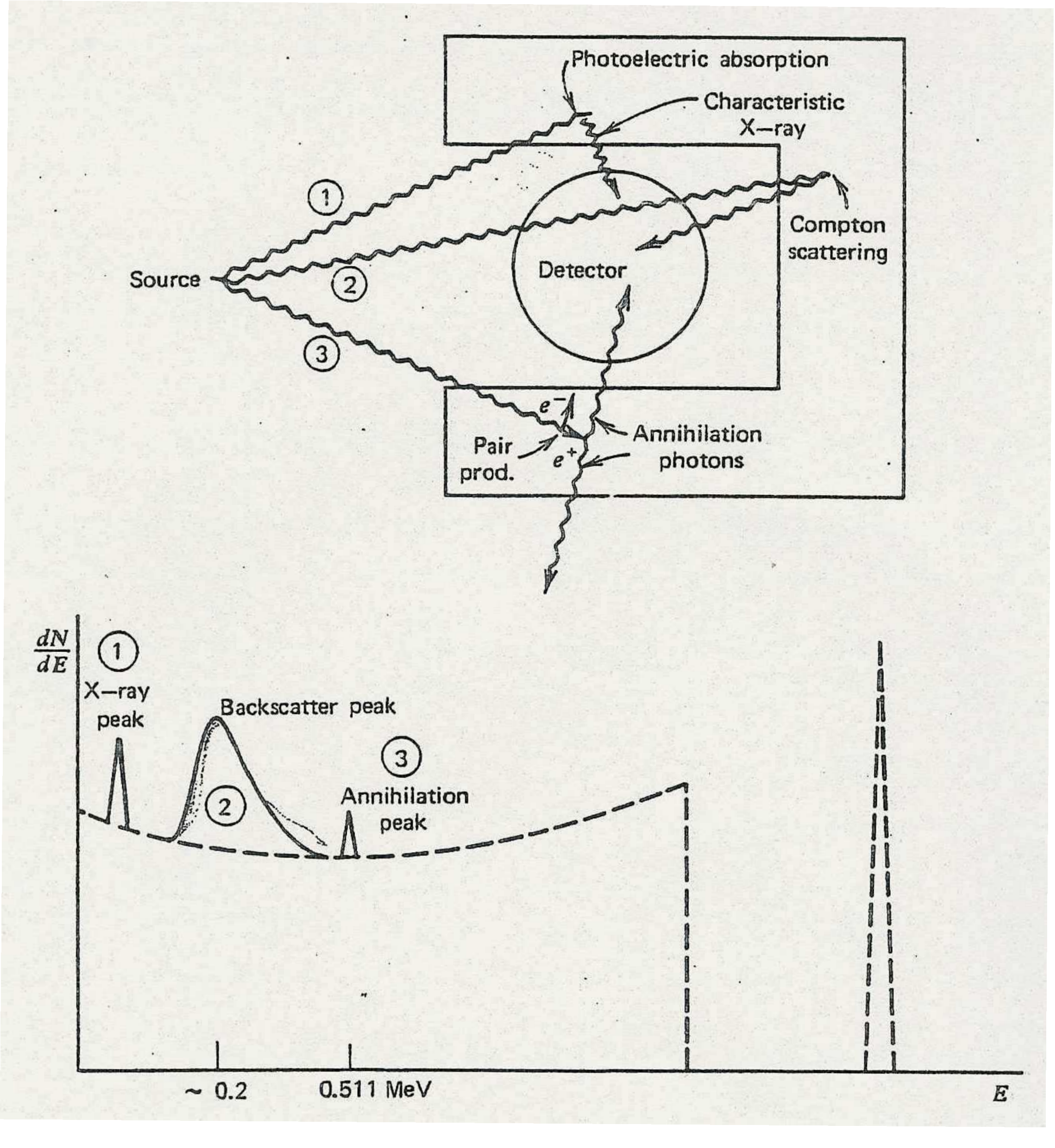

Figure 3.4: Illustration of various processes contributing to the response of a detector to a gamma–ray source

some useful mathematical form the following fundamental information on the instrument's response:

•*Efficiency*: this is the ratio between the number of measured counts and the number of incident photons for a radiation beam of given energy and from a given direction. It gives the probability that the photon will interact and deposit all or part of its energy into the crystal. Detectors efficiency depends on the physical and geometrical properties of the detector, of the materials constituting its entrance window and the surrounding environment, and thus on the interaction mechanisms of gamma–rays with matter described in the previous section. It is usually expressed in terms of *effective area*, in cm^2, corresponding to the geometrical area of an ideal detector with unit efficiency and which would measure the same number of events. Thus it can be expressed as:

$$A_{eff} = \epsilon A_{geom} \tag{3.9}$$

, where A$_{eff}$ is the effective area, ϵ the efficiency and A$_{geom}$ the geometrical area;

•*Response function*: the detector response function gives the probability that a photon of energy E undergoing an interaction into the detector will be measured as a count at an energy E' in the measured spectrum. Thus, the response function contains all the information on energy deposition in the crystal (the physics of the interaction of gamma–rays with the detector) and on crystal and PMT response (i.e. the energy resolution factors). Given the complexity of gamma–ray spectra, the determination of the response function is very complex. Usually (e.g. Band et al. 1992), its reconstruction is practically divided in two main tasks: a) the estimation, by means of Monte Carlo simulations, analytical calculations and experimental measurements (e.g. Pendleton et al. 1995), of the probability that the photon interacts with the detector (thus including efficiency modeling), that a given type of interaction takes place and of the relative energy loss distribution; b) estimation of the energy resolution as a function of photon energy and interaction placement in the detector by means of experimental measurements of monochromatic sources photo-peaks characteristics and the analytical modeling of crystal, PMT and electronic behaviors;

- *Channel to energy conversion*: as we have discussed in previous section, the physics of the interaction of gamma–ray with the detector and the finite detector energy resolution cause the fact that for a given incident photon energy different final PMT pulse amplitudes can be generated. Thus, the PHA channels do not correspond to a single photon energy. Conventionally, the energy range of a PHA channel is identified with the energy range of incident photons whose photo-peaks centroid in the PHA spectrum fall within the channel. The effective values of channels *energy bounds* are determined by means of on–ground calibrations with monochromatic sources, as will be described below for the GRBM. For an ideal detector, there would be a linear and stable relationship between the centroid of the photo-peak corresponding to each incident photon energy and the final PMT output pulse amplitude. In practice, different factors, the most common of which are changes in the light yield of the scintillator and in PMT gain can alter significantly the energy to channel relationship. The determination of the effective energy bound of each channel is performed by means of on–ground calibrations with monochromatic sources, as will be described below for the GRBM, and the in–flight stability of the energy to channel conversion can be monitored and adjusted by automatic gain control techniques (as for the PDS main detectors) or the use of gain calibration sources (as for the GRBM detectors);

- *Thresholds effects*: to better delimitate the energy band of the detector, or to divide it into different ranges (as e.g. for BATSE), discriminator circuits in the associated electronics are used. The discrimination is based on PMT pulse amplitude, and thus the upper and lower thresholds nominal energy values do not correspond to incoming photon energies, depending on energy deposition mechanisms and instrument finite resolution. At low energies, photo–electric absorption occurs for most of the photons interacting with the crystal; thus, the cut–off in the detector' s band is close to the nominal energy of the threshold, with uncertainties due to the finite energy resolution which can cause photons with energies below the energy threshold to generate final pulses with amplitude above it. At high energies, i.e. when Compton scattering is the main interacting mechanism, in addition to the energy resolution effect, it can happen that photons with energies even much higher than that of the threshold deposit in the detector an energy below it. In other words, the effect of thresholds on the measured spectrum of a monochromatic source of high energy photons (say above 200 keV), will be to exclude the photo-peak (or a portion of it if photons energy is close to the threshold) and to generate a cut–off in the Compton continuum. Other threshold effects on the detector response include the change of the threshold energy value, due to changes in PMT gain or change in crystal light response, and the non perfect threshold cut–off due to the electronics.

These are the 'ingredients' needed for the construction of the detector *response matrix*, which is the conventional and practical form in which the detector response is expressed. The response matrix is a bi–dimensional matrix in which each element is the probability that an incoming photon with energy belonging to a given energy range will be assigned to a given PHA channel. The width and number of the ranges (or channels) in which the energy of the incoming photons is divided depends on the instrument energy resolution (i.e. at energies greater than $\sim$ 20 keV a channel width of 1 keV oversamples detector's resolution) and the complexity and the dependency on energy of the response function. In principle, the incoming photon energy range should go from 0 to infinite, but in practice, it is determined on the basis of the window transparency, detector efficiency and electronics thresholds. At low energies, where almost all the absorption is through the photo-electric process , it is possible to estimate a photon energy below which the photons will not be detected by the instrument. The estimation of the upper limit of the detectable photon energy range is much more complex, because the response matrix is not diagonal, Compton scattering preveals and the energy deposited in the detector can be much less than the incoming photon energy, thus bypassing the high energy threshold, if any. Nevertheless, crystal total absorption coefficient goes down with increasing photon energy, reaching, e.g. for CsI, a minimum around 2000 keV, where pair production becomes the main absorption mechanism. Accounting for this and for the effect of the eventual high energy threshold, it is possible to estimate an energy such that photons with energies above it have negligible probabilities of being detected or at least to evaluate the flux with the help of some auxiliary assumptions on the source.

3.2.2 Spectral fitting

If we indicate with $R(i,j)$ the generic element of the response matrix, i.e. the probability that an incoming photon with energy comprised in the range of input energy channel j gives a count in the PHA channel i, and $F(E)$ the incident photon flux giving the number of incoming photons for each response matrix input energy range j, the corresponding expected value of the number of counts in the channel i is given by:

$$C(i) = \sum_{j=1}^{n} F(j)R(i,j) \tag{3.10}$$

, where n is the number of the response matrix input energy bins and

$$F(j) = \int_{E_{j-1}}^{E_j} F(E)dE \tag{3.11}$$

, E_{j-1} and E_j being the energy bounds of the response matrix input energy channel j.

Conventionally, $F(E)$ is expressed in photons cm^{-2} s^{-1} keV^{-1}, $R(i,j)$ in cm^2 (i.e. in terms of effective area) and $C(i)$ in counts s^{-1} channel^{-1}.

As we have discussed, the response matrix R is not diagonal, and thus it cannot be inverted to directly extrapolate the incident photon spectrum $F(E)$ from the measured spectrum C. In other words, this means that different incident photon spectra $F(J)$ may result in the same value of $C(I)$. The standard technique adopted to analyze spectral data of hard X–ray and gamma–ray experiments is the *spectral fitting*, which consists in assuming a parametrical photon spectrum model $M(E, P1, ..., Pn)$, integrate it in each response matrix input energy bin as in eq. 3.11 to obtain $M(j, P1, ..., Pn)$, generate a theoretical count spectrum $T(i)$ by using equation 3.10 replacing $F(j)$ with $M(j)$, compute the value of χ^2 as:

$$\chi^2 = \sum_{i=1}^{m} \frac{(T(i) - C(i))^2}{\sigma(i)^2} \tag{3.12}$$

, where $\sigma(i)$ is the standard deviation of $C(i)$ and m the number of PHA channels, find the parameter values which minimize the χ^2 and test the goodness of the fit by means of the χ^2 test.

To perform the χ^2 minimization and find the best fit parameters, together with associated errors, for a given model standard software packages are used, like XSPEC (NASA/HEASARC), developed at HEASARC, or MINUIT (James 1994) developed at CERN. It is important to stress that more than one model may fit well the measured spectrum; the choice between models can be done basing on statistical tools (like the F–Test) and/or on scientific interpretation.

It is important to note that $C(i)$ is not measured directly, because the actually measured spectrum is the sum of the background plus the source spectrum, and thus it is calculated as:

$$C(i) = M(i) - B(i) \tag{3.13}$$

, where M(i) is the measured spectrum and B(i) the background spectrum. The error $\sigma(i)$ is then given by:

$$\sigma(i) = \sqrt{\sigma(i)_M^2 + \sigma(i)_B^2} = \sqrt{M(i) + B(i)} \tag{3.14}$$

, because M(i) and B(i) are Poissonian distributed and thus their standard deviation is equal to their mean value.

Finally, the χ^2 statistics can be used to test the model hypothesis only if the number of counts in each channel $C(i)$ is greater than about 20, so that its distribution can be assumed Gaussian. Therefore, in case of weak signals, the PHA channels are grouped in order to have a measured spectrum with at least 20 counts in each channel. test must be adopted, e.g. the C test.

3.3 Response in the GRBM and AC ratemeters bands

3.3.1 On–axis efficiency

The expected photon flux incident on the shields from the calibration sources was calculated by taking into account the distance of the source, air absorption and the source physical properties reported in Table 2.1, i.e. activity, half life, lines branch ratios. By multiplying these fluxes for the slab geometrical area (1136 cm^2) we obtain the expected counts/s at each energy. The on-axis detection efficiency at different energies in the GRBM and AC bands was estimated by dividing the on-axis counts measured in these bands by the incident photon rates. To evaluate the efficiency of each LS at energies lower than 60 keV we used the fluorescence lines provided by Ce^{139} (energies between 33 and 39 keV) and Sn^{113} (energies between 24 and 28 keV).

To derive the detection efficiency at energies > 200 keV it was mandatory, as discussed in previous section, to take into account the back-scattering component superimposed to the Compton spectrum associated with the given line.

As mentioned above, this component may be due to source photons back-scattered by the walls of the room in which the calibration tests where performed or by the satellite structures. It is very important to separate the contribution coming from the environment, that is only present in the calibration site, from that coming from the satellite, that there will be also in orbit, in order to achieve a reliable estimation of the expected in-flight efficiency at energies greater than about 200 keV. A good solution of the problem will be given by Monte Carlo (MC) simulation of the satellite/calibration room system, now in progress (Rapisarda et al. 1997), but so far we can also arrive to a first order estimate through a calibration analysis. The comparison of the GRBM detectors spectra with the NaI spectra and the ENEA calibrations sources spectra shows that most of the back-scattering contribution comes from the walls of the room. Indeed, the ratio between the photo-peak photons and the Compton photons is about 1 for the spectra measured by GRBM and those measured with the NaI detector in the place of the satellite (Fig. 2.28)

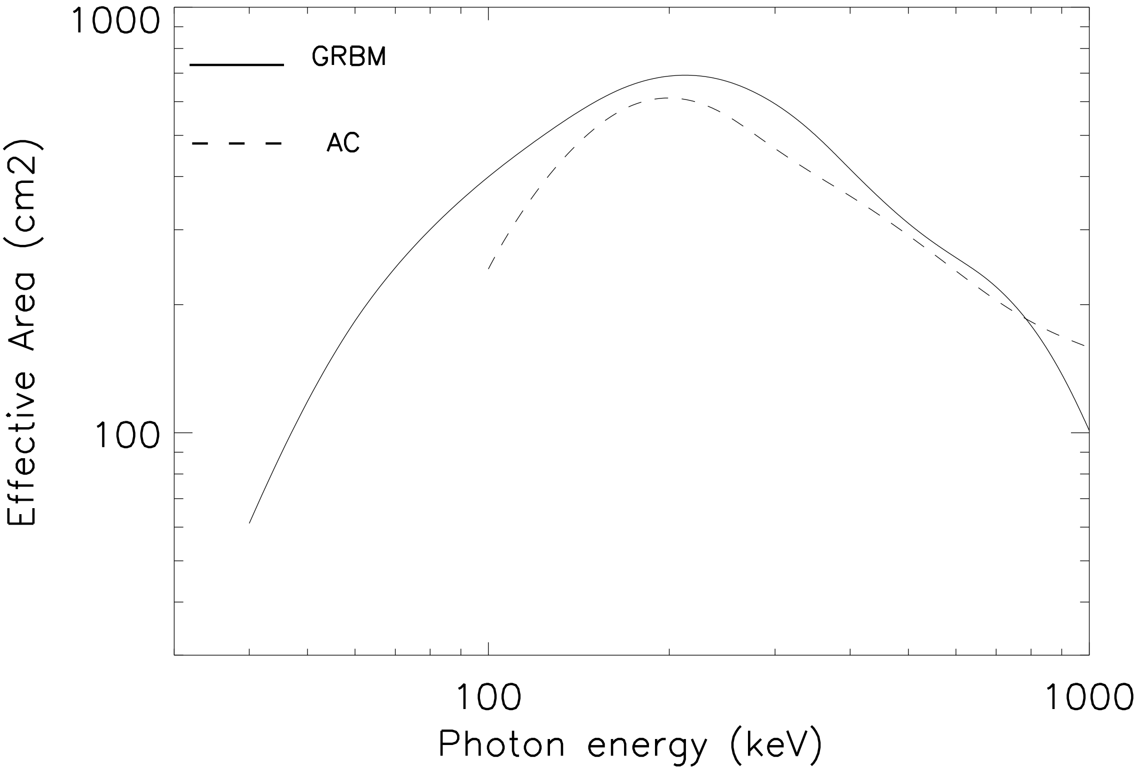

Figure 3.5: LS1 On-axis efficiency in the GRBM and AC ratemeters band as a function of photon energy.

. In addition, the source spectrum measured with the Germanium detector shows very low back-scattering component (Fig. 2.29). Thus, we corrected the > 200 keV measured on-axis count rates by subtracting the counts due to back-scattered photons, modeling the high energy lines spectra Compton continuum in the way described in section 2.5.5.

In figures 3.5 and 3.6 we report the on–axis efficiencies in the GRBM and AC bands for LS1 and LS3, after the correction for the back-scattering. The efficiency at energies greater than 662 keV was obtained for extrapolation taking into account the CsI Compton cross sections.

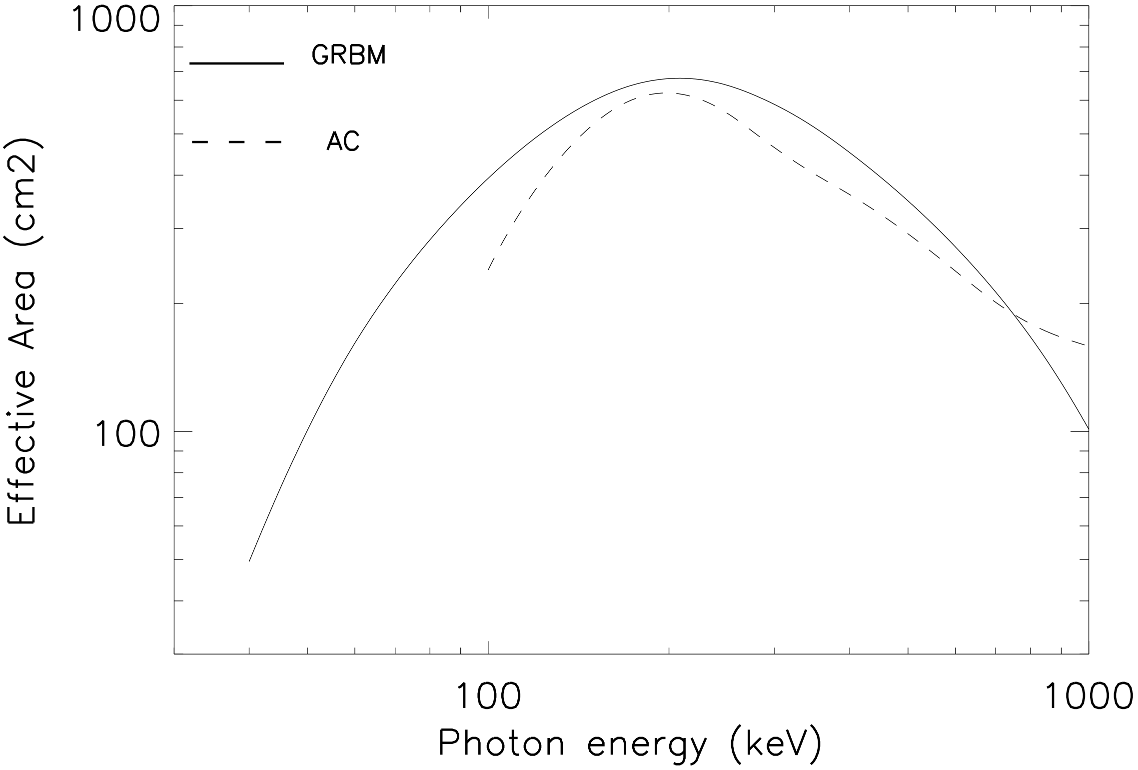

Figure 3.6: LS3 On-axis efficiency in the GRBM and AC ratemeters band as a function of photon energy.

3.3.2 Analytical interpolation of LS1 and LS3 efficiency angular dependency

The measured response of LS1 and LS3 with azimuth, elevation and energy of the incident radiation beam was fitted with analytical functions in order to simplify the estimate of the incident fluxes from celestial sources. These functions are also used to compare results of the MC code developed for the GRBM with the calibration tests results. As we discussed in the previous section, the ESTEC calibrations angular light curves of LS1 and LS3 are pretty close to an absorbed (i.e. multiplied by an exponential photon extinction function) cosine. Thus we used an analytical function, based on physical, geometrical and partly empirical considerations, to fit LS1 and LS3 response curves. We described the response function of LS1 and LS3 as the sum of three components:

A) a component that describes the angular dependency of the projected surface area of the shield on photon direction, the dependency of the transparency of the material in front of the shield on photon direction and the CsI crystal absorption dependency on photon energy and direction:

$$N_A(\phi,\theta,E) = \begin{cases} F \cdot \cos\phi \cdot \cos\theta \cdot \exp\left(-\dfrac{\tau(E)}{\cos\phi \cdot \cos\theta}\right) \cdot \exp\left(\dfrac{1-\mu(E)}{\cos\phi \cdot \cos\theta}\right) & \text{if } -90 < \phi < 90 \\ 0 & \text{otherwise} \end{cases}$$

where F is the direct flux from the radioactive source in photons/cm^2/keV; $\tau(E)$ is the average optical depth of the absorbing material in front of the shield, and $\mu(E)$ is the 1 cm thick CsI transparency.

B) a component that takes into account the environmental back-scattering contribution to the total measured counts:

$$N_B(\phi,\theta,E) = N_A(\phi,\theta,E) \cdot \left(\frac{bk(E)}{1-bk(E)}\right)$$

where: $bk(E) \equiv$ (fraction of back-scattering counts)/(total counts).

C)a semi-empirical component which includes possible side-scattering effects from the satellite structure and PDS subsystems including materials of the lateral shields themselves. These effects are particularly relevant at high energies where we can observe that the counts do not go to zero even when the shield is not directly illuminated by the source. This term is given by:

$$N_C(\phi, \theta, E) = a(E) - b(E) \cdot \cos\phi \cdot \cos\theta$$

Thus, the total count is given by:

$$N_{Tot}(\phi, \theta, E) = N_A(\phi, \theta, E) + N_B(\phi, \theta, E) + N_C(\phi, \theta, E)$$

with 5 free parameters F, $\tau(E)$, $bk(E)$, $a(E)$ and $b(E)$.

The only deviation of the angular response of LS3 from the above function is a slight change in the slope of the curve at an azimuth angle of about $-60°$. The value of this "critical" angle varies of some degrees at the different energies. To reproduce this feature we introduced a change of the optical depth at $-60°$, thus adding one free parameter to the basic function.

The angular response of LS1 is well fit at low energies (60 keV and 122 keV) by the basic function. At higher energies we have a double change in the slope at about $-60°$ (as for LS1) and $+65°$. Thus, we introduced two changes in the optical depth at the critical angles to describe these features. We also applied other minor elevation dependent corrections to the basic form to better describe small features present in negative elevation angles response curves of both LS1 and LS3.

We found good fits (χ^2) values lower than 1.2 for 139 d.o.f) of these functions to the data for azimuthal angles between -75° and +75° and elevation angles between -30° and +30°. Outside these intervals, the angular response curves show features which will be probably better described by MC simulations. Fits results for LS3 at θ=0° are reported in figures from 3.7 to 3.13, where the analytical function is superimposed to the measured data and also fit residuals are plotted.

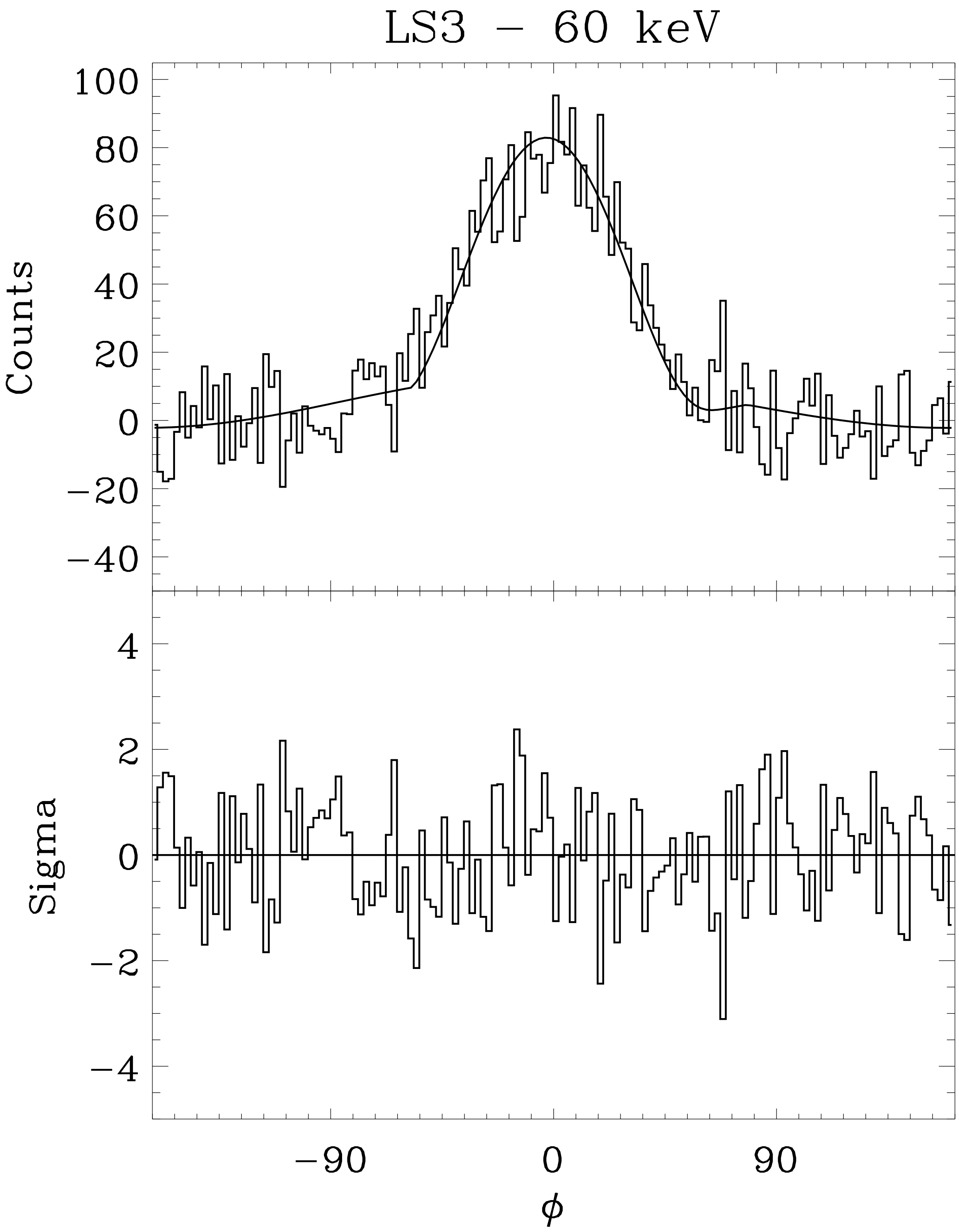

Figure 3.7: Analytical fitting of LS3 azimuthal angular response at 60 keV and θ=0

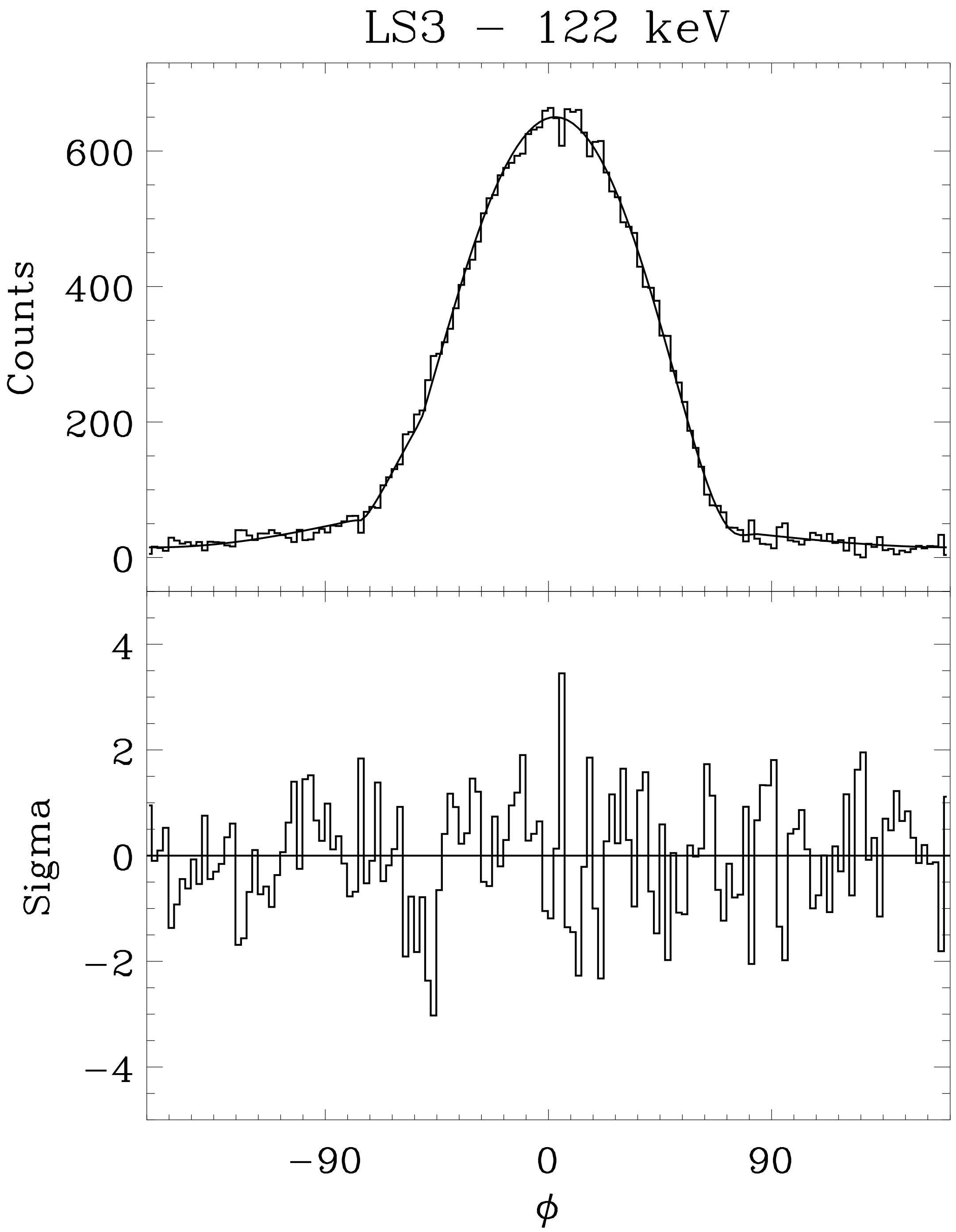

Figure 3.8: Analytical fitting of LS3 azimuthal angular response at 122 keV and θ=0

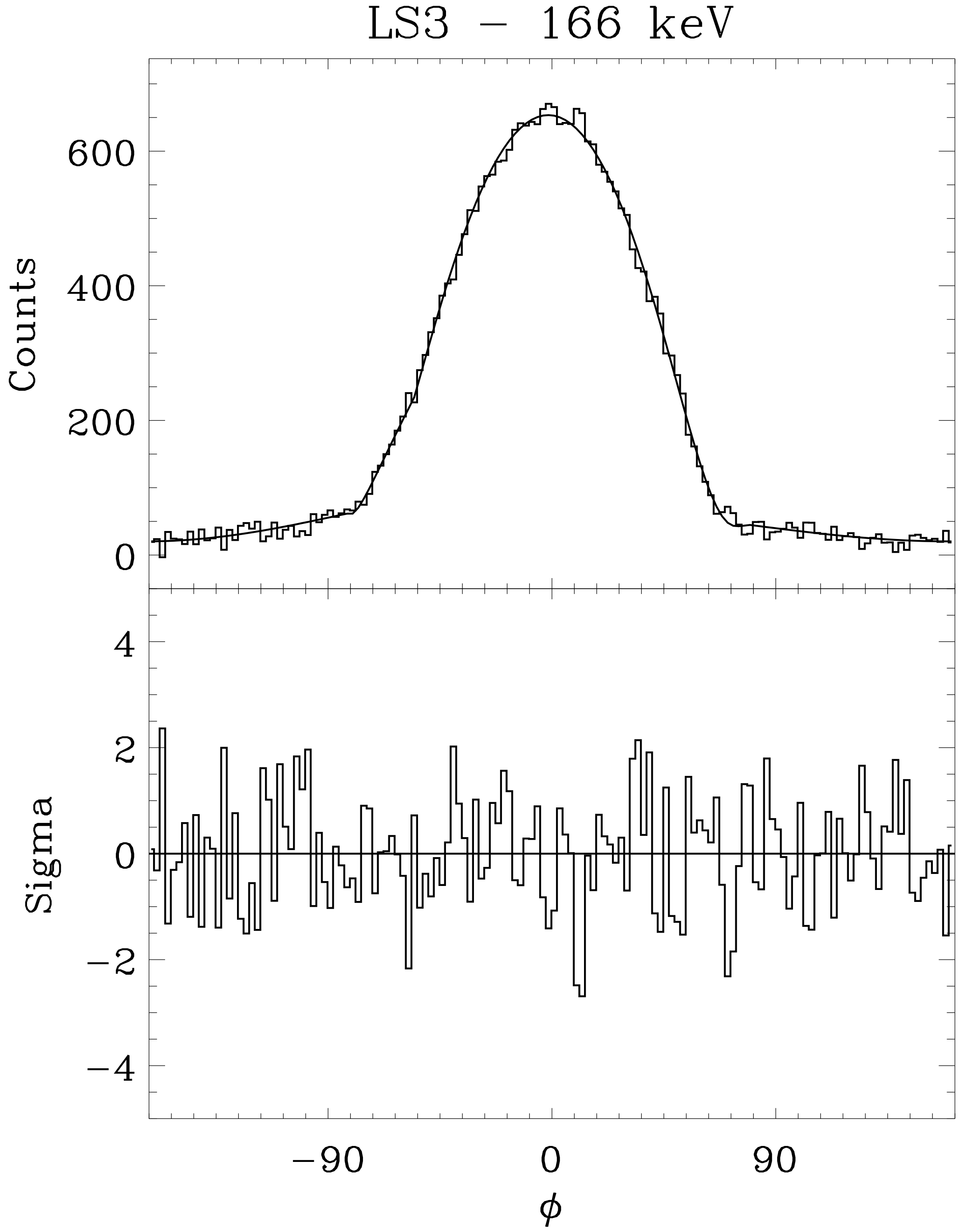

Figure 3.9: Analytical fitting of LS3 azimuthal angular response at 166 keV and θ=0

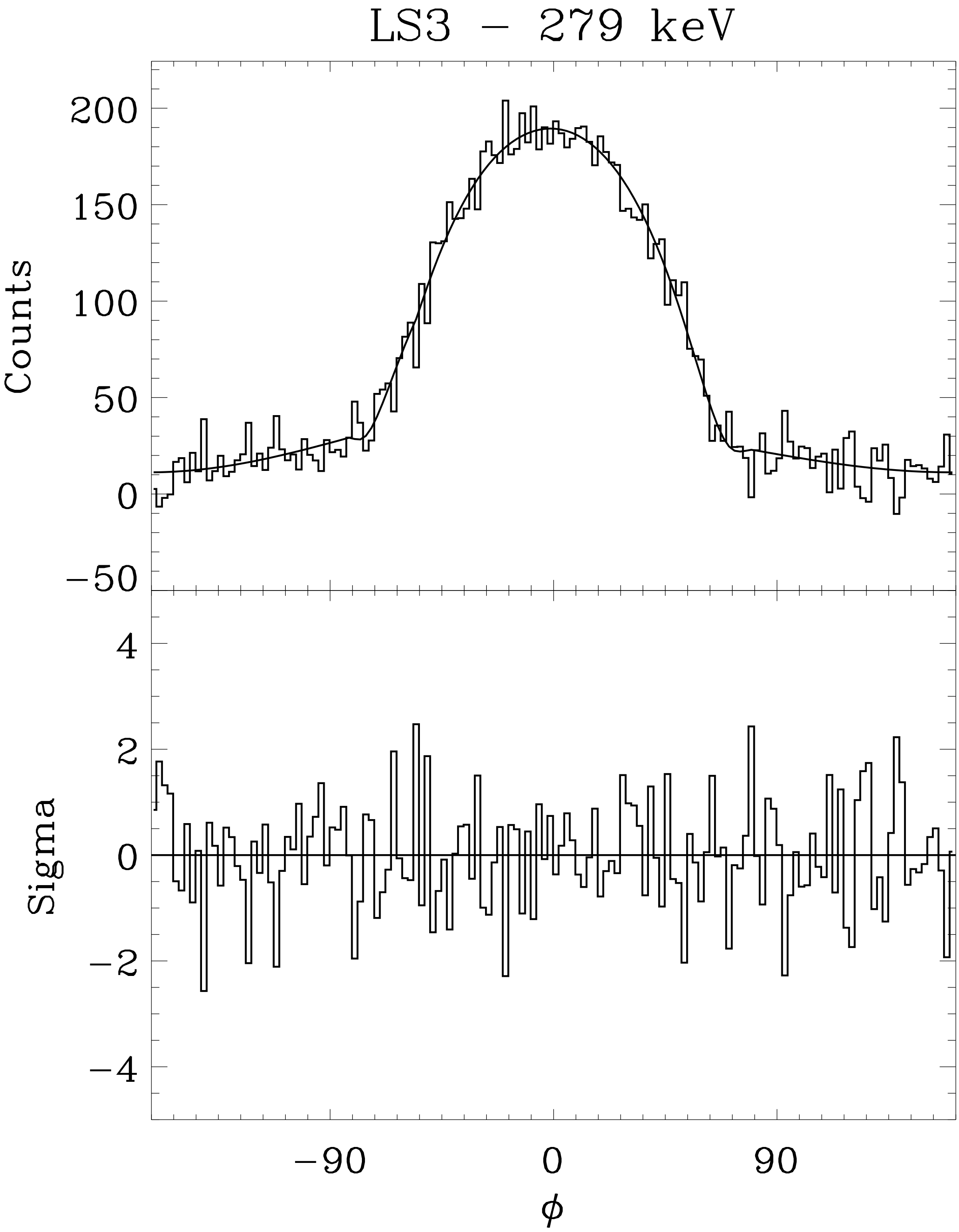

Figure 3.10: Analytical fitting of LS3 azimuthal angular response at 279 keV and θ=0

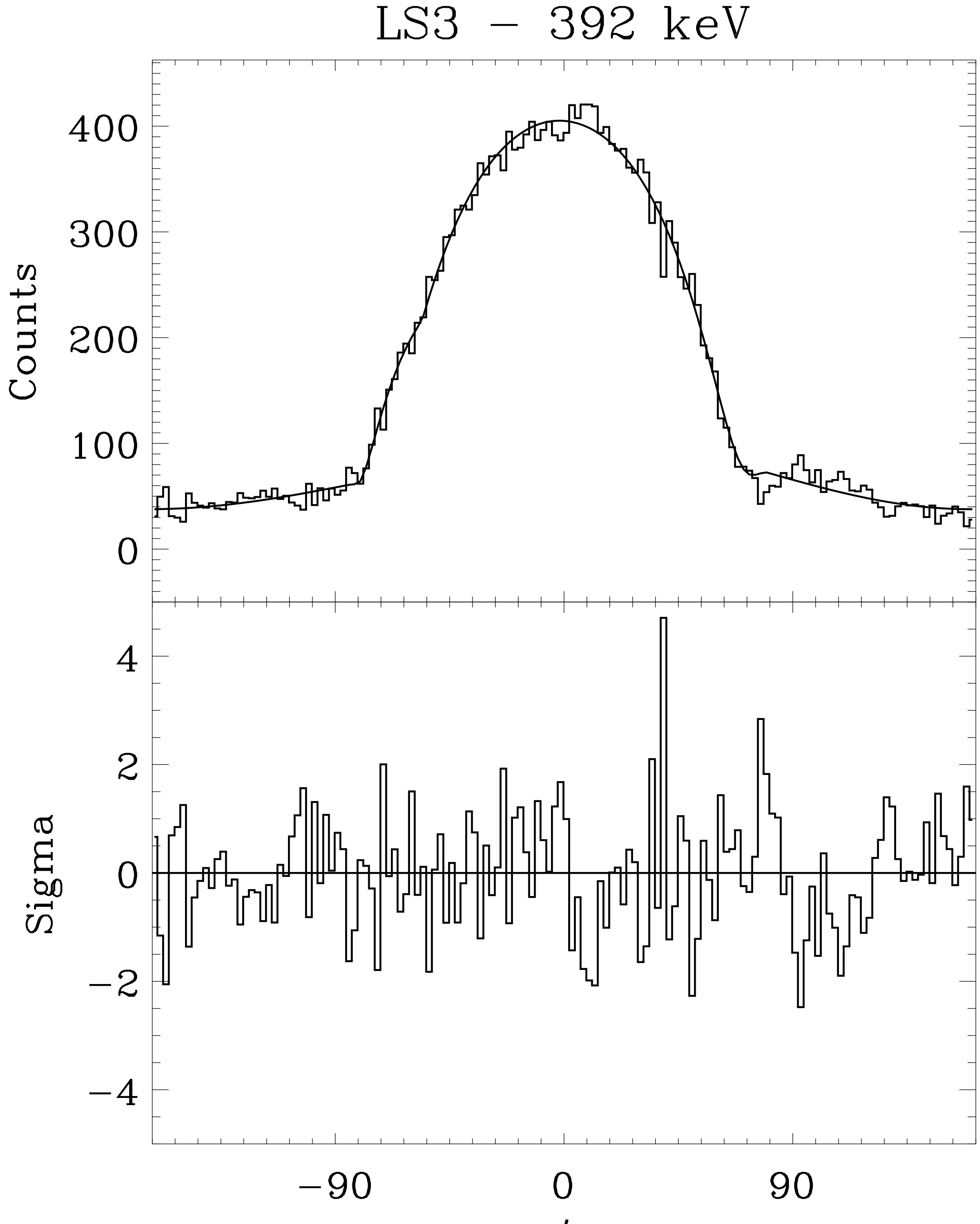

Figure 3.11: Analytical fitting of LS3 azimuthal angular response at 392 keV and θ=0

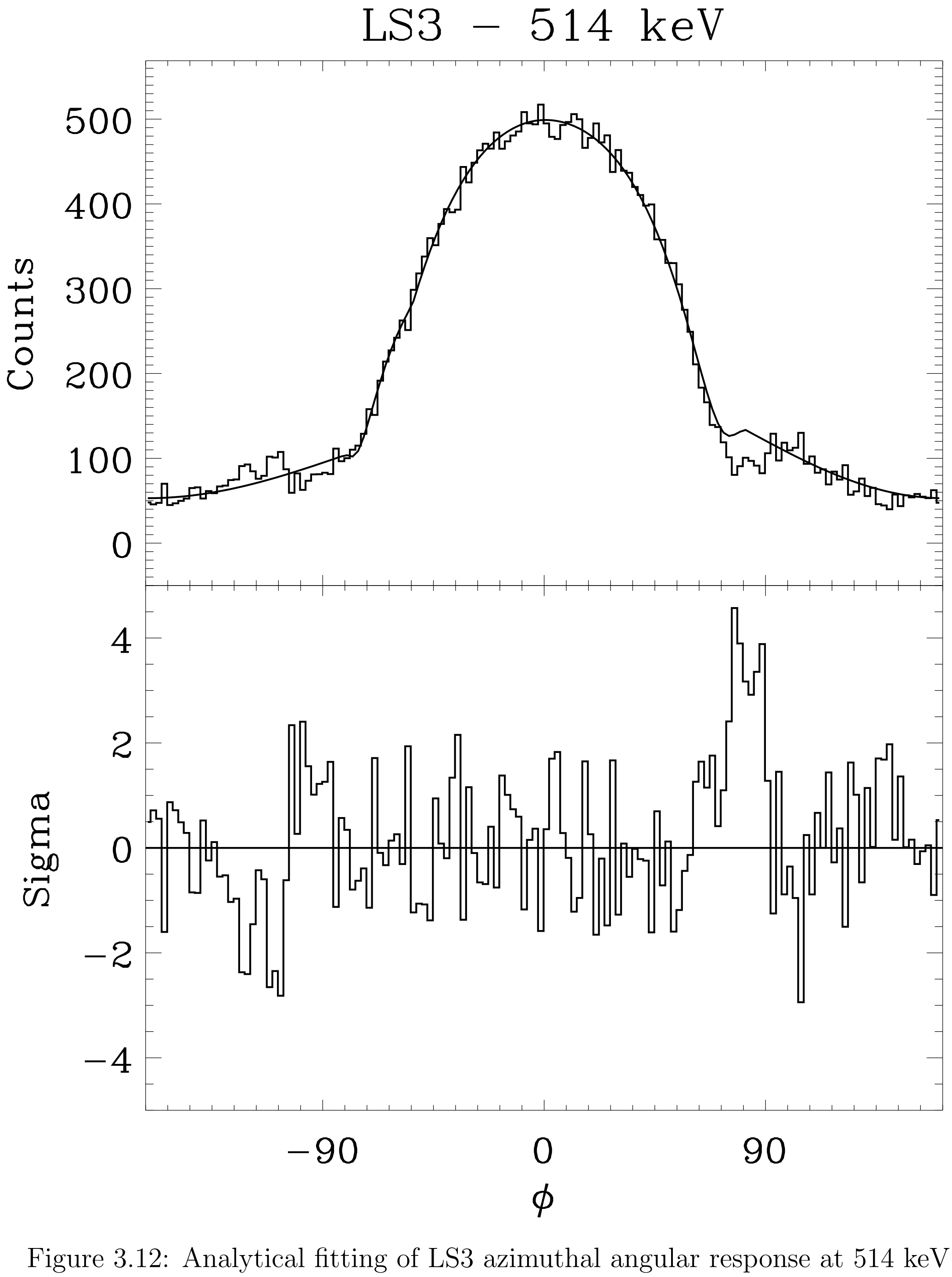

Figure 3.12: Analytical fitting of LS3 azimuthal angular response at 514 keV and θ=0

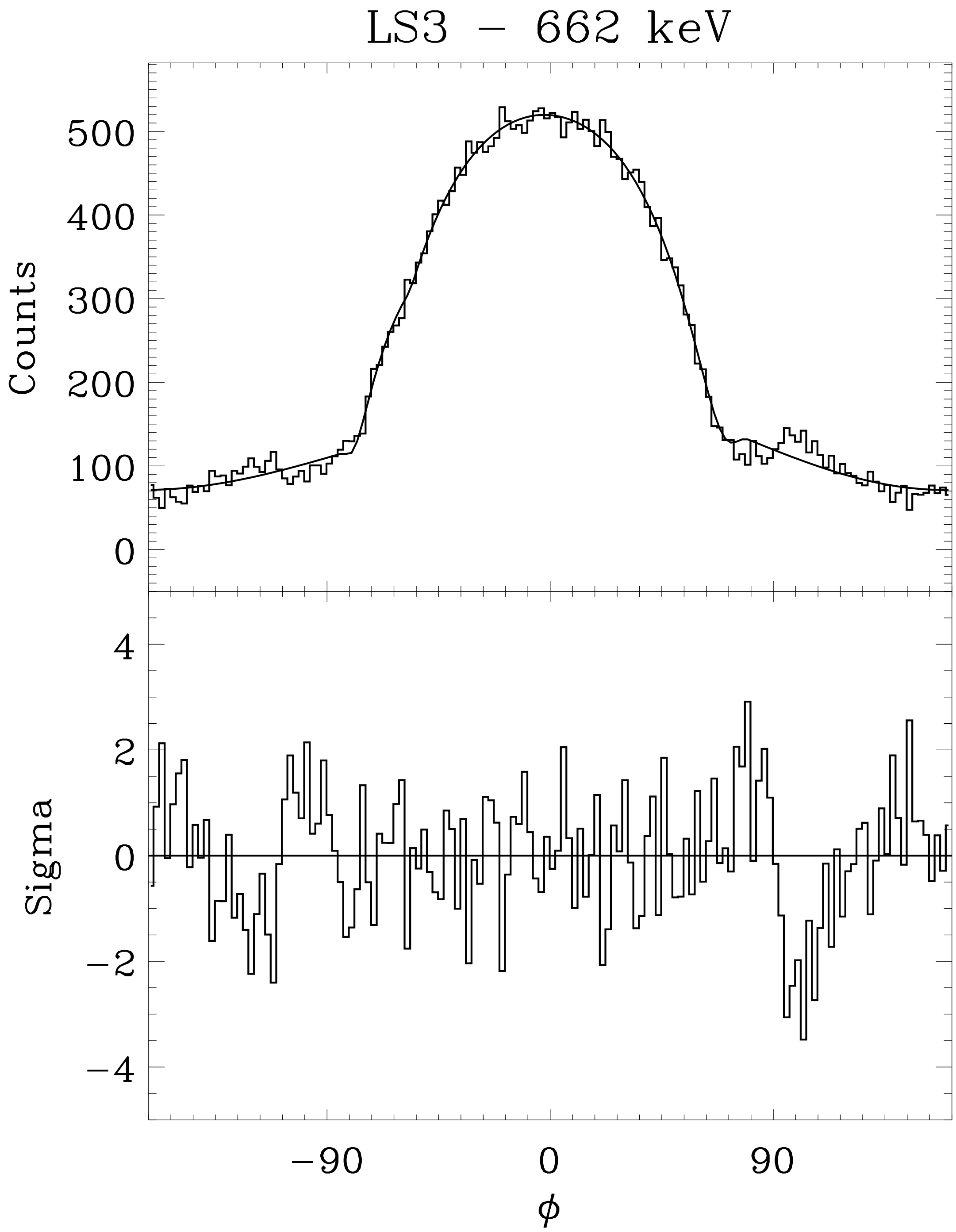

Figure 3.13: Analytical fitting of LS3 azimuthal angular response at 662 keV and θ=0

To estimate in-flight efficiencies we neglect the N_B component that, as discussed above, is mainly due to back-scattering photons from the room walls. Thus, the function describing the in-flight angle-energy dependency of shield efficiency has the form:

$$N_{Tot}(\phi, \theta, E) = N_A(\phi, \theta, E) + N_C(\phi, \theta, E)$$

with N_A and N_B including the various shield and elevation specific corrections mentioned above.

3.3.3 Interpolation of LS2 and LS4 efficiencies

As we have discussed in section 2.3, the dependency of LS2 and LS4 efficiencies on source direction is much more distorted with respect to the simple 'absorbed' cosinusoidal geometrical form. Moreover, the urgency for a good description of LS1 and LS3 responses delayed the study of these two detectors, which is now a wok in progress.

The description of the efficiencies and spectral responses will be obtained with the Monte Carlo model when it will be sufficiently refined. Neverthless, because the study on GRBM source localization capabilities (chapter 6) is already in progress, we developed specific software that interpolates the calibration data basing on cubic spline inteprolations of the available measurements. The subtraction of spurious contributions is performed basing on the results of the analysis of LS1 and LS3 spectral responses.

Although this is a very preliminar nd rough method to estimate LS2 and LS4 efficiencies dependency on photon energy and direction, it allows to perform an estimate of source direction basing on the ratio of the counts in each shield both in GRBM and AC bands. Results of these analysis are reported in Preger et al. (1999).

3.4 Spectral response matrices of LS1 and LS3

The building–up of LS1 and LS3 response matrices for the deconvolution of the 240 channels PHA spectra was based on the analysis described in section 3.2,namely:

- reconstruction of detectors efficiency as a function of photon energy and incoming direction (described in previous section);

- channel to energy conversion;

- energy resolution as a function of energy;

- modeling of the different line spectra components and their dependency on energy;

- thresholds effects (from LABEN calibrations)

3.4.1 Channel to energy conversion and energy resolution

By gauss-fitting the photo-peaks at the various energies, we estimate channel centroid and intensity of the photo-peak. Comparing the estimated source flux with the total measured counts under the peak, we obtain the photo-peak efficiency. In this way we derived the channel and energy resolution vs. energy relationships (figures 3.14, 3.15). The energy to channel relationship shows in both cases a slope change at about 90 keV energy.

The LS1 and LS3 energy resolution, defined by $R = \mathrm{FWHM}/H_0$, where H_0 is the centroid channel of the photo-peak, as a function of photon energy, is shown in figures 3.16 and 3.17. The best fit function to LS1 and LS3 energy resolution data are given by:

$$R = \begin{cases} 1.935 \cdot E^{-0.40} & \text{for LS1} \\ 1.216 \cdot E^{-0.32} & \text{for LS3.} \end{cases}$$

3.4.2 Spectral shape modeling

In section 2.4.4 we have shown and discussed the different components of LS1 and LS3 spectra taken during ESTEC calibrations. To reconstruct detectors response functions it was necessary to model each component dependency on energy. The photo-peak component was modeled utilizing the energy resolution relationship and the photo-peak efficiency versus energy. The Compton continuum was modeled as a (semi)rectangular component of area calculated from the ratio of the CsI Compton and photo-electric absorption cross

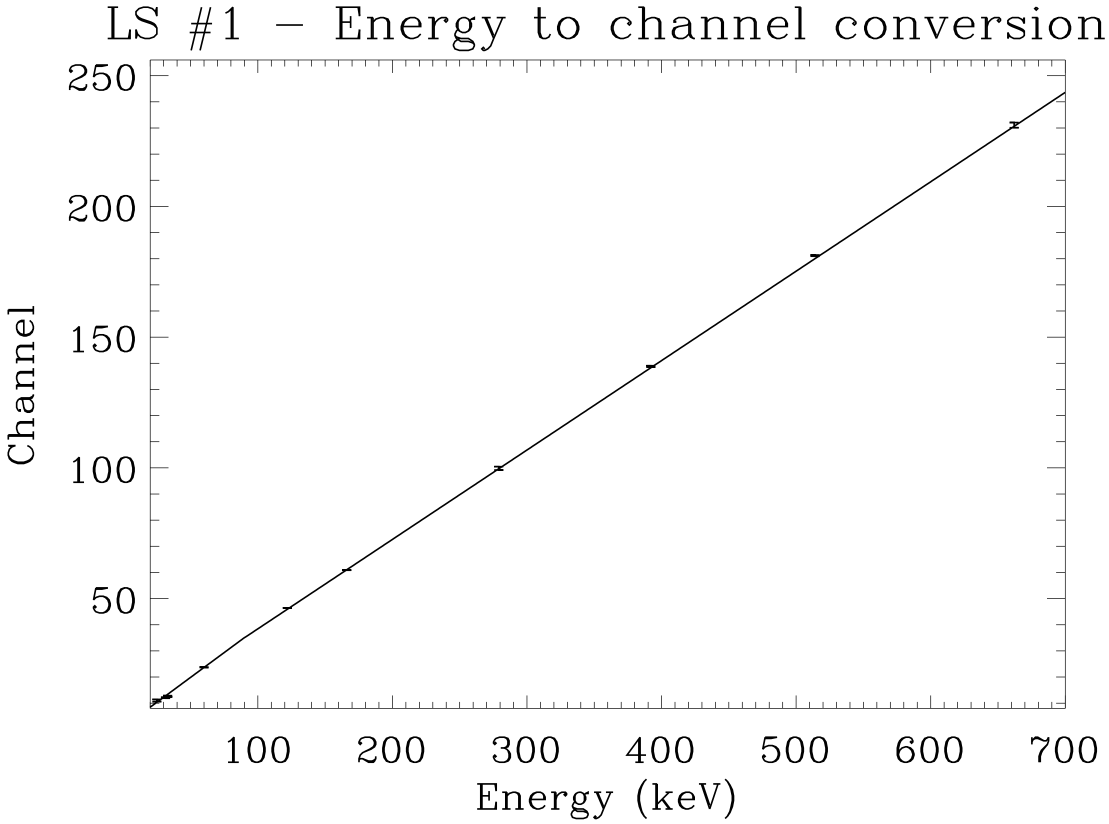

Figure 3.14: LS1 channel to energy conversion

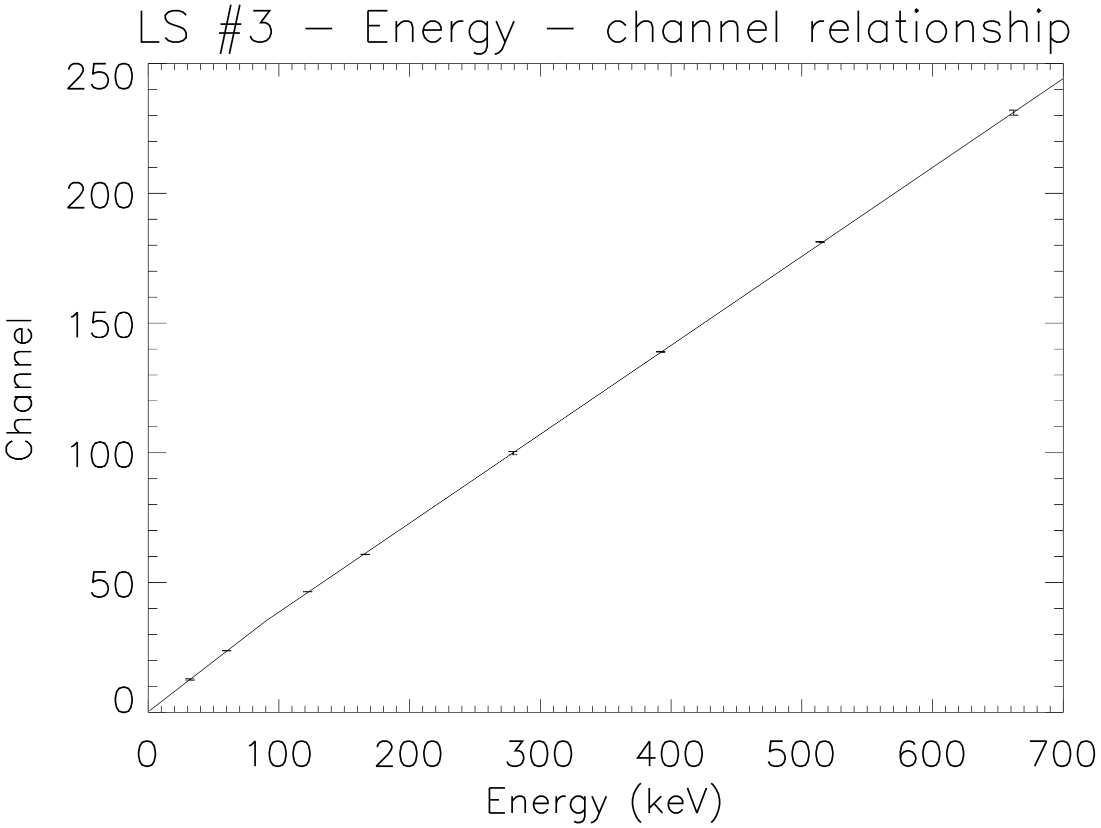

Figure 3.15: LS3 channel to energy conversion

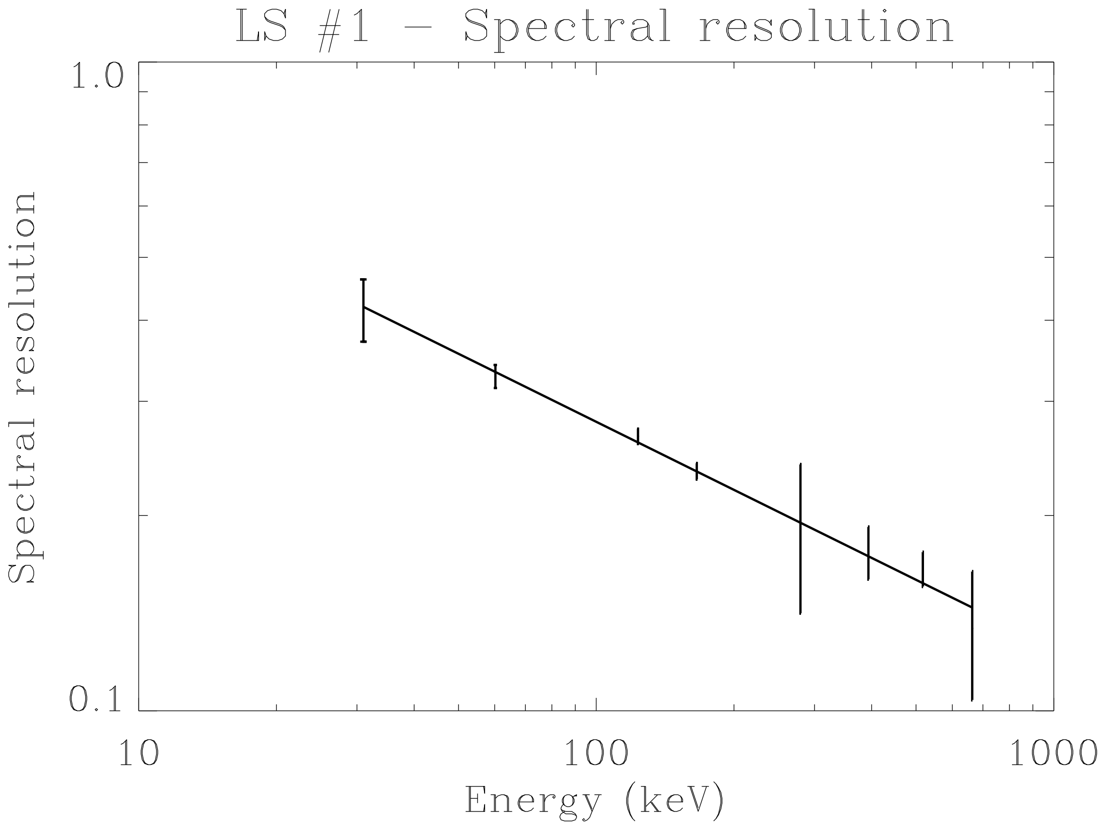

Figure 3.16: LS1 Energy resolution.

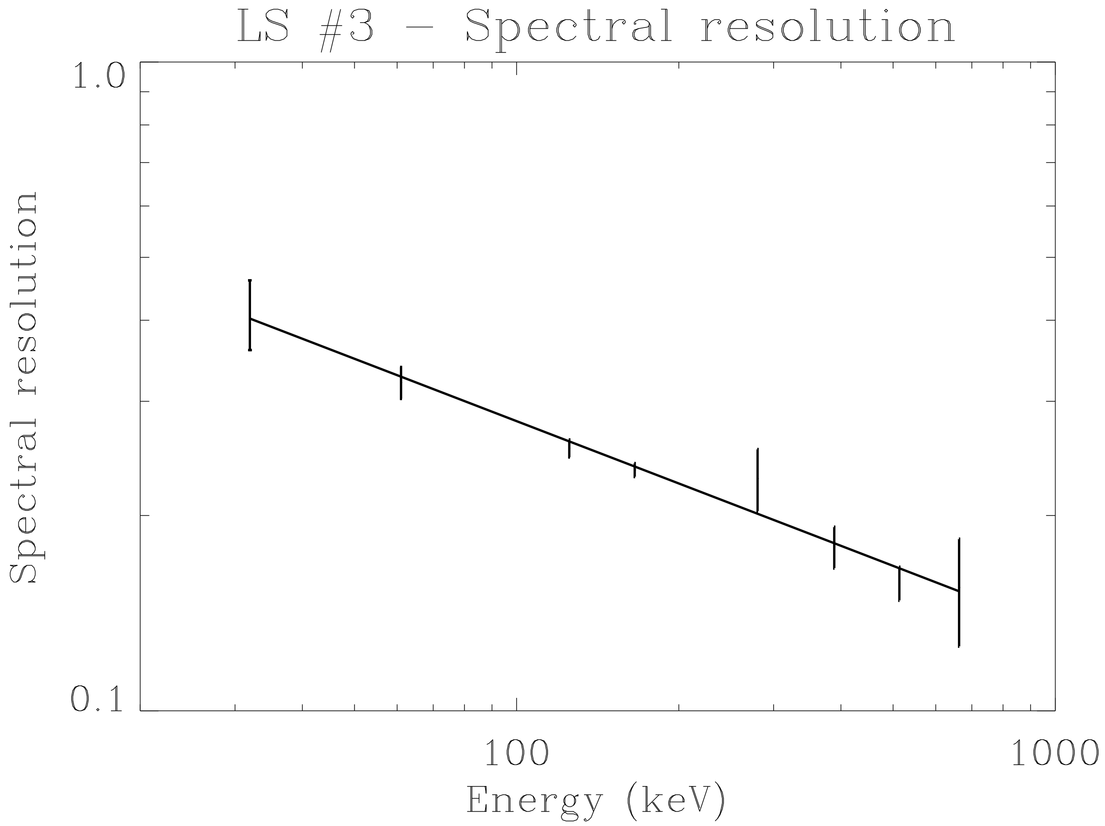

Figure 3.17: LS3 Energy resolution.

section. To the Compton area we subtracted the counts due to multiple scattering events which fill the gap between photo-peak and the Compton edge (modeled as a Gaussian edge with FWHM equal to the detector resolution at the edge energy) and whose quantity was determined empirically. At low energies, the escape peak was modeled as a Gaussian with FWHM equal to the energy resolution at the escape energy. At these energies the Compton continuum component was assumed to be zero.

The LS1 and LS3 spectra obtained by convolving input line spectra at the calibrations sources energy, and with the same fluxes, with the response matrices are shown in figures 3.18 and 3.19 superimposed to the relative measured data.

3.4.3 Thresholds effects

The effects of the GRBM LLT and ULT thresholds on the lines spectra shape at the low and high energy sides were included in the response modeling basing on the calibrations performed on the standing alone PDS described in section 2.3.2. In particular, the modeling of the low–energy cut–off due to the LLT is well seen in figures 3.18 and 3.19.

3.4.4 Standardization of response matrices formats

Specific software was developed, using the IDL package and a specific routines contained in the *astrolib* library, to convert GRBM spectra and response matrices in FITS–OGIP format to be used and tested with standard spectral analysis software packages like FTOOLS and XSPEC.

This has been done not only with the 240 channels spectra and response matrices, but also for the analysis of ratemeters data, by expressing the response in the GRBM and AC bands in the form of a response matrix and the counts in the two bands in the form of 2–channels spectra.

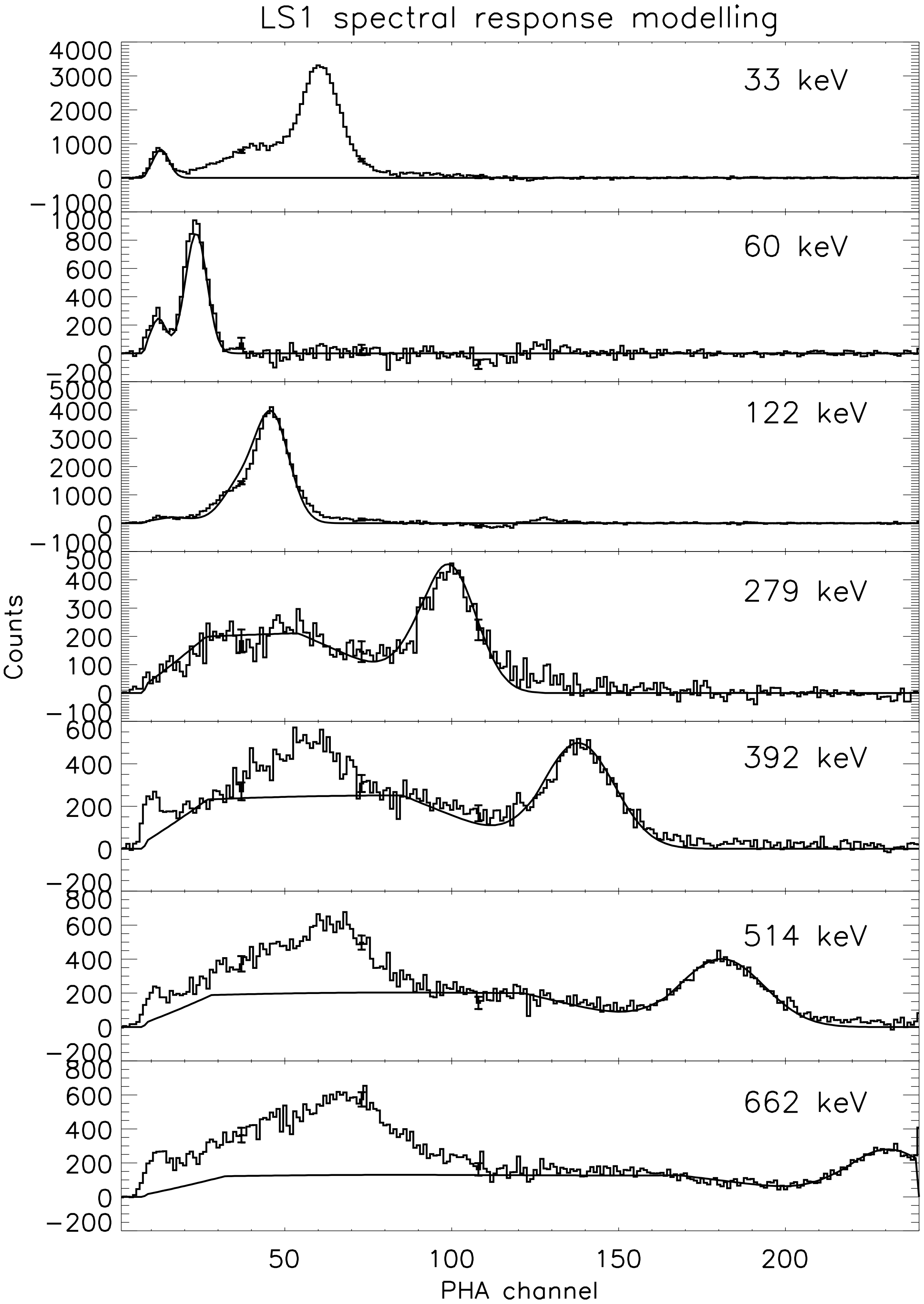

Figure 3.18: Modelization of LS1 response at the various calibration energies

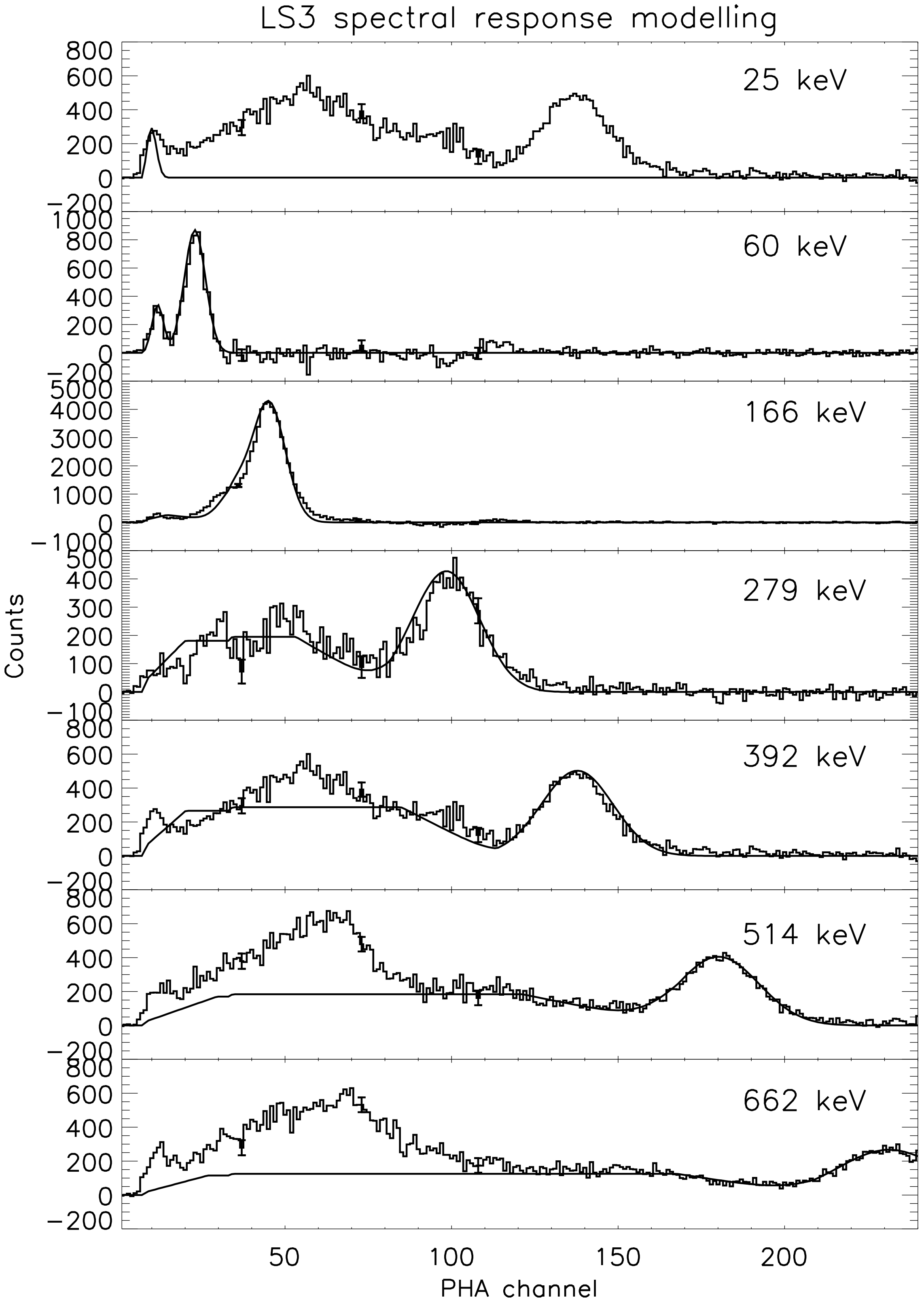

Figure 3.19: Modelization of LS3 response at the various calibration energies

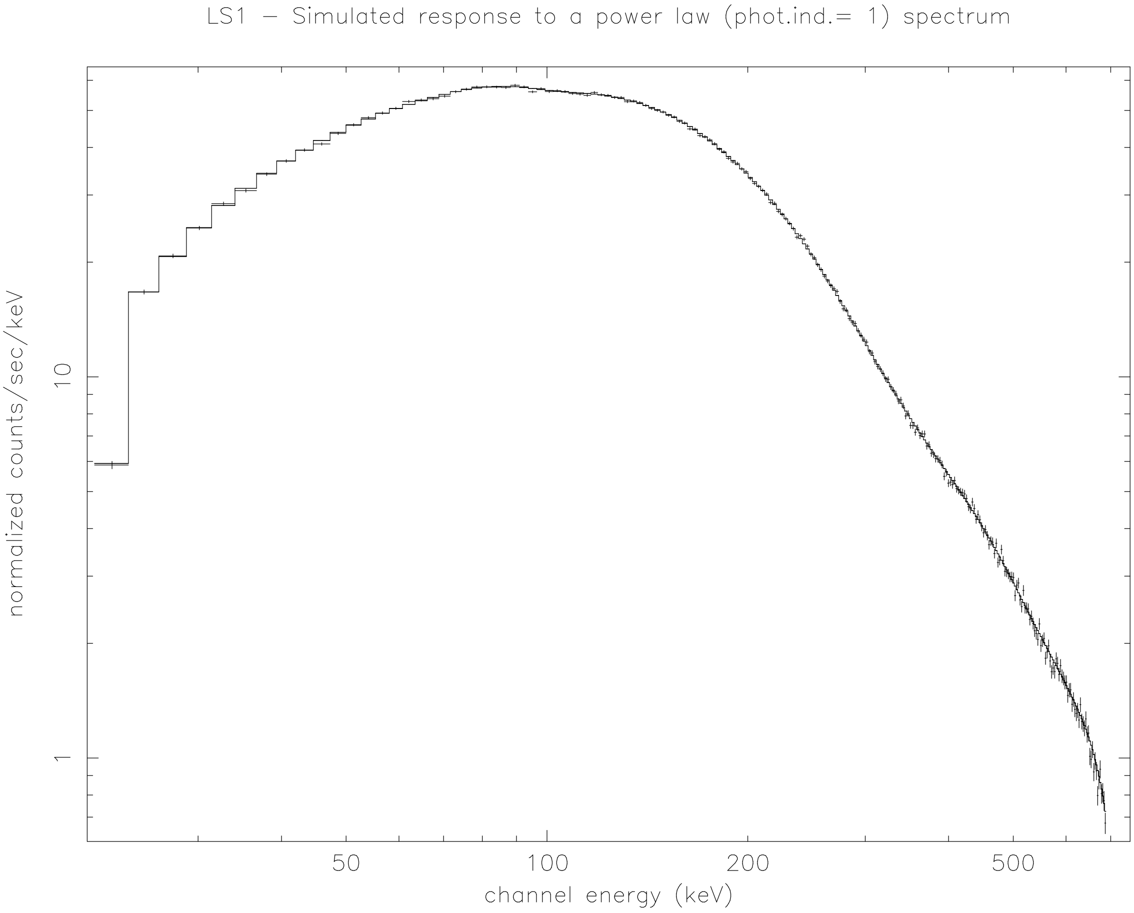

Figure 3.20: LS1 simulated counts spectra for a α = -1 power–law source photon spectrum

3.4.5 Expected counts spectra for different source photon spectra

In figures 3.20, 3.21 and 3.22 we report the expected LS1 counts spectra for the following source photon spectra respectively: a power–law with photon index = 1, a typical Band form spectrum (see section 4.1) with α=−0.5,β=−2,E_0=150 keV and a Crab–like spectrum (α=−2.1, norm = 9.7 photons cm−2 s−1 keV−1) integrated over the GRBM spectra accumulation time of 128 s.

These simulations were performed with the XSPEC package using the FITS LS1 response matrix.

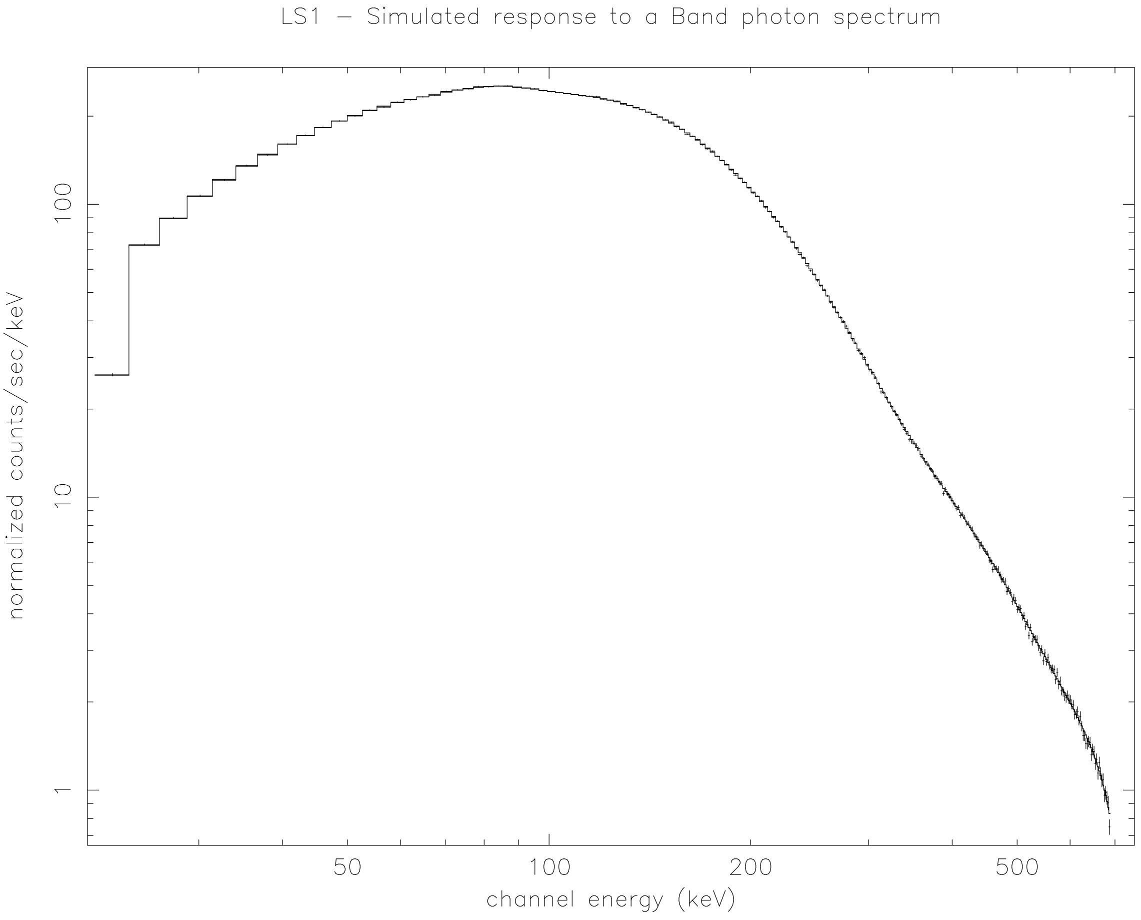

Figure 3.21: LS1 simulated counts spectra for a typical Band form source photon spectrum

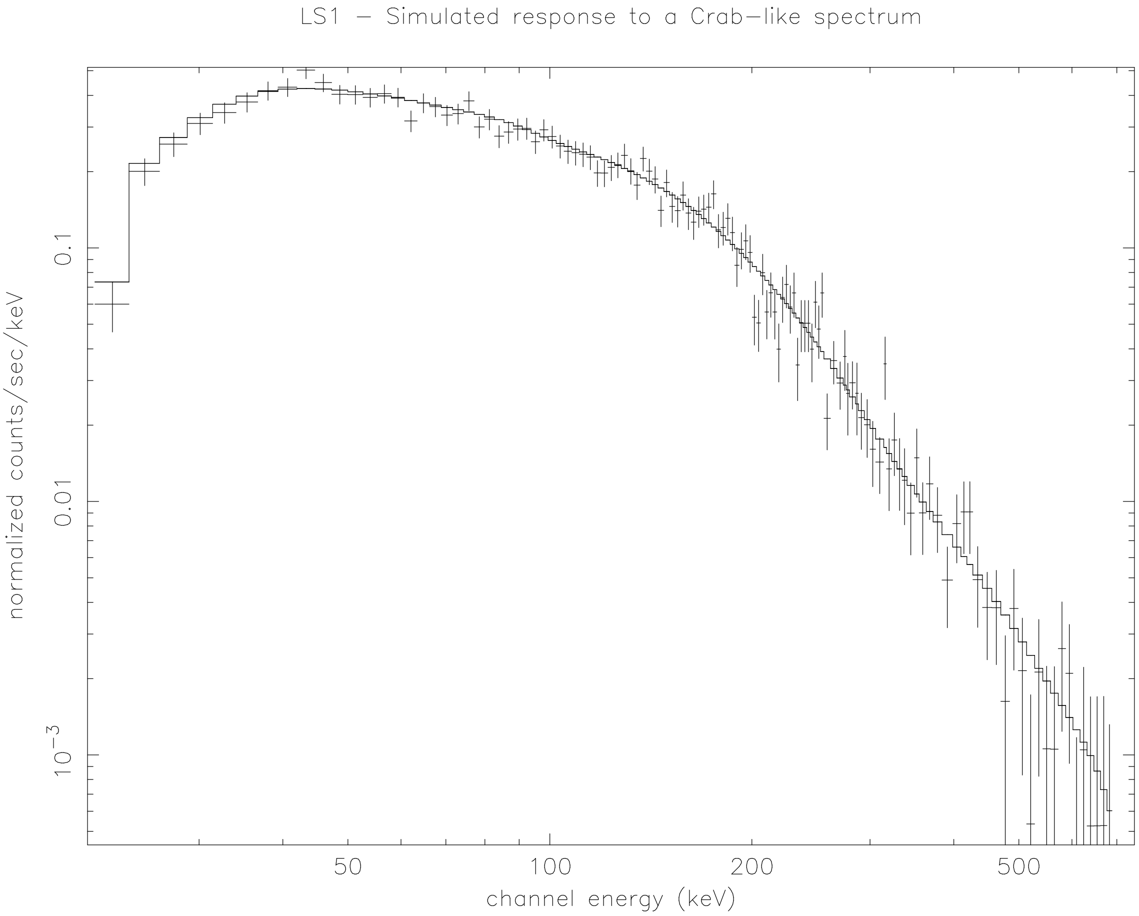

Figure 3.22: LS1 simulated counts spectra for a Crab–like source photon spectrum

3.5 Comparison between calibrations results and preliminary Monte Carlo simulations

A complex activity of Monte Carlo simulation has been started by the GRBM hardware team in which the entire SAX satellite is described in a 3D geometrical reconstruction (Rapisarda et al. 1997). This code is being used for the simulation of the on-ground calibration set-up, and once a good level of confidence is reached on that, it will be used to reconstruct direction, intensity and spectrum of the cosmic Gamma Ray Bursts. In this section we briefly describe the Monte Carlo set-up, discussing the approach to the work and the approximations that need to be done. Then the first results of the simulations are shown and compared, for some monochromatic energies and for several incoming directions, to the results obtained during the on-ground calibrations.

3.5.1 The Monte Carlo model

The code chosen to perform the simulation is MCNP (Monte Carlo N-Particles)8 version 4.2. It allows to transport photons (and neutrons and electrons) from 1 keV to 100 MeV through the matter. Every kind of three- dimensional geometry can be described, defining separate cells whose compositions and densities are chosen by the user. Photon interactions are treated very accurately. Coherent and incoherent scattering processes are treated according to the atomic form factors. Photo-electric absorption results in the generation of Auger electrons or fluorescence photons from the K and L shells (provided that the energy of the emitted photons is within the working range). The energy transferred to the electron is assumed to be lost locally and all the bremsstrahlung photons, that would have been created during the path of that electron, are assumed to be produced in the interaction point, with the direction of the electron (Thick Target Bremsstrahlung option of MCNP). A minor modification has been done to the code, to write the energy losses into an external file. The satellite has been modeled to a high level of detail. The process of refinement is still in progress. To date about three hundreds objects are present in the model (not counting as independent objects the collimator cells). In building the model the first obvious criterion has been that the closer to the GRBM where the components, the more detailed had to be the geometrical description. Where possible the exact material composition has been used. When it was impossible to detail tiny features, approximations have been made, but care was taken to preserve the overall opacity of the simplified components, following the other criteria that the masses should be the same of the real ones (changing the density accordingly) and the average atomic weight too.

Every object encountered by a gamma ray in its way to the scintillator slabs must be accurately described.

3.5.2 Simulation of on–ground measurements and comparison with the calibrations data

The model described in previous section has been employed to calculate the response of the four CsI slabs constituting the GRBM. A monochromatic point source is located at 5 meters from the center of the detector. The program is run to produce a statistically significant number of pulses in the four shields (typical error of 3-5 % for a well exposed shield). The source is then moved to the adjacent position, 10 degrees farther along the circumference, and another run is performed. With 36 of these positions the whole circumference is completed and the diagram with the angular response can be drawn. The results thus obtained are compared with the ESTEC on-ground calibration.

The simulation in the equatorial plane has been performed with sources of different energies, and the same job will be performed at other angles of latitude (15, 30, 45, 60, -15, -30) to benchmark the measurements made during the experimental on-ground calibration.

Figure 3.23 reports the response functions of the four Lateral Shields (LS) to a monochromatic ^{57}Co source located in 36 positions, along the equatorial circumference of radius 5 m, 10 degrees one from the other. The dashed lines represent the experimental response function, the solid lines the response simulated by the Monte Carlo, and the

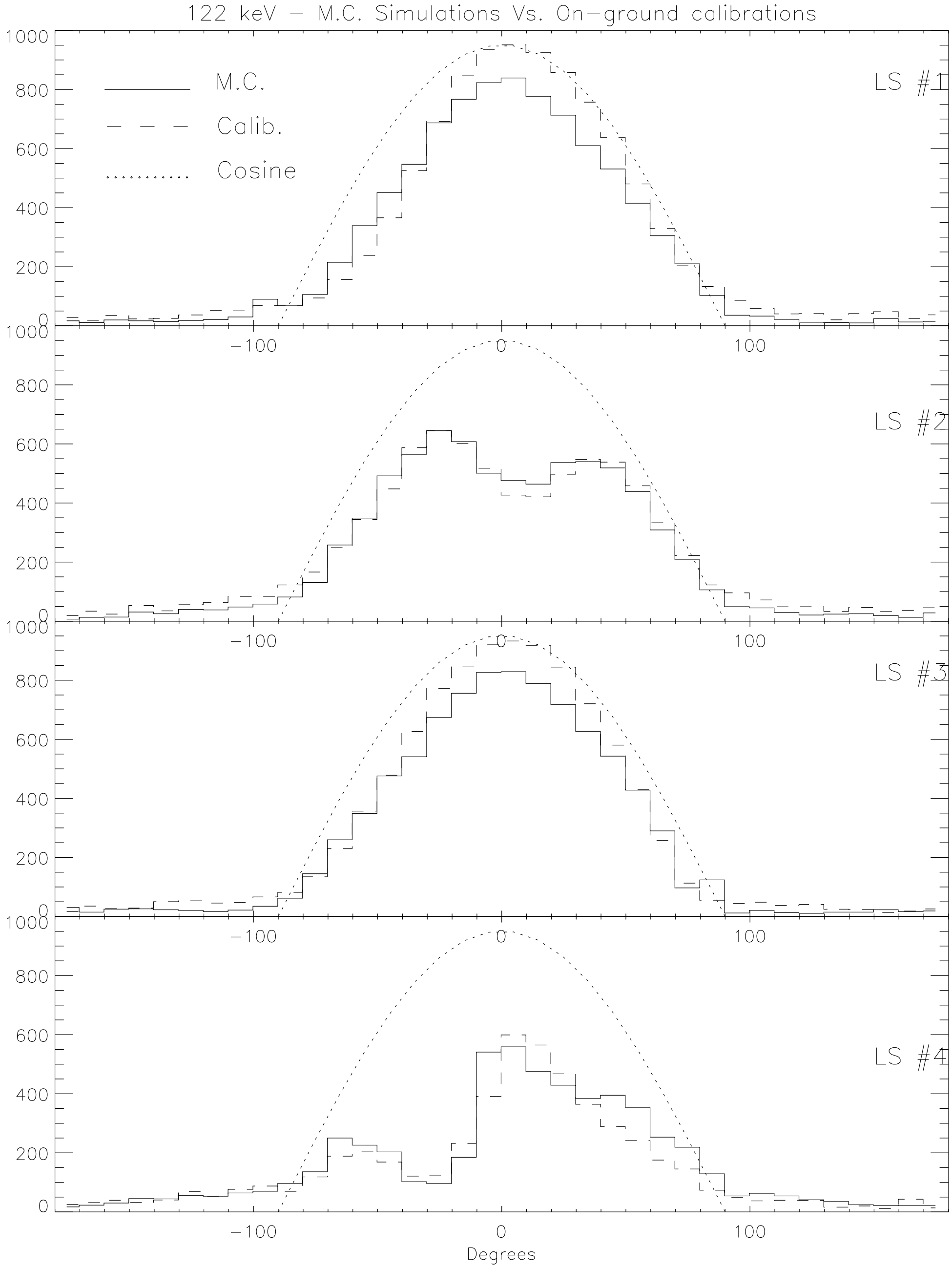

Figure 3.23: Response functions of the GRBM to a source of ^{5}7Co (122 keV)

dotted lines the simple cosine response that one would expect if the effects were purely geometrical. The experimental response, obtained during the slow rotation of the satellite was averaged along the ten degrees path and rebinned to match the simulated point source. LS1 is the shield behind the concentrators of the two MECS, LS2 behind the HPGSPC, LS3 behind the MECS and LECS concentrators, and LS4 behind the WFCs. At present we have not yet attempted to simulate the absolute response of the shields to the source, due to some refinements in the model still in progress. Thus, to compare the results, the experimental and the simulated responses are normalized in the shield 2 with the assumption that the total area under the two curves is the same. In first approximation the agreement between the two curves is remarkable. The Monte Carlo simulation confirms that the fields of view of LS1 and LS3 (those behind the carbon-fiber tubes of the X-ray telescopes) are practically free of obstacles and show a response close to the geometrical one. The agreement between the simulated and the experimental response is very close also in the LS2 and LS4, where the main features of the curves are reproduced.

A closer view shows, however, that the small differences are significant. For instance, the rise and fall of the source in LS4 is broader in the simulation than in reality. Moreover, if the normalization in LS2 is correct, the efficiency of the 'good' shields (LS1 and LS3) is underestimated by the Monte Carlo. The discrepancies between the simulated and experimental responses are more visible at the lower energy of ^{241}Am. If also in this case the overall normalization on the shield LS2 is correct, too much material is present in one of the two concentrators in front of the shield LS1, which are simulated equal. The worst situation is in the response of the LS4, where the presence of some material must have been underestimated. Other energies and other latitudes are being investigated at the moment, giving results substantially in agreement between the simulation and the experiment, but still with lesser discrepancies that suggest a further work of refinement along particular lines of sight.

Chapter 4

The in–flight data: source detection, data analysis and response functions verification

In this chapter, after briefly reporting on GRBM in–flight performances and operational status and describing the in–orbit background level and properties, we outline the techniques for the application of the ratemeters and spectra response functions described in chapter 3 to the estimate of flux, spectral evolution and average spectral properties of high energy transients, in particular Gamma–Ray Burst. We also show how we can derive flux and spectrum of bright hard sources by exploiting their occultation by the Earth and how this technique has been applied to obtain the Crab nebula fluxes in the GRBM and ratemeters band and the 240–channel spectrum, allowing in–flight verification of LS1 and LS3 response functions. Finally, we describe joint GRBM + WFC data analysis methods and the cross–calibration of the two instruments.

4.1 GRBM in–flight performances

The BeppoSAX GRBM started its in–flight operations one month after the satellite launch. The overall performances were successfully tested during the BeppoSAX Commissioning Phase, and during the Scientific Verification Phase the proper setting of all thresholds and trigger parameters, on the basis of the radiation environment in which the experiment had to operate, were identified (Feroci et al. 1997a).

At the beginning of the mission the default values for the energy thresholds were 1 (nominally corresponding to 24.67 keV, calibrated to 32.8 keV) for the LLT of the four shields and 6 (corresponding to a calibrated energy of 604 keV for the photo-peak) for the ULT. The ACT was set as a default at 0 (lowest value, nominal 100 keV). The trigger condition at that time was set with LIT=128 s, SIT=4 s and n=8. Considering also that the low efficiency of the GRBM detectors at the lower energies, due to the opacity of the materials in their field of view (chapter 3), it was decided to rise the LLT to its step 3, that is a calibrated value of 42.5 keV, for the four shields. This new threshold setting is therefore almost ineffective from the point of view of the source detection, but it largely suppresses the noise due to spikes and also reduces the background count rate (see next section). We note, however, that single spikes do not affect the trigger condition, that requires the time coincidence of the trigger on at least two shields, but a SIT of 4 s increases the probability of getting by chance a simultaneous trigger condition on two shields is enhanced by the fact that the temporal coincidence is extended to 4s. Furthermore, we note that the intensity of many spikes frequently exceeds the 8σ level over the background, and therefore the n=8 condition cannot be considered an efficient discrimination method of the real GRB signals from the spikes.

Another important calibration and setting concerned therefore the triggering parameters. With a SIT value of 4 s and n=8 the trigger condition selects GRBs with high intensity and long duration (i.e. one second or more). Given the typical duration of GRBs the SIT was lowered to 1s in order to be able to catch also shorter/weaker events. The high value of n was no more needed after the GRBM count rate was reduced to a almost–Poissonian statistics with the suppression of most of the spikes. Taking into account that the trigger condition must be satisfied simultaneously on at least two shields in order to give a proper GRB trigger, then the value of 4 for n can be considered safe enough against false triggers. In fact, considering that in one orbit (97 minutes) we get about 4000 s of good data (due to the data acquisition interruption at the passage over the

South Atlantic Geomagnetic Anomaly, SAGA), following a Gaussian statistics we expect that the count rate exceeds by 4σ the average background count rate with a probability of 6x10^{-5} each second in one shield. Since the non-source events must be uncorrelated on two shields the probability of having a GRB trigger by chance in Gaussian statistics is about 2x10^{-8} each second, that is of the order of 8x10^{-5} each orbit. Nevertheless, as we still discuss later, the in–orbit background is not Gaussian, and this causes the number of false triggers to be about 1 per orbit.

4.2 In–orbit background

The in–flight background in hard X–rays experiments in space is the sum of different contributions, the relative importance of which depends on the experiment energy band, the experiment configuration and the orbit height and inclination. The different contributions can be classified in:

- internal background, due to photons and particles generated inside the detector itself following e.g. the interaction of high Z particles that excite meta-stable atomic states of the crystal (see next section) and the spallation of photons producing short lifetime isotopes;

- local background, due to photons generated by the interaction of particle trapped in the Geomagnetic field or primary cosmic rays with the satellite structures ;

- diffuse cosmic X–ray background, whose spectrum can be described by a thermal bremsstrahlung with kT=∼41 keV at energies between 3 and 60 keV and by a double power–law with photon indexes of 2 and 0.7 at energies from 60 keV to 6 MeV (e.g. Comastri et al. 1995 and references therein)

- Earth gamma–ray albedo: the spectrum of the gamma–ray radiation radiated as extreme upwards tail of air showers in the atmosphere is approximated by a power–law with photon index 1.7 and a cut–off at energies below 27 keV; it contributes most of the background above ∼100 keV;

- charged particles background, constituted by primary cosmic rays, trapped protons, splash albedo electrons. These are detected as high height pulses and in general are not so important in GRBM background due to the SAX 'good' orbit.

4.2.1 Background level and variations in the GRBM and AC ratemeters

The measured in–orbit background level in the GRBM and AC ratemeters ranges between ∼900 counts/s to ∼1100 counts/s. In Fig. 4.1 we show a typical time profile along two satellite orbits of the four GRBM and AC ratemeters with a default set of thresholds. The very good stability and low modulation of the background along the orbit in the GRBM band is apparent, as well as the number of spurious signals ("spikes") that make the time variation of the ratemeters not consistent with simple counting Poisson statistics. These spikes are mainly due to cosmic rays of high atomic number Z exciting meta-stable states in the CsI crystal, giving rise to a phosphorescence on short time scales, but long enough when compared to the response of the detector electronics, therefore allowing the electronics to detect a high number of counts. From the behavior of the simultaneous AC ratemeters, however, we see that the typical amplitude of the signals composing the spikes corresponds to a small equivalent energy. This fact was confirmed by the in-flight thresholds calibration, that showed that they progressively diminish as the energy threshold rises.

Since the satellite is in a low-earth, almost equatorial orbit it crosses the South Atlantic Geomagnetic Anomaly (SAGA) once per orbit, at a latitude that varies during the day from about +4 to -4 because of the Earth rotation. During the SAGA crossing, the experiment is switched off, to avoid fatiguing or damages to the PMT due to the very strong particles flux. The CsI activation during "deep" passages over the SAGA causes an increase of the measured background level when the instrument is turned on again.

Moreover, an unpredicted situation whose origin is not clear and is still under study was discovered. In an orbit portion preceding the SAGA of about 10 minutes, sometime we detect an increase in the count rate of all detectors, mainly concentrated in the lower energies (i.e. smaller than 100 keV). The increase is typically negligible, but at times it becomes important, and rarely dramatic. We call this phenomenon ”pre–SAGA”, and we tried to investigate its origin. We first have searched for a correlation with solar flares, but we did not find anything significant. Considering that the phenomenon shows up in a fixed portion of the orbit, we expect it could be due to some Geomagnetic effect.

The excess intensity is at its maximum during those orbits with the most distant passage from the SAGA, that are clearly distinguishable thanks to the PDS Particle Monitor. In Fig. 4.2 the most dramatic example of the pre–SAGA we have detected is shown. As it is visible the pre–SAGA was exceptionally intense at time around -5000, and it was still intense in the next orbit. We note that during this second orbit, over-imposed to the pre–SAGA, we detected the famous GRB970228 (more visible from the expanded views in the two bottom panels). This GRB was triggered by the GRBM thanks to the fact that because of the pre–SAGA effect the LIT (see section 1.2.3) was set at 32 s(the initial value was 128 s), in order to properly follow these possible variation of the background.

From Fig. 4.1 it appears that the GRBM ratemeters of LS2 has a higher background with respect to the other three. This is due to the fact that, as discussed in section 2.5.3, this detector is illuminated by the four ^{109}Cd radioactive sources (main emission 88 keV, 462 days half life) that are part of the in-flight calibration system of the HPGSPC. The 88 keV line is efficiently detected by the shield LS2 in the energy range of the GRBM ratemeters, but due to its higher low energy threshold the AC ratemeter is not affected by the same problem. On the other hand, LS4 is influenced by another ”local” source of background. This is the linear Co57 movable calibration source of the PDS experiment

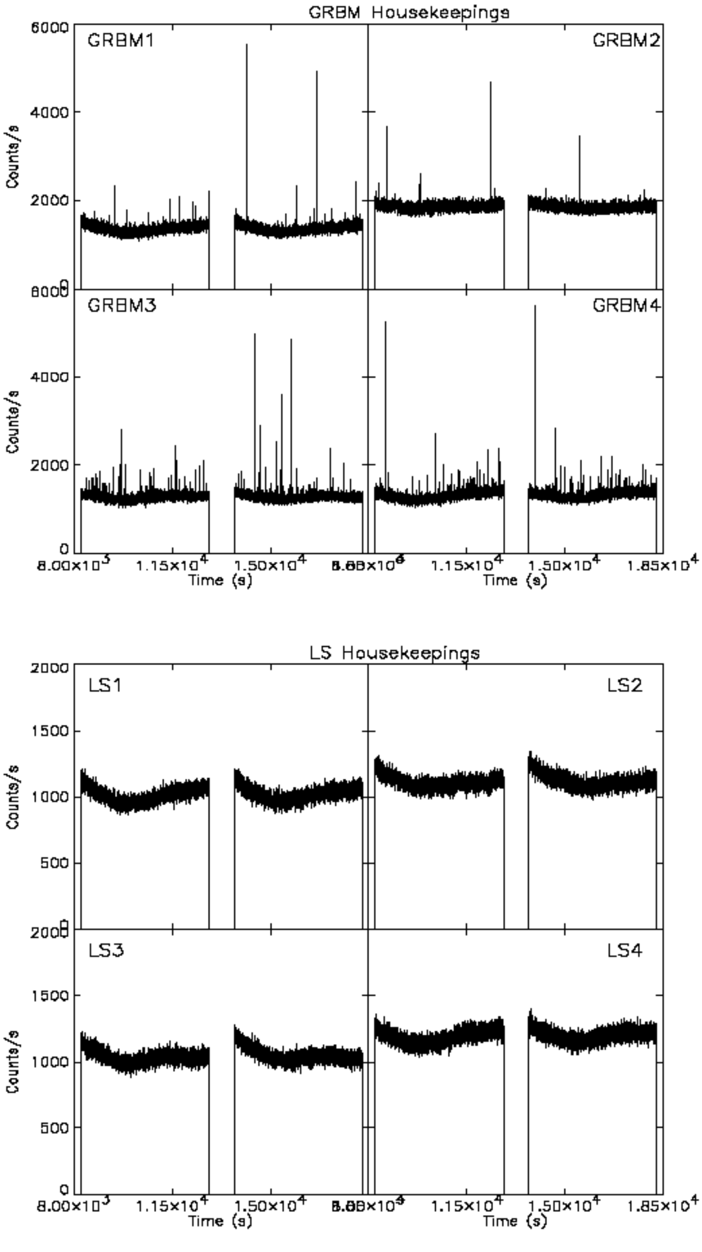

Figure 4.1: Typical on-orbit background level of the four GRBM and LS ratemeters of the GRBM experiment with GRBM energy thresholds LLT=1 and ULT=6, and ACT=0. The data gaps are due to the satellite passage close to the South Atlantic Anomaly and therefore identify the single orbits. The low energy channel (GRBM) shows the presence of several spikes, whose associated energy is within the energy difference between the GRBM LLT and the ACT.

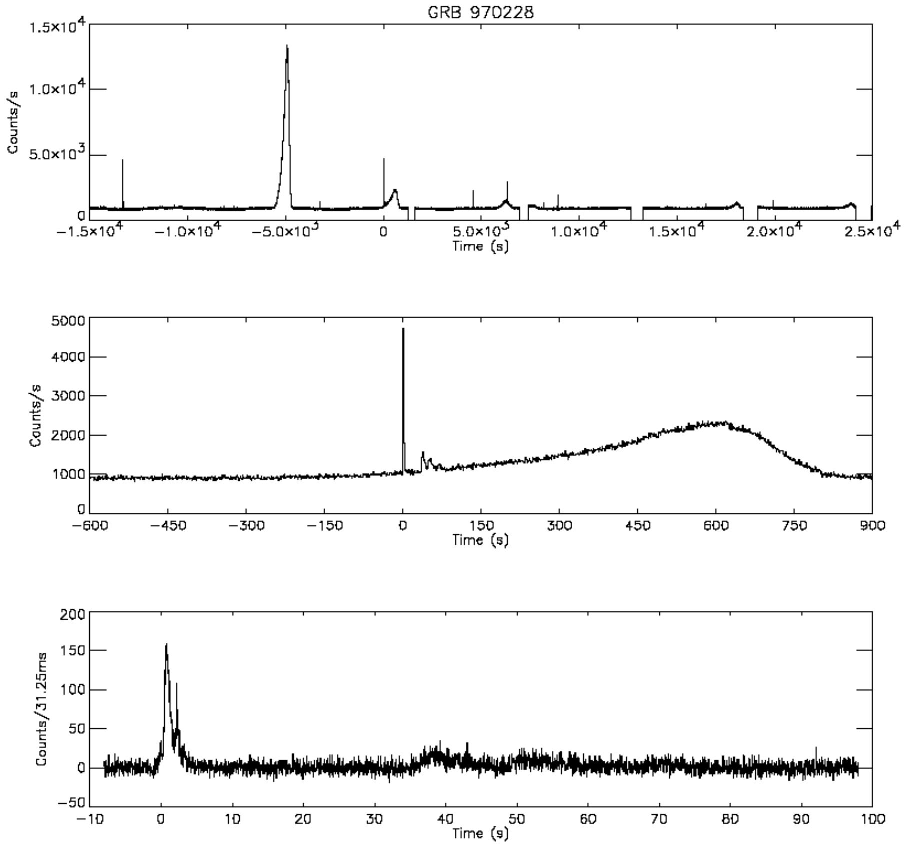

Figure 4.2: GRB970228 as detected in the LS1 ratemeter (T= 0 s, corresponding to the trigger time: 1997, Feb. 28, 02:58:00 UT). The pre–SAGA anomaly is huge in the previous orbit and evident in the orbit of GRB970228 itself. In the middle panel the GRB region is enlarged in order to make GRB970228 visible. In the bottom panel the burst profile (31.25 ms bins) as seen with the high time resolution data, in which the minor structures of the first peak can be clearly identified.

itself, whose parking position is located just above the top of shield LS4. The standard emission (122-136 keV) of the source is efficiently shielded by a properly heavy "parking strip", but a secondary line at 692 keV is emitted by the source with a branch of 0.16% (compared to the 68% and 3.8% of the main lines) and due to its high energy it is not efficiently shielded, therefore causing a higher background in the shield LS4.

4.2.2 Background spectral properties

As can be seen in Fig. 4.3, the in–orbit background spectrum presents characteristics very similar to that measured during on–ground calibrations, i.e. a continuum with superimposed the gain calibrator line. Actually this kind of calibrator, however, is rather sensitive to temperature variations, and can therefore be used only for comparing situations with similar experiment temperatures.
In addition, the prominent 88 keV line is clearly visible in the LS2 with an energy resolution of about 36% FWHM.

The spectral properties of the background are normally stable during an orbit. Significative variations occur when exiting the SAGA anomaly, during the pre–SAGA and in presence of spikes.
As discussed above describing the ratemeters background, CsI activation effects during the SAGA passage, the pre–SAGA crossing and spikes contribute all to soften the measured spectrum. In these cases, a very careful background subtraction has to be done in order to extract weak/short transient source spectra (see next section) without being affected by these effects.

4.3 Gamma–ray burst detection

With the setting of the thresholds described above, we detect about 12 triggers per day, that is roughly 0.8 triggers per orbit. These triggers are uniformly distributed along the orbit and there is no evidence for any "hot spot". Most of them are of course false triggers

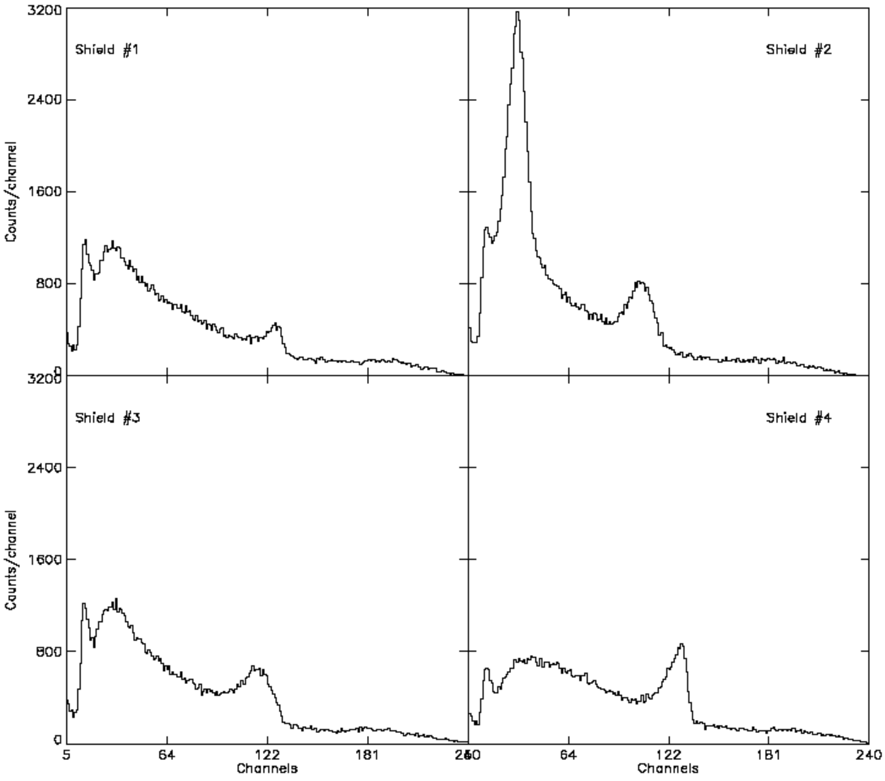

Figure 4.3: In-flight background energy spectra of the four detectors of the GRBM experiment. The 88 keV line due to the HPGSPC calibration radioactive source is clearly visible in the spectrum of shield LS2.

due to the lack of any particle anticoincidence (the GRBM detectors are themselves an active anticoincidence of the PDS experiment). Actually what we experienced is that the false triggers are due to correlated events in two contiguous shields. The physical origin of this kind of events is the same as the spikes, that is high Z particles that excite meta-stable atomic states of the crystals, but they are due to the crossing of two shields by the same particle, and therefore in time coincidence. In fact, what we see in our data is that most of the false triggers are composed by fast events (from few to tens of milliseconds) with slightly different time histories in two shields that are always close by. This characteristic, apart from the statistical considerations given above, almost excludes the possibility that these false triggers can be due to independent spikes in time coincidence on two shields. In this case one would expect they should be equally distributed on the four shields and not always from adjacent pairs. Their outlined characteristics make this kind of false triggers indistinguishable from real, short GRBs and we could reject them only by renouncing to the possibility of detecting very short events. On this regard, an interesting point is that we detect a small amount of short events that has similar characteristics to those described above. They are weak, short, on two adjacent shields (a viewing angle effect on a real GRB could also cause this) in which they show a very similar time profile. Among them we think that there can be some real GRB that can only be confirmed through the simultaneous detection by some other experiment.

In Fig. 4.4 we show few examples of light curves in the GRBM band of the GRBs detected by the GRBM. Some of them were simultaneously detected by other experiments like the BATSE experiment on-board CGRO or the GRB detector on-board the Ulysses. interplanetary probe or the Konus experiment on-board the Wind satellite.

In this figure, GRB start time is zero on the time axis. From the top left: GRB960720 (20/Jul/1996, 11:36:53 UT, also detected by BATSE) as visible from the high resolution time profiles of shield LS1, rebinned at 62.5 ms (data gaps are due to an on-board software bug, later fixed); GRB960805 (05/Aug/1996, 21:55:59 UT, also detected by Ulysses,

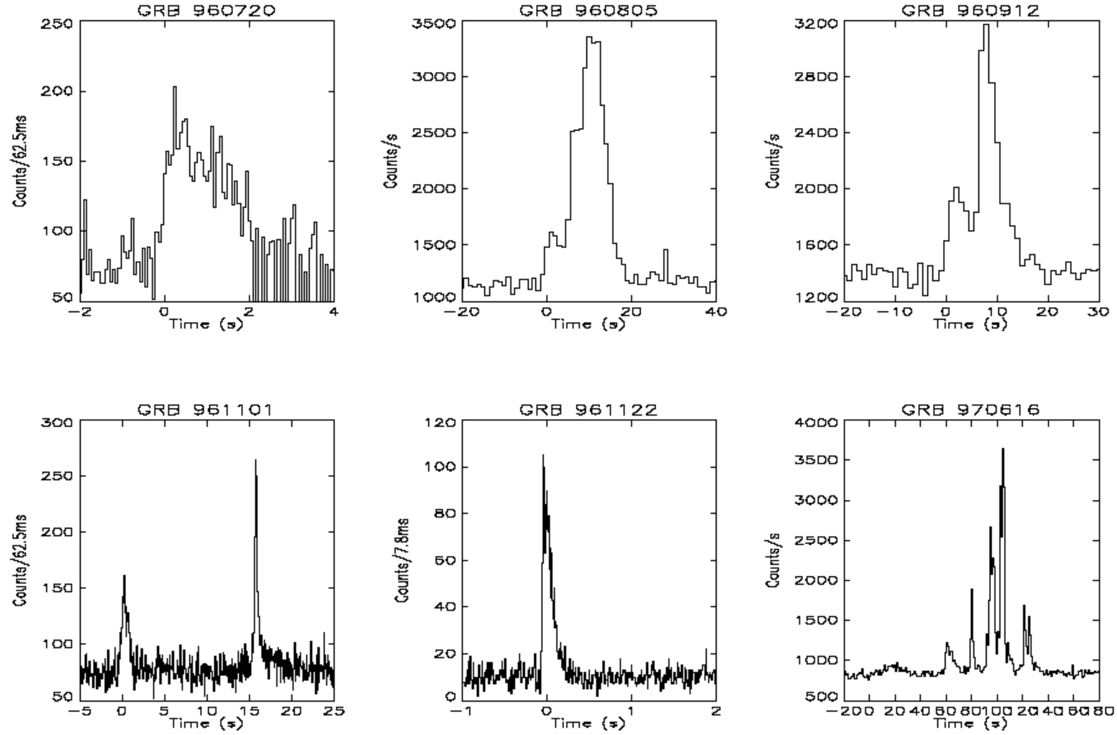

Figure 4.4: Six GRBs detected by the GRBM

not detected by BATSE) as visible in the LS3 GRBM ratemeter (1 s time resolution); GRB960912 (12/Sep/1996, 13:57:28, also detected by BATSE) from LS1 GRBM ratemeter; GRB961101 (01/Nov/1996, 16:07:44 UT, also detected by Konus, not detected by BATSE) at 62.5 ms from shield LS2; GRB961122 (22/Nov/1996, 02:17:40 UT, also detected by BATSE) at 7.8 ms from shield LS2; GRB970616 (16/Jun/1997, 18:09:48 UT, also detected by BATSE and Ulysses) at 1 s from shield LS1.

As can be seen from Fig. 4.4, the BeppoSAX GRBM was able to trigger on several different types of GRBs. As an example, GRB960720 (the first GRB detected also in the WFCs) is a FRED (Fast Rise Exponential Decay) type, and lasted for about 4 seconds; GRB961122 is also FRED type, but it lasts about 500 ms; GRB961101 has a small precursor, and GRB970616 has a very complex structure, even more complicated when seen at higher time resolution.

4.4 Detection of sources with the Earth occultation technique

The GRBM detectors can also be used as an All Sky Monitor. Given their large area they can be able to detect transient hard X-ray sources in the sky at any time. However, since the GRBM experiment has no imaging capabilities, steady sources can only be monitored by using the Earth Occultation Technique, as well as currently done by BATSE. When a bright hard X-ray source is obscured by the Earth during a satellite orbit, its contribution to the detector count rate disappears, and it will be visible again when the source will rise from behind the Earth. Due to the repetitive cycle of the satellite orbit, this situation will occur once per orbit as long as the same satellite pointing is maintained, producing a count rate ”step” at any rise/set of the source. One can therefore take advantage of summing several ”steps” due to the source in subsequent orbits and therefore reduce the statistical error on the measurement. The occultation profile is smoothed by the Earth atmosphere and in particular it depends on the time needed to the source to cross the

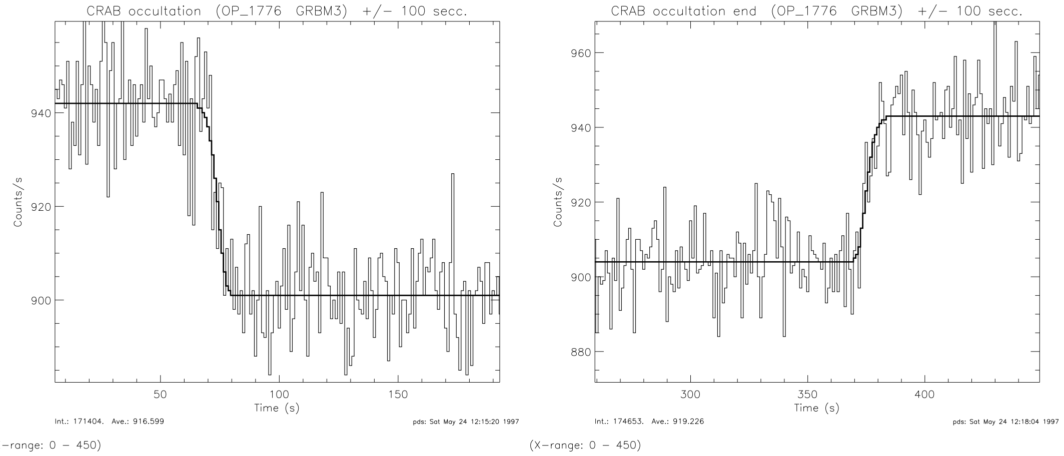

Figure 4.5: Crab Nebula occultation step in the GRBM detector LS3, with LLT=3 and ULT=6. Rise and set of the source behind the Earth disk are visible and modeled by an earth atmosphere absorption profile.

atmospheric profile, that is by the inclination of the line of sight to the source with respect to the orbital plane. In Fig. 4.5 we show the occultation step due to the Crab Nebula in the GRBM band with LS1, obtained with the thresholds configuration given above and with the source on–axis. Over-imposed to the detector time profile is the result of a modeling of the atmospheric absorption. The inferred net Crab count rates are reported in Tab. 4.1

4.5 Derivation of flux and spectral evolution from 1 s ratemeters

The ratio between counts in the GRBM and AC bands depends on source direction and spectrum. Because, as we have discussed in chapter 3, these data are equivalent to 2–channels spectra, we must assume simple model spectra, like a single power-law (PL) or an optically thin thermal bremsstrahlung (OTTB). Given the response in the two ratemeters bands (chapter 3), i.e. the efficiency as a function of photon energy at the given source direction, the GRBM/AC counts ratio is a function of the photon index (in case of PL) or temperature (in case of OTTB). Off course, these functions do not depend on the incident spectrum normalization. Thus, to derive these relationship we have con-

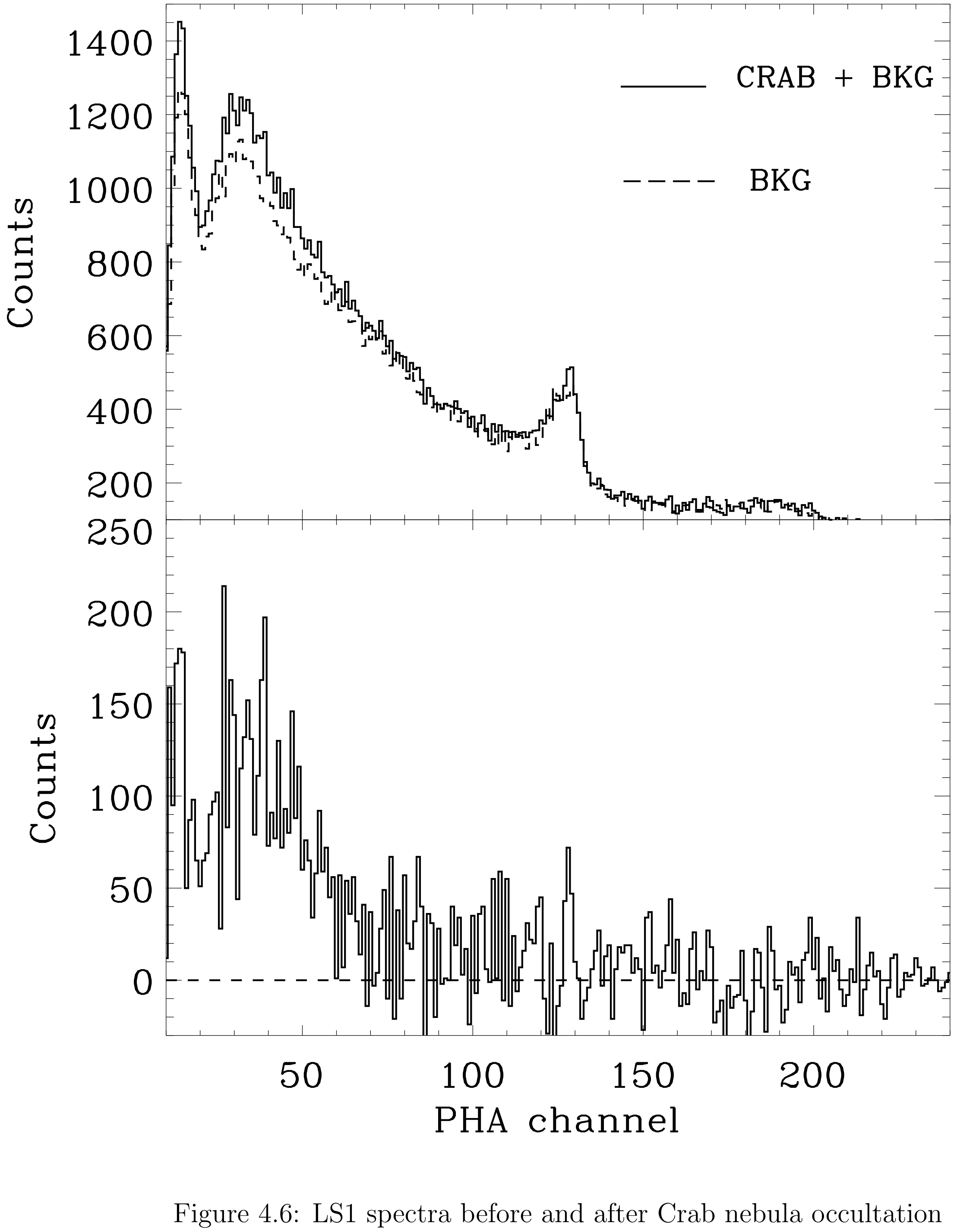

Figure 4.6: LS1 spectra before and after Crab nebula occultation

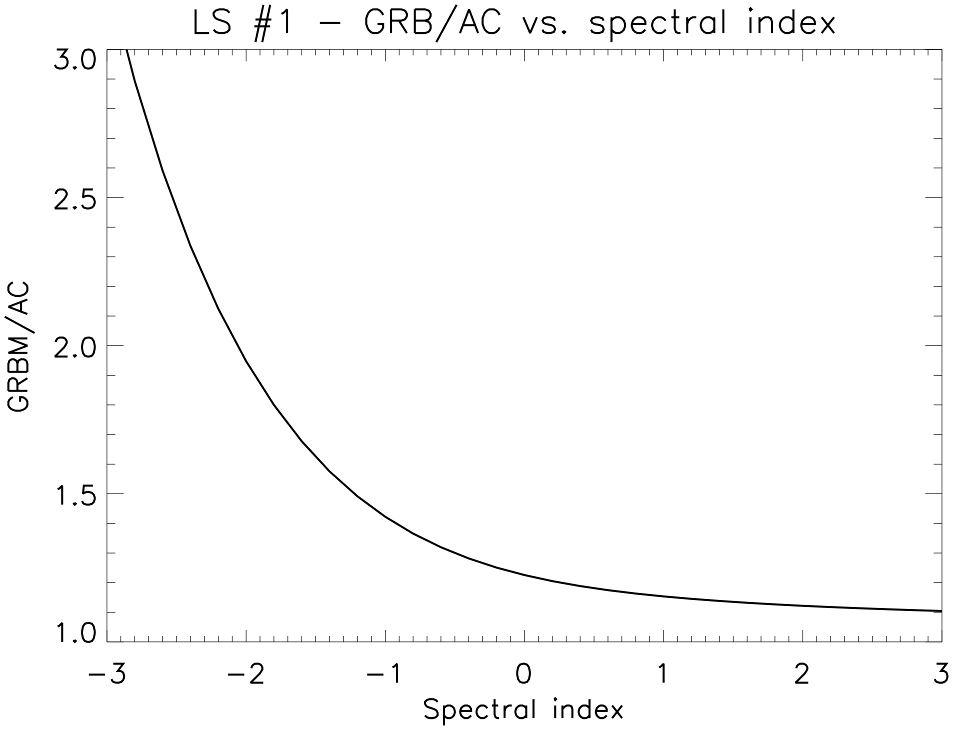

Figure 4.7: LS1 - Relationship between the ratio of GRBM and AC counts and spectral index for on–axis source assuming an high energy break in the photon spectrum at 700 keV

volved spectra having different photon indexes or temperature values with the detector response in the two ratemeters bands. In Fig. 4.7 we show the relationship between spectral index and counts ratio for LS1 and for on–axis source. Given the measured ratio, the spectral index or temperature is then derived by means of a cubic spline interpolation.

The normalization parameter of the spectrum can then be calculated by convolving an input spectrum of the extrapolated spectral index or temperature with the the responses of the GRBM detector in the entire energy band and comparing the measured counts to expected counts.

Background subtraction, for both the ratemeters , is generally a safe procedure, due to stable background. Exceptions have occurred, as for GRB970228 (Frontera et al., 1998) which occurred during the above mentioned 'pre–SAGA' anomaly and required specific efforts to extrapolate the background during the event. Generally, we interpolate the background in the GRBM and AC ratemeters during the event with a polynomial fit to the data before and after the event (about 150 s time intervals). After background subtraction, ratemeters data are analyzed through software which applies the methods described above to infer spectral index or temperature evolution together with photon flux evolution. Data are usually grouped to obtain more statistics quality for weak GRBs or to obtain average values in correspondence of the rise or fall of the pulses. It is important to note that with the actual thresholds values the energy bounds are 40–700 keV for the GRBM band and > 100 for the AC band. Because of the low efficiency of the detectors above 700 keV and the general shape of GRB spectra, we make the assumption that, except for the very first instants of some events, the source contribution to the counts above 700 keV is negligible. Thus, the difference between the counts in the GRBM and AC bands can be assumed to be almostly due to photons leaving in the detector an energy between 40 and 100 keV. Moreover, the 2 bands are overlapped in the region 100–700 keV, where the data are completely co–variant. This is taken into account when estimating the variance of the GRBM – AC (40–100 keV band) computed counts. In this computation we introduce the variance of the background above 700 keV, which is estimated by comparison of the AC average counts with the 240 channel spectra counts, from which it is possible to estimate the average 100–700 keV background contribution. A typical result of GRBM spectral evolution analysis of a GRB obtained by applying the above methods is shown in Fig. 4.8 for GRB970111 (Amati, L. et al. 1999), One of the brightest events detected by the GRBM. The source were close to the LS3 axis (θ=12.4°,ϕ=7.7°); the GRB position was derived with high accuracy from WFC data.

4.6 Energy spectra analysis

The analysis of the 240 channels energy spectra follows the standard steps of data reduction, background subtraction, analysis with specifically developed and/or standard

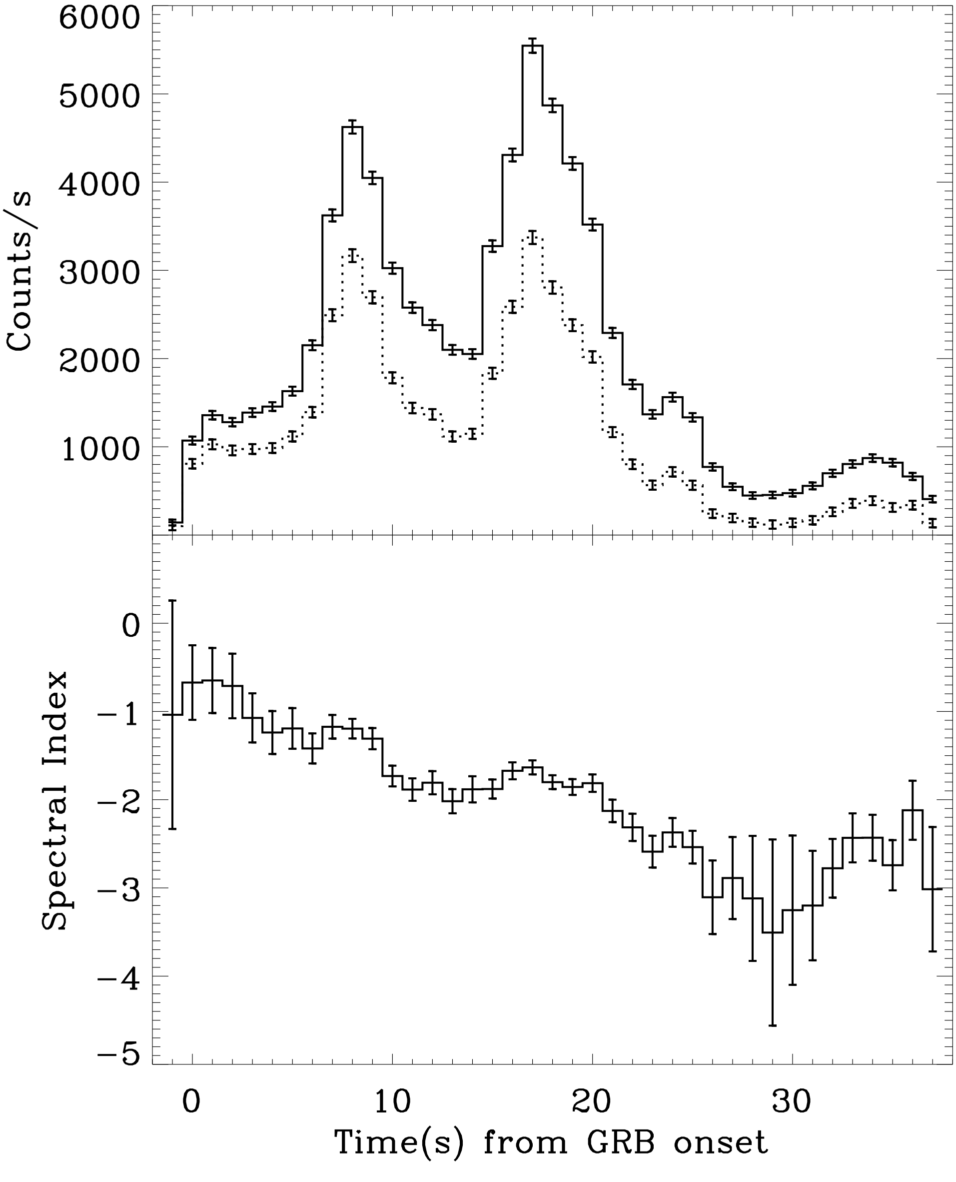

Figure 4.8: Upper panel: GRB970111 1s light curves in the GRBM and AC (dashed) bands; lower panel: GRB970111 1s spectral index evolution inferred from the ratio between GRBM and AC counts assuming a power–law spectrum

software.

For the background subtraction, the interpolation is performed by fitting the trend of the counts in groups of channels from 1–2 packets before and after the packet containing the event spectrum. Because PHA spectra are accumulated over 128 s, the GRB event is usually contained in 1 GRBM packet, but it may happen, as for GRB990123 and SGR1900+14 (see chapter 5), that the duration of the event covers more than one packet, , thus allowing 240 channels time resolved spectral analysis of the event. Possible changes in detectors gain between before and after the event are checked and spectra of the background in the same portion of previous orbits are analyzed and compared.

In figures 4.9 we show the average counts and photon spectrum of GRB980329, another very bright event (in 't Zand 1998). The fit is a single power–law. Also this burst is part of the WFC detected GRB sample and thus its position is known with very good accuracy.

4.7 Source direction

In chapter 3 we have discussed the dependency of GRBM detectors responses both in the GRBM/AC ratemeters and the energy spectra on incoming photons direction. The position of a celestial source of known coordinates with respect to each LS can be easily reconstructed utilizing the satellite attitude data, which are part of the final FOT (section 1.1.3) and are expressed in terms of the θ and ϕ angles defined in section 2.4.4. This is the case, for instance, of Crab nebula or SGR1900+14 (chapter 5) observations, sources having well known celestial coordinates.

Because, as discussed in chapter 6, the GRBM source localizing capabilities are still under investigation basing on the work on the response functions described in this thesis (Preger et al. 1999), in the case of GRBs it is possible to analyze only those events whose positions have been determined by the WFC (with few arcmin accuracy) or other missions, like BATSE (some degrees positioning accuracy for strong GRBs).

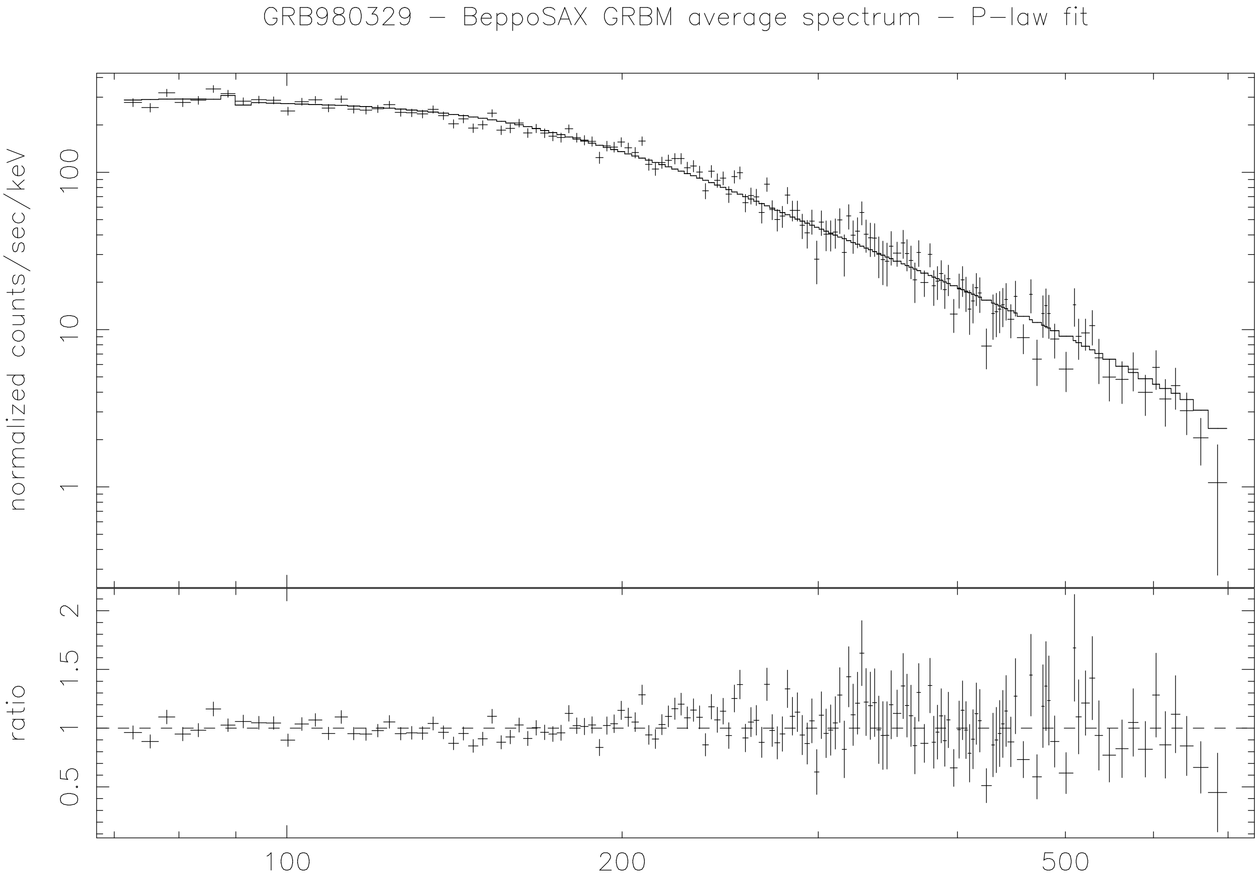

Figure 4.9: GRB980329 average count spectrum; the fit is with a power–law

Nevertheless, for what concerns this thesis work, we have applied GRBM response functions and data analysis techniques to the study of GRBs simultaneously detected by the GRBM and WFC and thus having a well known position in the sky and directions very close to LS1 or LS3 axis. As discussed in chapter 3, for these directions we have a satisfactory knowledge of the detectors energy response functions both for ratemeters and 240 channels spectra.

4.8 Dead time and counter recycling corrections

4.8.1 Dead time

In nearly all detector systems there is a fraction of time when, for some reasons, the system is not active, namely not able to detect events. For instance, a minimum dead time must separate two events in order that they be recorded as two separate pulses. The dead time can be set by processes in the detector itself or may arise in the associated electronics, as is for the GRBM. The dead time gives a probability that if an event occurs too close with respect to a preceding event it will be no recorded by the instrument. The dead time losses can become severe in case of very bright sources.
The relation between the true interaction rate n, the recorded count rate m and the system dead time τ is (e.g. Knoll 1989):

$$n = \frac{m}{1 - m\tau} \tag{4.1}$$

As anticipated in section 1.2.4, the GRBM 1s ratemeters and 240 channels spectra dead time is 4μs and 14μs respectively. Applying the above formula, we find that for a count rate of 10000 counts/s the dead time loss in the ratemeters in 4%, while in the 240 channel spectra it is 14%. Thus, the energy spectra data are significatively affected by dead time losses in the case of bright sources, like GRB970111 or GRB980329. The ratemeters data, in turn, become severely affected by dead time when the count rate reach very high value (40% for a count rate of 100000 counts/s), as in the case of SGR1900+14 (see section 5.4), which had a peak count rate (corquickly)rected for counter recycle as discussed below) in the GRBM band of 147000 counts/s.

4.8.2 Counters recycling

The memory allocated to the 1s ratemeters and to each energy spectra channel is 16 bit. This means that if the counts in one ratemeters bin or PHA channel exceeds 2^{16}=65536, the counter will be reset to 1 and restart counting. The result will be that if the counter recycles n times, the true measured count rate or count per PHA channel will be equal to the final counter value summed to $n65536$.

Counters recycling affected the GRBM measurements of SGR1900+14 outburst (August,27 1998) in the first 2 seconds. The recycling was apparent from the comparison with other experiments results and also by counts in the GRBM and AC ratemeters. In this case the recycling heavily affected also the HRTP, making it impossible to reconstruct the real high time resolution event profile in the first second.

4.9 Systematics due to uncertainties in detectors efficiencies

When estimating source flux and spectral evolution from 1s ratemeters data or fitting the 340 channels spectra, we have also to account for systematic effects due to the uncertainties in the description of detectors efficiencies.

As we have discussed in chapter 3, the dependency of LS1 and LS3 efficiencies have been obtained by fitting the calibration data with an analytical function. Thus, the error on the estimated efficiency for a given energy and direction is calculated by propagating the errors on the function parameters, which in turn are determined by the errors on the calibrations data. The errors on the calibrations data are obtained by propagating in the background subtraction the Poissonian variance and by accounting of the uncertainty in the calibration source flux, which is taken to be 10%.

In this way it is possible to estimate the uncertainty in detectors efficiency for each ratemeters band and PHA channel for the source position. The uncertainty in finally quadratically added to the data statistical variance.

4.10 Data reduction and analysis software

The various data processing steps leading from raw or FOT data reduction to the final spectral analysis results involve different sets of programs, belonging n part to public packets and in part to specific GRBM data analysis software.

4.10.1 Data reduction software

The BeppoSAX data, and specifically the GRBM data, are available in the form of Final Observation Tape (FOT, see section 1.1.3). Because the production of FOT from the telemetry data requires typically 2–3 days, GRBM data are also made available to the GRBM hardware group directly in the raw format (section 1.1.3) for prompt preliminary analysis. This is the case of GRBM+WFC detected GRB, for which a quick and prompt estimation of gamma–ray duration, peak flux and fluence is can be very useful for the scientific community.

Raw and FOT data reduction require different procedures to produce data in the final XAS format.

Raw data processing

The raw data are continuously archived at the BeppoSAX mission SOC, in the form of a compressed unique telemetry file for each orbit. The GRBM hardware team, through a PC Linux workstation installed directly at SOC, can access a local machine in which the last 20 orbits data are archived. The data can be retrieved via ftp from the PC Linux workstation.

The specific PDS/GRBM data files are unpacked from the telemetry file using a program specifically implemented by the GRBM hardware group. Finally, GRBM 1s ratemeters and energy spectra in XAS format are obtained by running XAS/PDS prototype programs, which allow the choice of the time interval in which the ratemeters are accumulated and of the 128s spectral packet(s) to be accumulated.

The time associated to each 1s ratemeters bin (corresponding to the end of the corresponding time interval) and to the start and end of each spectral packet is given in On–Board Time (OBT). The OBT can be converted in Universal Time (UT) by means of the OBT–UT time synchronization file, which is part of the set of files produced by the unpacking program.

For each trigger that has occurred during the relevant orbit, the trigger time in OBT can be read from one of the HRTP (see section 1.2.4) packet by means of a specific program developed in PERL language by the GRBM team, which also converts it in UT. Finally, the HRTP are converted in ASCII files using the programs described in section 1.2.4.

FOT data processing

The FOT data formats and reduction softwares have been described in section 1.1.3. For GRBM 1s ratemeters and 240 channels energy spectra accumulation we use specific XAS procedures. As for the raw data, GRBM trigger times and the HRTP are managed by means of specifically developed software.

XAS software allows the accumulation of GRBM ratemeters and spectra in specific time windows. The time associated to the ratemeters and spectral packets is converted from OBT to UT directly by the accumulation procedures. The satellite attitude and ephemeris files contained in the FOT allow for the reconstruction of the position of a source of known celestial coordinates with respect to each LS axis. The data contained in these files allow also for the reconstruction of the Earth center position with respect to each GRBM detector and thus to calculate the start and end times of the occultation of each celestial source, as for the Crab nebula (section 4.4).

4.10.2 Specific GRBM data analysis software

Except for the preliminary analysis software, the software for the analysis of GRBM ratemeters and spectra has been developed in the frame of this thesis work. This software has been mainly developed with the IDL packages ver. 4.1 and 5.0; in the 240 channels spectra fitting procedures, the IDL programs have been interfaced with the CERN/MINUIT minimization software.

IDL is a licensed software particularly oriented to scientific data analysis; its main features and advantages are:

- an high level FORTRAN–like programming language, which is easy to be learned by people experienced in FORTRAN and allows to reduce substantially the length of programs with respect to FORTRAN and to perform operations directly on vectors and matrices;
- it permits to write events–driven programs with window graphic user interface (as the XASPLOT procedure described below);
- it contains instructions that allows excellent and flexible 2D and 3D plotting, surface//shade plotting, contour plotting, image plotting, etc.
- the standard distributions library is very rich of statistics, scientific and general data analysis purposes subroutines and functions; in addition, specific physics and astronomy libraries (e.g. the astrolib library) are available on the net.

The preliminary analysis of GRBM data is performed using XASPLOT, a graphic user interface interactive program developed by the PDS/GRBM hardware group in the IDL environment as a XAS contributed software. XASPLOT allows the user to perform many tasks, between which the most commonly used for GRBM data analysis are: preliminary data checks and plotting, rough background subtraction and conversion from XAS to ASCII formats.

Subsequent GRBM data analysis steps described in the previous sections of this chapter like background interpolation and subtraction, dead time corrections, introduction of systematics, flux and spectral evolution derivation from the 1 s ratemeters with the technique described in section 4.3, are performed by means of flexible programs and routines specifically written in IDL. Due to the capabilities of IDL, these programs do not only perform data analysis, but they perform also the plotting on video or postscript files and the creation of reports containing the results.

Although, as discussed in chapter 3 and in next subsection, the spectral fitting of the GRBM 240 channels energy spectra can be performed using standard public software, we have developed a specific fitting procedure composed by IDL routines interfaced via FORTRAN routines to the CERN/MINUIT software. The IDL part of the procedure perform data reading, pre–processing and final plotting and reporting. The MINUIT routines perform the χ^2 minimization. In this way we take advantage both of the IDL package data handling and plotting capabilities and of the MINUIT software very powerful function minimization capabilities. The MINUIT algorithms allow for easier local minimum identification and new minimum search and better and more flexible error analysis with respect to e.g. XSPEC. The interface between IDL routines and MINUIT routines can be realized in two ways, depending on the machine operating system. One way is to create a specific module, written in C language, which has to be compiled with the MINUIT routines creating a share library, and use specific IDL call instruction to the C routine. With this method the data are transferred dynamically from the IDL routine to the MINUIT routines via the C module. Because this IDL instruction doesn't work in all operative systems, we have developed another interfacing method, which makes use of temporary files to transfer data.

4.10.3 GRBM data analysis with standard softwares

As discussed in chapter 3, the GRBM response matrices are also available in FITS format. Thus, after the specific data reduction and pre–analysis, the two channels (40–100 and 100–700 keV) data for each temporal bin and the 240 channels energy spectra can be converted to FITS–OGIP spectra to be analyzed with standard software packages like

XSPEC and eventually fitted simultaneously with WFC spectra (chapter 4).
While the response matrix conversion is more complex and needed the development of specific IDL programs, the conversion of spectra from ASCII files to FITS is more straightforward. This task is performed using simple scripts based on FTOOLS programs. FTOOLS programs are also used for simple arithmetical operations on the PHA files and to group the data in order to achieve a number of counts per channel sufficient for the application of the χ^2 statistics.

4.11 In–flight verification of the response functions

4.11.1 Measurements of Crab nebula flux and spectrum

LS1 and LS3 Crab Nebula count fluxes and PHA spectra were obtained by exploiting the occultation by the Earth (as described in section 4.4) when the source was pointed by one of the WFC and thus at the center of the detectors fields of view. At the time of observations (autumn 1996), the LLT threshold was set to step 1, corresponding to a calibrated value of 20 keV, thus allowing the verification of the GRBM response functions down to low–energies.
The Crab Nebula measurements results confirm the substantially good calibration of LS1 and LS3 near–axis responses in the ratemeters and spectra energy bands.

The Crab Nebula as a standard candle

Because of its stable and intense emission and its well–known spectrum, the Crab Nebula is commonly used in X-ray astronomy as a standard candle for in–flight calibration of instruments response. Several measurements of the total (nebula + pulsar) emission have been performed in X and gamma rays. In the X–rays, the canonical spectrum is taken to be the one measured by Toor & Seward (1974) in the 2–60 keV band, i.e. an absorbed single power–law with photon index 2.1±0.03, normalization at 1 keV 9.7±1.0 photons cm^{-2} s^{-1} keV^{-1} and column density N$_H$=3x10^{21} cm^{-2}. Other measurements in

Table 4.1: Crab Nebula expected vs. measured counts/s fluxes and photon index and 100 keV fluxes (photons cm^{-2} s^{-1} keV^{-1}) estimated from 1s ratemeters ratio

Detector	Band	Exp. counts/s	Meas. counts/s	Ph. Index	Flux(100 keV)
LS1	GRBM	44.2±3.3	46.1±1.6	2.25±0.11	(61±5x10^{-5})
LS1	AC	22.9±1.4	21.1±0.8		
LS3	GRBM	42.8±3.3	42.2±2.3	2.27±0.20	(60±5x10^{-5})
LS3	AC	21.4±1.5	19.3±1.3		

similar energy ranges give photon index values close to this. Extending the measurements to soft gamma–rays and still adopting the single power–law model, softer values of the photon index are obtained. In the 40–700 keV energy band typical photon index and 100 keV flux values are around 2.15–2.2 and (55–65)x10^{-5} photons cm^{-2} s^{-1} keV^{-1} respectively (e.g. Bartlett 1994). Moreover, the variable pulsar emission becomes a more significant percentage of the total emission as the energy increases. Thus, the hard X–rays to gamma–rays spectrum of the Crab is more likely to be a broken power–law with variations of the high energy component due to the variability of the pulsar emission.

The GRIS experiment (Bartlett 1994), which makes use of high energy resolution Germanium detectors, found that the Crab Nebula total spectrum between 20 keV and 8 MeV is best fitted by a broken power–law with the following average values: break energy at 61±10 keV, low energy photon index 2.00 ±0.03 and high energy photon index 2.22±0.03.

Crab Nebula flux and photon index from the 1 s ratemeters

The expected on–axis Crab flux in the GRBM and AC 1s ratemeters bands have been calculated by convolving the canonical Crab Nebula spectrum reported above with the detectors on–axis efficiencies as a function of energy (section 3.3.1). In Tab. 4.1 we report for each LS and each band the expected count fluxes, the measured count fluxes and the photon indices inferred from the ratio of the GRBM and AC counts. As can be seen, the measured flux values are consistent with the expected ones, and the photon index and 100 keV flux values are consistent with the hard X–rays values measured in other experiments and discussed above.

Crab Nebula 240 channels spectrum

We have fitted LS1 and LS3 on–axis Crab Nebula spectra with a single power–law, to compare the results with those obtained with the 1s ratemeters. Also, because the very low signal above ∼400 keV reduces the energy band in which we can be confident of not being influenced by background subtraction effects to ∼20–∼400 keV, we cannot constrain significatively the parameters of a broken power–law model.

By comparing the data with the expected spectrum obtained by convolving the canonical Crab spectrum with detector response matrix, we find a discrepancy in the range ∼40–∼70 keV, in terms of a 'depression' in the measured spectrum. This effect is seen both in LS1 and LS3 Crab spectra, and is also generally seen in sufficient bright GRBs when fitted with a continuous law. The reason for this is still under investigation (see section 6.2) and therefore we exclude channels in this energy range when performing fits on GRB sources. If we fit GRBM Crab spectra with a single power–law fixing the photon index to the X–ray canonical value of 2.1, we obtain a normalization of 9.4±0.5 and 9.3±0.6 photons cm^{-2} s^{-1} keV^{-1} for LS1 and LS3 respectively. This normalization values are fully consistent with the canonical value of 9.7 photons cm^{-2} s^{-1} keV^{-1}. This indicates a good normalization of the response matrices.

The power–law fits with both parameters free to vary give photon indices of 2.25±0.09 and 2.27±0.11 for LS1 and LS3 respectively, fully consistent with the 1s ratemeters values and other hard X–rays measurements. The χ^2_ν of these fits are of 1.12 and 1.15 for 81 d.o.f. Extending the energy range of the fits to 600 keV we find higher (∼1.4) values of χ^2_ν despite the increased number of d.o.f. (188). This indicates that in the region were the source contribution is negligible, the BKG subtracted spectrum is affected by distortion due to background variations effects that are not well interpolated with the technique described in section 4.4. Thus, Crab Nebula measurements tell us that LS1 and LS3 240 channels around axis response matrices are satisfactory in the region 20–400 keV (excluding the 40–70 keV region), and don't give significative information above 400

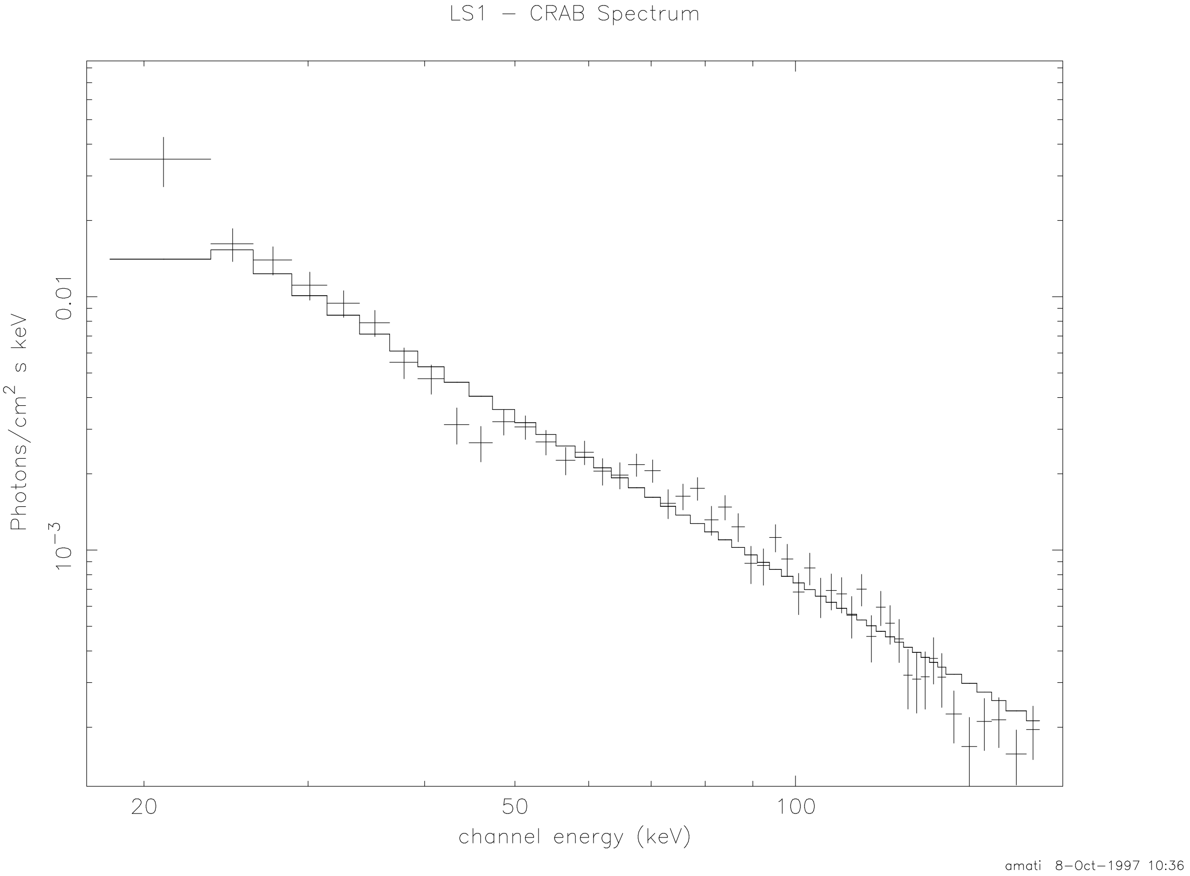

Figure 4.10: LS1 photon spectrum of the Crab fitted with a single power–law

keV. Nevertheless, the fits of the spectra of bright GRB (e.g. GRB980329, see Fig. 4.9), show us that the spectral response description of the two detectors is good also above this energy.

The LS1 Crab Nebula spectrum fitted with a simple power–law is shown in Fig. 4.11.1. The fit obtained excluding the 40–70 keV region is oplotted to the data, which have been grouped in order to obtain good statistics in each channel. The 40–70 keV depression in the data with respect to the model is apparent.

4.11.2 Comparison with CGRO/BATSE results

The BATSE experiment and GRB catalogue

The Burst and Transient Sources Experiment (BATSE, Fishman et al. 1994) on–board the NASA Compton Gamma–Ray Observatory (CGRO) is the main in–flight GRB experiment since early nineties. It has detected and classified more than 2200 events. It consists of eight detector modules made of 58.5 diameter by 1.27 cm thick NaI scintillator, sensitive to gamma–rays from ∼25 to ∼1000 keV. The geometry of the experiment allow for burst direction reconstruction with an accuracy down to few degrees.
The BATSE GRB data are made public on the web, at *http://www.batse.msfc.gov*; the on–line basic catalogues contain informations on trigger times, durations, photon peak fluxes in the 50–300 keV, fluences in the 25–50, 50–100, 100–300 and >300 keV energy bands.

Simultaneous detection of GRBM and BATSE

A cross check between BATSE and GRBM detections of GRB has been made. A deep study carried out over about one year has given the results listed in Tab. 4.11.2, from Preger et al. 1999, where with "Hardware OFF" we indicate that the instrument is switched off, and this can occur for example during the passage of the satellite over the South Atlantic Geomagnetic Anomaly, or in case of satellite maintenance. With "Software OFF", instead, we indicate that the instrument is on, but the software is not enabled: data are stored and can be analyzed, but the trigger function is inactive.
A particular care was devoted to the study of possible selection effects on the GRBM trigger efficiency, showing a clear selection on duration (only 2 events shorter than 1 s), a partial correlation between intensity and incoming direction (weaker events are preferably triggered at directions close to the satellite's equatorial plane). The angular distribution of these GRBs in the satellite rest frame reveals the pair of detectors GRBM2 and GRBM3 as the most efficient in triggering GRBs (we remind here that a valid GRB is recognized

Number of days	374
BATSE triggers	322
GRBM simultaneous triggers	61
GRBM hardware OFF	119
GRBM software OFF	3
Detected but not triggered	24
Data not available	11
Common triggers	32%
Common detections	46%

Table 4.2: BATSE/GRBM relative trigger efficiency from May, 23th 1997 to June, 6th 1998 (from Preger et al. 1999).

when at least 2 detectors trigger on the same event).

Comparison between GRBM and BATSE results

Given that BATSE gives for each detected GRB a 'rough' direction, peak fluxes values and fluences in 4 bands (from which some spectral information can be derived) and that it is expected to be a well calibrated experiment, we can use the GRBM+BATSE detected GRB sample to perform an in–flight verification of the calibration of the GRBM.

We performed a power–law fit to the BATSE fluences in the 25–50, 50–100 and 100-300 energy bands, to obtain a spectral model for each event. Then, given the source direction reported by BATSE or the high accuracy position given by the WFC for the BATSE/GRBM/WFC detected events, we calculated the expected counts in the GRBM and AC ratemeters bands by convolving the photon spectrum derived from BATSE fluences with LS1 or LS3 efficiency at the source direction.

We find that for those events with directions at an angular distance from LS1 or LS3 axis of ±30° the agreement between expected and measured counts is good. The consistency between expected and measured data increases with the brightness of the event, indicating that for weak events there can be differences in BATSE and GRBM fluences estimations due to the different sensitivity of the two experiments.

In Tab. 4.11.2 we report results of this analysis for some of the GRBs also detected

Table 4.3: Comparison between the expected count fluences from BATSE data and the measured ones

GRB	LS	θ	ϕ	Expected	Measured
960720	LS1	11.2	0.4	3700±500	3250 ± 200
970111	LS3	12.4	7.6	66000±15000	77200 ± 1500
970228	LS1	7.6	15	15000±2000	13500 ± 800
971214	LS1	-15.3	6.3	14000±1700	12200 ± 1700
980109	LS3	12.0	-0.4	5400±1200	4800 ± 500
980329	LS3	11.0	0.4	85000±12000	82100 ± 3200

in the WFC. The expected count fluences refer to the GRBM band. The expected count fluences error computation accounts for errors of the power–law parameters and GRBM response systematics.

4.12 WFC and GRBM joint data analysis and intercalibration with Crab spectrum

4.12.1 WFC + GRBM detections of GRB

The GRBM has become world wide popular in the last two years thanks to the simultaneous detection of some (15 up to now) GRB with the WFC and the consequent capability of quickly locating the GRB in the sky with a 3 arc-minutes accuracy. The co–alignment of GRBM detectors LS1 and LS3 offers the possibility not only to precisely localize GRBs and detect very faint X-ray afterglow emission of a GRB event down to $1 \times 10^{-13}\,\mathrm{erg/(cm^2\,s)}$, but also to perform in a broad energy band (1.5–700 keV) temporal and spectral study of those primary events from which afterglow emission is originated. In chapter 5 we show results of GRBM joint data analysis spectral data analysis of GRB.

The first simultaneous detection of a GRB was GRB960720, discovered by means of off–line screening of GRBM and WFC data. After this discovery, an operative strategy was developed in order to examine on–line each orbit the WFC light curves in correspondence of GRBM trigger. This search has been successively extend to trigger from GRB experiments other than the GRBM (e.g. BATSE triggers). Up to now, the GRB simultaneously detected by the two instruments are 15 (Tab. 5.1), the last (but not least) being the very recent and interesting GRB990123.

4.12.2 Data analysis and intercalibration

The joint data analysis of WFC and GRBM is possible thanks to the availability of PHA spectra and response matrices of the two experiments in the same formats. For WFC data analysis we used the public response functions and Crab Nebula spectra available at *http://www.sdc.asi.it*

The WFC instrument consists of two coded aperture cameras, each with a field of view of 40° × 40° full width at zero response and an angular resolution of 5 arcmin. WFCs have an energy resolution $\approx 20\%$ at 6 keV, were operated in normal mode with 31 channels in 1.5–26 keV and 0.5 ms time resolution (Jager et al. 1997). The on-axis effective area of WFCs No. 1 and 2 averaged in the 2–26 keV energy band is 118 cm^2.

The fits to the WFC Crab Nebula on–axis spectra are consistent with the canonical photon index, normalization and column density.

As it has been done for the BeppoSAX NFI (Cusumano et al. 1998), an intercalibration between WFC1/WFC2 and the GRBM detectors LS1 and LS3 can be performed by means of simultaneous Crab nebula measurements. We attempted both fits with a single power–law and fits with a broken power–law. The single power–law fits give a photon index of 2.05 ± 0.08 for WFC1/LS1 and 2.07 ± 0.1 for WFC2/LS3. If we untie the normalizations of the two data sets we obtain very close values, consistent between 1 sigma. This means that no normalization correction factor has to be introduced when simultaneously fitting data of the two instruments.

As expected, the best fit of the WFC + GRBM Crab Nebula spectrum is a broken power–law. For WFC1/LS1 the break energy is 66 ± 29 keV, the low energy photon index

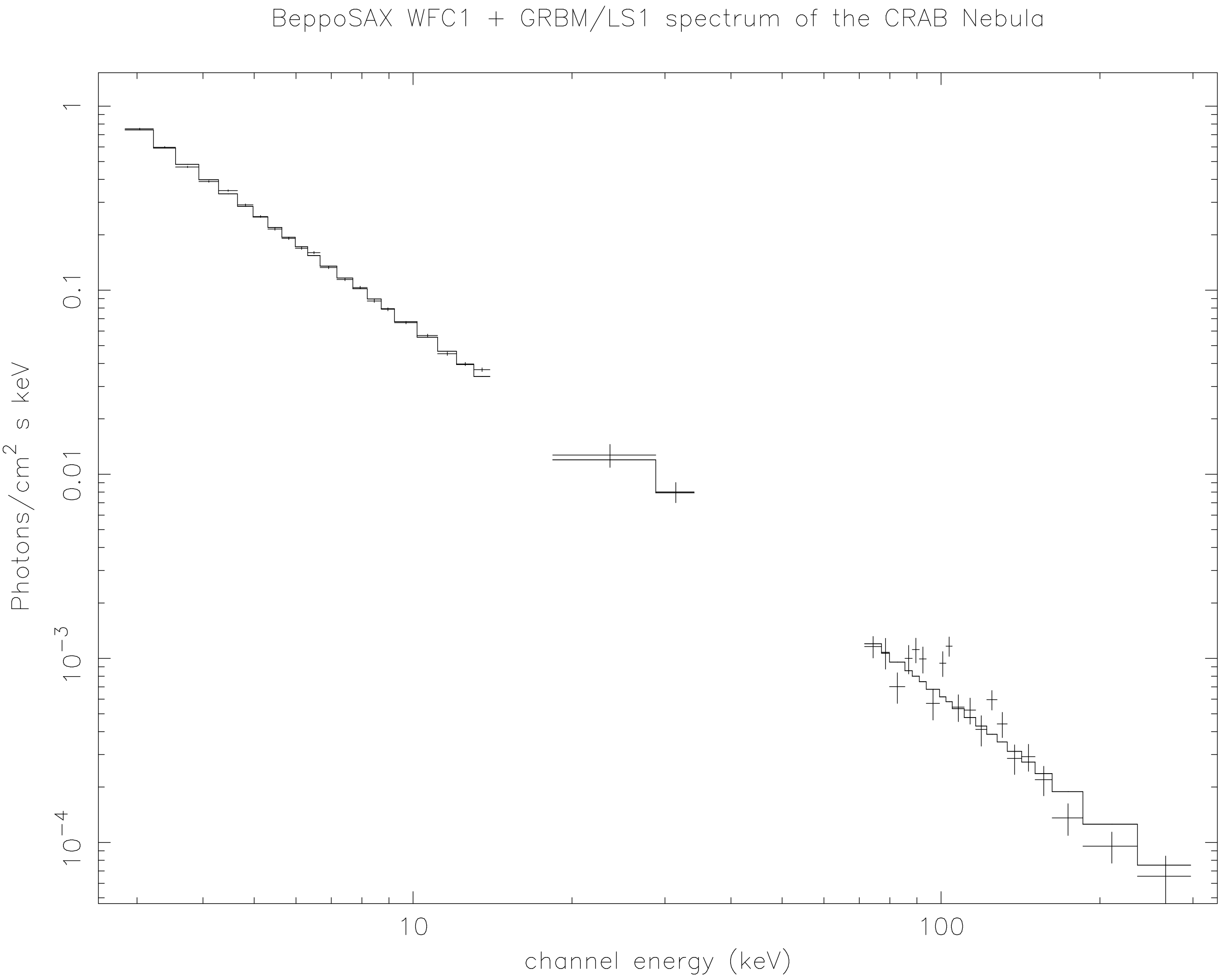

Figure 4.11: WFC1 + GRBM/LS1 photon Crab spectrum

is 2.06±0.07 and the high energy photon index is 2.18±0.6. Similar values are obtained for LS3. These values are fully consistent with those found by other experiments in similar energy bands (see above).

The results on the Crab nebula spectrum (4.12.2 show that the inter–calibration of the two detectors is very good, both for LS1/WFC1 and LS3/WFC2.

Chapter 5

Astrophysics with the GRBM: Gamma–Ray Burst and Soft Gamma Repeaters

In this chapter, after briefly reviewing the history and status of GRB science, we present some astrophysical results of the application of the GRBM response functions and data analysis techniques, presented in chapters 3 and 4, to the flux and spectral study of Cosmic SOurces, mainly Gamma–Ray Bursts. Particular emphasis is given to the study of those events detected also by the WFC, for which a nearly unprecedented broad band (1.5–700 keV) spectral analysis is possible. Many results of these analysis have been included in published papers, the more relevant of which are attached in Appendix A and are complementary to the content of this chapter.

Finally, a specific section is dedicated to GRBM study of SGR1900+14, whose results are included in a paper (Feroci et al., 1999) accepted for publication on Astrophys. J. and have a relevant astrophysical value.

5.1 Astronomy of cosmic gamma–ray burst

The gamma-ray bursts (GRBs) are one of the greatest mysteries of the high energy astrophysics. After their discovery in 1967, more than two thousands events have been observed by several experiments, but still today no astrophysicist can surely state what the GRBs are and where they come from. Before the advent of BeppoSAX only a statistical approach to the problem gave some results. The first, but still recent, achievement of such investigations are the isotropy of the GRBs arrival directions in the sky, and the paucity of weak events with respect to a homogeneous spatial distribution. The BeppoSAX satellite, not specifically designed for GRB observations, carries the right instrumentation for a novel approach to the GRB problem. It has been able to detect, localize and follow-up few GRBs on very short time-scales. This allowed for the discovery of the first X-ray afterglow of a GRB. The precision and rapidity of the detection, and the wide dissemination of information has permitted other observatories to point the directions, discovering the first optical/radio afterglow, and the measurement of its distance and size of a host galaxy.

5.1.1 Observations

The gamma-ray bursts are intense, short flashes of gamma-rays arriving from any direction in the sky, at unpredictable times. They usually emit most of their energy in the hard-X/gamma-ray range, but they have been detected from few keV up to tens of GeV.

They were discovered in 1969 by gamma-ray detectors on-board the military satellites *Vela* 5A, 5B, 6A, 6B, employed by the USA to monitor against possible Russian and Chinese nuclear tests in the atmosphere, in violation of the 1963 Nuclear Test Ban Treaty. After their discovery they were also found in older data and the first event came out to be recorded on 2 July 1967. Being a result of military investigations they were classified and were announced to the scientific community only in 1973 (Klebesadel et al. 1973).

After their discovery several gamma-ray experiments were included in the scientific payload of subsequent satellites, and continued to detect GRBs. Today the instrumental sensitivity has reached about 10^{-8} $erg\ cm^{-2}\ s^{-1}$ and they are then detected at a gross rate of one per day, corresponding to a rate of ∼3/day from the whole sky, taking into account the coverage.. A crucial contribution to the study of GRBs has been gained by the launch in 1991 of the *Burst And Transient Source Experiment* (BATSE Fishman et al. 1994) on-board the *Compton Gamma-Ray Observatory.*

Morphology and duration distribution

It is almost impossible to define a general morphology of the GRBs. It changes from one to the other, passing from single pulse events to multiple pulses, through a wide variety of shapes and time-scales. The single pulse events can last from few ms to hundreds of seconds. The multiple events are usually longer than a few seconds. Often the multiple structure of an event is found only at very high time resolution (of the order of few ms). In figure 4.4 an example of the zoo of the GRBs detected by the GRBM is shown.

Thanks to its high detection efficiency, the BATSE experiment has built a duration distribution of the GRBs. The duration of a GRB is defined as the time needed to go from the 5% to the 95% of the total counts detected from a given event. This distribution has a bi-modal shape, with the two broad peaks at about 0.3 and 30 s.

Angular distribution

In Figure 5.1 is shown the distribution of the arrival directions of 1429 GRBs from BATSE. Each point in the plot is located at the galactic coordinates of the arrival direction of one GRB, and the graphic representation is given in the Aitoff-Hammer projection (characterized by the equivalence between solid angle and area). As can be seen by eye, and tested through statistical methods, there is no evidence for any kind of anisotropy in the angular distribution.

Since any class of galactic object has a characteristic distribution in this representation (for instance, the youngest stars are mainly distributed in the galactic plane, where the spiral arms are and where the star formation is confined), this characteristic of the GRBs is a first indication that the GRBs are not easily associated to any known class of objects in our Galaxy. Moreover, given that our Solar System is located about 9 kPc away from the center of the Galaxy (that has a diameter of about 23 kPc), then the measurement of the isotropy can exclude an origin of the GRBs from sources uniformly distributed in the Galaxy. In fact, in this case one should observe a dipole momentum in the angular

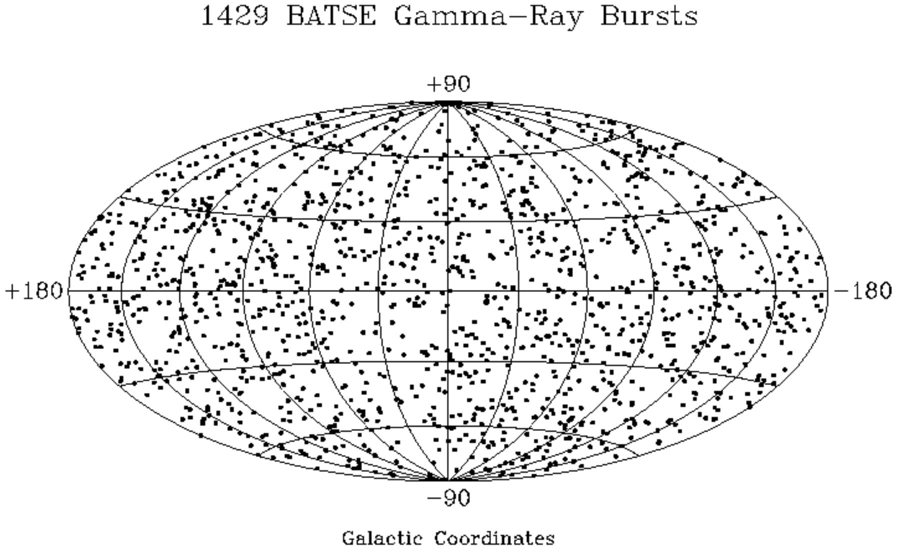

Figure 5.1: Sky distribution of the GRB arrival directions, as derived from the detection of 1429 events by BATSE.

distribution. The upper limit to the dipole anisotropy is 1.5 %.

Peak intensity distribution

Given that the distance scale of the GRBs is unknown, the typical representation of the GRB intensity is given in "peak intensity", in $photons\ cm^{-2}\ s^{-1}$ in a given energy range. If one plots the number of events with peak intensity greater than the abscissa value (i.e. the cumulative function) in a log-log scale, in case of homogeneous distribution of GRBs throughout an Euclidean space (that is, a constant number density and luminosity distribution over the space), one would expect a power law distribution with index -3/2, that interrupts at the sensitivity limit of the instrument. This can be easily understood just thinking that the volume increases as the third power of the distance, while the electromagnetic flux decreases as the square power of the distance. What we observe in a typical representation of the available data, like the one shown in figure 5.2, is that the distribution bends for low peak intensities from the -3/2 trend, due to a paucity of the weaker events. This is an indication that we may be observing the end of the

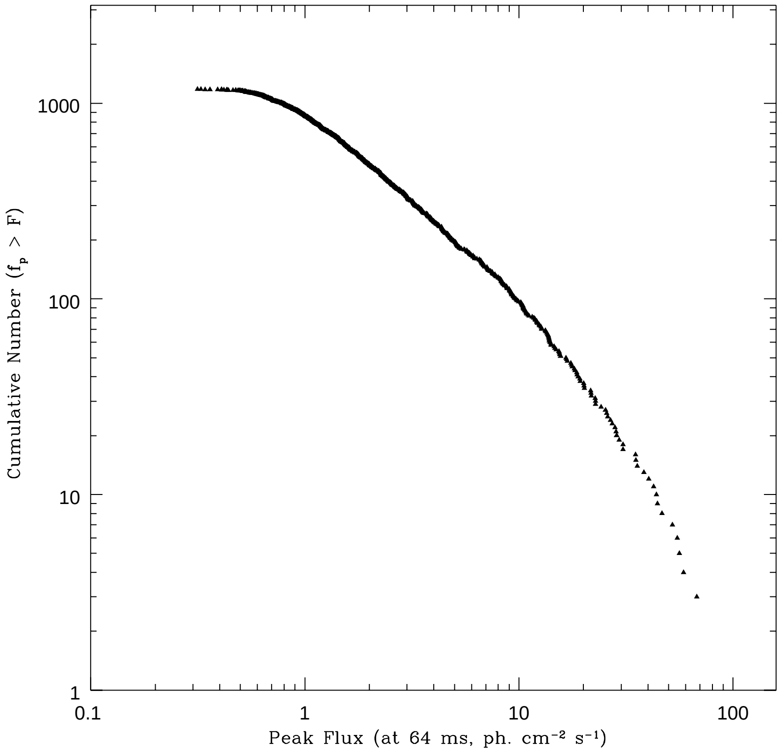

Figure 5.2: Peak intensity distribution of the BATSE GRBs

homogeneous spatial distribution. Of course any conclusion must deal with the intrinsic emission mechanism of the GRB emitters, that is still unknown, and with its possible evolution in the cosmological time. What we can exclude on the basis of this measurement is an homogeneous distribution in our Galaxy, with a fixed intrinsic luminosity.

Spectral properties

With no realistic information on the emission mechanism the interpretation of the energy spectra of the recorded events must start with an empirical approach. This was done by several authors who have tried to classify the GRBs on the basis of their spectral properties. An interesting result is that there is a general correlation between the hardness (that is, the ratio between a high energy channel and a low energy one) and the duration of the GRB: shorter bursts tend to be harder (Kouveliotou et al. 1993).

Another general spectral property of the GRBs is the characteristic *hard-to-soft* evolution during a single peak (Norris et al. 1986, Ford et al. 1995, Piro et al. 1998a). This is observed basically in every GRB for which time-resolved spectra, or at least hardness ratios, are available. Possibly connected with this (in case a synchrotron emission mechanism is responsible for the observed radiation) is also the observed property that the duration of single-peaks increases with the square root of decreasing energy (Fenimore et al 1995).

A very recent analysis on the global spectral properties of GRBs has been performed by Pendleton et al. (Pendleton et al. 1997) with the very intriguing result of a classification of GRB pulses in HE (High Energy) and NHE (No High Energy) types, on the basis of existence of emission at energies above 300 keV. These two classes seem rather well separated and the NHE type shows an effective homogeneous intensity distribution, unlike the NHE one.

Finally, for what concerns the time-averaged GRB spectra, Band et al. (Band et al. 1993) found a good analytical description over the energy range covered by the BATSE experiment, that is 30 keV to 2 MeV. This law is basically consisting of two power laws smoothly connected through an exponential:

$$N(E) = A \cdot \left(\frac{E}{100keV}\right)^{\alpha} \cdot \exp\left(-E/E_0\right)\,, \qquad (\alpha-\beta)\cdot E_0 \;\geq\; E$$

$$N(E) = A \cdot \left[\frac{(\alpha-\beta)\cdot E_0}{100keV}\right]^{\alpha-\beta} \cdot \exp\left(\beta-\alpha\right) \cdot \left(\frac{E}{100keV}\right)^{\beta}\,, \qquad (\alpha-\beta)\cdot E_0 \;\leq\; E$$

The physical parameters of this functional are the two photon indices and the break energy. They are almost free to vary, but for the fact that the high energy power law index β must always be larger than the low energy one α. Band et al. find, on a sample of 54 GRBs detected by the BATSE experiment from 1991 to 1992, that the parameters vary in a rather limited range. In particular $-1.5 < \alpha < +1.0$, $-5.0 < \beta < -1.5$ and E_0 ranges from below 100 keV to above 1 MeV, but with a distribution peaked around 200 keV.

It is very interesting that the Band law is able to account for the GRB energy spectra on the basis of only 3 parameters. The values of these can be actually biased by the restricted energy range of the BATSE experiment. Unfortunately the available sample of energy spectra of GRBs in energy ranges other than the BATSE one is pretty limited. In the past a good sample of GRBs (about 122) were detected by the X and Gamma detectors aboard the Japanese-US satellite *Ginga*. An analysis of about one third of them by Strohmayer et al. (Strohmayer et al. 1998) in the energy range from 2 to 400 keV suggests the possible existence of a further energy break at low energies. A drastic change has been inferred by BeppoSAX satellite that has so far detected 15 GRBs in the energy range from 2 to 700 keV and will detect more in the next two years. The analysis of these events (see chapter 6) reveals a substantial agreement with the Band law.

5.1.2 Theory

The rapid evolution the GRB observational astronomy is undergoing in this last year is affecting the theoretical scenario as well. However, for what concerns the pre-BeppoSAX era the observed properties of GRBs were compatible with three basic models for the possible site of the GRBs emitters: close to our Solar System, an extended halo of our Galaxy, at cosmological distances.

Local origin

The closest site compatible with the observed GRBs properties is the Oort cloud. The latter is the supposed birth place of the comets, that sometimes are scattered into our Solar System. It is a diffuse cloud extending from the edge of our Solar System up to a diameter of the order of 100,000 astronomical units or more (where the fairest planet, Pluto, lies at a mean distance from the Sun of 40 a.u.). This site is geometrically compatible with the isotropic distribution of the GRBs and it is far away enough to account for the unobserved parallax of the GRBs (that is, the absence of a displacement in the apparent position when the event is observed from two or more observers at a distance to each other not negligible with respect to the distance to the object). As for the physical mechanism that could be at the origin of a GRB, it has been suggested that comet-comet collisions (White 1994, Luchkov 1994) could give an appropriate energy release. Reviews of these models, however, conclude that they are unlikely, though still possible (Maoz 1993, Horack et al. 1994, Clarke et al. 1994). More recently, upper limits to parallax with VLA of a few BeppoSAX afterglows rule out completely these models, at least for these GRBs.

Extended galactic halo

The other possible galactic solution is given by an extended halo around our Galaxy. This structure should be large enough to account for the GRB isotropy, compensating for the off-center position of our Solar System with respect to the Galaxy. This lower limit is set at about 125 kPc. On the other hand, if this halo would be largely extended we should observe it in the close-by Andromeda galaxy. The absence of this observation places the upper limit at about 400 kPc (Hakkila et al. 1994). The main concern on this geometrical location is that the existence of the extended halo must be postulated *ad-hoc* for the GRBs, since no evidence for it is gained for any other class of celestial objects.

However, if the GRBs are emitted at a distance of the order of 100 kPc, then the observed intensities imply an intrinsic luminosity of the order of 10^{42} $erg\ s^{-1}$. This amount of energy can be easily obtained from compact galactic objects (i.e. neutron stars) undergoing non-destructive phenomena, like internal reassessment or surface explosions. The most common scenario in this case would be a thermal cooling of the star surface after the GRB explosion.

Cosmological origin

From a geometrical point of view, to place the GRB emitters at cosmological distances is the most suitable way to match the observed properties of isotropy and apparent inhomogeneity. The former would be an automatic result of the large distance to the emitters, while the latter could come from redshift effects and/or intrinsic source evolution. The main argument against this model is the lack of unambiguous observational evidences, like time dilation effects (Norris et al. 1994) or gravitational lensing.

If the mean emission distance is at redshift $z \sim 1$ (that is about 10^{12} times the radius of our Solar System) then the implied intrinsic luminosity would be of the order of 10^{51} $erg\ s^{-1}$. This can only be obtained through catastrophic events, like the merging of two compact components of a binary system such as a neutron star-neutron star or a neutron star-black hole binary (Paczynski 1986). The needed rate for taking into account the observed distribution of GRBs is about 10^{-6} per galaxy per year (Fishman et al. 1995).

Given the destructive nature of the emission process, an experimental proof against the cosmological model would be the detection of a repeating source of GRBs. This has been actually detected in three cases so far, but they have shown peculiar spectral characteristics compared to the GRBs and have been therefore reclassified as *Soft Gamma-ray Repeaters*. Their counterparts seem to be hosted in supernova remnants.

In case such a catastrophic event such as the merging of two compact stars takes place, it is hard to think to an evolution other than that described by the *fireball* model (Cavallo et al. 1978, Rees et al. 1992). In its basic version this is a relativistic expanding shell of electron-positron pairs deriving from the annihilation of neutrinos and anti-neutrinos carrying out most of the energy of the initial explosion. The expanding shell, possibly enriched with a few highly energetic protons, collides with the interstellar medium provoking a shock front that accelerates the electrons, causing them to emit (for example, synchrotron radiation). The Lorentz factor of the expanding shell can account for the blue-shift of the X-rays into the gamma-ray band typical of the GRBs. The morphological/temporal diversity can be accounted for by the possible diversity in the environmental conditions and/or by the existence of more than one shell and therefore from the interaction of one with the other (Fenimore et al. 1996).

5.2 The 1997 breakthrough in GRB astronomy: BeppoSAX results

5.2.1 Pre–SAX experimental scenario

After the accidental discovery by the *Vela* satellites the search for GRBs continued with small experiments on-board the later on-going space missions. GRB experiments flew on-board: *Orbiting Geophysical Observatory 3 and 5; Orbiting Solar Observatory 6, 7 and 8; Apollo 16; Solrad 11A and 11B; Helios 2; Prognoz 6* and *7; Pioneer Venus Orbiter; International Sun Earth Explorer 3*; the *KONUS* and *SIGNE* experiments on-board *Venera 11* and *12* and *Wind; SIGNE 3; Solar Maximum Mission; HEAO-1*; the *MIR* space station; *GINGA; WATCH* and *SIGMA* on-board *GRANAT* and *EURECA; Ulysses; TGRS* on *Wind*. The output of these experiments were limited catalogues of events, with some of them localized at the arcmin precision.

The first experiment dedicated to the systematic study of the GRBs is the BATSE experiment on-board the *Compton Gamma Ray Observatory*. It was conceived to study the angular distribution of the arrival directions in order to associate it, or not, to the distribution of known objects in our Galaxy. The strategy chosen by BATSE was to detect a large number of GRBs, localizing them with a precision from few to tens of degrees. In fact BATSE has already detected about 2.200 GRBs and continue on detecting them at a rate of about six per week.

Given the excellent but not resolutive results achieved by the previous experiments, a new mission was conceived, dedicated to the study and prompt reaction to GRBs. This mission, *High Energy Transients Explorer (HETE)* (Ricker et al. 1997), was launched at the end of 1996, but the deployment of the payload failed. The results achieved by BeppoSAX indicate that the HETE concept was correct and therefore the satellite is scheduled be launched again on 1999 as *HETE-2*.

5.2.2 Afterglow discovery

Before the advent of BeppoSAX the search for counterparts, mainly based on IPN locations, was unsuccessful, and the GRB astronomy has done some progress a statistical approach. This approach has led to an important global characterization of the GRB class mainly thanks to the BATSE experiment. The revolution introduced by BeppoSAX is the capability to study the GRBs on a single-event basis, therefore fixing some fundamental parameters. Before BeppoSAX no one had the idea of what could happen to a GRB emitter soon after the event. If it is visible or not, at what wavelength, and how long.

The operations for a prompt reaction to GRBs started on December 1996. The first detection was on January 11, 1997: GRB970111. Even if an important observational effort has been spent on this event, no immediate result was obtained neither from BeppoSAX or from any ground-based observatory. The second chance was on February 28, 1997: GRB970228.

BeppoSAX detection and X-ray follow-up observation

The 28th February 1997 has been a date that changed the thirty-years old history of the GRB astronomy. On 02:58:00.8 Universal Time (UT) a moderately intense, multi-peak GRB triggered the GRBM on-board BeppoSAX . The same GRB was also detected in one of the two WFCs and therefore localized at about 10 arcmin precision, later reduced to 3 arcmin. The peak intensity of the GRB in the GRBM band (40-700 keV) was 3×10^{-6} $erg\ cm^{-2}\ s^{-1}$, while it was 1.4×10^{-7} $erg\ cm^{-2}\ s^{-1}$ in the WFC band (2-26 keV). Figure 5.3 shows the light curve of this GRB as seen from the GRBM and WFC instruments.

The NFI were pointed to the GRB location in the sky in a time as short as 8 hours after the trigger detection. The previously unknown X-ray source 1SAXJ0501.7+1146 was detected in the field of view of the LECS and MECS instruments at the celestial coordi-

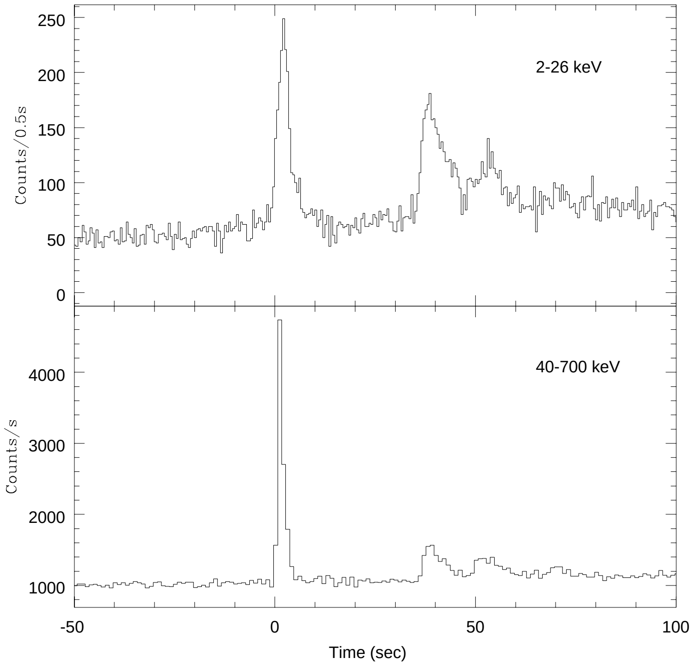

Figure 5.3: BeppoSAX GRBM and WFC light curves of GRB970228.

nates: Right Ascension (R.A.)=$05^h01^m44^s$ and Declination (Decl.)=+11°46'.4 (equinox 2000.0). This first observation lasted about 14.000 s of net observing time, and the source mean flux in the 2-10 keV energy range was 3×10^{-12} $erg\ cm^{-2}\ s^{-1}$ (that is about 10.000 times weaker than the reference celestial source for X-ray astronomy, the Crab Nebula, in the same band).

What was particularly intriguing in this detection is that the new source appeared to be fading away during the observation. So, we found in a small region of the sky that few hours earlier hosted a GRB a previously undetected source with a time behavior indicating it was disappearing. We therefore decided to point again the NFI to the source, and this happened on March 3, 17:37 UT, for an exposure time of 16.000 s. Figure 5.4 shows the comparison between the results of the two observations and the discovery of the first 'afterglow'.

The evaluation of the temporal decay law of the X-ray flux detected from the counterpart of GRB970228 was initially performed by using the two NFI observations only. The

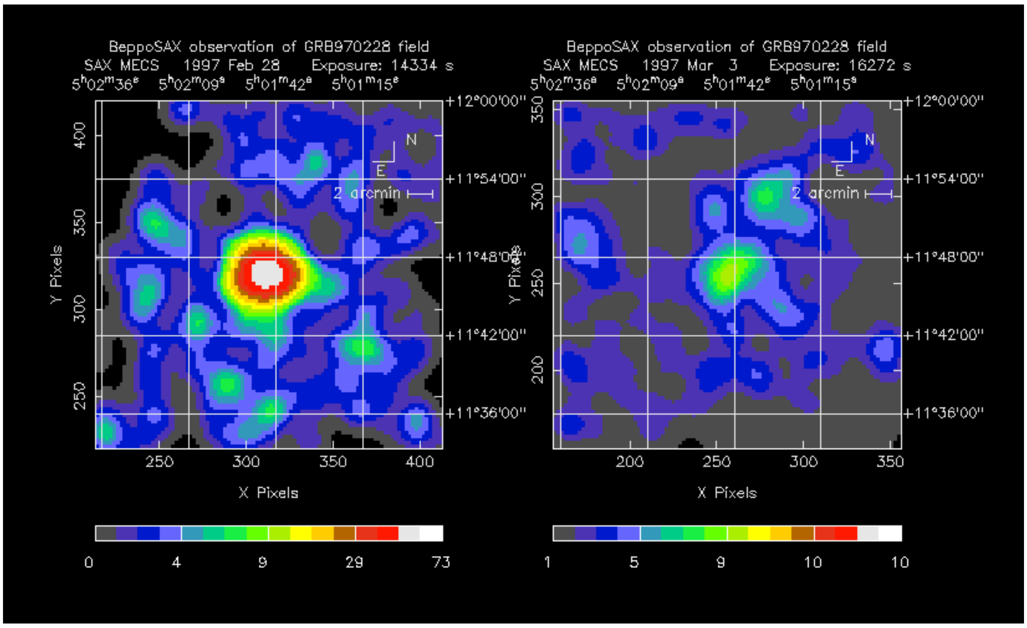

Figure 5.4: BeppoSAX MECS images of the GRB970228 afterglow, 8 hours after the GRB (left) and 3 days after the GRB (right)

mean flux of the source appeared to decrease following a power law dependency on time ($\sim t^{-\alpha}$) with index $\alpha = (1.3 \pm 0.1)$. A further X-ray observation with the Japanese X-ray satellite ASCA detected again the source about one week later with a flux consistent with the same law (Yoshida et al. 1997). This kind of temporal behavior agrees with the general predictions of the fireball models for GRBs (Wijers et al. 1997).

If one observes the GRBM and WFC light curves of the GRB970228 in figure 5.3, it appears rather clearly that the second train of pulses of the GRB are much more soft than the first pulse, that is, the ratio between X-rays and gamma-rays is higher. We therefore decided to compare this second part of the GRB flux with its afterglow. In figure 5.5 the result is shown: the mean X-ray flux of the second part of the GRB (indicated as WFC (35-70 s) in the figure) is perfectly consistent with the backward extrapolation of the power law decay derived from a fit to the NFI data only. In the same figure is also shown the average X-ray flux of the entire GRB (indicated as WFC (0-100 s) in the figure) and it appears less clearly correlated to the above law. Our guess from this analysis is therefore that the afterglow to GRB970228 actually started soon after the GRB. A further

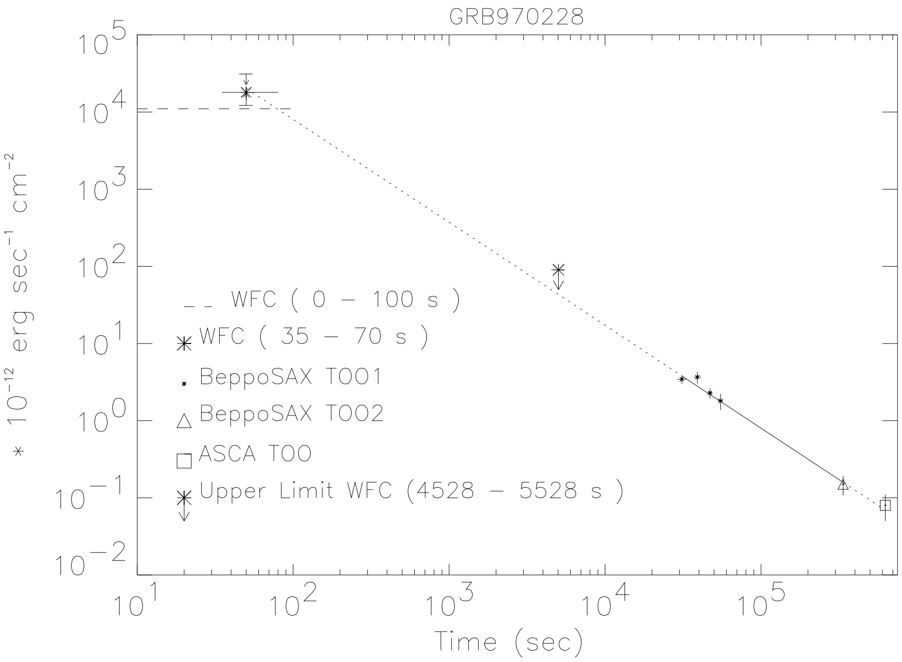

Figure 5.5: BeppoSAX decay curve of the GRB970228 afterglow in the 2-10 keV energy range, obtained with the WFC and the NFI. The result of the ASCA observation is also shown at the bottom right (from Costa et al.,1997)

confirmation of this comes from the spectral analysis that shows a spectral continuity of the GRBM/WFC spectra with the NFI only for the second set of pulses.

Another important result of the spectral analysis of the GRB970228 afterglow is that it seems to exclude a thermal origin of the emission, therefore suggesting that a model in which the radiation comes from the cooling of the surface of a neutron star cannot work in this case.

5.2.3 Optical follow-up observation

While the X-ray monitoring of GRB970228 was going on, an observational campaign of the same object was simultaneously started with the most important optical telescopes. This campaign led to the discovery (van Paradijs et al. 1997) of an optical transient associated with the X-ray afterglow. This new optical source was discovered in the images taken the same night of the GRB and about one week later with the Isaac Newton Telescope (INT) and the William Herschel Telescope (WHT) at the Canary Islands. The source showed a brightness decline from the first to the second observation of about 2.5 magnitudes (V band), corresponding to a flux decrease of about a factor of 300. This was the first discovery of an optical afterglow of a GRB.

The source was continuously monitored up to September 1997 from the most important world-wide telescopes. As in the X-ray domain, the optical flux of the source showed a decrease well described by a power law with index -1.12 (Garcia et al. 1997), again in agreement with the general predictions of the fireball model. But there was still another information to gather from the optical observations. Very important in this respect are the two pointings of the Hubble Space Telescope (HST) (Sahu et al. 1997, Fruchter et al. 1997), the optical telescope orbiting around the Earth and therefore not suffering for the disturbances due to the Earth atmosphere. In the images taken with HST the presence of a nebulosity emerges around the point source located by the ground-based telescopes. An indication of this was also derived from the first images taken at the WHT and INT and other on-ground telescopes. Since both the source and the nebulosity were very weak, there is still today no clear agreement among the scientists if the intensity of this fuzziness is constant with time and what is its interpretation. Many people thinks that the nebulosity was actually constant, and in this case the easiest interpretation would be that it is the host galaxy of the object. If this interpretation will be someday confirmed, this would be the first experimental evidence for an extra-galactic origin of GRB970228.

Confirmation of the positional consistency between GRB970228, the X-ray afterglow and the optical counterpart also comes from other measurements. In fact, the German satellite ROSAT, that is able to locate a X-ray source with an accuracy of about 10 arc-sec, pointed the GRB970228 field on 10 March 1997 (Frontera et al. 1997). It detected the X-ray source 1SAX J0501.7+1146 at a flux level consistent with the extrapolation, in the assumption of a constant spectrum, of the decay law derived from the BeppoSAX measurements and refined its position at few arc-sec accuracy, still coincident with the location of the optical transient.

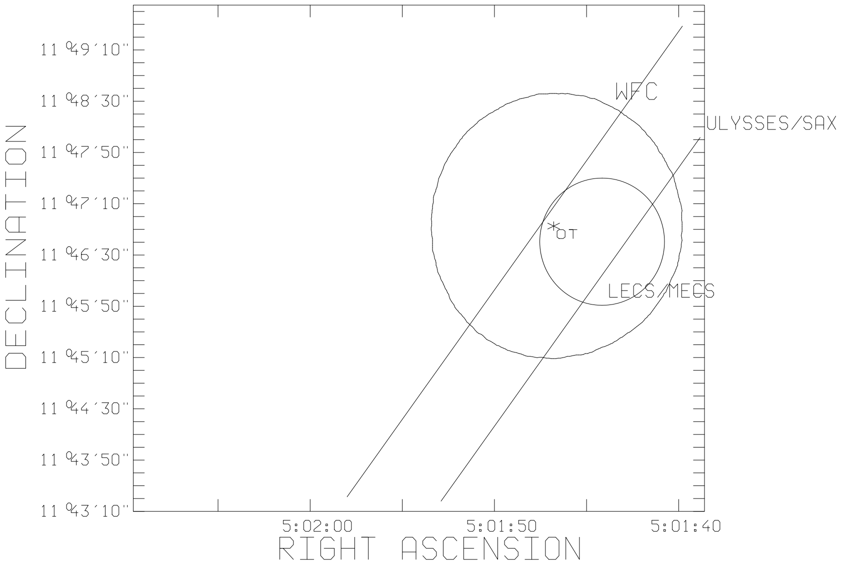

Figure 5.6: Error boxes for GRB970228, obtained with the BeppoSAX WFC and the NFI (larger and smaller circles) and with the Ulysses/BeppoSAX triangulation (strip).

Furthermore, using the GRB arrival times at the BeppoSAX GRBM and at the Ulysses (an interplanetary mission at that time about 2.000 light seconds away from the Earth) GRB detector, Hurley et al. (Hurley et al. 1997) were able to derive an annulus in the sky of the possible arrival directions of GRB970228. This annulus crosses the WFC, NFI error boxes. The X-ray/optical afterglow lies just within the sky area derived from the overlap of all of these error boxes. In figure 5.6 the final location of the source is shown together will all the error boxes.

Other wavelengths

The field of GRB970228 was also observed at wavelength other than X and optical. Radio follow-up observations were carried out at the *Very Large Array* (VLA, Socorro, New Mexico) at a frequency of 1.43 and 8.46 GHz starting less than one day after the GRB and continuing up to August 1997. No positive detection has been obtained for the X/optical source, at a level of tens of microJansky (1 Jy is the typical units of radio astronomy and corresponds to 10^{-26} $watt$ m^{-2} Hz^{-1}). Searches at the wavelength of 3.5 mm (Smith et al. 1997) gave null detections as well, at a level of few mJy.

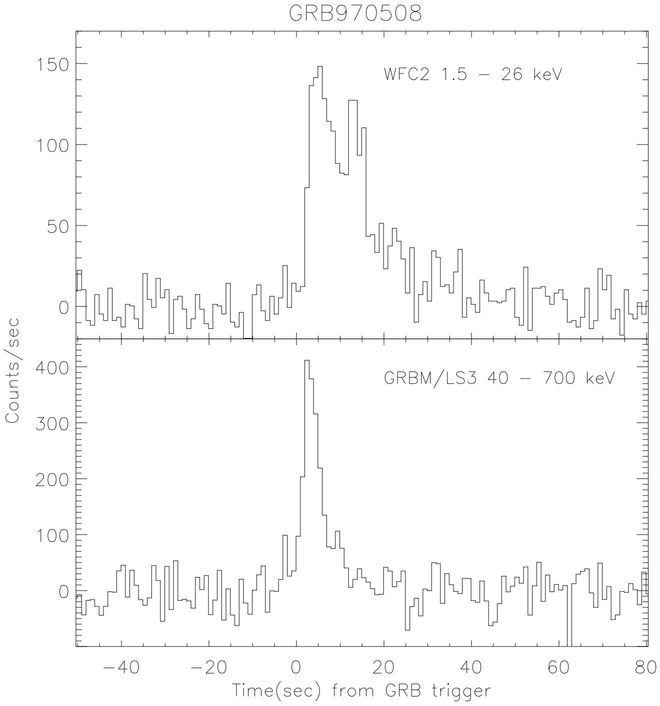

Figure 5.7: WFC and GRBM light curves of GRB970508

The first measurement of a GRB distance: GRB970508

If GRB970228 was the first GRB event for which a X-ray and optical counterpart was found, the event that triggered the BeppoSAX/GRBM on 8 May 1997, had to carry even more striking results. The GRBM detected the trigger for GRB970508 at 21:41:50 UT, just few minutes before than the satellite was passing over the ground station in Malindi (Piro et al. 1998b). The event was simultaneously detected in one WFC, thus providing a prompt localization of the event at the coordinates R.A.=$06^h 53^m 28^s$ and Decl.=79°17'.4 (equinox 2000.0), with a 99% error radius of 3'. In figure 5.7 the light curve of the event is shown in the energy ranges of GRBM and WFC, showing a single-peak structure in the GRBM and a double-peak structure in the WFC. This event was much weaker than the February event. The peak flux was 3.4×10^{-7} $erg\ cm^{-2}\ s^{-1}$ in the 40-700 keV energy range and 6×10^{-8} $erg\ cm^{-2}\ s^{-1}$ in the 2-26 keV band.

Given the favorable detection condition (i.e. just before the data down-load in Malindi) and the experience gained from the BeppoSAX team, the NFI were pointed to the GRB location just 5.7 hours after the event was triggered, and stayed on source for an exposure time of 28.000 s. This was again a world record at that time. As in the GRB970228 case (and in the GRB970402 case, see below) a previously unknown X-ray source was detected at the position R.A.=$06^h53^m46.7^s$ and Decl.=+79°16'02" (equinox 2000.0), consistent with the GRB error box, 1SAXJ0653.8+7916. The BeppoSAX NFI pointed the source again three more times, after 2.7 days (24.000 s exposure), 4.1 days (12.000 s exposure) and 5.7 days (73.000 s exposure). The source was detected in each of the four NFI pointings. Also, an analysis of the WFC data have revealed that the X-ray counterpart of the GRB was detected in the WFC up to 4.000 s after the GRB.

As in the case of GRB970228 we have plotted the mean source flux in a log-log plot, and the result is shown in the upper panel of figure 5.8. In this case the time history of the GRB in the 2-10 keV band is plotted. Unlike the GRB970228 the source power law decay is far from being smooth and uniform, but shows the presence of new activity after a first decay. The ability of the BeppoSAX team to point the source very quickly and the peculiar decay law have also allowed for the first time to study the spectral evolution of the afterglow of a GRB over the four NFI pointings (Piro et al. 1997). A clear evolution can be seen in X–ray afterglow data (Amati, L. et al. 1998), with the hard-to-soft trend typical of the GRBs, that therefore seems to apply at their afterglows as well.

Also the optical follow-up of this event benefited of the experience and better organization of the BeppoSAX team. The first observations of this event started as early as 4 hours after the event (Castro-Tirado et al. 1997). The optical counterpart was identified independently by several observers (Bond 1997, Djorgovski et al. 1997, Sokolov et al. 1997, Pedersen et al. 1997, Castro-Tirado et al. 1997) at a position R.A.= $06^h53^m49.43^s$ and Decl.= +79°16'19".6 (equinox 2000.0). This world-wide effort allowed to follow the temporal behavior of the optical transient from the very beginning to the current days. In figure 5.9 we show the collection of the observations from many telescopes. The time history of the source appears very complicated, and qualitatively different from what de-

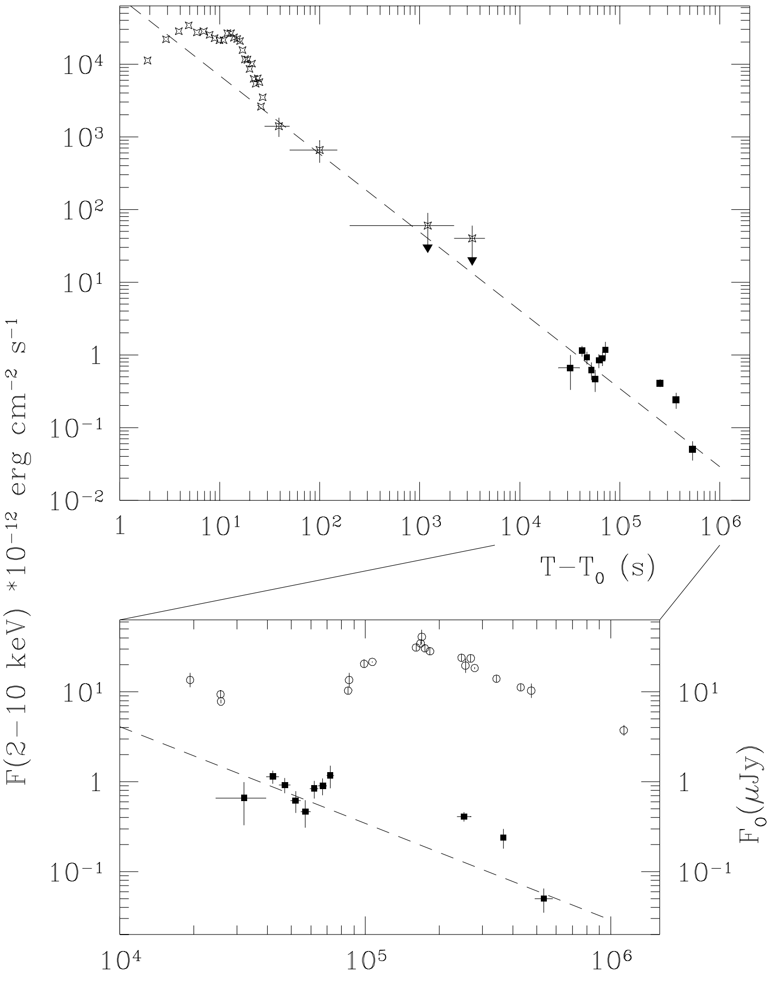

Figure 5.8: Top panel: Decay law of the GRB970508 afterglow as detected by the BeppoSAX WFC and NFI. The WFC provided the data up to 5.000 seconds after the burst. Bottom panel: enlargement of the X-ray decay law and comparison with the simultaneous time history of the optical transient (open circles,)

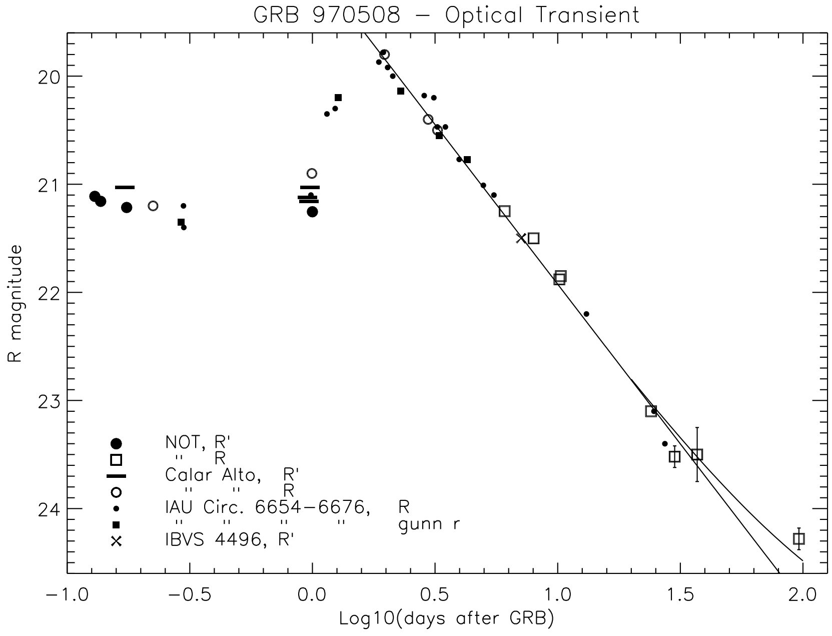

Figure 5.9: Light curve of the optical transient associated to GRB970508

tected in the case of the February event, or better, it looks like in that case we missed the first brightening of the optical transient.

The most important thing, however, is that the optical counterpart was catched up so quickly that it was still bright enough to allow for an optical spectrum to be taken. This was actually done at the Keck telescope (Hawaii) from Metzger et al. (Metzger et al. 1997) and revealed the presence of some absorption line features. These were identified to be FeII and MgII absorption lines cosmologically redshifted, because of a distance corresponding to $z = 0.835$. This is the first direct measurement of the distance of a GRB, and it definitely shows that GRB970508 came from outside our own Galaxy.

This GRB was also seen with the *Hubble Space Telescope* in order to find evidence for a host galaxy, like the one supposed to be detected in the GRB970228 case. The results (Pian et al. 1997) of the observation show a perfectly point-like source, with definitely no evidence for any host galaxy.

Moreover, evidence for a possible redshifted iron line (with z consistent with the value measured with optical spectra) has been recently discovered by means of a more time resolved analysis of the X–ray afterglow spectra (Piro et al. 1999).

The GRB970508 has entered the astronomy books not only because of its X and optical counterpart, but also because it is the first GRB with a radio afterglow. In fact, the radio observations of the GRB970508 field started at the VLA just 3.7 hours after the GRB trigger (Frail et al. 1997b). A new radio source, VLA J065349.4+791619, was seen in a position consistent with the optical transient associated to the GRB. The source flux was monitored at the frequencies of 1.43, 4.86 and 8.46 GHz. Soon after the GRB the source was not detectable, but after about one week it started brightening, reaching a mean flux of about 0.6 mJy at 4.86 GHz. The source exhibited short-term variations with amplitude of a factor of 2 or more. These variations can be interpreted as due to *diffractive scintillation* because of scattering of the radio wave with the interstellar matter. If this interpretation is correct, and if the source distance is taken to be $z = 0.835$ (this would correspond to a distance of $10^{28} cm$), then the short-term variations allow to estimate the source size: after few weeks the linear dimension of the source should have been of the order of $10^{17} cm$.

Furthermore, a monitoring of the same source with the *Very Large Baseline Interferometer* (VLBI) (Taylor et al. 1997) has allowed to derive a positioning as accurate as 0.2 milliarcseconds. The measurement of a null proper motion at the level of 50 milliarcseconds per year is fully consistent with a cosmological distance to the object.

5.2.4 Further developments

After the GRB970508 BeppoSAX observations were interrupted since after the failure of a gyroscope the standard pointing mode (based on three gyroscopes) was no more operative. BeppoSAX observations of GRBs restated after three months and on December 14 1997 a new GRB was detected in WFC. Since then a total of 15 GRBs has been observed in the field of view of WFC and GRBM. We cannot discuss the properties of each GRB in detail, but we remind here the GRBs that had major impact on the development of this new branch of Astrophysics.

The redshift and GRB971214

After the result of GRB970508 no more redshift has been detected on the GRB optical transient itself but 3 redshift have been detected on an host object overimposed to the transient itself. Of course while the association of the absorption features of GRB970508 provides an unambiguous lower limit to the distance, the association of the GRB to each individual host is less compelling. The probability of a random association is in average of the order of 1% even if data come from instruments used at the limit of sensitivity and to be compared with a relatively poor statistics. Since more than 3/4 of the cases optical transient are associated to an (slightly) extended object the following list is very likely true. Ordering by the redshift:

- GRB970508: z=0.835
- GRB980703: z=0.964
- GRB980613: z=1.096
- GRB971214: z=3.418

The result on GRB971214 is the most impressive since, assuming an isotropic emission (no beaming), it corresponds to a significant fraction of a solar mass (around 0.3) converted into electromagnetic energy in the 40–700 keV band. The impact of this datum was high. Until that date the most popular model for the "central engine" was the merging of a Neutron Star-Neutron Star binary system. The energy of GRB971214 requires a beaming if the emission but this makes unlikely the observed rate of GRBs. On the other hand the Optical Transients, when imaged at high resolution, are usually in the central regions of their nebular hosts while the expectation on runaway velocity of binary systems including a collapsed object, combined with the long time required for the merging, makes more likely a location external to the galaxy at the moment of the collapse.

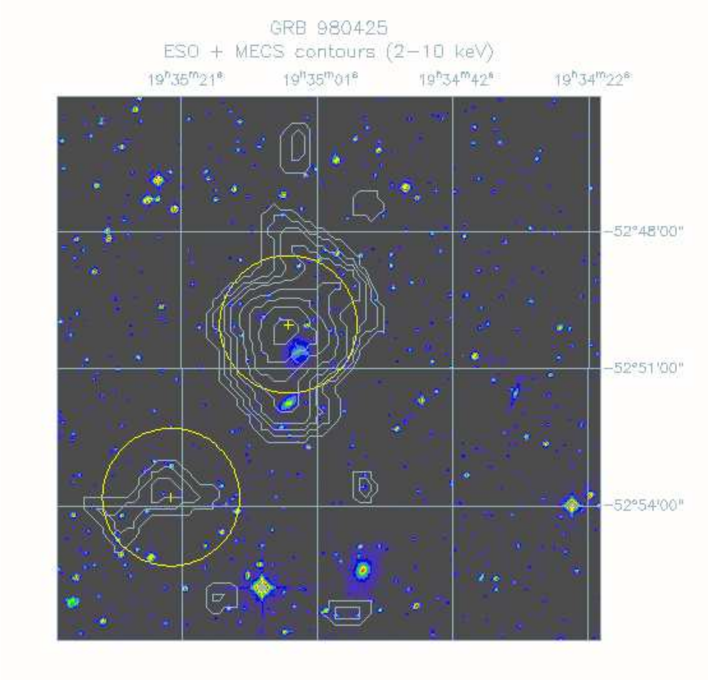

Figure 5.10: Error boxes of the two X–ray sources detected by BeppoSAX NFI in the error box of GRB980425 superimposed to the Palomar Digital Sky Survey

The intriguing GRB980425 and the Supernova Connection

Another GRB which impacted significantly on the evolution of GRB science was the GRB980425. Not peculiar in any particular feature from the point of view of Gamma/X-ray features it had no outstanding afterglow source associated. A very faint source, not unlikely a field object was marginally detected only during the first 12 hours. This could be compared with the fading behavior of the well established X-ray afterglows and is the best "X-ray selected" candidate as the afterglow source. But the optical search following th X-ray position found a really unusual object. A Supernova (SN1998bw) with a very bright radio emission (5 times brighter of any radio SN previously known). The extrapolation to time 0 of the radio curve is coincident (± 1 day) with the GRB. This could open the way to an entirely new perspective. Is this the first finding of a separate class of GRBs or is it a different phenomenology of GRBs observed from a peculiar sight angle?

5.3 Broad band spectral analysis of GRB with the GRBM

The joint X and gamma ray emission study of GRB is a crucial diagnostic of theoretical models for the main mechanism responsible of the emission, the most popular of which are Synchrotron Shock Models (SSM, e.g. Tavani 1997, Sari et al., 1998), in which a flux of relativistic particles (originated e.g. by neutron stars coalescence) radiates through thin synchrotron emission in the presence of a weak to moderate magnetic field (Tavani, 1997).

BeppoSAX WFC + GRBM broad band spectral data can put constraints on this kind of models:

- **average spectra:** the extension to low–energy of average spectra allows to determinate if the nature of the emission is thermal or non–thermal. Pure synchrotron models reproduce very well the average spectral shape of GRBs, which have been found to be well fit by the functional form, a smoothed broken power-law, proposed by Band et al, 1993. The same form seems to fit well also the 2–300 keV Ginga spectra, also if systematically lower values of the spectrum peak energy (i.e. the incident photon energy at which the maximum of the νFν occurs) with respect to BATSE data. Deviations from the Band spectral shape at low energies may be present, due to absorption by the environment surrounding the source, intrinsic synchrotron self-absorption, X–ray excess due to the existence of a quasi–thermal extra component with temperature in the keV range or to effects due to the opacity of the material surrounding the source or to substantial hard to soft evolution of the peak energy. Uncertainties in the incident angles of GRBs detected by Ginga make their low–energy measurements somewhat uncertain;

- **spectral evolution:** the availability of broad band time resolved spectra is crucial to the study of peak energy evolution towards the end of GRB pulse, when the spectrum generally softens. Moreover, there has been indication from a small fraction of BATSE

GRB	Detector	Offset wrt inst. axis	X–ray$^{(a)}$ peak flux	T$_x$ (s)	γ–ray$^{(a)}$ peak flux	T$_\gamma$ (s)
GRB960720	LS1	12.2°	0.25	17	10	8
GRB970111	LS3	12.57°	1.4	60	56	43
GRB970228	LS1	15.38°	1.4	77	37	77
GRB970402	LS1	1.82°	0.16	150	3.2	150
GRB970508	LS3	10.31°	0.35	25	5.6	15
GRB971214	LS1	6.25°	0.2	35	6.8	35
GRB971227	LS1	3.41°	0.36	7	3.8	7
GRB980109	LS1	1°	0.16	20	3.9	20
GRB980326	LS3	19.8°	0.84	9	2.7	9
GRB980329	LS3	19.2°	1.3	53	51	35
GRB980425	LS3	19.0°	0.61	45	2.4	25
GRB980515	LS1	18°	0.3	20	3	15
GRB980519	LS3	7.3°	0.51	190	13	28
GRB980613	LS3	13°	0.13	50	12	50

$^{(a)}$Peak fluxes in units of 10^{-7} erg cm^{-2} s^{-1}

Table 5.1: Basic GRBM + WFC detected GRBs X and gamma properties

events of an initial low–energy suppression, thus indicating changes in the radiative environment. Low energy SSM emission below about 50 keV may be temporarily suppressed by relativistic plasma effects, with the radiative environment relaxing from a complex to a thinner medium. Finally, the study of the spectral properties evolution of GRB emission is crucial for the search of connections with the associated X–ray afterglow emission.

5.3.1 The GRBM + WFC events database

In table 5.1 we report the sample of GRB simultaneously detected by the GRBM and the WFC. For each event we report the interested detector, the offset angle (computed in the way described in chapter 4), and the 1s gamma and X peak fluxes and durations. The gamma peak fluxes have been obtained by means the GRBM ratemeters data analysis.

For all these events GRBM spectral evolution and average spectra analysis have been performed. The estimated fluences in the 40–700 keV, obtained by integrating the best–fitting photon spectrum to the average spectrum, and peak fluxes, obtained by integrating the power–law inferred from the GRBM and AC counts ratio in the time bin corresponding to the peak count rate, were compared to the BATSE results for those events detected by both experiments. The results are consistent, accounting for errors and the different instrument band.

WFC spectral analysis and GRBM+WFC spectral analysis has been performed on a sub–sample of 8 events, that were chosen on the basis of statistical quality of the data. For the WFC spectra and light curves, the background level is estimated using an equivalent section of the detector area not illuminated by the burst or other known X-ray sources. Many of the results of these analysis have been published in specific papers, were the GRB event spectral properties are also compared to the afterglow properties. Some of them have been attached in section A2; the complete list is reported in section A1.

In the next subsections we discuss the results for some of the most interesting events.

5.3.2 Average spectra

The study of GRB average spectra is complementary to that on spectral evolution and can help in better classify the events. Extensive works have been done on BATSE GRB average spectra (Band et al. 1993) from 20 to 2000 keV. The importance of extending average spectrum measurements to energy as low as ∼2 keV is underlined by theoreticists and has been demonstrated by the Ginga results. There is an evidence of a systematic lowering of E_{peak} values when using X and gamma–ray data together, also if Ginga measurements are affected by normalization problems. Thus WFC + GRBM average spectrum measurements can give crucial informations, with the advantage with respect to Ginga data of a much well known X–ray detector response function. Also, with respect to spectral evolution study, average spectra analysis make use of higher statistical quality data, i.e. obtained integrating on entire GRB duration.

In figures 5.11, 5.12, 5.13 results of this spectral analysis for GRB970111, GRB970228 and GRB970402 are shown. Again, XSPEC software package (v. 10.0) was used to derive spectral parameters and their uncertainties (1 σ).

From the fit results, both GRB970111 and GRB970228 spectra are fit with the Band

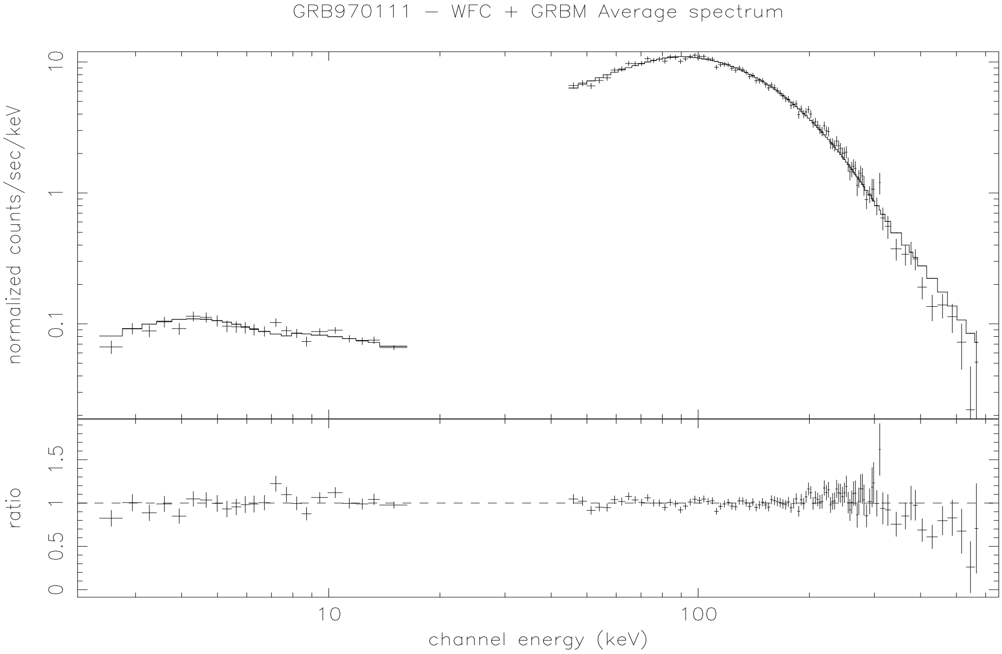

Figure 5.11: WFC/GRBM Time averaged spectrum of GRB970111. The best fit in the 1.5 to 700 keV energy band is obtained with a Band form (see continuous line) with the following parameters: $\alpha = 0.50 \pm 0.04$, $\beta = 2.13 \pm 0.03$, $E_0 = 101 \pm 1$ keV, ($\chi^2/195 = 1.24$).

form, while the spectrum of GRB970402 is fit with a single power law. By comparing the break energy of the GRB970111 spectrum with that of the GRB970228 spectrum, we see that it is much higher for GRB97011 than for GRB970228: 101 keV vs. 13 keV. This fact could be a hint that the peak energy of the νF_ν spectrum evolved much more rapidly towards lower energies in the case of GRB970228. A fast evolution of νF_ν was actually observed in GRB970228 (next section, Frontera et al. 1997b). How this different evolution can influence the presence or not of an afterglow emission is not clear.

5.3.3 Spectral evolution

Spectral evolution study can give more constraints to theoretical models. Models of GRBs and afterglow emissions are mainly based on mechanisms of dissipation of the kinetic energy of a relativistic expanding fireball (Mészáros and Rees 1997, Wijers et al. 1997,

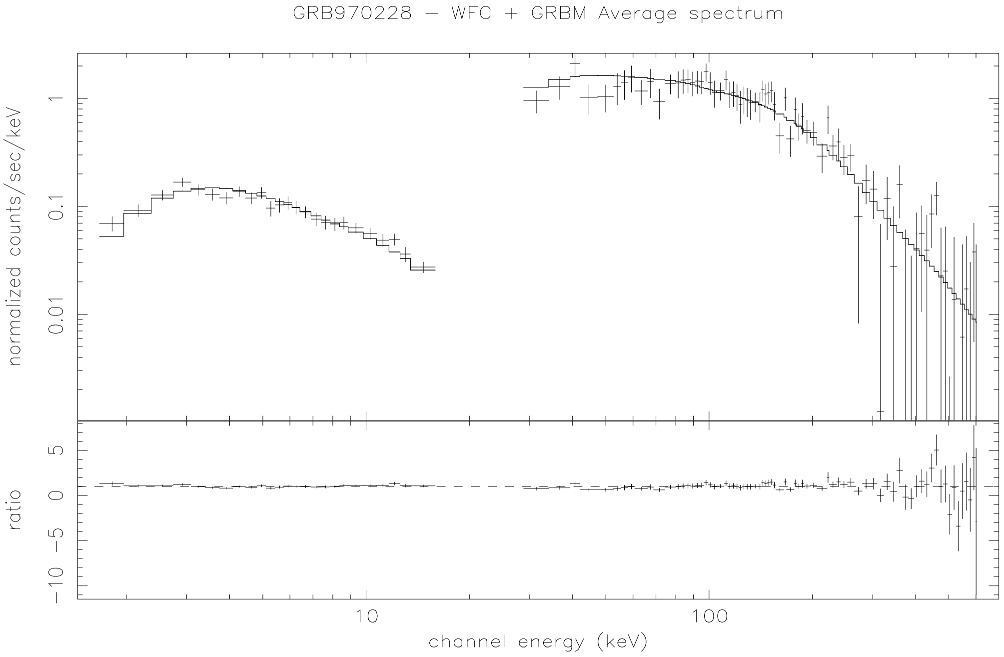

Figure 5.12: WFC/GRBM Time averaged spectrum of GRB970228. The best fit in the 1.5 to 700 keV energy band is obtained with a Band form (see continuous line) with the following parameters: $\alpha = 1.35 \pm 0.07$, $\beta = 1.95 \pm 0.05$, $E_0 = 13 \pm 3$ keV, $\chi^2/195 = 1.05$

Vietri et al. 1997). The origin of the fireball – either merging of neutron stars (NS/NS), neutron star/black holes (NS/BH) (Narayan, Paczyński and Piran 1992), Helium Star/Black Hole (He/BH) (Fryer and Woosley 1998) or the collapse of a massive star (hypernova) (Paczynski 1998), or a type I supernova explosion (Wang and Wheeler 1998), or the adiabatic implosion of a supra-massive NS (supra-nova) (Vietri and Stella 1998) – is still unclear at this stage. In spite of that, the spectral properties of both GRBs and afterglows seem to be consistent with a shock synchrotron model (Tavani 1996), while Inverse Compton emission is expected in the early times (Waxman 1997). Many questions are still open, like those related to the 'engine' of the main event and its radiation production process (e.g., internal shocks, Kobayashi et al. 1997 , the evolution of the spectral properties during GRB, the rise time of the afterglow and its relation with the GRB emission (Sari 1997), the radiation emission process of the afterglow (e.g., radiative shock

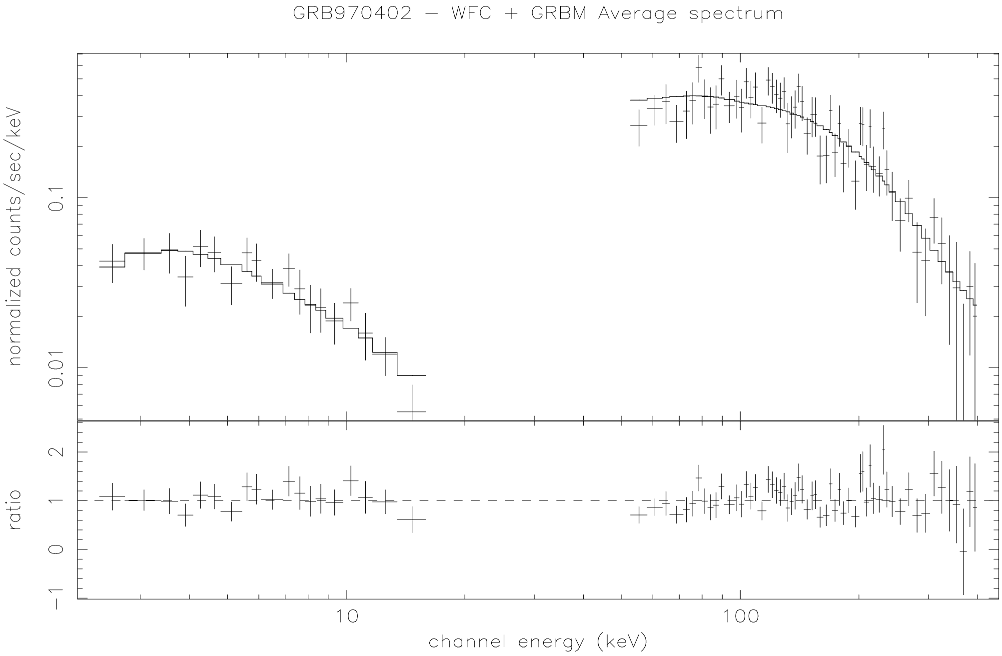

Figure 5.13: WFC/GRBM Time averaged spectrum of GRB970402. The best fit in the 1.5 to 700 keV energy band is obtained with a single power law (see continuous line) with photon index $\alpha = 1.35 \pm 0.08$ ($\chi^2/199 = 0.96$).

vs. adiabatic shock, Sari, Piran and Narayan 1998). All these issues require observations to constrain models.

The time profile in two energy bands (1.5–26 keV and 40–700 keV) of the GRBs investigated is shown in figures 5.14,5.15,5.16. In some cases the X-ray emission is observed to lead the rise of the GRB (e.g., GRB970111), while in other cases (e.g., GRB970508) it is the γ-ray emission to lead the event. Time duration and shape of the GRB time profiles change from one GRB to the other, even if some similarity is observed between GRB980329 and GRB980425.

Each time profile was divided into a given number of temporal sections (see Fig. 5.14,5.15,5.16), and a spectral analysis in the 1.5–700 keV energy band was performed on the average spectrum of each section. The duration of the sections was chosen short during the rise of the burst and and then longer, also taking into account the statistical

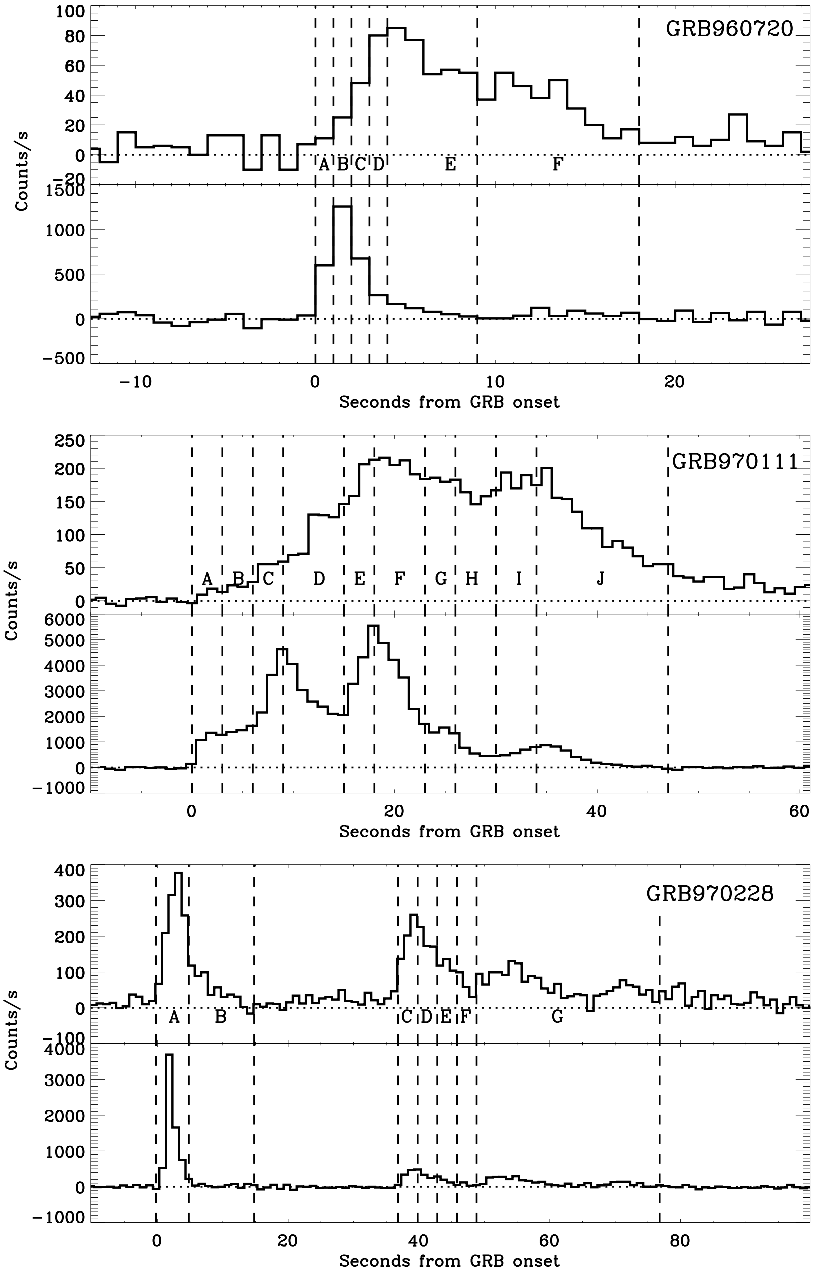

Figure 5.14: Time profiles in the 1.5–26 keV (upper panels) and 40–700 keV (lower panels) energy bands of the GRBs included in our sample. Also shown are the temporal sections in which we performed the spectral analysis.

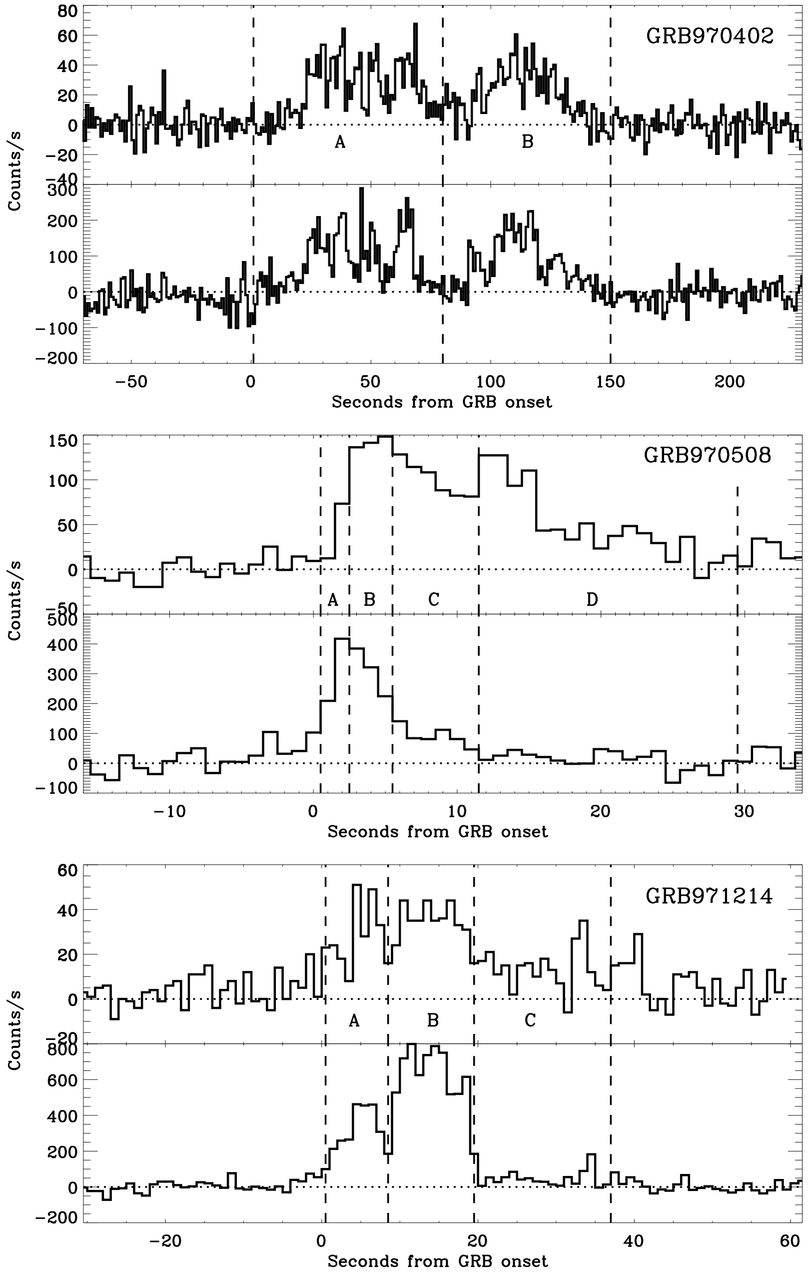

Figure 5.15: Time profiles in the 1.5–26 keV (upper panels) and 40–700 keV (lower panels) energy bands of the GRBs included in our sample. Also shown are the temporal sections in which we performed the spectral analysis - continued

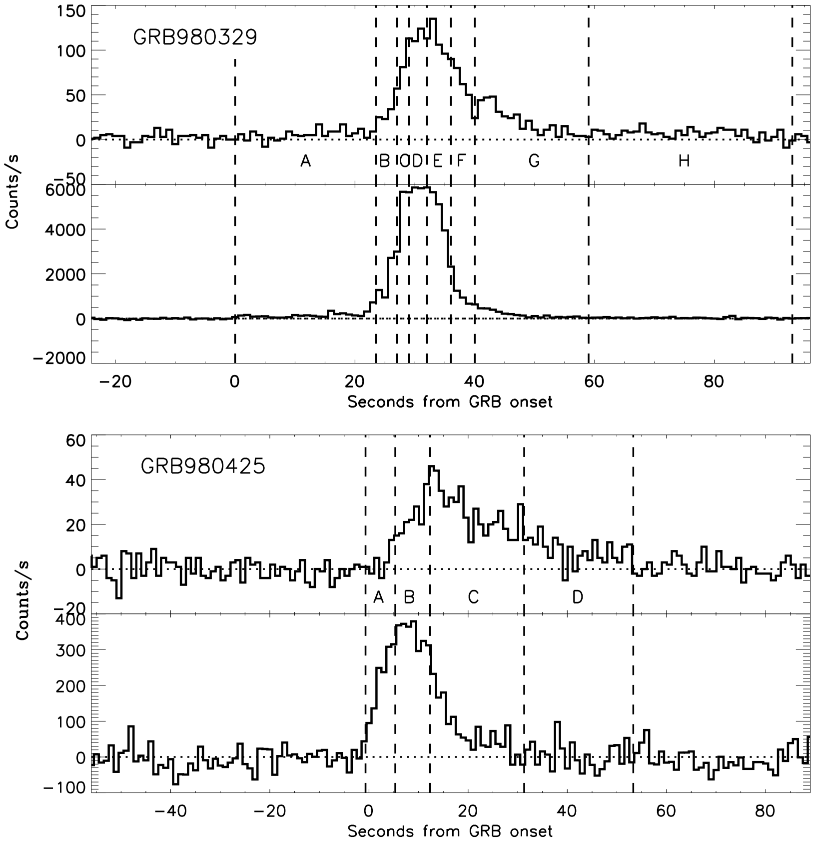

Figure 5.16: Time profiles in the 1.5–26 keV (upper panels) and 40–700 keV (lower panels) energy bands of the GRBs included in our sample. Also shown are the temporal sections in which we performed the spectral analysis - continued

quality of the data. A simultaneous fit to the time averaged WFC and GRBM spectra was performed, by using as input model the Band form.

The fits were performed by fixing the N_H columns to the galactic values in the directions of the GRB.
The derived best fit parameters (photon indices $-\Gamma_X$ and $-\Gamma_\gamma$, peak energy E_p of the logarithmic power per photon energy decade (the $\nu F(\nu)$ spectrum) are shown in Tab. 5.2 , for each of the temporal sections. The value of E_p is given by $E_p = E_0(2 - \Gamma_X)$, under the condition that $\Gamma_\gamma > 2$. The lower limits in passband, reported in Tab. 5.2, were obtained in the cases in which the $\nu F(\nu)$ spectrum showed a bending, with the value of $\Gamma_\gamma > -2$. The lower limit was obtained by deriving the value of E_0 that corresponds to a reduced $\chi^2 \geq 1.2$ for a number of degrees of freedom (dof) ≤ 22 in the fit to the data, with Γ_X frozen to the value obtained from the best fit and Γ_γ assumed slightly lower than -2 (-2.1). The reduced χ^2 values obtained from the best fits were always acceptable (less than 1.1 for 20 dof). Notice that Γ_X is mainly determined by the WFC X-ray spectral data, while Γ_γ by the GRBM data (γ-ray band).
We see how GRB spectrum evolves with energy and with time is apparent. The spectra are generally harder at lower energies or they exhibit the same slope at high and low energies. We do not find bursts with low energy excesses with respect to the Band law (see eq. 1) as found by other authors (Preece et al. 1996, Strohmayer et al. 1998) and only in one case (970111) we find a photon index Γ_X significantly larger than -2/3 . Other authors find larger fractions of GRB with this feature (Preece et al. 1998, Strohmayer et al. 1998).
The spectra become generally softer during the tail of the GRB. A remarkable exception is observed in the spectrum of GRB970228 (Frontera et al. 1998a) discussed below.

In figures 5.17,5.18,5.19, we show the $\nu F(\nu)$ spectrum in each of the temporal sections in which we subdivided the time profile (ν is the photon energy in keV and F_ν is the specific energy flux in keV cm^{-2} s^{-1} keV^{-1}) for GRB960720, GRB970111 and GRB970228, some of the most interesting events from the point of view of spectral evolution.

Table 5.2: Results of GRBM + WFC spectral evolution analysis

#	GRB	Sect.	$\Gamma_X{}^{(a)}$	$\Gamma_\gamma{}^{(a)}$	$E_p{}^{(b)}$
1	GRB960720	A	-1.5 fixed	0.67 fixed	> 700
		B	-1.5 fixed	0.67 fixed	> 700
		C	0.67 fixed	2.44 fixed	293 ± 75
		D	0.67 fixed	2.44 fixed	41 ± 17
		E	0.67 fixed	2.44 fixed	5.1 ± 4.6
		F	0.67 fixed	2.44 ± 0.62	< 2.
2	GRB970111	A	0.95 ± 0.03	0.95 ± 0.03	> 700
		B	-0.14 ± 0.1	1.55 ± 0.02	> 149
		C	-0.11 ± 0.1	1.78 ± 0.02	> 111
		D	-0.16 ± 0.04	2.53 ± 0.05	40.0 ± 2.2
		E	0. ± 0.15	2.93 ± 0.02	30.1 ± 2.
3	GRB970228	A	0.92 ± 0.03	1.54 ± 0.18	> 700
		B	1.4 ± 0.1	2.5 ± 0.1	35 ± 18
		C	1.8 ± 0.1	1.8 ± 0.1	< 2
		D	1.84 ± 0.09	1.84 ± 0.09	< 2
		E	1.92 ± 0.15	1.92 ± 0.15	< 2
		F	1.5 ± 0.4	> 0.6	< 2
		G	1.6 ± 0.1	1.4 ± 0.3	< 2
4	GRB970402	A	1.38 ± 0.03	1.38 ± 0.03	?
		B	1.36 ± 0.04	1.36 ± 0.04	?
5	GRB970508	A	0.97 ± 0.05	0.97 ± 0.05	> 700
		B	1.74 ± 0.14	1.74 ± 0.14	?
		C	1.8 ± 0.4	> 1.4	< 24
6	GRB971214	A	0.37 ± 0.23	1.4 ± 0.03	> 700
		B	0.33 ± 0.27	2.1 ± 0.5	> 224
7	GRB980329	A	0.78 ± 0.14	1.50 ± 0.03	> 285
		B	0.82 ± 0.13	1.5 ± 0.1	> 223
		C	0.79 ± 0.6	1.6 ± 0.2	> 175
		D	1.2 ± 0.5	2.3 ± 0.3	105 ± 80.
8	GRB980425	A	0.92 ± 0.46	2.1 ± 0.2	65 ± 43
		B	1.3 ± 0.9	3.3 ± 0.7	38 ± 33

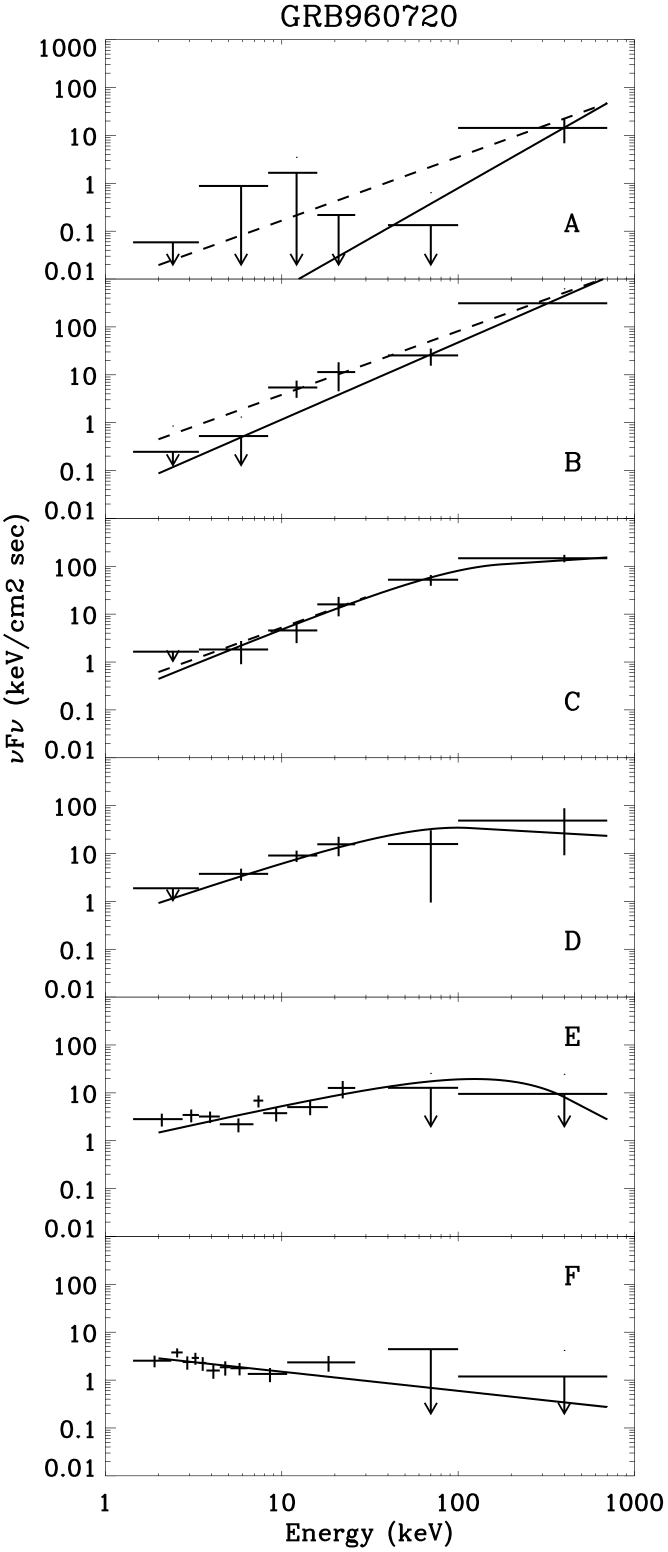

Figure 5.17: $\nu F \nu$ spectrum of GRB960720

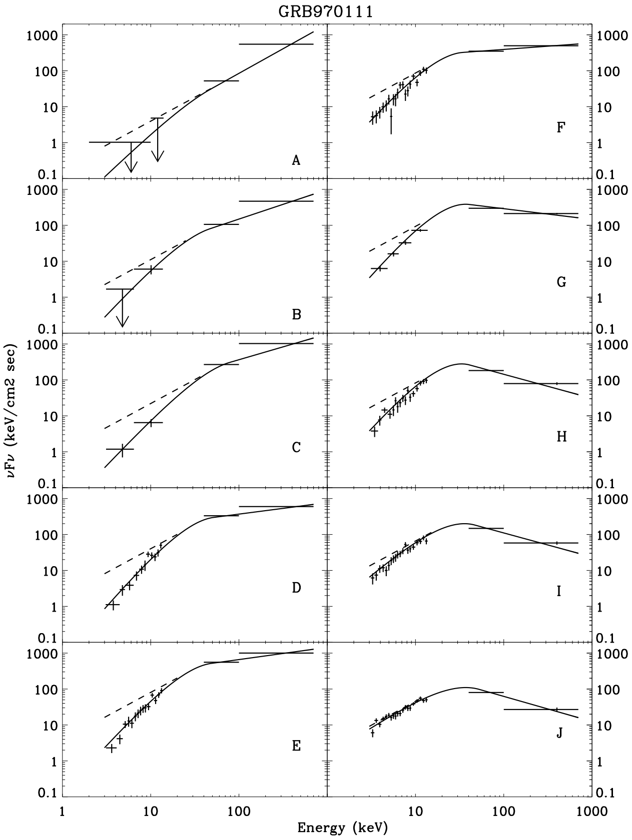

Figure 5.18: $\nu F\nu$ spectrum of GRB970111

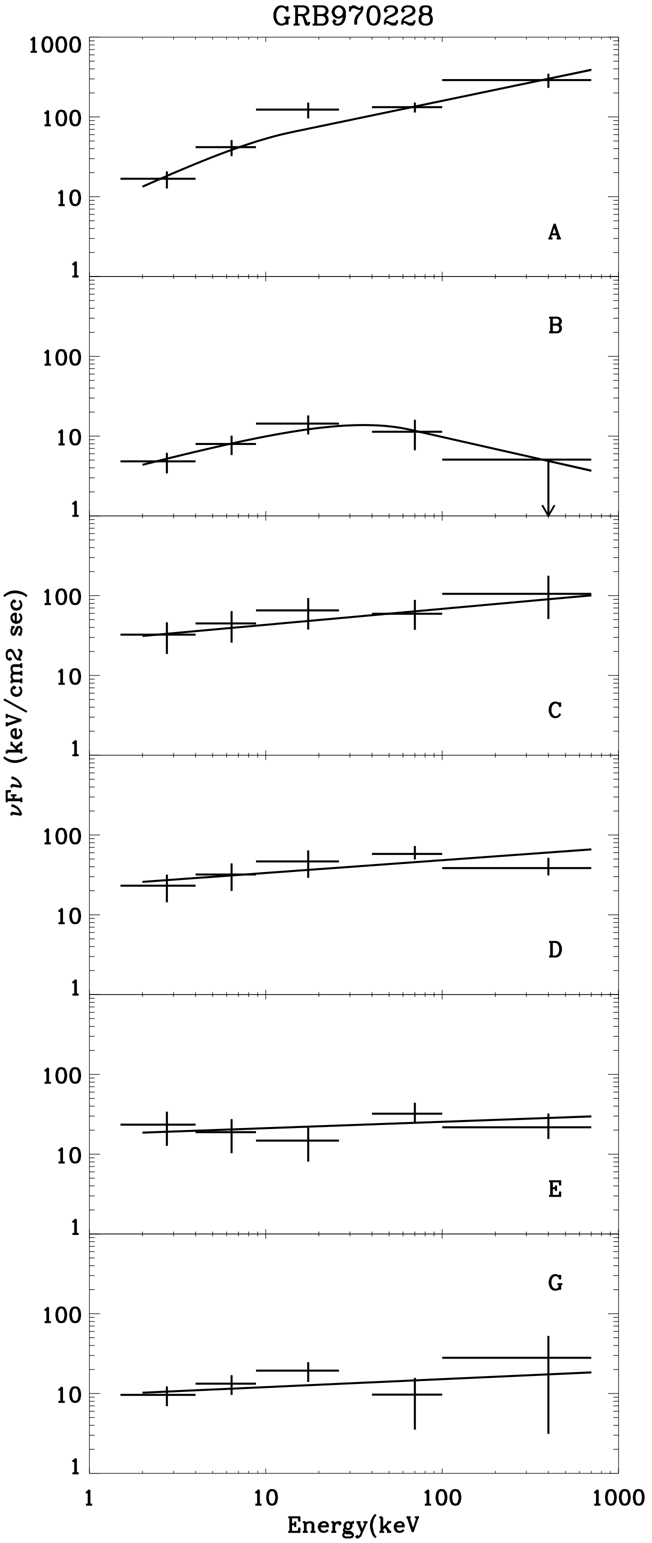

Figure 5.19: νFν spectrum of GRB970228

5.3.4 GRB960720: very fast spectral evolution

As can be inferred also from the X and gamma light curves, this event, in front of the relatively short duration (∼8s in gamma and ∼17s in X) presents a very strong and fast spectral evolution. The lack of X–ray emission in the first s indicates some absorption mechanism operating during the very beginning of the event. Due to the low statistical quality of the data, broad band spectral analysis of GRB960720 (Piro et al. 1998a) has been performed by assuming a fast evolving synchrotron spectrum characterized by self–absorption at a critical energy E_c and a break energy E_0 corresponding to the minimum energy of the electron distribution. Below E_c we assumed the optically thick slope of 1.5; between E_c and E_0 we have adopted the slope of -0.67, expected by optically thin emission below the minimum energy of the electron distribution. Finally, we assumed for the emission determined by the electron distribution a power–law spectral index of -2.4, corresponding to the asympotical value obsered in the last part of the event.

The fits were performed by using the Band form, with alpha, beta and E_0 corresponding to 1.5, E_c and -0.67 in the first two time intervals, and to -0.67, E_0 and -2.4 in the subsequent intervals.

The results, reported in Tab. 5.2, indicate a very fast spectral evolution, with E_c evolving from ∼ 520 keV to ∼6 keV in 1s. Also the evolution of E_0 is extrimely fast. These results challange some fireball models in which self–absorption should be observed only at much lower energies (**?**).

5.3.5 GRB970111: high statistics

GRB970111 spectral evolution shows a peculiar behavior not clearly observed in the other GRBs in our sample: its photon index Γ_X does not change with time, while Γ_γ becomes softer and softer. our energy passband during the primary events, while the Γ_γ variation does not appear to be consistent with the expected change in the case of a synchrotron shock that propagates in a medium of uniform density with constant electron energy distribution. It appears more consistent with a softening of the electron distribution slope with time. If this interpretation is correct, this could account of the non detection or, at most, detection at a very low flux level of X-ray afterglow emission ($1.2 \pm 0.3 \times 10^{-13}\, erg cm^{-2} s^{-1}$ after 17 hrs from the GRB onset (Feroci et al. 1998). Indeed in this case the spectral index p (= -2(Γ_γ+1) or = -2Γ-1, Sari, Piran and Narayan 1998) could become higher than 3. As a consequence, if no electron re-acceleration occurs, we would expect an index of the afterglow power law decay ($\propto t^{-\delta}$), that in the case the peak energy is below our energy passband is given (Sari, Piran and Narayan 1998) by $\delta = (3p-2)/2$ for adiabatic cooling and $\delta = (6p-2)/2$ for radiative cooling (in the case E_p is above our energy passband is given by $\delta = 3(p-1)/4$) (Wijers et al. 1997, Sari, Piran and Narayan 1998). In both cases it results δ at least higher than 1.5, that is consistent with the likely result obtained by Feroci et al. (1998) .

5.3.6 GRB970228: the GRB–afterglow connection

The specific work on the spectral properties of GRB970228 (Frontera et al. 1998a) indicates the existence of a connection between GRB event and the associated X–ray afterglow. showed a strong evolution during the main peak (Fig. 5.14).

The maximum value of α_Γ (-0.9 ± 0.2) achieved at the onset of the 1^{st} pulse as well as the corresponding α_X during the first 5 s are consistent with the asymptotic spectral index below the peak energy E_p (-0.67), as expected in synchrotron emission models (e.g. the Synchrotron Shock Model (SSM) (Tavani 1996). The spectral index of the 1^{st} pulse rapidly evolves to $\alpha_\Gamma = -2.3 \pm 0.3$ at the end of the γ–ray pulse. In the SSM framework the final value of α_Γ during the 1^{st} pulse corresponds to an index of the non-thermal electron energy distribution function $\delta = 3.7$. During the first 3 s of the 2^{nd} pulse the spectrum is significantly harder than during the last part of the 1^{st} pulse. This indicates significant re-energization or relaxation of the particle energy distribution function within the ~ 20 s between the 1^{st} and the 2^{nd} pulse. It appears that the last three GRB pulses and the X–ray afterglow have a similar non-thermal spectrum and that this spectrum does not appear to change from the first to the second TOO. These results are not consistent with simple cooling models of excited compact objects. An analysis of *Ginga* data suggested the existence of black-body spectral components in the ‘precursor’ or ‘delayed’ GRB emission in the 1–10 keV band. In this burst we find no evidence for a black-body spectral component of temperature $\sim$ 1–2 keV or for a prominent soft X–ray component. Furthermore, there is no evidence of upturn in the soft X–ray intensity with respect to the higher energy spectrum.

An evolving non-thermal spectrum for both the burst and afterglow emission is generally expected in relativistic expanding fireball models (Mészáros and Rees 1997, Tavani 1997). In these models, the physics and locations of the shocks associated with the fireballs heavily influence the photon emission mechanisms. Simple fireball models, in which only the forward blast wave radiates efficiently, predict an evolution of the peak energy as a function of the time t from the burst onset, $E_p \propto t^{-3/2}$ (Tavani 1997, Wijers et al. 1997). By extrapolating our data for the 1^{st} pulse of GRB970228 we obtain an initial $E_p \simeq 1$ MeV. In this model, the overall evolution of the X–ray intensity is expected to evolve as $\propto t^{\delta}$ with $\delta = (3/2)(\alpha + 1)$ and α an appropriate photon index (Wijers et al. 1997). If we use our best value of α_{Γ} for the decay part of the 2^{nd} pulse (-1.94 ± 0.13), we obtain $\delta = (-1.4 \pm 0.2)$, a value that is consistent with the observed decay of the GRB970228 afterglow . However, if we use the value of α_{Γ} determined at the end of the 1^{st} pulse (-2.3 ± 0.3), the resulting value of δ (-1.95 ± 0.45) would not agree with our observations. The discontinuity in the γ–ray spectral index observed from the end of the 1^{st} pulse to the beginning of the 2^{nd} pulse requires an interpretation. Given the continuity of the spectral index, starting from the 2^{nd} pulse, any physical relation between the X–ray component of the GRB and the afterglow emission most likely holds with the last set of hard GRB pulses, not with the 1^{st} one. This suggests that the emission mechanism producing the X–ray afterglow might be already taking place after the 1^{st} pulse.

5.4 GRBM observations and spectral analysis of SGR1900+14

The GRBM detection of the August 27, 1998 giant outburst of the soft gamma–repeater SGR1900+14 has given us the oportunity of testing the LS1 response outside the WFC field of view (θ=48°, ϕ=29°) and to obtain very interesting astrophysical results. Also, as anticipated in section 4.8, due the extremely high flux, dead time and recycle corrections were extremely important in the analysis of this source.

In this section, after giving a briefly resuming soft gamma–ray repeaters properties, we outline the specific data analysis steps followed dor this source and the assumptions made, and finally show the results of the spectral analysis.

5.4.1 Soft Gamma Repeaters

Soft gamma-ray repeaters (SGRs) are compact objects undergoing spasmodic instabilities producing X-ray super-Eddington outbursts (sometimes in rapid succession, even 38 events in 350 s as in the case of SGR 1900+14 on May 30th 1998. Recently, the accurate positioning of X-ray outbursts from SGR 1806-20 confirmed that some SGRs are within Galactic supernova remnants. Also the remarkable source SGR 0525-66 that produced the 'March 5th event' ,showing the first evidence of a ∼8 s periodicity following a very intense initial pulse, is positionally coincident with the N49 supernova remnant in the Large Magellanic Cloud. The combination of a relatively long time-scale oscillation (interpreted as rotation of a magnetized compact object) and a lifetime comparable with that of the associated remnant supported a model based on a strongly magnetized ($B \sim 10^{14} - 10^{15}$ G) neutron star for SGR 0525-66. The recent detection of 7.47 s pulsations in the persistent flux from SGR 1806-20 with period derivative $8.3 \times 10^{-11}\mathrm{s\,s}^{-1}$ confirmed this model for that repeater.

5.4.2 SGR1900+14

Among the four SGRs confirmed today, SGR 1900+14 is peculiar for the absence of a surrounding supernova remnant (however, close to the recently determined position a less than 10^4 years old supernova remnant, G42.8+0.6, lies. Three outbursts of moderate intensity from this source were first detected in 1979. The source was detected again in 1992 and in May 1998. ASCA and RXTE observations after the May 1998 activity revealed a periodicity of 5.16 s in the quiescent X–ray (2–10 and 2–20 keV, respectively) emission with period derivative $\sim 1 \times 10^{-10} \mathrm{s\,s^{-1}}$. On 1998 August 27 a very strong outburst from SGR 1900+14 was detected by Konus-Wind, Ulysses and BeppoSAX . The 5.16 s periodicity was unambiguously detected during the outburst. Transient emission was also detected in the radio band with the *Very Large Array* radiotelescope: a previously unknown radio source appeared in the error box of SGR 1900+14 on 1998, September 3 and faded away in less than one week. These observational elements support an interpretation of these phenomena in the framework of the *magnetar* model .

5.4.3 GRBM Observation

The strong outburst from SGR 1900+14 triggered the GRBM on 1998 August 27 10:22:15.7 UT.

The event from SGR 1900+14 was detected with a high signal-to-noise ratio by the 4 detection units, both in the main energy range (40–700 keV) and in the harder energy range (above 100 keV). The event occurred at an elevation angle of 48° with respect to the GRBM equatorial plane, at an azimuthal angle of 29° with respect to the unit #1 axis, and 61° with respect to the unit #4. Since the shadow of the mirrors of LECS and MECS The average effective area of unit #1 at the event direction varies from ∼56 cm^2 at 60 keV to ∼365 cm^2 at 280 keV, while the count rates in units #2 and #3 are strongly affected by scattering effects. For the analysis presented here we used only the signal from unit #1 for which we have the highest signal-to-noise ratio and for which we have an analytical description of the efficiency as a function of energy and source direction. The estimated event duration is about 300 s. The total net counts were 1,007,699 in 40–700 keV and 301,235 above 100 keV. The net peak count rate in the (40–700 keV) energy range was 147,812 counts/s (the average background count rate was 880 counts/s) and 67,025 counts/s in the >100 keV band (the average background count rate was ∼1,000 counts/s). In particular, we corrected our 1-s light curve in the 40–700 keV range for one counter recycle (one recycle implies an additive contribution of 65535 counts/s), by comparing the 1-s resolution data with the high time resolution data (see below) and also comparing the GRBM light curve with that of Ulysses. The correction with only one recycle is what we consider the most likely correction to be applied. However some uncertainty remains, and we present lower limits to the peak flux and fluence.

The 40–700 keV peak flux is detected 1 s after the pulse rise and is $> 2.10 \times 10^{-4}$ erg cm^{-2} s^{-1}. The measured fluence in the same band is $> 1.5 \times 10^{-3}$ erg cm^{-2}. Assuming a source distance of 5 kPc and isotropic emission, we obtain a luminosity of 6×10^{41} erg s^{-1} at the peak and a luminosity of $\sim 3 \times 10^{40}$ erg s^{-1} in the subsequent ∼70 s. The total energy detected by the GRBM in the 40–700 keV band corresponds to $\sim 5 \times 10^{42}$ erg. These flux values are obtained assuming a power law spectrum whose index is computed on the 1-s time-scale from the two GRBM energy bands.

High time resolution data are only available for the first 98 s. After that time, only a 1-s resolved light curve is available. Given the intensity of the event, the counters of the high-resolution data were saturated (and therefore recycled several times) at the event peak. For this reason we cannot determine the event rise time for time-scales shorter than 1 s.

In Fig. 5.20 the 1-s background-subtracted light curve is shown (top panel), together with the 7.8 ms light curve (rebinned at 31.25 s, bottom panel, a) for the time period when it is not affected by saturation. The 5.16-s periodicity, first reported by Hurley et al. (1998c), is clearly detectable in the 1-s resolved light curve over-imposed to the general decay for the entire duration of the event. After a rapid decay during the first 2 seconds (faster in the 100-700 keV band, with respect to the 40-100 keV range), the decay can be approximated with two exponential laws, with time constant $\tau \sim 5$ s for the first ~ 15 s and $\tau \sim 80$ s for the subsequent decay. We also note a modulation of the oscillation with a ~32 s period due to the sampling effect of a 5.16-s period at a 1 Hz frequency. The 31.25 ms light-curve shows that in addition to the 5.16-s periodicity after $35 \sim 40$ s from the beginning of the event the 5.16-s pulse is composed of 4 pulses equally separated in time by approximately 1 s and a dip (see next paragraph).

In the high-resolution light-curve we see no statistically significant evidence of the precursor reported by Hurley et al. (1998b) (about 0.4 s before the sharp rise in the 25–150 keV band). Given the comparable statistical and temporal quality of our data in the 40–700 keV, we are led to the conclusion that the spectrum of the precursor appears to be much softer than the rest of the emission.

5.4.4 Spectral Analysis

Time-averaged Analysis

We obtained 3 240-channel energy spectra for this event of initial and final times with respect to the trigger time as follows: -60–67 s (interval A), 68–195 s (interval B) and 196–323 s (interval C). We fitted to the three spectra the phenomenologically established spectral law for SGRs: an optically thin thermal bremsstrahlung (OTTB). A 10% systematic error has been added to the statistical error in order to take into account the calibration uncertainties at the large off-axis location of the event.

The time integrated spectrum in interval A cannot be fitted with a simple OTTB law, showing an excess at high energies (also reported for the March 5th event. This is likely due to the strong spectral evolution as it appears from the 1-s ratemeters (see below). In fact, from the ratemeter data we note that during the first seconds the emitted spectrum is very hard and it becomes much softer soon after the peak. Assuming different spectral components for these two fractions of interval A, we fitted the energy spectrum with the sum of an OTTB and of a single power law (PL, $I(E) \propto E^{-\alpha}$). The best fit parameters are kT=(31.2 ± 2.5) keV and photon index $\alpha = 1.47 \pm 0.16$ (reduced χ^2=0.705 with 186 d.o.f.). We note, however, that the spectrum can equally be fit with the sum of a PL and a blackbody (BB). In this case the photon index is $\alpha = 1.71 \pm 0.15$, the BB temperature is kT=(16.4 ± 0.8) keV, and reduced χ^2=0.74. We have also tried to fit the spectrum two OTTB laws, two power laws and a broken power law (that usually fits time-averaged spectra of classical gamma-ray bursts) but the fits are unacceptable.

In interval B from the ratemeter data we do not deduce strong spectral variation, therefore we first used a simple OTTB law. However, the best fit to the spectrum for interval B has a kT=(34.2 ± 1.2) keV and the reduced χ^2 is 1.996 (75 d.o.f.). We note the existence of a hard excess, that is likely biasing upward the determination of the effective temperature. Thence we added a PL component to the fit, and the best parameters are kT=(27.6 ± 1.9) keV and $\alpha = 4.5 \pm 0.2$ (reduced χ^2=1.360, 73 d.o.f.). In this case substituting the OTTB with a BB gives a only slightly worse fit (reduced χ^2=1.424, 73 d.o.f.) with kT=(15.5 ± 1.0) keV and $\alpha = 4.5 \pm 0.1$.

In the case of interval C we obtain a satisfactory OTTB fit with kT=(28.9 ± 1.4) keV (reduced χ^2 1.06 with 71 d.o.f.).

Fig. 5.21 shows the energy spectra and best fit models for the time intervals A, B and C. For A and B we reported the OTTB+PL fit and for C the OTTB.

Time-resolved Analysis

We use the 2-channel, 1-s ratemeters to gain information on short time scales spectral variation. Our results can be presented either in terms of an hardness ratio HR (counts in the 100–700 keV band divided by those in 40–100 keV) or of the equivalent temperature kT of an OTTB law. We remind that this is only a functional exponential spectral shape, since the object cannot be thin due to the compactness inferred from the fast variability. The first two seconds can be described by the extraordinary high kT=3200 keV evolving to 60 keV, or with a value of HR=4.06 decreasing to HR=0.75, respectively. (It should be noted, however, that the peak values of kT and HR could be affected by the approximation mentioned in paragraph 2 and therefore it could be significantly smaller.) The subsequent evolution is shown in Fig. 5.20 (bottom panel) for the time interval for which also the high time resolution data are available, both in terms of HR and of kT. We note that the HR and kT vary with the same ∼5-s periodicity observed in the light curve, with the hardness of the pulse increasing almost linearly with phase, in a ramp-like fashion, with distinct maxima correlated with the dips in the light curve.

Alternatively, we have also described the spectral evolution using a PL, deriving a variation of the photon index with time. We find that the first two seconds the 2-channel spectrum can be approximated by a photon index $\alpha = 0.7$, evolving to about 3 in the next two seconds and then varying from 4 to 5 in the subsequent ∼100 s and between 5 and 6 in the rest of the event.

5.4.5 Discussion

Our results show a complex behavior of SGR 1900+14 in outburst that can be resumed in the following points.

(1) A clear determination of the 5.16 s periodicity from the onset of the outburst. We note that such a feature is not detected by the Ulysses experiment suggesting that the capability to detect the periodicity during this part of the outburst is related to the bandpass, similarly to the fact that GRBM did not detect the precursor, while Ulysses did. It is also interesting that we detect a period consistent with the period measured with ASCA within the uncertainty in the period determination (0.02 s), implying that such a large outburst caused a glitch with $\Delta P/P < 3.1 \times 10^{-3}$.

(2) We see a clear transition after ∼35 s in the shape of the 5.16-s pulse profile. At the beginning the pulse is composed of two broad pulses, with relative intensity gradually changing from one period to the next one. At the 6-th pulse from the onset of the outburst the two peaks become sharper and gradually two additional narrow peaks appear. A striking feature of these 4 pulses is their equal mutual distance in time and

their phase stability within the 5.16-s period. This feature is apparent in the PSD as a net enhancement of the n=5 harmonic with respect to the others, corresponding to a periodicity of (1.03±0.03) s. It looks like the 5.16-s periodicity in this part of the outburst is basically due to the lack/occultation of the 5-th peak that one would have expected in correspondence of the 5.16-s dip. The occurrence of such a 5-th peak would have resulted in the disappearance of the 5.16-s periodicity.

(3) The determination of a complex spectral evolution showing a very hard initial outburst pulse followed by softer emission (parameterized with an OTTB with kT$\simeq$ 30 keV) that is strongly modulated in agreement with the periodic pulse structure. We notice a ‘see-saw’ behavior of the HR, with the highest hardness in correspondence of the dips of the light curve. If the dip would be due to an occultation this would imply that a persistent hard component is present in the emitted spectrum. A hard component is also suggested by the persistence for hundreds of seconds of a PL spectral component additional to the single OTTB (see Fig. 5.21, top and middle panel).

(4) Finally, we note that the decay of the event light curve as detected by the GRBM is well approximated by a double exponential law and cannot be described by a power law $I(t) \propto t^{-\alpha}$ as derived for the Ulysses light curve. Also this difference is likely to be ascribed to the different Ulysses-BeppoSAX/GRBM band passes.

The emerging picture is that of a complex phenomenon, involving a highly non-trivial response of a compact object, most likely a highly magnetized neutron star with a structured emitting region, to a major explosive event. Our point no. 2 is worth of special attention. The emitting region surrounding the compact object is first subject to a violent readjustment following the initial strongly super-Eddington outburst (possibly related to a relativistic ejection producing transient radio emission). Subsequent evolution and settling of the 1-s periodic feature reveals a highly structured emitting region with the excitation of higher order, possibly resonant oscillating modes. In particular, the strong enhancement of the fifth harmonic that we observed is unprecedented among SGR strong outburst detections. Trapping in a magnetosphere of emitting ‘blobs’ co-rotating with the surface of a neutron star, or having their proper oscillation mode, might explain the harmonic content of the time variable power spectrum of SGR 1900+14.

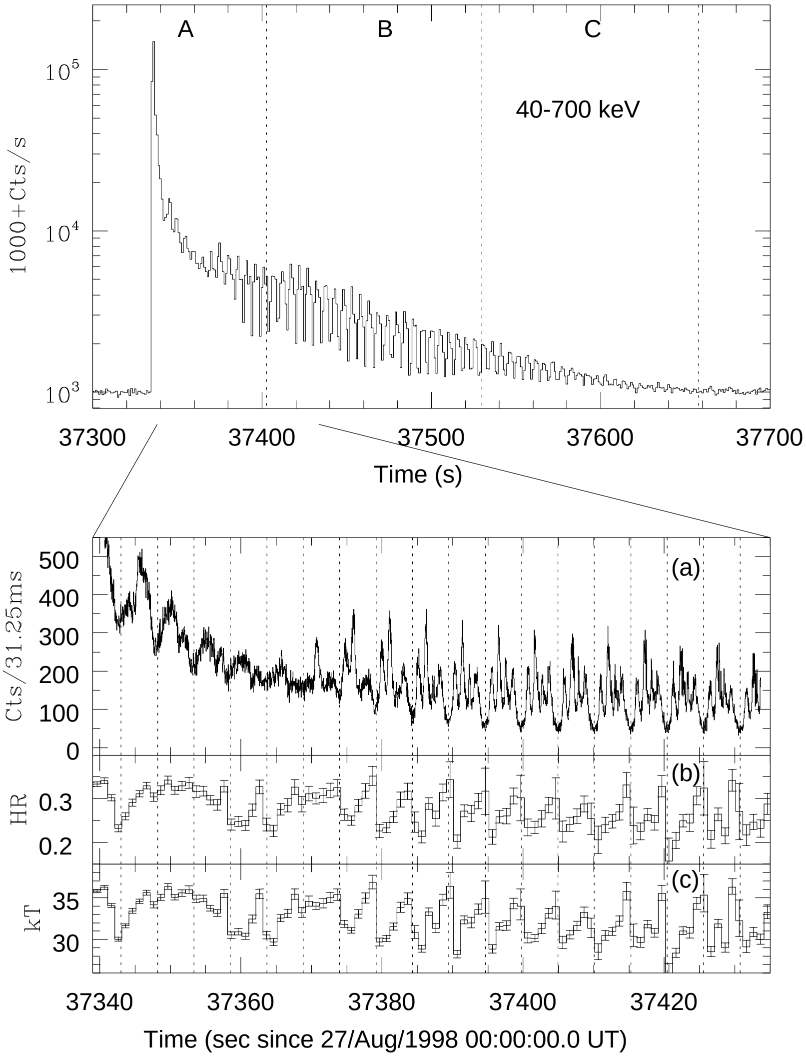

Figure 5.20: Top: 40–700 keV 1-s background subtracted light curve of the event (a value of 1000 counts/s has been added for display purposes). The dashed vertical lines define the intervals A, B and C for which we have the time averaged energy spectra. Bottom: (a) high resolution light curve (rebinned at 31.25 ms) of the available portion of the event ($\sim$100 s); (b) 1-s resolved spectral evolution described in terms of the simple hardness ratio HR=(100–700 keV)/(40–100 keV) and (c) in terms of an equivalent kT of an optically thin thermal bremsstrahlung. 1-σ errors are shown. The vertical dotted lines are spaced by one spin period of the neutron star according to Hurley et al. (1999b).

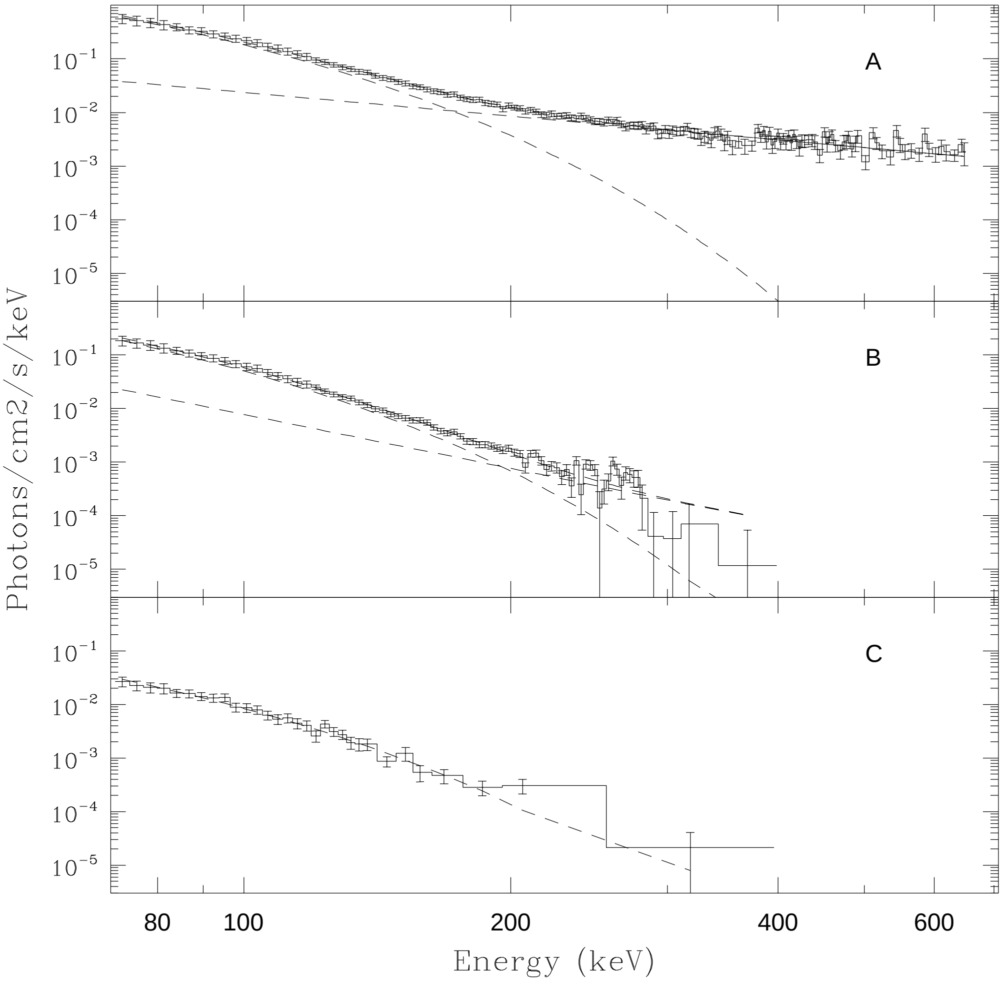

Figure 5.21: Fit to the GRBM spectrum (the individual spectral components are shown as dashed lines) in the energy range 70–650 keV (A) and 70–400 keV (B and C) with a model including: (A) An Optically Thin Thermal Bremsstrahlung (OTTB, kT=31 keV) plus a Power Law (PL, α=1.47) for the time interval from 0 to 68 s with respect to the trigger time; (B) OTTB plus PL with kT=28 keV and α=4.5 for the time interval from 68 to 195 s; (C) OTTB with kT=29 keV for the time interval from 196 to 323 s.

Chapter 6

Conclusions and future perspectives

6.1 Summary of thesis work results

The BeppoSAX Gamma–Ray Burst Monitor, which had in design and realization stage a lower priority with respect to the other experiments on–board the satellite, thanks to the work described in this Thesis, can be used to perform photometry and spectroscopy in the hard X–ray band. GRB broad band study and spectral evolution are unprecedented results having a relevant scientific impact in the field. Indeed, also if GRB X, optical and radio afterglows have undergone a quite rapid comprehension and interpretation just few months after their discovery, it is also true that the burst event itself, although the main physical parameters have been fixed by distance scale determination, remains an elusive object. The measurements reported in chapter 5, and in particular the study of rapid spectral variability, by the joint use of GRBM and WFC data, can surely contribute to the improvement of knowledge in the following items:

- in the frame of the synchrotron shock models: diagnostic of the parameters of the shock and study of the relative role of external/internal forward/reverse shocks;
- testing the possible presence of (Photoelectric, Compton or Self-Synchrotron) absorption, particularly in the first instants of the GRB;
- contribution to the evaluation of the total luminosity of the prompt event;

- study of the transition from the GRB to the afterglow, also to evaluate the total energy content.

The analysis of the data of the giant outburst of SGR1900+14 have provided another instance of the capabilities of GRBM. In presence of a strong signal also the GRBM itself, without the simultaneous data of WFC, can provide information of extreme value: in this case the high sensitivity measurement of the pulse structure, the peculiar hardness ratio and the average spectra, with clear evidence of the hard component.

All these results are still based on the study of sources of known position in the Sky.

6.2 Work in progress

The successful results on the spectral response matrix don't exploit completely GRBM potential. A more detailed study of crystal non–linearity phenomena and of escape and backscattering effects is already under development via analytical methods. The count deficit in the Crab spectrum (chapter 4) is explained at 50% level by this more precise modeling. A better modeling of the materials transparencies at low energies and the use of the Monte Carlo software will allow for a more precise description of these effects, in particular between 40 and 70 keV, where relevant fluxes arrive from the sources.

At higher energies a first application of the Monte Carlo has already produced a correction of the photo peak efficiency. Unfortunately the data from the Crab occultation are very reliable at lower energies, when the source is relatively strong versus the background. At higher energies the application of the earth Occultation Technique requires a better, channel by channel, modeling of the background variation: a first improvement has been already done for the analysis of GRB971214, detected soon after a SAGA passage.

A further development towards a better knowledge of the response matrix should be pushed by a recently defined activity of conjunct analysis of BATSE and SAX/WFC+GRBM data of very luminous GRB. While the BATSE/GRBM comparison has been (see Chapter 4) successful for integrated bands, the analysis of multichannel spectra should provide a good cross calibration of the two experiments.

6.3 Future perspectives

The work described in the present Thesis has consistently pushed to an important astrophysical exploitation of GRBM data. Further significant steps forward are possible and an effort has already been made to do them as fast as possible.

Two major improvements are needed to go from the study of independendetly known transient events only to a study of all the transients detected from GRBM: an independent and possibly automatic and robust trigger capability and the capability of deriving position of transients by GRBM alone.

To arrive to these targets we are doing an extensive use of BATSE data. We are creating a catalogue of events detected by both satellites. The directional information from BATSE (jointed with solar flares and Soft Gamma repeaters data), will allow the spectral and positional calibration of the GRBM. In this way, the GRBM will refine its localizing capabilities, which will not reach the BATSE accuracy in all directions, but could be very useful for events in directions where GRBM response is less ambiguous. Even a coarse localization may result in data of high interest. The Inter Planetary Network (IPN3) is mainly based on the Ulysses/Low Earth Orbit Satellites. In the case of GRBM/Ulysses coincidences we remind that Ulysses detector is relatively small and in a high background environment. Nowadays Ulysses is at about 2500 light seconds from the earth. In absence of any directional information, a transient detected by GRBM must be searched in around 1.5 hours data of Ulysses and many marginal detections may be missed. Even a rough direction may limit the search of at least one order of magnitude making easier the automatic inclusion of BeppoSAX GRBs in IPN-3 (so far performed in a more manual way).

Also the joint exploitation of GRBM and RossiXTE All Sky Monitor, will benefit significantly of this improvement in the positioning capabilities of BeppoSAX GRBM.

Nowadays GRBM triggers are sent to ASM Operation Center to start the search of ASM transient vents. An additional, even coarse positioning information will help to overcome the present difficulty in associating the GRBM events to the ASM transients.

Conclusioni e prospettive future

Il Gamma Ray Burst Monitor di BeppoSAX, nato come uso in bassa priorita' progettuale e esecutiva rispetto agli altri esperimenti del satellite, grazie al lavoro illustrato nella Tesi e' utilizzabile per fare della fotometria e della spettroscopia in banda X-dura. Lo studio dei GRB a larga banda e della loro evoluzione spettrale sono un risultato senza precedenti e di rilevante portata scientifica per lo studio di questi oggetti. Se e' vero che gli "afterglow" X , ottici e radio dei GRB, a pochi mesi dalla scoperta , sono stati rapidamente compresi ed interpretati, e' anche vero che il Burst stesso, ancorche' i principali parametri fisici siano stati fissati dalla definizione della scala delle distanze, rimane un oggetto piuttosto elusivo e le misure illustrate nel capitolo 5 sono sicuramente discriminanti alla luce delle interpretazioni basate sul modello di synchrotron shock (o anche di qualunque altro modello).

Il risultato spettrale, pur positivo, non utilizza ancora tutte le potenzialita' dello strumento GRBM. Uno studio piú dettagliato dei fenomeni di non linearita' dei cristalli e degli effetti degli escape e del backscattering e' gia' in corso con metodi analitici. Il deficit di conteggi riscontrato nello spettro della Crab Nebula (capitolo 4) e' giustificato per oltre il 50% da questa modellazione piú precisa. Una migliore modellazione degli strati piú trasparenti alle basse energie e l'uso del programma di montecarlo dovrebbero arrivare ad una descrizione piú precisa di questi effetti, anche ad energie tra 40 e 70 keV alle quali dalle sorgenti arrivano flussi rilevanti.

Una ulteriore evoluzione verso una migliore definizione della matrice dovrebbe arrivare anche dalla attivita', appena definita, di analisi congiunta di GRB luminosi con dati SAX

WFC/GRBM e dati BATSE.

Un progresso legato anche esso alla analisi congiunta di dati GRBM/BATSE e' quello della creazione di un catalogo di GRB rivelati contemporaneamente dai due satelliti. L'informazione direzionale da BATSE (integrata con dati sui flare solari e sui Soft Gamma Repeaters) consentira' una calibrazione spettrale e posizionale congiunta e quindi la possibilita' per SAX di fornire le posizioni dei GRB con precisioni non comparabili con quelle di BATSE in molte direzioni, ma sicuramente utili in certe direzioni per le quali la risposta dello strumento e' meno ambigua. Giova ricordare che una capacita' di localizzare i GRB anche in maniera approssimativa consentirebbe una presenza autonoma del GRBM in attivita' di "rete" GRB tra le quali la partecipazione alla rete interplanetaria (Ulysses e' a 2000 secondi/luce dalla terra e una direzione approssimativa e' necessaria per associare eventi rivelati dai due satelliti) e la fornitura di Trigger GRBM all'All Sky Monitor di XTE, attivita' gia' in atto ma con scarsa efficienza considerata la difficolta' ad associare i molti eventi SAX ai molti eventi transienti visti da ASM.

References

Amati, L. et al. 1997, SPIE Proceedings, 3114, 176

Amati, L., Piro, L., Antonelli, L.A., et al. 1998, Nucl. Phys. B, 69/1–3, 656

Amati, L. et al., 1999, Astron. Astrophys. Suppl. Ser. , in press

Arnaud, K.A. 1996, Astronomical Data Analysis Software and Systems V, eds. Jacoby, J. and Barnes, J., ASP Conf. Series 101, 17.

Bambynik, W. et al. 1972, Reviews of modern physics, 441, 716

Band, D., Ford, L., Matteson, J. et al. 1992, Exp. Astron., 2, 307–330

Band, D. et al. 1993, Astrophys. J. , 413, 281

Bartlett, L.M., 1994, in *High resolution gamma–ray spectroscopy of the Crab*, PhD Thesis, Nasa Goddard Space Flight Center

Birks, J.B., 1964, in *The theory and practice of scintillation counting*, Pergamon press, Oxford

Boella, G., Butler, R.C., Perola, G.C., et al. 1997a, Astron. Astrophys. Suppl. Ser. , 122, 299–307

Boella, G., Chiappetti, L., Conti, G., et al. 1997b, Astron. Astrophys. Suppl. Ser. , 122, 327–340

H. Bond, IAU Circular n. 6654, May 1997.

Bruca, L., Capalbi, M., Daniele, M.R., et al. 1998, Nulcear Physics B, 69/1–3, 731–734

Castro-Tirado, A. J. et al., 1997, Science submitted.

G. Cavallo and M.J. Rees 1978, Monthly Not. Roy. Astr. Soc., 183, 359.

Chiappetti L., Dal Fiume D., 1997, The XAS data analysis system, in Proceedings of the 5th International Workshop on Data Analysis in Astronomy, eds. di Gesú V., Duff M.J.B., Heck A., Maccarone M.C., Scarsi L., Zimmermann H.U. World Scientific Publ. Co., 101, held at CCSEM Center, Erice, Italy on October 1996

Clarke, T.E. et al. 1994, Astron. Journal, 107, 1873.

Comastri, M., Setti, G., Zamorani, G. et al. 1995, Astron. Astrophys. , 296, 1

Costa, E. et al. 1997, Nature , 387, 783

Costa, E., Frontera, F., Dal Fiume, D. et al. 1998, Adv. Sp. Res., Vol. 22, No.7, 1129–1132

Cusumano, G., Mineo, T., Guainazzi, M. et al. 1998, Astron. Astrophys. , in press

Dal Fiume, D. et al. 1999, in preparation for Astron. Astrophys.

G. Djorgovski et al., 1997, Nature 387, 876.

Dyson, N.A., 1990, in *X–rays in atomic and nuclear physics*, Cambridge University Press

E. Fenimore et al. 1995, Astrophys. Journal Letters, 448, L101.

E. Fenimore et al. 1996, Astrophys. Journal, 473, 998

Feroci, M., Frontera, F., Costa, E., et al. 1997a, SPIE Proceedings, 3114, 186

Feroci, M. et al., 1997b, Astron. Astrophys. Letters submitted.

Feroci, M. et al., 1997c, IAU Circular n. 6610, 4 April 1997.

Feroci, M. et al. 1998, Astron. Astrophys. , 332, L29

Fishman, G. J. et al. 1994, Astrophys. Journal Suppl. Ser., 92, 229.

Fishman, G. J. and Meegan, C. A. 1995, Annual Review Astron. Astrophys., 33, 415.

Ford, L. A., et al. 1995, Astrophys. J. , 439, 307

Frail, D. A., et al. 1997a, Astrophys. J. , 483, L91

Frail, D. A. et al., 1997b, Nature, 389, 261

Frail, D. A. et al., 1997d, Astrophys. J. , 483, L1

Frail, D. A., et al. 1997e, Astrophys. J. , 483, L91

Frenzen, W., 1989, in *X–ray detectors in Astronomy*, Cambridge Astrophysical Series

Frontera, F., Dal Fiume, D., Poulsen, J.M., et al., 1992, Nuclear Instruments and Methods in Physics Research A, 324, 589

Frontera, F., Costa, E., Dal Fiume, D., et al. 1997a, Astron. Astrophys. Suppl. Ser. , 122, 357

Frontera, F., Cinti, M.N., Dal Fiume, D., et al. 1997b, Il Nuovo Cimento 20C, ,5, 797–809

Frontera, F. et al., Astron. Astrophys. Letters (1997) sumbitted.

Frontera, F. et al., 1998, Astrophys. J. , 493, L67

Frontera, F. et al. 1998, in Proc. Fourth Huntsville Symp. on Gamma-Ray Bursts, ed. Meegan, C. A., Preece, R. and Koshut, T. M.

Frontera, F. et al., 1998, in Proc. Fourth Huntsville Symp. on Gamma-Ray Bursts, ed. C.A. Meegan, R. Preece and T.M. Koshut

Fruchter, A. et al., IAU Circular n. 6747, September 1997.

Fryer, C.L., and Woosley, S.E. 1998, Astrophys. J. , 502, L9

Galama, T. et al. 1997, Astrophys. J. , 486, L5

Galama, T. et al. 1998a, Astrophys. J. , L97

Galama, T. et al. 1998, Nature , 395, 670

Garcia, M. R. et al., Astrophys. Journal Letters, submitted (1997) (astro-ph/9710346)

Gatti, E., Cottini, C., Donati, S., et al., 1970, Energia Nucleare, 17, 34

Giacconi, R. and Gursky, H., 1974, in *X–ray astronomy*, Center for Astrophysics, Cambridge, Mass., USA

Gorosabel, J. et al. 1997, Astron. Astrophys. , 339, 719

K. Hakkila et al. 1994, Astrophys. J. , 422, 659.

Harshaw Radiation Detectors manual, 1984, Harshaw/Filtrol

Heitler, W., 1984, in *Quantum theory of radiation*, Dover, N.Y.

Heise, R., et al. 1999, in preparation for ApJ

Horack, J. M. et al. 1994, Astrophys. J. , 429, 319

Jager, R., Mels, W.A., Brinkman, A.C., et al. 1997, Astron. Astrophys. Suppl. Ser. , 125, 557

Hurley, K. et al., 1997, Astrophys. J. , 485, L1.

James, J., 1994, *MINUIT minimization package, Reference Manual, Version 94.1*, 1994, CERN/PACKLIB software library, ftp://asis01.cern.ch/cernlib/doc/ps.dir/minuit.ps

Klebesadel, R. W. et al. 1973, Astrophys. J. , 182, L85.

Knoll, G.G., 1989, in *Radiation detection and measurement*, John Wiley & Sons

Kobayashi, S., Piran, T. and Sari, R. 1997, Astrophys. J. , 490, 92

Kouveliotou, C. et al. 1993, Astrophys. J. , 413, L101.

Kulkarni, S. R. et al. 1998, Nature , 395, 663

Luchkov, B. 1994, Astron. Letters, 20, 253.

Manzo, G., Giarrusso, S., Santangelo, A., et al. 1997, Astron. Astrophys. Suppl. Ser. , 122, 341–356

E. Maoz 1993, Astrophys. J. , 414, 877

F. Marshall et al., IAU Circular n. 6727, 29 August 1997.
T. Murakami et al., IAU Circular n. 6732, 4 September 1997.

N. Masetti et al., 1997 (astro-ph/9710338).

Mészáros, P. and Rees, M.J. 1992, Astrophys. J. , 397, 570

Mészáros, P. and Rees, M.J. 1997, Astrophys. J. , 476, 232

Metzger, M. R. et al., 1997, Nature, 387, 878

Morrison R. and McCammon, D. 1983, Astrophys. J. , 270, 119

Narayan, R., Paczyński, B., and Piran, T. 1992, Astrophys. J. , 395, L83

Nicastro, L. et al. 1998, Astron. Astrophys. , 338, L17

Norris, J. P. et al. 1986, Astrophys. J. , 301, 213.

Norris, J. P. et al. 1994, Astrophys. J. , 424, 540.

Paczynski, B. 1986, Astrophys. J. , 308, L43

Paczynski, B. 1998, Astrophys. J. , 494, L95

Palazzi, E. et al. 1998, Astron. Astrophys. , 336, L95

Pamini, M., Natalucci, L., Dal Fiume, D., et al., Il Nuovo Cimento, 13C, 337, 1990

Parmar, A.,N. et al. 1997a, Astron. Astrophys. Suppl. Ser. , 122, 307–326

Pedersen, H. et al., 1997, Astrophys. J. , 496

Pendleton, G. N., Paciesas, W. S., Mallozzi, R. S. et al. 1995, NIMS A, 364, 567==577

Pendleton, G. N. et al. 1997, Astrophys. J. , 489, 175.

Pian, E. et al., 1997, Astrophys. J. , 492, L103

Pian, E. et al. 1998, paper presented at the Workshop on *Gamma-Ray Bursts in the Afterglow Era*, Rome, 3-6 Nov. 1998.

Piro, L., et al. 1995, *SAX Observers' Handbook*, http://www.sdc.asi.it/pub/sax/doc/handbook/

Piro, L. et al., Proc. 4th Huntsville Gamma-Ray Burst Symposium, Huntsville (AL) 15-20 September 1997.

Piro, L. et al. 1998a, Astron. Astrophys. , 329, 906

Piro, L. et al. 1998b, Astron. Astrophys. , 331, L41

Piro, L., Costa, E., Feroci, M., et al., 1999, Astrophys. J. , in press

Preece, R. et al. 1996, Astrophys. J. , 473, 310

Preece, R. et al. 1998, Astrophys. J. , 506, L23

Preger, B. et al. 1999, Astron. Astrophys. Suppl. Ser. , submitted

Rapiarda, M., Amati, L., Cinti, M.N., et al. 1997, SPIE Proceedings, 3114, 198

Rees, M. J. and Meszaros, P. 1992, Monthly Notes of the Royal Astronomical Society, 258, 41p.

Remillard, R. et al., IAU Circular n. 6726, 28 August 1997.

Ricker, G. et al. 1997, Proc. 4th Huntsville GRB Symposium, Huntsville (AL) 15-20

Sahu, K. C. et al., 1997, Nature, 387, 476.

Sahu, K.C. and Sterken, C. 1998, IAU Circ. No. 6808

Sari, R. and Piran, T. 1997a, Astrophys. J. , 485, 270

Sari, R. and Piran, T. 1997b, Mon. Not. R. Astr. Soc. , 287, 110

Sari, R. 1997, Astrophys. J. , 489, L37

Sari, R., Piran, T. and Narayan, R. 1998, Astrophys. J. , 497, L17

Scarsi, L., 1993, Astron. Astrophys. Suppl. Ser. , 97, 371–383

Siegbahn, K., 1966, in *Alpha, Beta and Gamma–Ray Spectroscopy*, North-Hollm Publ.C., Amsterdam

Smith, I. A. et al., 1997, Astrophys. J. , 487, L5.

Sokolov, V. V. et al., Proc. 4th Huntsville GRB Symposium, Huntsville

Strohmayer, T.E., et al. 1998 Astrophys. J. , 500, 873

Tavani, M. 1996, Astrophys. J. , 466, 768

Tavani, M. 1997, Astrophys. J. , 483, L87

Taylor, G. B. et al., 1997, Nature, 389, 263

Toor, A. and Seward, F. D., 1974, Astronomical Journal, 79, 995

van Paradijs, J. et al. 1997, Nature, 386, 686.

Vietri, M. 1997, Astrophys. J. , 478, L9

Vietri, M., and Stella, L. 1998, astro-ph/9808355

Wang, L. and Wheeler, J. C. 1998, astro-ph/9806212

Waxman, E 1997, Astrophys. J. , 485, L5

Wijers, R. A. M. J. et al. 1997, Mon. Not. R. Astr. Soc. , 288, L51

White, S. 1993, Astrophys. Space Sci., 208, 301

XSPEC, An X–Ray Spectral Fitting Package, Users's Guide for Version 10, 1997, NASA Goddard Space Flight Center

Yoshida, A. et al. 1997, IAU Circular n. 6593

in 't Zand, J. J. M., 1992, Ph.D. Thesis, SRON/Utrecht

in 't Zand, J. J. M., 1998, Astrophys. J. , 505, 119

Appendix A

Thesis work related publications

Many results from the research work reported in this thesis have been included in papers published (or in press) in international refereed scientific journals and in conference proceedings.
In the part of this appendix we report the complete list of these publications divided into four main categories. In the second we attach copies of papers having the more relevant scientific impact and are complementary to what is written in the thesis in explaining the research work results.

GRBM description, calibration, response function and data analysis

- E. Costa, F. Frontera, D. Dal Fiume, **L. Amati**, M.N. Cinti, P. Collina, M. Feroci, L. Nicastro, M. Orlandini, E. Palazzi, M. rapisarda & G. Zavattini, 1998, *"The Gamma–Ray Burst Monitor onboard SAX"*, Advances in Space Research, Vol. 22, 7, 1129–1132

- **L. Amati**, E. Costa, F. Frontera, M. Feroci, M.N. Cinti, J. M. Muller, P. Collina, C. Guidorzi, E. Palazzi & B. Preger, 1999, *"Spectral analysis of GRBs with the Gamma Ray Burst Monitor on–board BeppoSAX"*, Astron. Astrophys. Suppl. Ser. , in press

- **L. Amati**, M.N. Cinti, E. Costa, F. Frontera, D. Dal Fiume, P. Collina, L. Nicastro, M. Orlandini, E. Palazzi, M. Rapisarda & G. Zavattini, 1997, *"Beppo-SAX/GRBM on-ground calibration data analysis"*, SPIE, 3114, 176

•**L. Amati**, M.N. Cinti, E. Costa, F. Frontera, M. Feroci, L. Nicas tro, M. orlandini, D. Dal Fiume, M. Rapisarda, G. Zavattini, E. Palazzi & P. Co llina, 1997, *"Spectral capabilities of the Beppo–SAX/PDS lateral shields a nd Gamma–Ray Burst Monitor"*, Conf. Proceedings of the Italian Physical Society, vol. 58, 7

•B. Preger, E. Costa, M. Feroci, **L. Amati** & F. Frontera, 1999, *"Towards Gamma Ray Burst localization with the BeppoSAX GRBM"*, Astron. Astrophys. Suppl. Ser. , in press

•M. Feroci, F. Frontera, E. Costa, D. Dal Fiume, **L. Amati**, L. Bruca, M.N. Cinti, A. Coletta, P. Collina, C. Guidorzi, L. Nicastro, M. Orlandini, E. Palazzi, M. Rapisarda, G. Zavattini & R.C. Butler,1997, *"In-flight performances of the Beppo-SAX Gamma–Ray Burst Monitor"*, SPIE, 3114, 186

•M. Rapisarda, **L. Amati**, M.N. Cinti, M. Feroci, E. Costa, P. Collina, G. Zavattini, F. Frontera, L. Nicastro, M. Orlandini, E. Palazzi & D. Dal Fiume, 1997, *"The Gamma-Ray Burst Monitor onboard BeppoSAX: the Monte Carlo simulation for the response matrix"*, SPIE, 3114, 194

•M. Feroci, F. Frontera, E. Costa, D. Dal Fiume, **L. Amati**, M.N. Cinti, L. Nicastro, M. Orlandini, E. Palazzi, G. Zavattini & A. Coletta, 1998, *"Performances and scientific results of the BeppoSAX Gamma Ray Burst Monitor"*, Proceedings of the 4th Huntsville Gamma-ray Burst Symposium, AIP Proceedings 428, 451)

•C. Guidorzi, **L. Amati**, M. Feroci, E. Costa, F. Frontera, D. Dal Fiume & M. Orlandini, 1998, *"Monitoring of high energy X-ray sources with the BeppoSAX GRBM"*, Nucl. Phys. B, 69/1–3, 664

Astrophysical applications of GRBM response functions and data analysis techniques

•L. Piro, J. Heise, R. Jager, E. Costa, F. Frontera, M. Feroci, J.M. Muller, **L. Amati**, M.N. Cinti, D. Dal Fiume, L. Nicastro, M. Orlandini & G. Pizzichini, 1998, *"The first*

X-ray localization of a gamma-ray burst by BeppoSAX and its fast spectral evolution”, Astron. Astrophys. , 329, 906

- F. Frontera, E. Costa, L. Piro, J.M. Muller, **L. Amati**, M. Feroci, F. Fiore, G. Pizzichini, M. Tavani, A. Castro–Tirado, G. Cusumano, D. Dal Fiume, J. Heise, K. Hurley, L. Nicastro, M. Orlandini, A. Owens, E. Palazzi, A.N. Parmar, J. in‘t Zand & G. Zavattini, 1998, *”Spectral Properties of the Prompt X-ray emission and Afterglow from the Gamma-Ray Burst of 28 February 1997”*, Astrophys. J. , 493, L97

- L. Nicastro, **L. Amati**, L.A. Antonelli, J.M. Muller, G. Cusumano, L. Piro, E. Costa, M. Feroci, F. Frontera, J. heise, J.J.M. in ’t Zand, A.N. Parmar & R.C. Butler, 1998, *”BeppoSAX observations of GRB970402”* Astron. Astrophys. , 338, L17

- J.J.M. in ’t Zand, **L. Amati**, L.A. Antonelli, E. Costa, M. Feroci, F. Frontera, J. Heise, L. Nicastro, E. Pian, L. Piro & M. Smith , 1998, *”GRB 980329 and its X–ray afterglow”*, Astrophys. J. , 505, L119-L122

- M. Feroci, F. Frontera, M. Tavani, **L. Amati**, E. Costa, M. Rapisarda, 1998, *”A Giant Outburst from SGR1900+14 observed with the BeppoSAX Gamma Ray Burst Monitor”*, Astrophys. J. , in press

- F. Frontera, **L. Amati**, E. Costa, M. Feroci, J.M. Muller, G. Pizzichini, M.N. Cinti, D. Dal Fiume, J. Heise, L. Nicastro, M. Orlandini, E. Palazzi & J.M.M. in ’t Zand, 1998, *”Broad band X-ray Spectral Properties of Gamma–Ray Bursts with BeppoSAX”*, Proceedings of the 4th Huntsville Gamma-ray Burst Symposium, AIP Proceedings 428, 446

- F. Frontera, E. Costa, D. Dal Fiume, M. Feroci, **L. Amati**, M.N. Cinti, A. Coletta, P. Collina, L. Nicastro, M. Orlandini, E. Palazzi, M. Rapisarda & G. Zavattini, 1997, *”Initial results from the Gamma-Ray Burst Monitor aboard the X–ray astronomy satellite BeppoSAX”*, Proc. of the XXV International Cosmic Ray Conference, Vol. 3, 25

GRB afterglows specific papers

•L. Piro, **L. Amati**, L.A. Antonelli, R.C. Butler, E. Costa, G. Cusumano, M. Feroci, F. Frontera, J. Heise, J.J.M. in't Zand, S. Molendi, J. Muller, L. Nicastro, M. Orlandini, A. Owens, A.N. Parmar, P. Soffitta & M. Tavani, 1998, *"Evidence for a late-time outburst of the X-ray afterglow of GB970508 from BeppoSAX"*, Astron. Astrophys. , 331, L41

•**L. Amati**, L. Piro, L.A. Antonelli, R.C. Butler, E. Costa, G. Cusumano, M. Feroci, F. Frontera, J. Heise, J. in 't Zand, S. Molendi, J.M. Muller, L. Nicastro, M. Orlandini, A. Owens, A.M. Parmar, P. Soffitta & M. Tavani, 1998, *"BeppoSAX observations of GB970508: first evidence of bursting activity continuing on very long time scale"*, Nucl. Phys. B, 69/1–3, 656

•E. Palazzi, E. Pian, N. Masetti, L. Nicastro, P. Vreeswijk, T.J. Galama, P. Groot, F. Frontera, M. Della Valle, C. Lindman, C. Kouveliotu, G. Pizzichini, J. van Paradijs, H. Pedersen, F. Mannucci, M. Di Martino, **L. Amati**, S. Benetti, A.J. Castro–Tirado, J. Clasen, E. Costa, D. Dal Fiume, R. Falomo, M. Feroci, J. Fynbo, J. Heise, J. in't Zand, F. Patat, L. Piro, C. Robinson, M. Tornikoski & E. Valtaoja, 1998, *"Optical and Near–Infrared Followup Observations of GRB980329"*, Astron. Astrophys. , 336, L95

•L. Piro, E. Costa, M. Feroci, F. Frontera, **L. Amati**, D. Dal Fiume, L.A. Antonelli, J. Heise, J. in 't Zand, A. Owens, A.N. parmar, G Cusumano, M. Vietri, 1998, *"The X–ray afterglow of the Gamma–ray burst of May 8, 1997: spectral variability and possible evidence of an iron line"* Astrophys. J. , in press

•M. Feroci, E. Costa, F. Frontera, **L. Amati**, L.A. Antonelli, R.C. Butler, M.N. Cinti, G. Cusumano, D. Dal Fiume, F. Fiore, J. Heise, J.J.M. in 't Zand, S. Molendi, J. Muller, L. Nicastro, M. Orlandini, A. Owens, E. Palazzi, A.N. Parmar, P. Soffitta & M. Tavani, 1998, *"Spectral behaviour of X-ray afterglows of GRB observed by BeppoSAX"*, Proceedings of the 4th Huntsville Gamma-ray Burst Symposium, AIP Proceedings 428, 404

- E. Costa, L. Piro, F. Frontera, J. Heise, M. Feroci, **L. Amati**, L.A. Antonelli, R.C. Butler, M.N. Cinti, G. Cusumano, D. Dal Fiume, F. Fiore, J.J.M. in 't Zand, S. Molendi, J. Muller, L. Nicastro, M. Orlandini, A. Owens, E. Palazzi, A.N. Parmar, P. Soffitta & M. Tavani, 1998, *”The temporal behaviour of Gamma Ray Burst and their afterglows from BeppoSAX data”*, Proceedings of the 4th Huntsville Gamma-ray Burst Symposium, AIP Proceedings 428, 409

Prompt GRB follow–up and SGR detections: IAU Circulars

- D. A. Frail, S. R. Kulkarni, L. Nicastro, D. Dal Fiume, M. Orlandini, E. Palazzi, G. Pizzichini, F. Frontera, G. Zavattini, **L. Amati**, M.N. Cinti, E. Costa, M. Feroci, L. Piro, R. Jager, J. Heise, K. Hurley, C. Kouveliotou, G. Fishman & C. Meegan, 1997, *”GRB970111”*, IAU Circular 6545 1F

- E. Costa, M. Feroci L. Piro, P. Soffitta, **L. Amati**, M. N. Cinti, F. Frontera, G. Zavattini, L. Nicastro, E. Palazzi, A. Tesserei, G. Gandolfi, M. Smith, D. Ricci, A. Coletta, J. Heise, J. in 't Zand, M. Tavani, 1997, *”GRB970508”*, IAU Circular 6649 1C

- J. Heise, J. in 't Zand, E. Costa, M. Feroci, L. Piro, P. Soffitta, **L. Amati**, M. N. Cinti, F. Frontera, G. Zavattini, L. Nicastro, E. Palazzi, A. Tesseri, G. Gandolfi, M. Smith, H. Muller, D. Ricci, A. Coletta, M. Tavani, H. E. Bond, 1997, *”GRB970508”*, IAU Circular 6654 2H

- Di Ciolo, L., Celidonio, G., Gandolfi, G., In 't Zand, J., Heise, J., Costa, E., **Amati, L**, 1998, *”GRB981226*, IAU Circular 7074 1D

- Feroci, M., Costa, E., **Amati, L.**, Piro, L., Martino, B., Di Ciolo, L., Coletta, A., Frontera, F., 1998, *”SGR1627–41”*, IAU Circular 6945 3F